IN VIVO AND *IN VITRO* EVALUATION OF AN ECM-BASED OA THERAPY

A Dissertation
Presented to
The Academic Faculty

by

David Sterling Reece

In Partial Fulfillment
of the Requirements for the Degree
Doctor of Philosophy in the
Wallace H. Coulter Department of Biomedical Engineering

Georgia Institute of Technology
Emory University
December 2017

IN VIVO AND *IN VITRO* EVALUATION OF AN ECM-BASED OA THERAPY

Approved by:

Dr. Robert E. Guldberg, Advisor
George W. Woodruff
School of Mechanical Engineering
Georgia Institute of Technology

Dr. C. Ross Ethier
Wallace H. Coulter
Department of Biomedical Engineering
Georgia Institute of Technology

Dr. Johnna S. Temenoff
Wallace H. Coulter
Department of Biomedical Engineering
Georgia Institute of Technology

Dr. Thomas J. Koob
MiMedx Group, Inc.

Dr. Krishnendu Roy
Wallace H. Coulter
Department of Biomedical Engineering
Georgia Institute of Technology

Date Approved: [July 20th, 2017]

ACKNOWLEDGEMENTS

I would like to start by acknowledging my dear wife, Rachel, and her part in encouraging me to start and to finish this PhD. Her encouragement and perseverance during these last six years, and especially the last few months, have made life a joy and helped me get through this endeavor. She has also brought two wonderful children, Jane and Alice, into the world and these two have given this time further meaning and enjoyment. My mother has always been one to encourage me to work hard and to be confident in myself and my abilities. Without the sacrifices she made to raise me and my siblings, I would not have been in a position to get a college degree, let alone a PhD. I would also like to thank my siblings and their families, Kimberly, Sean, Reece, James, Emiley, and little Dillon; Amy; Kevin and Emma; Julie and Race; and Melanie. They have encouraged and supported this entire endeavor. Thank you, also, to my Woodfield family, Brian, Julie, Kellie, Travis, and Abby. They have, in so many different ways, supported my PhD work and Rachel and I wouldn't have made it through this time without them.

This work would not have been possible without the guidance of my mentor, Dr. Robert Guldberg. He has always encouraged me to do better and has given me plenty of opportunities to improve myself and my research capabilities. I would also like to thank my committee for the enjoyable discussions of my research and how to improve the work I have done. Thank you all for taking the time to sit and listen and provide feedback

When it comes to animal work, it isn't possible to do anything without a large group of people to help you in the surgery suite. The Guldberg Lab members have always been willing to help me with my surgeries and to make life during a PhD an enjoyable

experience. I looked forward every year to attending conferences with them and other get-togethers where I could get to know them better and just enjoy their company. I would especially like to thank Laxmi for being willing to sit next to me the last four years and answer so many of my questions. And without Olivia and her assistance with the cell culture work, I would never have finished the third aim of this thesis.

Finally, I would like to also thank my church community. This community has been there to help my family whenever we needed them; to make life enjoyable through the associations, friendships, and various activities; and to provide me with perspective and wonderful opportunities to serve others. This community has touched my heart and has made the prospect of leaving Atlanta a difficult one to face.

TABLE OF CONTENTS

LIST OF TABLES

LIST OF FIGURES

LIST OF SYMBOLS AND ABBREVIATIONS

ADAMTS	A disintegrin and metalloproteinase with thrombospondin motif
CT	Computed Tomography
EPIC-μCT	Equilibrium Partitioning of an Ionic Contrast agent using μCT
ECM	Extracellular Matrix
GAG	Glycosaminoglycans
G-CSF	Granulocyte-Colony Stimulating Factor
GUI	Graphical User Interface
IVIS®	In Vivo Imaging System
IL	Interleukin
MRI	Magnetic Resonance Imaging
MMP	Matrix Metalloproteinase
MMT	Medial Meniscus Transection
MCP-1	Monocyte Chemoattractant Protein-1
μCT	micro Computed Tomography
μ-dHACM	micronized dehydrated Human Amnion/Chorion Membrane
OA	Osteoarthritis
PG	Proteoglycans
RANTES	Regulated on Activation, Normal T-Cell Expressed and Secreted
RPS μ-dHACM	Reduced Particle Size μ-dHACM
sGAG	sulfated Glycosaminoglycans
US	Ultrasound

SUMMARY

Osteoarthritis (OA) is a disease estimated to affect 10-12% of the adult US population and there are currently no clinically proven disease modifying therapies. Micronized dehydrated human amnion/chorion membrane (μ-dHACM) is an extracellular matrix (ECM)-based therapy that has been shown to attenuate OA progression in rats but many of the underlying mechanisms and design variables involved with μ-dHACM are not well understood. The primary objective of this proposed research is to investigate factors that influence the therapeutic benefit of potential disease modifying OA therapies. Specifically this work (i) developed a technological platform using contrast enhanced μCT to quantify cartilage surface roughness and utilized this platform to characterize early articular joint tissue changes in a rat OA model (Chapter 3), (ii) used contrast enhanced μCT and near-infrared fluorescent tracking to evaluate the effect of μ-dHACM particle size on the intra-articular residence time and therapeutic efficacy in a rat OA model (Chapter 4), and (iii) characterized and utilized synoviocyte and cartilage co-culture models to investigate the effect of interactions between synovium and μ-dHACM on OA disease progression (Chapter 5). This work increased the scientific community's understanding of the factors influencing the efficacy of μ-dHACM treatment for OA. It also increased the characterization and understanding of the *in vivo* and *in vitro* models used to investigate these factors.

CHAPTER 1. INTRODUCTION

1.1 Motivation

Osteoarthritis (OA) is a disease characterized by articular cartilage degeneration, subchondral bone sclerosis, and synovitis [1]. An estimated 10-12% of the adult US population are diagnosed with OA, including 37% of those over 60 years of age with knee OA alone, and the total number of cases is expected to increase as the population ages [2].

Currently, there are no FDA approved OA therapies that modify or prevent disease development. One of the challenges in the development of disease modifying OA therapies is the need for better tools and models to understand the factors that influence the therapeutic benefit of potential therapies [3], [4]. Current methods of measuring cartilage surface roughness, an important first indicator of cartilage degradation, do not allow for non-destructive measurements over large surfaces, such as the tibial plateaus of rats.

Micronized dehydrated human amnion/chorion membrane (μ-dHACM) is an extracellular matrix (ECM)-based therapy that has been shown to attenuate OA development in the rat medial meniscus transection (MMT) model. However, many questions remain about μ-dHACM treatment, including: 1) how μ-dHACM particle size effects the treatments intra-articular residence time and overall therapeutic benefit, and 2) how μ-dHACM treatment interacts with the synovium, in which it becomes embedded, to influence the health of the cartilage. This proposed research will seek to answer the questions on μ-dHACM treatment and develop additional tools and models to aid in this investigation.

The objective of this research was to investigate factors that influence the therapeutic benefit of potential disease modifying OA therapies.

1.2 Specific Aims

Specific Aim 1: Develop technological platform for quantifying cartilage surface roughness and use to characterize early articular joint tissue changes in rat OA model. The working hypothesis of this aim was that there were quantifiable morphological and compositional changes detectable by EPIC-μCT in the tibial bone and cartilage one week after MMT surgery. An algorithm for quantifying cartilage surface roughness from EPIC-μCT scans was developed and a MATLAB® program was written to run the algorithm. Changes in cartilage and bone were quantified one and three weeks post-MMT surgery. The outcome of this aim was a software program capable of measuring cartilage surface roughness and an increased characterization of the early morphological and compositional changes in the rat MMT model. These results are presented in Chapter 3.

Specific Aim II: Evaluate the effect of particle size on μ-dHACM treatment. The working hypothesis of this aim was that reducing the particle size of μ-dHACM will alter the attenuation of OA progression and result in faster clearance of the μ-dHACM particles from the joint. μ-dHACM treatments of two different particle size profiles were used in this aim. The efficacy of the two treatments in preventing OA progression was compared in the rat MMT model using EPIC-μCT. The clearance of fluorescently tagged particles of both treatments were also compared in the rat MMT models. Through this aim, we achieved a better understanding of the effect of particle size on μ-dHACM treatment in the rat MMT model. The results of this aim are presented in Chapter 4.

Specific Aim III: Investigate the interactions between synoviocytes and μ-dHACM. The working hypothesis of this aim was that μ-dHACM will influence the cytokine, chemokine, and MMP production from IL-1 and TNF-α stimulated synoviocytes. It was also hypothesized that interaction of synoviocytes and μ-dHACM will provide protection against IL-1 and TNF-α induced PG loss from chondrocyte pellets. The results of this aim are presented in Chapter 5.

1.3 Significance

This research will result in 1) a surface roughness measurement algorithm that allows for a large-scale, high-throughput, non-destructive measurement of cartilage surface roughness; 2) increased characterization of early (one-week post-surgery) disease progression in the MMT rat model; 3) a better understanding of how particle size affects intra-articular residence time and therapeutic effectiveness; 4) increased characterization of synovium/cartilage co-cultures; and 5) increased understanding of how μ-dHACM affects the synovium secretome and, in turn, potentially affects cartilage health.

CHAPTER 2. BACKGROUND AND LITERATURE REVIEW

2.1 Osteoarthritis

2.1.1 Normal Joint Tissues

2.1.1.1 Cartilage

Articular cartilage consists of three main components: the chondrocytes, or cells within the cartilage; the interstitial fluid; and the macromolecular matrix consisting of proteoglycans and collagen, with trace amounts of other macromolecules and proteins. Each plays a vital role in the function of the overall tissue [5].

Cartilage is sparsely populated with cells and the only cells within the cartilage are chondrocytes. These cells are responsible for any matrix remodeling and maintain the integrity of the cartilage [6]. Because there is no vascularization within the cartilage, nutrition and waste transport is achieved through diffusion in the interstitial fluid, aided by joint movement [7].

Water is abundant in both the synovial fluid inside the joint and the cartilage lining the bones, making up 70-80% of the tissue. It permeates through the entire tissue, carrying salts and proteins, and is extremely important for both the function of the cartilage under loads (which will be discussed later) and for nutrient supply. Cartilage has no vascularity and diffusion through the interstitial fluid is the only mechanism by which nutrients and waste can be taken to and from the chondrocytes. Interstitial fluid flow, caused by joint movement, facilitates this transport.[8], [9]

Collagens and proteoglycans make up most the dry weight of cartilage. 50-75% of the weight is collagen and 15-30% is proteoglycans. The remaining dry weight consists of minor proteins and the chondrocytes. [10]

Collagen is a prominent structural molecule throughout the body and provides a semi-rigid frame for the rest of the macromolecules and the chondrocytes. Collagen type II accounts for most the collagen in the cartilage[11] and provides the structural support for the cartilage. There are smaller amounts of types V, VI, IX, and XII[12] and it is thought that these other types help stabilize type II and participate in intermolecular interactions[10]. The structure, amount, and orientation of collagen fibers vary with both depth in the tissue and proximity to chondrocytes [13].

Proteoglycans are protein cores surrounded by long polysaccharides. They form into large globular groups that are kept in place by the collagen frame. These proteoglycans have a net negative charge and attract water into the cartilage, especially following compression of the cartilage. Most the proteoglycan is aggrecan but amounts of biglycan, decorin, and fibromodulin are also present. The minor proteoglycans are thought to assist in the development and repair of the cartilage. [14]

The overall structure of articular cartilage can be divided into different zones delineated according to their depth in the cartilage. These zones vary by both macromolecular and cellular composition and material properties. The zones, in order from the articulating surface bordering the synovial fluid to the subchondral bone, are called the superficial/tangential zone, middle/transitional zone, and deep/radial zone[15].

On the surface of cartilage, there is also the lamina splendens, a very thin, acellular, fibrous layer[16]. Though the exact purpose and origin of this layer is uncertain, it is thought that it could assist in reducing the friction within the joint.

The superficial or tangential zone is the upper 10-20% of the articular cartilage. The collagen fibers have small diameters and are densely packed, aligned parallel to the surface of the cartilage. There is low proteoglycan content and low permeability to fluids. The cells are flat and discoidal in shape, aligned with the collagen fibers, and are densely packed. They secrete specialized proteins thought to help with the overall wear and frictional properties of the cartilage.

The middle 40-60% section is called the middle or transitional zone. Here the collagen fibers have a more random alignment as they transition from the tangential alignment to a more radial alignment in the deep zone. This zone has the highest proteoglycan content. The cells are spherical and there are fewer in number than in the superficial zone.

The deepest of the zones, the deep or radial zone, usually consists of 20-50% of the cartilage depth. Here the collagen fibers are bundled together and aligned radially, anchored to the underlying bone. The proteoglycan amount is much less than the middle zone and the cell amount is the lowest of the three zones. The cell shape is generally elliptical and the cells are aligned in columns in the same direction as the collagen. [5]

The tidemark marks the transition from the deep zone to the calcified zone of articular cartilage. This calcified zone is the transition from cartilage to subchondral bone, the anchor of the cartilage to the bone.[17]

The structure of the cartilage also changes with proximity to the individual chondrocytes. The pericellular matrix immediately surrounds the cell and has fine collagen fibers, high proteoglycan amounts, fibronectin, and collagen type VI. The territorial matrix surrounds the pericellular matrix and is a transition from that matrix to the surrounding extracellular matrix. The extracellular, also called the interterritorial, matrix is furthest from the cell and the makeup depends on the depth of the cartilage at that point. It is thought that these three matrices around the cell help to alter the strains felt by the chondrocytes as a result of forces within the cartilage.[5]

Function

The function of articular cartilage is to provide a low friction shock absorber to facilitate joint movement and load transfer. The overall biochemical and mechanical structure of tissue are both important for this to occur. If one or both is damaged or changed, the force profile within the tissue changes and a general overall loss of function can occur, leading to disability and pain in that joint. [5]

In normal use, cartilage experiences compression, tension, and shear; compression being the primary loading mode while there is also substantial shear stress that are relevant to cartilage degeneration. These different modes are the result of the complex intermolecular interactions between the macromolecules, cells, fluid, and surrounding bone.[10], [18]

The interstitial fluid is extremely important to the cartilage function, especially under compression. When suddenly loaded, the fluid is forced out of the cartilage, but because of the low permeability of the surrounding matrix, there is a great deal of friction going against the flow. This causes a pressurization of the fluid and the fluid carries the initial loading,

sparing the solid matrix. The high friction between the fluid and the matrix also acts as a damping system to dissipate the energy from the loading. As the fluid leaves the matrix, the solid phase carries more of the load, but the impact has been reduced. The cartilage also deforms with the loading which increases the contact area and decreases the pressure on the solid matrix. [19] Because of this interplay between the fluid and matrix, healthy cartilage can hold up for decades of use without deteriorating.

Tension and shear also occur throughout the tissue as a result of the interactions between the collagen fibers and the proteoglycan network. Tension is a result of the tissue sliding across one another and when the tissue is compressed, pulling the fibers in to the point of contact. Shear is a result of the normal rotation and translational movements of the joint.

Another important function of articular cartilage is to provide a low friction environment for rotation of the joint. This low friction is thought to be facilitated through proteins in the lamina splendens and the superficial zone. There are also some other theories, including squeeze film lubrication, elastic-hydrodynamic lubrication, boundary lubrication, and fluid pressurization. The latter is assumed to be the major player in reducing friction within the joint.[5]

Chondrocyte Function

Crucial to the overall tissue function of articular cartilage is the function of the individual chondrocytes. Chondrocytes, from their position within the cartilage, are the main metabolic unit of cartilage. They are responsible for the turnover and production of collagen and proteoglycans, thus maintaining the cartilage around them.[6]

The general low density of chondrocytes within the cartilage is one of the main reasons cartilage is unable to heal itself after injury. Without chondrocytes to shore up and repair the surrounding matrix, the cartilage quickly degenerates and ceases to function properly. This leads to fissures within the cartilage and bone and results in the pain and disability associated with osteoarthritis.[20]

When healthy, chondrocytes remodel the cartilage makeup in their immediate vicinity. This leads to the territorial zones that were mentioned earlier with finer collagen fibers and higher proteoglycan content surrounding the chondrocytes. Further out, the fibers thicken and the proteoglycan content drops.[5]

When cartilage is first developing, there is a high number of chondrocytes within the cartilage as well as higher vascularization to provide nutrition for the chondrocytes. As the person ages and the cartilage matures, cell division is rarely seen in the cartilage. Fewer new chondrocytes are present, metabolic output and growth factor response decreases, and apoptosis increases. Though this is normal chondrocyte behavior, this leads to the inability of cartilage to heal itself properly.[5]

2.1.1.2 The Synovium

The synovial membrane or synovium is a specialized connective tissue that surrounds the joint cavities of synovial joints. Synovium consists of two main layers, a thin intimal layer roughly 20-40um thick and the subintimal layer which can be up to 5mm thick. The characteristics of the subintimal layer are used to classify synovium into three types: areolar, adipose, and fibrous. The areolar is the most specialized type, being crimped into folds to allowing stretching during joint movement and containing layers of intimal cells,

capillaries, and then blood and lymphatic vessels in deep subintimal layer. Adipose synovium consists of the layer of intimal cells followed by deeper fat tissue and is present as fat pads and within villi. Fibrous synovium, consisting of fibrous tissue, is less well defined and often difficult to distinguish from fibrocartilage.[21]

The intimal layer of the synovium consists of two main types of cells: fibroblast-like synoviocytes (FBLS) and macrophage-like synoviocytes (MPLS), with the FBLS being the dominant cell type in healthy synovium. MPLS are often identified through CD68 positive staining and are responsible for removing debris and regulating the inflammatory environment. In disease, the proportion of MPLS can rise to 80% as more macrophages are recruited to the synovium. FBLS produce hyaluronan and other proteoglycans which form the synovial fluid within the joint space[22] and can be identified through CD55 positive staining [21].

The synovium provides several important functions within the joint space[22]. It maintains a malleable but intact surface around the joint that is nonadherent to allow free movement of the joint. This surface provides lubrication for the cartilage by providing various glycoproteins such as lubricin and superficial zone protein. Through the secretion of hyaluronan, the synovium also maintains the fluid volume within the joint cavity. Finally, the synovium is the major path by which articular chondrocytes receive nutrients and waste clearance.[21]

2.1.2 OA Pathology

Originally thought to involve just the cartilage, OA has been recently recognized as a disease involving the entire joint, with cartilage, bone, and synovium all playing a role in

disease progression [23]. While the precise etiology of this disease is not known, risk factors include age, previous joint injury, obesity, and abnormal joint development [24]. Some researchers have postulated that these factors could result in pathological changes in the joint biology, structure, and mechanics which lead abnormal joint remodeling and the progressive degenerative changes seen in osteoarthritis [25]. Whatever the etiology may be, OA is characterized "by localized loss of cartilage, remodeling of adjacent bone, and associated inflammation [1]." All of these degenerative changes result in failure of the joint as a whole organ, leading to the pain and disability seen in those who suffer from OA [23], [25], [26]

2.1.3 OA Prevalence

An estimated 10-12% of the adult population in the US (~27 million people) has clinical OA with an estimated 37% of the U.S. adult population over 60 years of age being affected by knee OA alone [2], [27]. It has been estimated that OA results in directs costs to US insurers and individuals of more than $185 billion annually [28]. As the population ages, the total number of patients with doctor diagnosed OA is expected to increase to 25% of the adult US population (~67 million people) by 2030 [29]. The lifetime risk of developing systematic OA has been estimated to be 44.7% with those with a history of knee injury having a risk of 56.8%[30].

2.1.4 OA Treatments

Current recommended OA treatment includes four main categories: holistic patient assessment (to assess how the clinical symptoms of the disease affect the patient), non-pharmacological treatment (appropriate information, activity and exercise, weight loss,

biomechanical interventions), pharmacological pain treatment (acetaminophen, non-steroidal anti-inflammatory drugs, capsaicin, duloxetine, cox-2 inhibitors, opioids, intra-articular corticosteroid injections) and joint replacement surgery, all of which require repeated follow-up and review [1], [31]–[34]. While hip and knee joint replacement surgeries have a very successful track record at improving quality of life [35]–[37], they are still major surgical procedures with associated risks and there is concern about long-term outcomes, especially in younger patient populations [38], [39].

Most current pharmacological treatments for OA are only designed for pain management, not to modify or cure the disease; there are currently no widely recommended disease modifying OA therapies. The search for such a therapy has included many strategies, including cell, growth factor, and extracellular matrix treatments. Micronized dehydrated human amnion/chorion membrane (μ-dHACM) is one such potential OA treatment derived from the amnion/chorion membrane of donated human placenta [40]. This ECM-based treatment has been shown to be anti-inflammatory and non-immunogenic [41], [42]; to secrete a number of beneficial growth factors, including platelet derived growth factor (PDGF), fibroblast growth factor (FGF), and tumor growth factor beta (TGF-β) [43], [44]; and to maintain chondrocyte phenotype [45], [46]. All of these properties are potentially beneficial in a treatment for the inflammatory, degenerated environment of an osteoarthritic joint and previous work in our lab demonstrated that intra-articular injection of μ-dHACM has been shown to attenuate osteoarthritis development in the MMT rat model of OA [40]. There are, however, several factors in the treatment of OA with μ-dHACM that have yet to be explored, including the effect of particle size on the retention and efficacy of the treatment and the therapeutic mode of action.

2.2 *In Vivo* Evaluation of OA Treatments

2.2.1 Models

Multiple species, including mice, rats, guinea pigs, rabbits, and larger animals, and disease induction strategies have been used as *in vivo* models of OA [4]. One commonly used model is the medial meniscal transection (or tear) model in rats [47], [48]. In this surgically induced OA model, the medial collateral ligament is cut to expose the joint space and the medial meniscus transected at the narrowest point. This destabilizes the joint and results in rapid focal cartilage degeneration and osteophyte development.

2.2.2 Imaging Techniques[1]

The most common assessment measure of osteoarthritis disease progression in *in vivo* models is through histopathological measurements [49]. These, however, are time consuming, semi-quantitative, display moderate inter- and intra-observer variability, and destructive. As such, histomorphometric measures of cartilage thickness, proteoglycan content, and subchondral bone size have been developed [50]. Though these allow for more quantitative analysis of joint parameters, they are still time consuming and result in the destruction of the sample.

MRI is the most appropriate imaging modality for assessing joint disease state in humans because it can detect pathologies in many different tissues involved in OA [51], [52]. In animals, MRI has been used to investigate OA models in mice, rats, guinea pigs, rabbits,

[1] Part of this chapter has been adapted from Reece, Lin, Guldberg. (2014) "Contrast Enhanced MicroCT Imaging" in *The Handbook of Imaging in Biological Mechanics*, Boca Raton, FL: CRC Press.

and dogs, among other animals [53]. This imaging of small animal models requires specialized, dedicated equipment that can produce the resolution necessary, and providing this high-resolution imaging in an acceptable amount of time remains a limitation of MRI use in small animal models [54].

Ultrasound has been heavily investigated for the use of measuring the surface roughness of cartilage plugs [55]–[60] and shows some utility in detecting cartilage lesions in intact joints [61] but has not been combined with bone analyses nor used to quantify an entire cartilage surface. In addition, ultrasound imaging has shown that disruptions on the cartilage surface detectible by ultrasound are correlated with histomorphometric measures of disease progression [62].

To overcome some of the shortcomings of other imaging techniques of cartilage joints, our lab has developed EPIC-μCT, a non-destructive, quantitative, faster method of cartilage and bone analysis for OA research. Palmer, et al. introduced equilibrium partitioning of an anionic contrast agent for μCT imaging (EPIC-μCT) to evaluate the morphology and proteoglycan (PG) content of cartilaginous tissues[63]. PGs are a key component of articular cartilage, playing an important functional role in cartilage matrix by regulating the osmotic pressure within the tissue, and PG loss is an early indicator of cartilage damage[64]. As PGs have a negative charge, areas of high PG content have a high overall negative charge density and areas of low PG content have low negative charge density. An anionic contrast agent diffused into cartilage until equilibrium would therefore be expected to distribute inversely proportional to PG content. Indeed, when cartilage is equilibrated with the contrast agent Hexabrix™ (ioxalgate meglumine and ioxaglate sodium, Guerbet) and is then scanned with μCT, areas of lower X-ray attenuation indicate lower contrast

agent concentration, which correlate to regions of greater PG content and healthy cartilage. Conversely, areas of higher X-ray attenuation indicate higher contrast agent concentration and correspond to regions of lower PG content, indicative of cartilage degradation[63].

Xie, et al. utilized EPIC-μCT to extract 3D cartilage morphological[65] data for distal femoral cartilage in the rat. Cartilage thickness measurements were repeatable and agreed well with experimental needle probe thickness measurements and 2D histomorphometry estimates. Significant differences were shown in cartilage volume, thickness, and surface area for rats of different ages. A later study demonstrated EPIC-μCT was also capable of quantifying significant changes in PG content (as measured by average volumetric EPIC-μCT attenuation and correlated to histological safranin-O optical density of a central 8μm section) resulting from chondroitinase ABC digestion[66]. These studies demonstrate that EPIC-μCT can be used to quantify morphological and compositional properties in healthy and degraded articular cartilage in intact joints, suggesting that the technique may be useful for evaluating therapeutics in small animal models of cartilage degeneration.

Thote, et al. showed that this analysis can provide quantitative analysis of the damage, including focal lesion volumes, resulting from both the MMT and the MIA small-animal OA models [3] and Willet, et al. demonstrated it can be used to evaluate the therapeutic benefit of μ-dHACM [40]. Different variations of this technique have also been used to evaluate cartilage damage and regeneration [67]–[70].

Cationic contrast agents have also been utilized for cartilage imaging[71]–[75]. These solutions contain positively charged molecules; therefore, contrast agent molecules can permeate readily into tissues of high negative charge or PG content such as healthy

cartilage. Use of cationic contrast agent has been shown to provide higher contrast enhancement and increased correlation with PG content within non-degraded cartilage when compared to the same concentration of anionic contrast agents[72], [73]. Hayward, et al. used this technique to calculate cartilage volume in calluses of a mouse femoral fracture model[76]. They showed that cartilage volumes matched in contrast-enhanced μCT and histomorphometric measurements. This suggests that cationic contrast-enhanced μCT can measure cartilage volume in callus formation and can provide better understanding of the fracture healing process.

The major assumption with EPIC-μCT is that the contrast agent distribution is most significantly dependent on the fixed charge density of the cartilage. However, a recent paper by Kokonnen, et al. showed that increased collagen crosslinking significantly decreased contrast agent diffusion into the cartilage while leaving the PG content unaltered[77]. These results may influence the interpretation of studies utilizing equilibrium based ionic contrast agent techniques. Other studies have also shown that cartilage degeneration can affect contrast agent diffusion, and this change in diffusion coefficient can therefore be used to identify cartilage defects[78], [79].

To measure cartilage changes in joint degeneration models *in vivo*, Siebelt, et al. employed μCT arthrography whereby Hexabrix^{TM} was injected into the knee joints of rats immediately prior to imaging[80]. In three different joint degeneration models, cartilage volume decreased and attenuation increased compared to baseline, signifying an increase in cartilage damage, and this correlated well with histological scoring. The authors acknowledged that joints were scanned before contrast equilibrium was reached. Thus, attenuation changes could not be directly correlated with PG content and instead were

likely due to combined changes in PG content and matrix properties. These factors, along with differences in diffusion properties, may have limited the sensitivity in detecting degradative changes. However, this study importantly showed that cartilage degradation changes were detectable *in vivo*, thus enabling longitudinal analyses.

Surface fibrillation and erosion and the presence of lesions in the articular cartilage are some of the hallmarks of OA progression and disease severity in human OA. Accordingly, they are used as indicators of OA progression in the histological grading of joints [81]. Local measurements of cartilage surface roughness have been performed in multiple studies, using optical coherence tomography [82], scanning electron microscopy [83], and atomic force microscopy [83]. These local measures are useful only in small areas in relation to the entire surface of a rat tibia and are usually destructive techniques. Ultrasound has been heavily investigated for the use of measuring the surface roughness of cartilage plugs [55]–[60] and shows some utility in detecting cartilage lesions in intact joints [61] but has not been combined with bone analyses nor used to quantify an entire cartilage surface. Calculating the surface roughness over the entire tibial plateau may be feasible using EPIC-μCT techniques, which also allows morphological and compositional analyses of cartilage and bone.

2.3 *In Vitro* Evaluation of OA Treatments

Ex vivo models of osteoarthritis involve removing sections of tissue from healthy or disease joints and exposing them to the potential OA therapies. Most commonly, cartilage or osteochondral explants have been used, but some researchers have investigated the effects of potential therapeutics on synovium or joint capsule tissues [84]. Some of the

studies using explant models include investigating the effect of autologous conditioned serum on cartilage explants [85], the effect of stem cells on osteoarthritic synovium and cartilage [86], and exploring the joint capsule effects on cartilage explant proteoglycan production [87]. Limitations to these explant culture models include tissue availability and variability as well as maintaining tissue viability for extended time periods.

2.3.1 Primary Cell Cultures

To address some of the limitations of explant cultures, many researchers have utilized isolated primary cells and investigated the effects of potential OA therapies. Most studies have used chondrocytes [68], [88] but some have started to explore the effect of therapies on other cell types that are present in the synovium, such as fibroblast-like synoviocytes and macrophages [89], [90]. One of the major limitations of chondrocyte cultures is their propensity to rapidly dedifferentiate in culture, requiring the formation of the cells into 3D pellets or hydrogel constructs to help maintain the chondrocyte phenotype. Other limitations include limitations in donor cell availability.

2.3.2 Stem Cell Cultures

Because of their high availability and proliferative ability, stem cells differentiated down a chondrogenic lineage have started to be used as therapeutic screening tools. Some examples include using mesenchymal stem cell pellets to test the effects of synovial cell lines and macrophage co-culture [90] and induced pluripotent stem cells to develop high-throughput OA drug screening models [91]. The limitations of these models include the lack of characterized models, the obvious distance from the in vivo or clinical setting and, accordingly, their translatability as effective screening tools for potential OA therapies.

CHAPTER 3. EARLY CHARACTERIZATION OF A RAT OA MODEL

3.1 Introduction

In osteoarthritis (OA) therapeutic testing, small animal models are commonly used to investigate the progression of the disease and the influence of potential disease modifying OA drugs [92]–[94]. The rat medial meniscus transection (MMT) model has been used extensively for both these purposes[40], [47], [48] and is characterized by rapid degradation of the cartilage surface with lesion and osteophyte formation evident as early as three weeks [47].

Histological grading is most commonly used to measure articular tissue changes in small animal models[49], but this technique is time consuming, destructive, sample intensive, and semi-quantitative[50]. Contrast-enhanced μCT provides a quantitative, non-destructive three-dimensional (3D) imaging modality that has been used to analyze the structure and composition of various tissues and organs[95]. Recent work with equilibrium partitioning of an ionic contrast agent micro-computed tomography (EPIC-μCT) has shown an ability to quantify both cartilage and bone changes in various small animal OA models[3], [96] and to investigate the efficacy of potential disease modifying OA drugs[40], [97], [98].

While the ability to quantify these cartilage and bone changes using EPIC-μCT has been previously demonstrated, early measures of joint degeneration such as cartilage surface fibrillation and the sequence of pathological changes in the MMT model have not yet been

fully investigated. Previous work with EPIC-μCT measurement of cartilage proteoglycan content and lesion volume did not reveal any statistical differences between sham and MMT samples at one-week post-surgery[99]. Janusz et al., however, showed that cartilage fibrillations, one of the earliest indicators of disease in human joints[81], are qualitatively apparent in two-dimensional (2D) histological sections at one-week post-surgery[48]. Therefore, a technique that provides quantitative 3D measurement of changes in cartilage surface roughness caused by fibrillation may enable statistical detection of changes in the MMT samples as early as one-week post-surgery and may provide additional insight on the progression of disease development in this commonly used OA model.

While many of the histological hallmarks of OA progression have been measured using EPIC-μCT analysis, cartilage surface roughness changes associated with fibrillation[81] has not yet been quantified using this technique. Quantitative local measurements of cartilage surface roughness have been performed with other imaging modalities, including optical coherence tomography[82], scanning electron microscopy[83], and atomic force microscopy[83], but these local measures are useful only in small areas in relation to the entire surface of a rat tibia and are usually destructive techniques. Ultrasound has shown some utility in detecting changes in cartilage surface roughness in cartilage plugs[55], [57], [58], [60], [61], intact rabbit joints[59], and ex vivo rat joints[100]. However, ultrasound measurements do not provide measurements of other hallmarks of OA progression such as proteoglycan loss, subchondral bone sclerosis, or osteophyte development.

Subchondral bone sclerosis and the development of osteophytes are also known to occur in OA[23], and other studies have shown osteophyte development in the MMT model[47], [48]. However, how these additional joint pathologies relate spatially and temporally to the

disease development in cartilage is unknown. Knowledge of the degree and timing of early cartilage and subchondral bone changes in this model will aid in understanding the effects of potential OA therapies[48].

This study provides quantification of early disease development and progression in cartilage and bone tissues in the rat MMT model using EPIC-μCT. To add an additional measure of cartilage surface roughness changes associated with fibrillation to this characterization, this work also describes the design and validation of an algorithm for measuring the cartilage surface roughness of the rat tibial plateau using non-destructive EPIC-μCT imaging.

3.2 Materials and Methods

3.2.1 Animal Study and EPIC-μCT Imaging

The Georgia Institute of Technology IACUC approved all animal studies (Protocol# A12018). Weight matched male Lewis rats (300-350g) underwent sham or MMT surgery in the left leg as described previously[48]. Briefly, for MMT surgery, the left medial collateral ligament (MCL) was exposed through blunt dissection and transected to reveal the joint space. The medial meniscus was reflected proximally towards the femur and transected at its narrowest point. The muscle was sutured closed, and the skin incision was stapled. For sham samples, the same procedure was performed up to and including reflecting the meniscus towards the femur, but the meniscus was not transected.

Animals were euthanized with CO_2 one or three weeks after surgery (n=7 for sham groups and n=8 for MMT groups at both time points). The left legs were harvested and prepared

for EPIC-μCT scans as described previously[3], [40], [65], [99]. Briefly, after fixation, soft tissue was removed from the tibias, and the tibias were incubated in 2mL of 30% Hexabrix™ 320 (Mallinckrodt Inc., St. Louis, MO, USA) contrast agent in phosphate buffered saline (PBS) without minerals at 37°C for 30 minutes. The tibias were then placed within covered sample chambers to retain a humid environment and scanned in air using a Scanco μCT 40 (Scanco Medical, Brüttisellen, Switzerland) at 45kVp, 177μA, 200ms integration time, 16μm voxel size, and with a scan time of 26min. After scanning, the tibias were incubated in PBS at 37°C for 30 minutes to remove contrast agent. The axial greyscale EPIC-μCT images were orthogonally transposed to both sagittal and coronal sections, and cartilage, subchondral bone, and lesion volume analyses of the medial tibial plateau were performed on both sets of images as described below. Osteophyte growth on the medial edge of the tibial plateau was measured using coronal slices as described below. Segmentation of cartilage, subchondral bone, lesions, and osteophytes was performed with global thresholds (based on visual inspection and histogram analysis) and Gaussian filtering (sigma = 1.00, support = 1) as described previously[3], [65], [101]. Direct distance transformation algorithms were used for the thickness measurements.

3.2.2 Cartilage Contouring and Analysis

The cartilage on the medial tibial plateau was separated spatially from regions of bone and surrounding air with a semi-automatic contouring process (that produces outer borders of the region of interest) and thresholds[3]. Cartilage x-ray attenuation (which is inversely proportional to proteoglycan content after contrast agent equilibration with Hexabrix™[63], [66]), volume, and thickness were calculated over the entire medial tibial plateau and in the lateral, central, and medial thirds of the medial plateau[3], [40], [65],

[99]. These cartilage measurements have been shown to have high reproducibility and correlation with histology, needle probe testing, and protein assays[63], [65], [66]. Figure 3.1.A, B, show representative images of the analyzed cartilage. Details and examples of cartilage evaluation procedures are included in Appendix A.

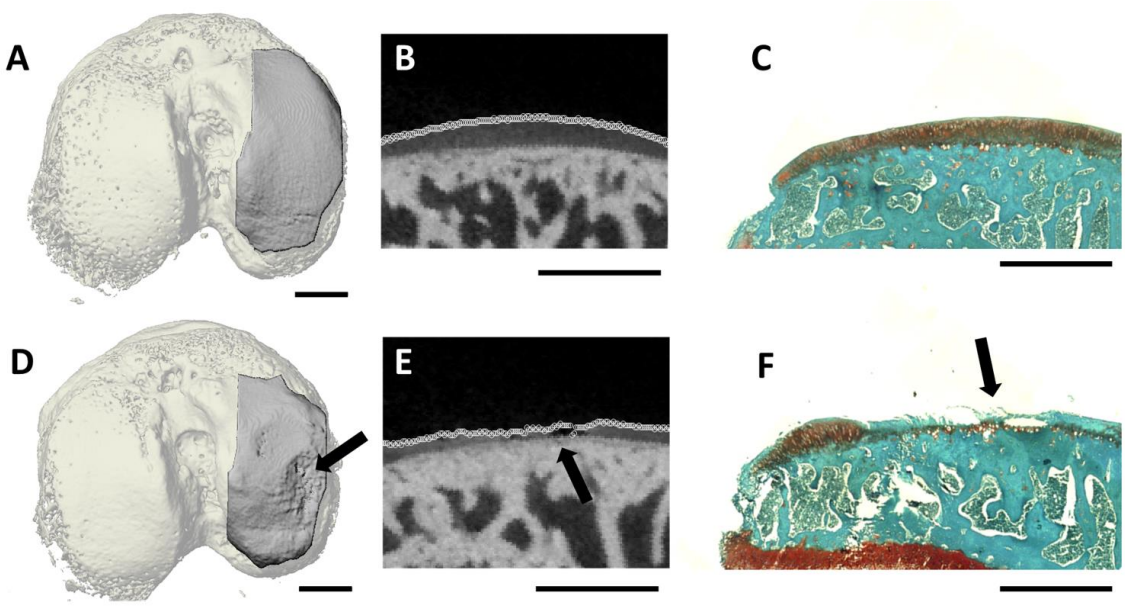

Figure 3.1: Representative images of EPIC-µCT VOIs and surface fibrillations. (A and D) 3D representations of the analyzed medial tibial plateau cartilage volumes (darker grey) overlaid on bone volumes of entire proximal tibia. (B and E) Representative sagittal EPIC-µCT images used in surface roughness analysis with white line representing cartilage surface. (C and F) Representative sagittal histological images of the same regions as the EPIC-µCT images. A, B, and C are from a single sham joint and D, E, and F are from a joint three weeks after medial meniscus transection. Cartilage fibrillations and lesions on the medial tibial plateau are indicated with arrows. Scale bars equal 1 mm.

3.2.3 Subchondral Bone Contouring and Analysis

Spatial separation by contouring and global thresholding was used to segment the subchondral bone from any pores, cartilage, or marrow space. Subchondral bone mineral density, volume, porosity, and thickness were calculated over the entire medial tibial

plateau and in the lateral, central, and medial thirds of the medial plateau. Details and examples of subchondral bone evaluation procedures are included in Appendix A.

3.2.4 Lesion Contouring and Analysis

Lesions were defined as cartilage defects extending through approximately 50% or more of the cartilage thickness. Volumes of interest (VOIs) of the lesions were defined by contouring of the lesion area, closely following the cartilage surface and extending into the subchondral bone while avoiding pores and trabecular spaces. Within this VOI, cartilage volume was segmented via thresholding and subtracted from total volume to give lesion volume[3]. Details and examples of lesion volume evaluation procedures are included in Appendix A.

3.2.5 Osteophyte Volume Contouring and Analysis

As measures of osteophyte growth along the medial edge of the tibial plateau, the thickness and volume of osteophyte cartilage and the volume of mineralized osteophyte tissue were measured, as previously described[99]. The edge of the medial tibial plateau was contoured to include any bony outgrowth and cartilage thickening. Two sets of VOIs were used, one for mineralized tissue outgrowth that included extraneous soft tissue on the tibial edge, and another for cartilage thickness and volume that excluded the soft tissue. After contouring, one range of thresholds was used to analyze mineralized tissue in the first set of VOIs and another to analyze cartilage in the second set. Details and examples of osteophyte evaluation procedures are included in Appendix A.

3.2.6 Surface Roughness Algorithm Design

A custom MATLAB® (MathWorks®, Natick, MA, USA) algorithm was created for measuring the roughness of surfaces from EPIC-µCT images. The program imports sequential 2D 8-bit images. Using a user-defined threshold, the program creates a 3D surface representation of the scanned object. The natural curvature of the surface can be removed by subtracting fitted surfaces using polynomial, LOWESS spline, or discrete cosine transform functions, similar to using low-pass frequency filters in other roughness measurements[102]. The surface roughness is calculated as the root mean square value of the deviation of every index point over the entire analysis surface (see Figure 3.2). The MATLAB® files for this algorithm along with instructions and sample files are available for download at http://guldberglab.gatech.edu/downloads. Descriptions of the files along with instructions and the text of the files is also contained in Appendix B.

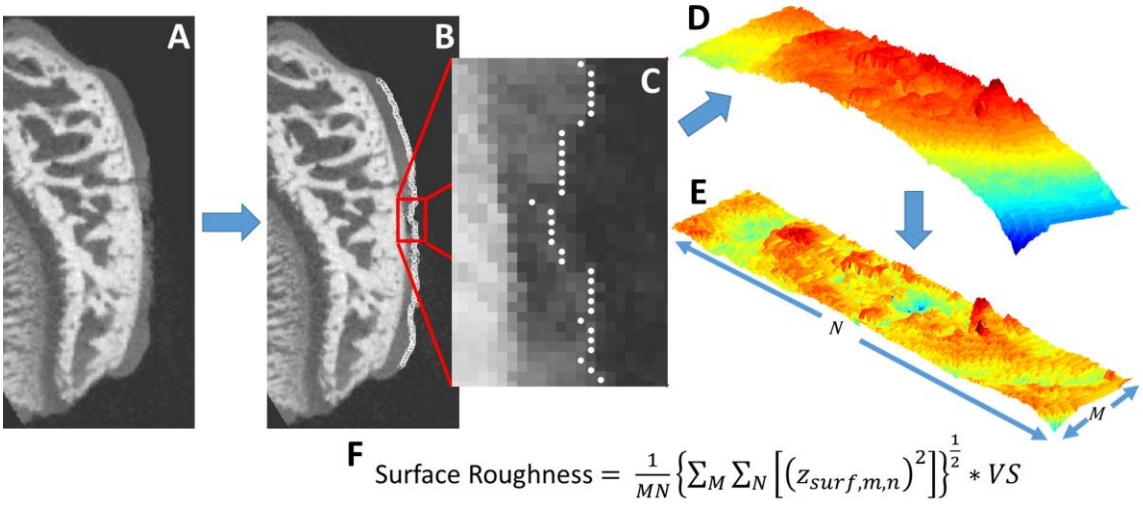

Figure 3.2: Schematic of surface rendering algorithm. (A) Greyscale 2D image exported from µCT. (B) Local threshold used to locate cartilage surface position (indicated by white circles). (C) Magnified inset of (B) with white circles marking the cartilage surface as determined by the cartilage threshold used in the analysis. (D) 3D cartilage surface rendered from 2D image stack. (E) Differential surface after fitted surface is subtracted from surface in (D). (F) Equation for calculating surface roughness where M and N represent the number of greyscale images

analyzed and the number of rows analyzed in each greyscale image, respectively; $z_{surf,m,n}$ is the value of the differential surface (E) at the index (m,n); and VS is the voxel size of the greyscale images determined by the voxel size of the μCT scan. In (D) and (E), red indicates the point is farther to the right in the greyscale images with blue indicating further to the left.

3.2.7 Surface Roughness Algorithm Validation

To validate the accuracy of the surface roughness algorithm and to understand the relationship between voxel size and surface roughness measurements, digital phantom surfaces (40x180 voxels) with varying roughness were created. The roughness of the surfaces was set using cosine waves along both surface axes such that the root mean square values of the surface roughness were 0.25, 0.5, 0.75, 1, 1.25, 1.5, or 2 voxels (n=5 for each roughness value). Using quadratic and quartic polynomials, curvatures were added to each surface to make three sets: with curvature in no planes (linear-linear), one plane (linear-quartic), or two planes (quadratic-quartic). The surfaces were then converted to TIFF images and imported into the custom algorithm described above. This algorithm measured the roughness of the phantom surfaces using subtracted linear-linear, linear-quartic, or quadratic-quartic fitted surfaces. Absolute percent error of the measured surface roughness was calculated using the formula:

$$Absolute\ Percent\ Error = \left|\frac{Measured\ Value - Actual\ Value}{Actual\ Value}\right| \times 100.$$

3.2.8 Surface Roughness Analysis

Greyscale images of the sagittal sections of the medial tibial plateau were imported into the custom algorithm, and a threshold equivalent to that used in the previous cartilage quantification was used to separate the cartilage surface from air. Cartilage surface

roughness was calculated using a polynomial fitted surface to account for the general curvature of the cartilage surface. The polynomial surface was 2nd order (quadratic) along the medial-lateral axis and 4th order (quartic) along the anterior-posterior axis. The lateral, central, and medial thirds of the medial tibial plateau were each analyzed separately. Figure 3.1 contains representative images of EPIC-µCT (Figure 3.1.E) and histology (Figure 3.1.F) showing the location of joint fibrillation.

3.2.9 Surface Roughness Evaluation of Acute Delivery of a Potential OA Therapeutic

Male Lewis rats weighing 300-325g were acclimated for 1 week after receipt and underwent MMT surgery in the left leg as described previously. 24 hours after surgery, 50µL of either micronized dehydrated human amnion/chorion membrane (µ-dHACM; AmnioFix® Injectable, MiMedx Group Inc, Marietta, GA, USA) suspended in saline at 80µg/mL or saline was injected intra-articularly into the knee of the left leg (n=5) using 25-gauge needles. The animals were euthanized with CO_2 three weeks after surgery and the left tibias were harvested and fixed in 10% NBF for 48 hours. EPIC-µCT imaging with surface roughness analysis was performed on the tibias as described in the previous sections.

3.2.10 Surface Roughness Evaluation of Delayed Delivery of a Potential OA Therapeutic

Male Lewis rats weighing 300-325g were acclimated for 1 week after receipt and underwent sham (n=7) or MMT surgery in the left leg as described previously. At either 24-hours (n=7) or three-weeks (n=5) after surgery, 50µL of µ-dHACM (EpiFix® Injectable, MiMedx Group Inc, Marietta, GA, USA) suspended in saline at 80µg/mL was injected intra-articularly into the knee of the left leg using 25-gauge needles. Other MMT

animals received saline injections at three-weeks post-surgery as control (n=6). The animals were euthanized with CO_2 six weeks after surgery and the left tibias were harvested and fixed in 10% NBF for 48 hours. EPIC-µCT imaging with surface roughness analysis was performed on the tibias as described in the previous sections.

3.2.11 Histology

After scanning, tibias were decalcified in Cal-Ex™ II (Thermo Fisher Scientific, Waltham, MA), embedded in paraffin, sectioned into 5µm sections, and stained with Safranin-O with fast green counterstain.

3.2.12 Statistics

All statistical analyses were performed using GraphPad Prism® Version 7 (GraphPad Software, Inc., La Jolla, CA), and all quantitative data are shown as mean ± 95% confidence interval of the mean. Two-way ANOVAs were used to determine significant effects of time (one-week vs three-week) and surgery (sham vs MMT) for all parameters except lesion volume and occurrence, and a Bonferroni post-hoc test was used to compare means across time points or surgery groups in each parameter that showed significant overall group effects or interactions. The Wilcoxon signed rank test was used to determine if lesion volume medians in the MMT samples were significantly different than a theoretical mean of 0.000 mm^3. In the surface roughness validation, the relationship between the actual and the measured roughness values of the digital phantom surfaces was analyzed using linear regression analysis. For the surface roughness analysis of the delivery of µ-dHACM, data is shown one-way ANOVAs with Bonferroni post-hoc tests were used to compare between groups. Significance for all statistical tests was set at $p<0.05$.

3.3 Results

After completing the analyses in both the sagittal and coronal planes, a greater number of significant differences (though similar overall results) between MMT and sham samples were observed in the sagittal datasets; therefore, only sagittal data will be presented here. The coronal analysis data are included in Appendix C for reference.

3.3.1 Cartilage Analysis

A complete summary of the cartilage EPIC-μCT parameter results is in Figure 3.3. One-week post-surgery, MMT resulted in significant positive effect sizes in attenuation, volume, and thickness (2.0, 1.9, 1.8, respectively) in the medial third of the medial tibial plateau compared to sham. At three-weeks post-surgery, MMT resulted in a significant positive effect size in attenuation (4.3) in the medial third while significant positive effect sizes in volume (5.4, 3.1, 3.3, and 3.6) and thickness (6.2, 2.6, 5.6, and 4.2, respectively) were seen in the entire medial tibial plateau and the lateral, central, and medial thirds, respectively, compared to sham controls.

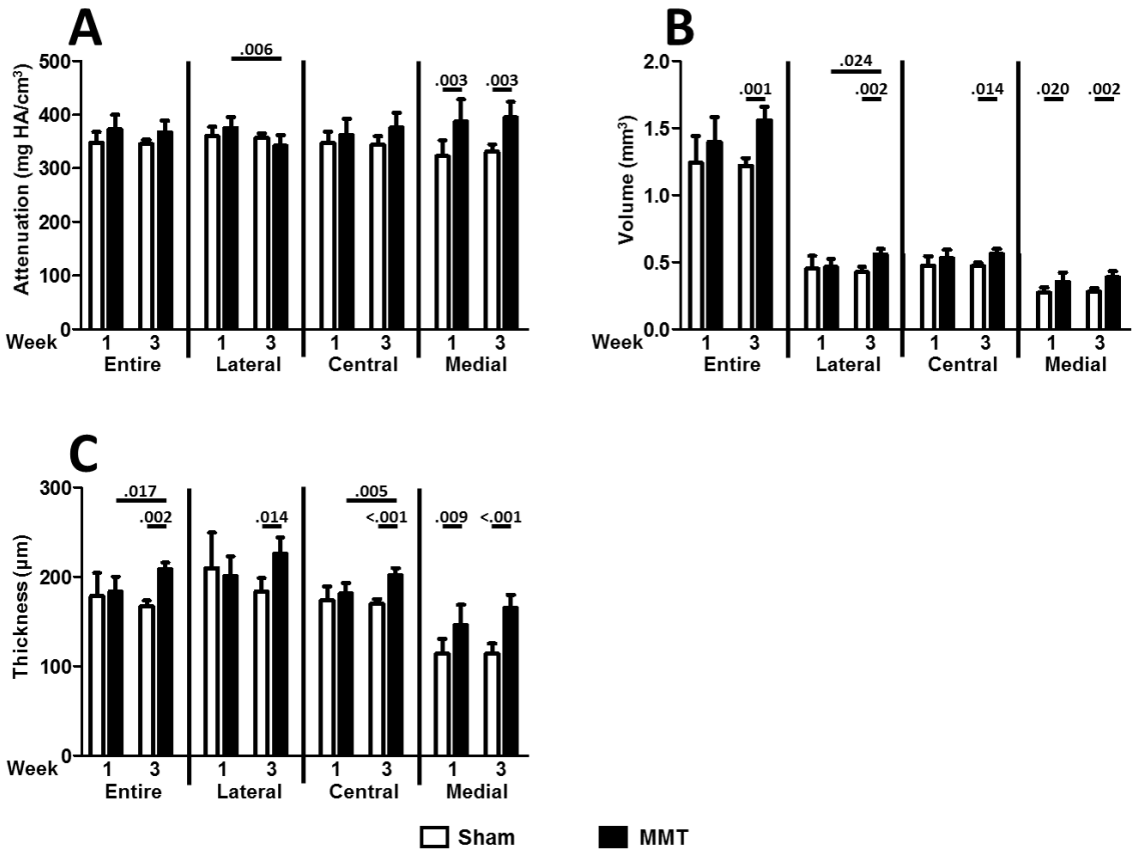

Figure 3.3: EPIC-µCT cartilage parameters – attenuation (A), volume (B), and thickness (C) in the sagittal slice method of analysis. Data are grouped by location (entire medial tibial plateau and lateral, central, and medial thirds thereof), time point (one- or three-weeks post-surgery), and surgery group (sham or medial meniscus transection {MMT}). Data shown as mean ± 95% confidence interval and significance was determined using two-way ANOVAs with Bonferroni post-hoc tests. n = 7-8.

3.3.2 Subchondral Bone Analysis

A complete summary of the subchondral bone parameter results is shown in Figure 3.4. In all parameters at one-week post-surgery and in most parameters at three-weeks post-surgery, there were no significant differences between sham and MMT samples. At three-weeks post-surgery, subchondral plate mineral densities of the entire plateau and in the medial third were significantly greater (effects sizes were 1.5 and 1.7, respectively) in

MMT samples when compared to sham controls. Subchondral plate volume and thickness of the medial third of the medial tibial plateau were significantly greater (effect sizes were 2.3 and 2.7, respectively) in the MMT samples compared to sham controls.

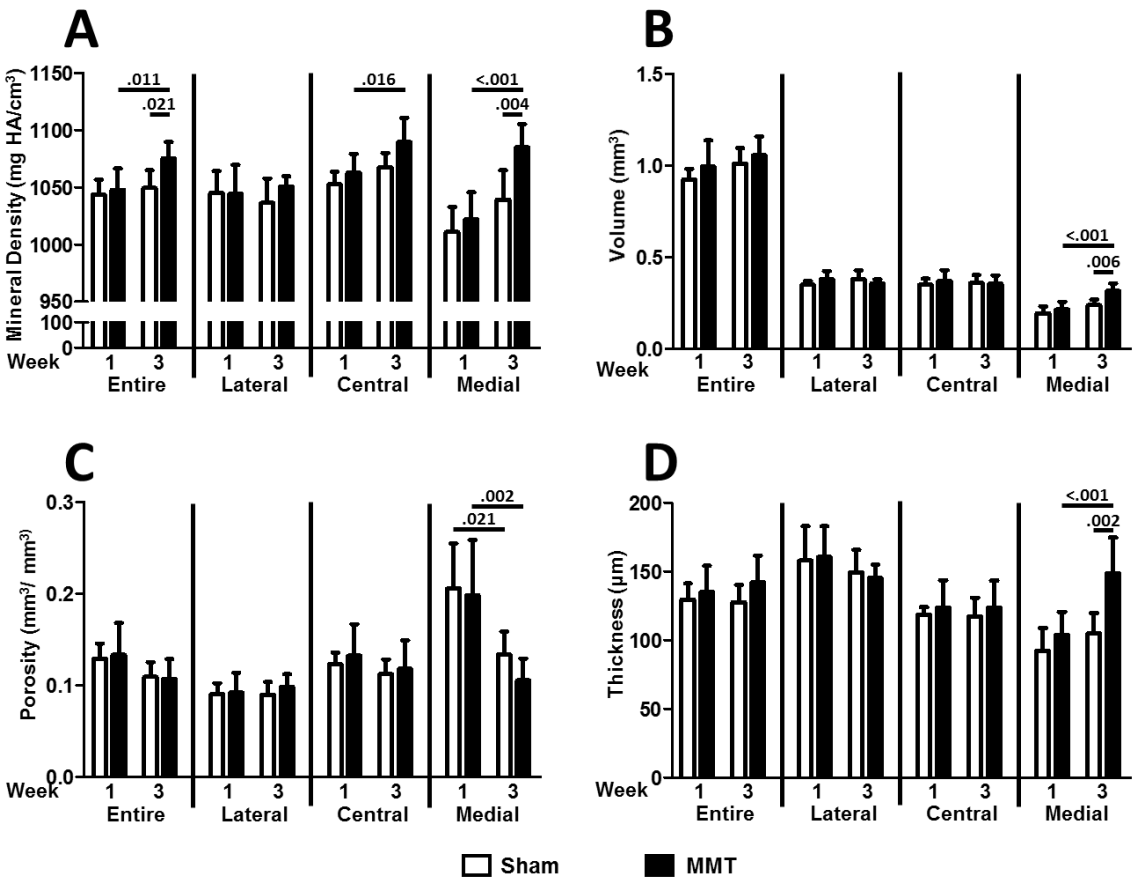

Figure 3.4: EPIC-µCT subchondral plate parameters – mineral density (A), volume (B), porosity (C), and thickness (D) in the sagittal slice method of analysis. Data are grouped by location (entire medial tibial plateau and lateral, central, and medial thirds thereof), time point (one- or three-weeks post-surgery), and surgery group (sham or medial meniscus transection {MMT}). Data shown as mean ± 95% confidence interval and significance was determined using two-way ANOVAs with Bonferroni post-hoc tests. n = 7-8.

3.3.3 Lesion Analysis

No lesions were detected in the sham samples but lesions were detected in 3 out of 8 one-week MMT samples and 7 out of 8 three-week MMT samples. At three-weeks post-surgery, the median lesion volume was significantly different than 0.0 mm^3 in MMT samples as determined by the Wilcoxon signed rank test (Figure 3.5.A).

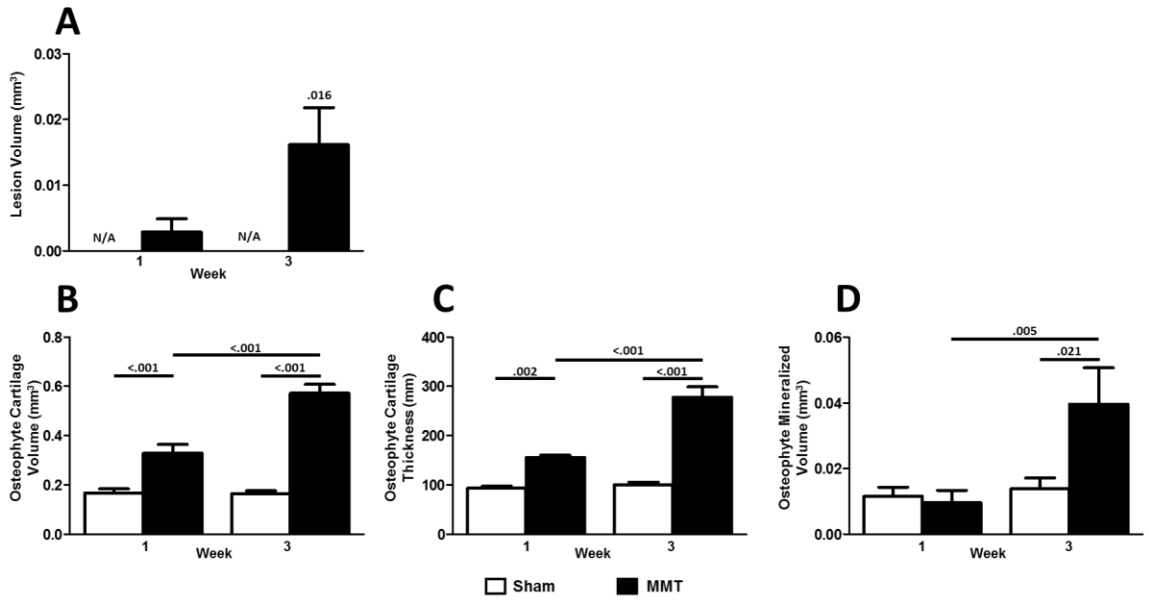

Figure 3.5: EPIC-µCT lesion and osteophyte (OP) parameters – lesion volume (A) in the sagittal slice method of analysis and OP cartilage volume (B), OP cartilage thickness (C), and OP mineralized volume (D) in the coronal slice method of analysis. Data shown as mean ± 95% confidence interval. n = 7-8. Significance for lesion volume was determined using from Wilcoxon signed rank test comparing if lesion volumes are significantly different from 0.000mm^3. Significance for OP parameters was determined using two-way ANOVAs with Bonferroni post-hoc tests.

3.3.4 Osteophyte Analysis

At one-week post-surgery, MMT samples showed a significant increase in osteophyte cartilage thickness and volume compared to sham samples (effect sizes were 5.7 and 3.7, respectively; Figure 3.5.B, C). At three-weeks post-surgery, osteophyte cartilage thickness

and volume, and osteophyte mineralized tissue volume were significantly higher compared to sham controls (effect sizes were 12.8, 13.1, and 2.9, respectively; Figure 3.5.B, C, D).

3.3.5 Surface Roughness Algorithm Validation

There was strong agreement between the actual and measured surface roughness values of all three sets of phantom surfaces (r^2 = 0.986, 0.997, and 0.999 for linear-linear, linear-quartic, and quadratic-quartic, respectively, with p-values <0.001 for each) (Figure 3.6.B). The average percentage error of the surface roughness measurements decreased as roughness value increased (Figure 3.6.C), and, when the relationship between roughness and average percentage error was fit using semi-logarithmic curves, surface roughness values greater than 0.6 voxels were related to average percentage errors below 10% for all three surface fits.

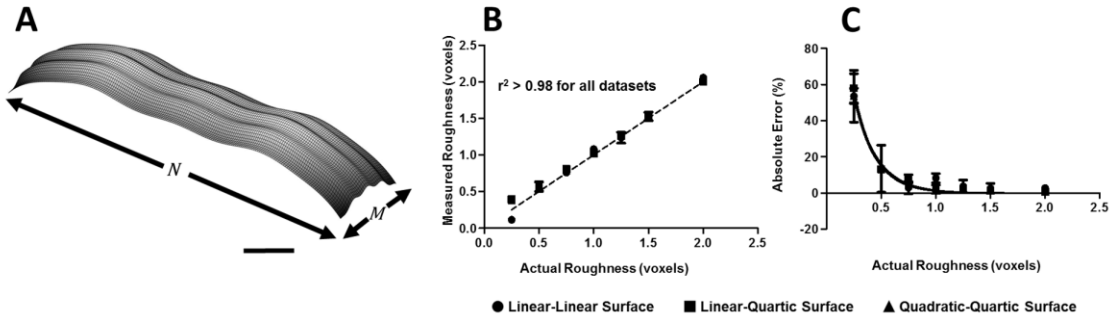

Figure 3.6: Surface roughness validation with digital phantom surfaces. Phantom surfaces of varying defined roughness (0.25 to 2 voxels, n=5 for each roughness value) were exported as serial TIFFs and imported into the custom surface roughness program for roughness measurement. (A) Representative phantom surface with curvature in two planes (quadratic-quartic in the M-N directions, respectively). (B) Relationship between actual roughness values and measured roughness values (mean ± 95% confidence interval) for linear-linear, linear-quadratic and quartic-quadratic surfaces at varying roughness values. (C) Percentage error (mean ± 95% confidence interval) of measured roughness values compared to actual roughness values of the phantom surfaces at varying roughness values. Scale bar equals 25 voxels.

3.3.6 Surface Roughness Analysis

One-week post-surgery, MMT cartilage surface roughness was significantly greater in the central and medial thirds of the medial tibial plateaus when compared to sham controls (effect sizes were 15.0 and 3.4, respectively). At three weeks, surface roughness was significantly greater in both the central and medial thirds compared to sham controls (effect sizes were 15.0 and 19.7, respectively; Figure 3.7).

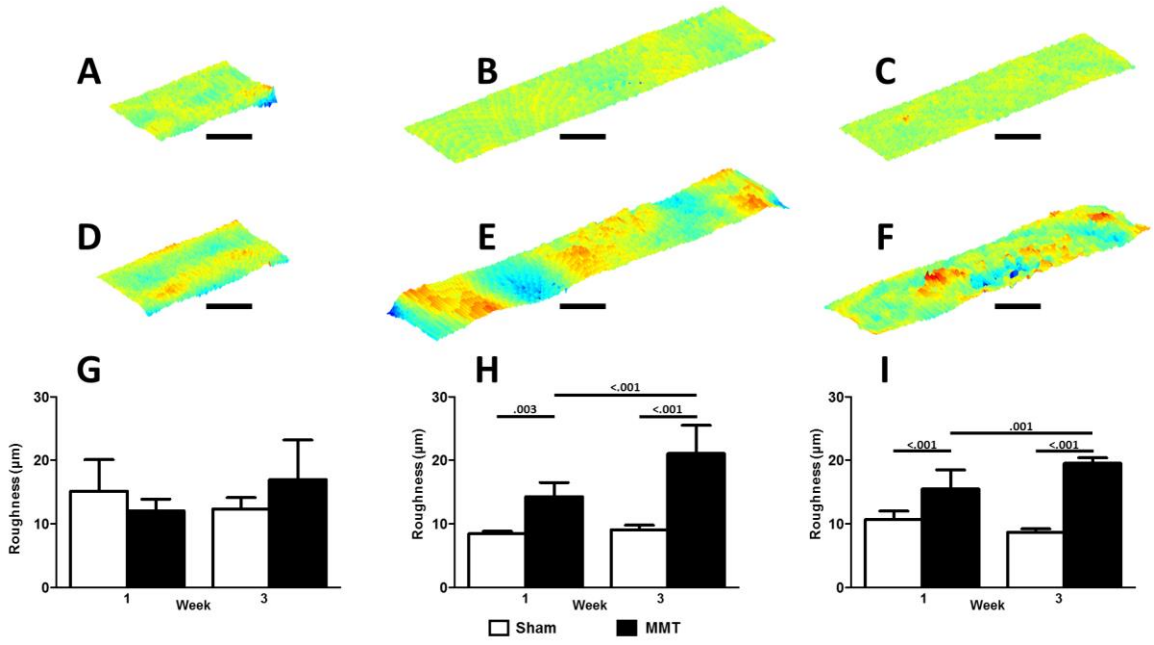

Figure 3.7: Cartilage surface roughness measurements. Representative differential surfaces of VOIs of lateral (A, D), central (B, E), and medial (C, F) thirds of the medial tibial plateau in rats that underwent sham (A, B, C) or medial meniscus transection (MMT; D, E, F) surgery. The differential surfaces were created by subtracting individual quadratic-quartic fits from the corresponding cartilage surface renderings. Surface roughness values for sham and MMT samples at one and three weeks in VOIs of the lateral (G), central (H), and medial (I) thirds of the medial tibial plateaus. Data shown as mean ± 95% confidence interval and significance was determined using two-way ANOVAs with Bonferroni post-hoc tests. n = 7-8. In A-F, red indicates the point is more proximal and blue indicates a point is further distal. Scale bars equal 500 µm.

3.3.7 Surface Roughness Analysis of Acute Delivery of µ-dHACM

Surface roughness was calculated using the surface roughness program. Analysis of medial third of the medial tibial plateau showed an increase in surface roughness in saline and µ-dHACM treatment compared to non-operated control limbs. (Figure 3.8).

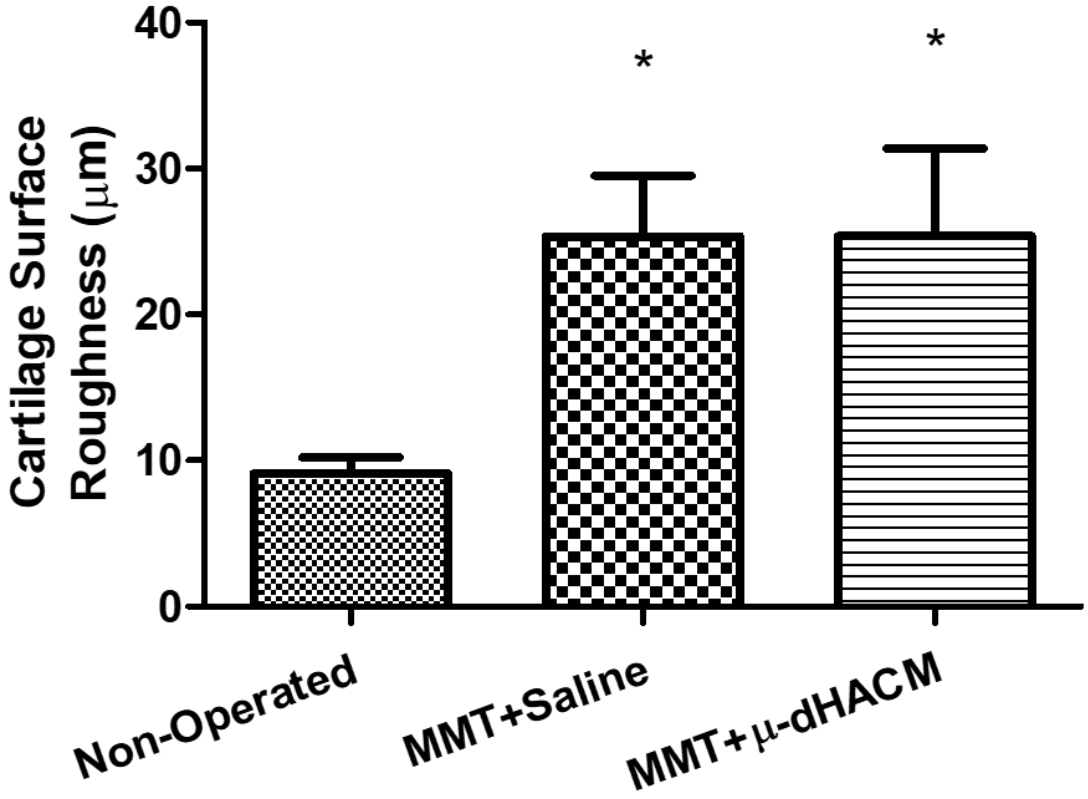

Figure 3.8: Cartilage surface roughness analysis of acute delivery of µ-dHACM. Surface roughness was significantly higher than non-operated control in both the saline and acute (24-hours post-surgery) micronized dehydrated human amnion/chorion membrane (µ-dHACM) treatment groups, Data shown as mean ± SEM. n = 5.

3.3.8 Surface Roughness Analysis of Delayed Delivery of µ-dHACM

Surface roughness was calculated using the surface roughness program. Analysis of medial third of the medial tibial plateau showed an increase in surface roughness in saline and acute treatment groups compared to sham and delayed treatment (Figure 3.9).

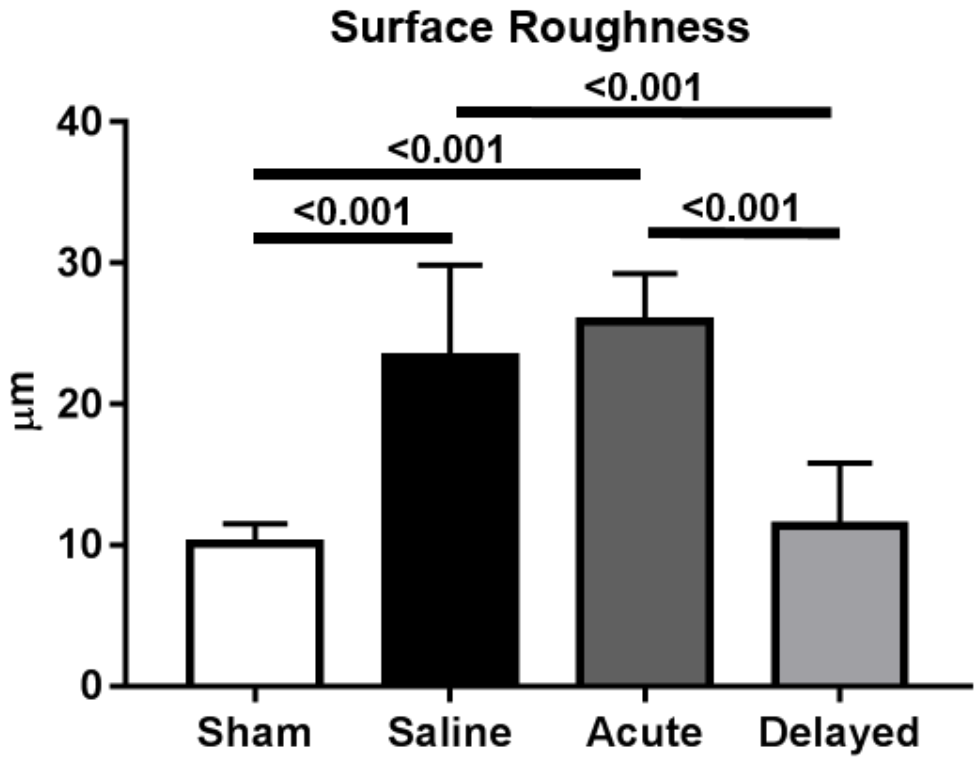

Figure 3.9: Cartilage surface roughness analysis of delayed delivery of µ-dHACM. Surface roughness was significantly higher than sham in the saline and acute (24-hours post-surgery) micronized dehydrated human amnion/chorion membrane (µ-dHACM) treatment groups, while surface roughness in the delayed µ-dHACM treatment (three-weeks post-surgery) group was significantly lower than saline and acute treatment groups. Data shown as mean ± 95% confidence interval. n = 5-7.

3.3.9 Histology

Safranin-O staining showed a qualitative decrease in cartilage proteoglycan content and the presence of fibrillation, lesions, and cartilage thickening in the MMT samples at both

one and three weeks compared to sham, supporting the results seen with EPIC-μCT (Figure 3.10).

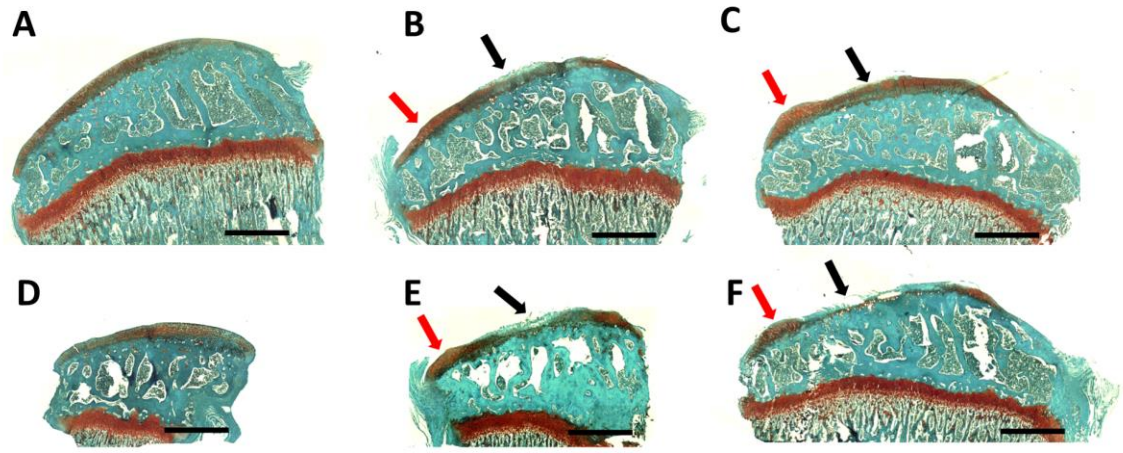

Figure 3.10: Representative histology sections. Sections (paraffin processing, Safranin O with fast green counterstain) from central (A, B, C) and medial (D, E, F) thirds of the medial tibial plateau for sham (A, D), one week medial meniscus transection (MMT; B, E), and three week MMT (C, F) groups illustrate differences in the fibrillations and lesions (black arrows) and cartilage thickening (red arrows). Red staining indicates presence of proteoglycans in the tissue. Sections are sagittal slices and scale bars equal 1 mm.

3.4 Discussion

Small animal pre-clinical models of OA are used for screening potential OA therapies because of their low cost, reproducibility, and ability to recapitulate disease manifestations similar to human OA[4]. Using these models requires accurate characterization of the models to verify their relevance to human disease and to inform the effects and mechanisms of the tested therapies. EPIC-μCT has been used to provide accurate characterization of multiple pre-clinical models and the effects of various potential OA therapies[3], [40], [65], [103]. The purpose of this study was to use EPIC-μCT to provide quantification of early

disease development and progression in cartilage and bone tissues, including a measure of cartilage surface roughness, in the rat MMT model.

Previous studies of cartilage changes in the MMT model have shown that degenerative changes progressively develop. Janusz, et al., demonstrated that degenerative changes, as measured with histological scoring, increased at three- and six-weeks post-surgery compared to one-week post-surgery[48]. EPIC-μCT quantification of degeneration in this model showed that decreases in cartilage proteoglycan content and increases in lesion and osteophyte volumes were present at two- and three-weeks post-surgery but not at one-week post-surgery[99]. Within these studies, there were no apparent changes at the earliest timepoint (one-week post-surgery) and no investigation of how the EPIC-μCT parameters develop spatially in the first three-weeks post-surgery. Understanding the location and timing of tissue changes in this model will assist researchers in relating data from the MMT model to clinical situations. Thus, this work has sought to 1) expand the capabilities of EPIC-μCT to include measuring surface roughness associated with cartilage fibrillation, one of the earliest indicators of human OA development[81], and 2) quantify early degenerative tissue changes within the MMT model.

The current study demonstrated that increases in cartilage surface roughness appeared at one-week post-surgery in the central and medial thirds of the medial tibial plateau while increases in cartilage attenuation (inversely proportional to proteoglycan content), thickness, and volume were apparent only in the medial third at one-week post-surgery. By three weeks, changes in multiple cartilage parameters were evident throughout the tibial plateau. These changes, similar to those presented in other studies[3], [40], [99], suggest that in EPIC-μCT analysis of the MMT model, quantifiable cartilage surface changes

appear earlier than changes in proteoglycan content, volume, and thickness. This is similar to the development of OA in humans where surface fibrillations have been shown to be one of the earliest disease indicators[81].

Subchondral bone thickening and changes in mineral density are known to occur early in human OA and to be evident before radiographic indications of joint space narrowing[104], [105]. In a previous study by Yu, et al., MMT resulted in increases in subchondral plate thickness and decreases in plate mineral density within the medial tibial plateau at eight- and twelve-weeks post-surgery[106]. In the current study, however, there were significant increases in mineral density, volume, and thickness in the subchondral bone at three-weeks post-surgery. This suggests that subchondral bone changes do occur in the MMT model at earlier timepoints than previously reported and initially develop later than and over a more focal region than changes in the cartilage.

While MMT resulted in changes in multiple parameters and locals in the medial tibial plateau, the largest effect sizes were in the surface roughness measures at three-weeks post-surgery with effect sizes of 15.0 and 19.7 in the central and medial thirds, respectively. Osteophyte cartilage thickness and volume measurements also resulted in large effect sizes of 5.7 and 3.7 at one-week post-surgery and 12.8 and 13.1 at three-weeks post-surgery. Within the cartilage volume and thickness measurements at three-weeks post-surgery, the largest effect sizes due to MMT were in analyses of the entire medial plateau and in the central third, not in the medial third of the medial tibial plateau where the changes first appear. Altogether, these results suggest surface roughness and osteophyte measurements may be the most sensitive in the MMT model. In addition, EPIC-μCT analysis of this model

need not be restricted to the medial third of the medial tibial. Rather, there could be benefit in quantifying changes throughout the medial plateau.

There are few previous studies of surface roughness changes in the rat tibial plateau cartilage. A recent study by Maerz et al. used a mesh parameterization technique to calculate cartilage thickness and surface roughness in contrast enhanced μCT images of rats that underwent ACLT surgery[107]; however, the authors defined surface roughness as deviation of cartilage thickness from an average thickness rather than deviation of the cartilage surface features from a smooth surface. Thus, their surface roughness measurement is a better measure of variations in the cartilage thickness rather than surface changes resulting from fibrillations as measured in the current study. The utility of one measure over the other would depend on the specific patterns of cartilage fibrillation and thickening determined by the model and the endpoint of the study.

For the work presented here, a polynomial surface (quadratic and quartic in the medial/lateral and anterior/posterior planes, respectively) was chosen to eliminate curvature of the tibial plateau, comparable to using a low-pass filter in other surface roughness measurement techniques[102]. When qualitatively comparing the fitted quartic-quadratic surface to the actual cartilage surface as imaged by EPIC-μCT, it appears that the use of this fitted surface captures not only cartilage surface roughness changes associated with fibrillations but also deviations in the more general cartilage surface shape of MMT joints when compared to sham-operated joints. These surface shape changes may indicate local changes in cartilage thickness caused by altered joint kinematics in the MMT animals. In humans, it has been found that knee kinematics are correlated with ratios of medial to lateral cartilage thickness, and these correlations change with age and presence of knee

OA[25], [108]. Future work combining gait mechanics and EPIC-μCT imaging in the MMT model could lead to greater understanding of the relationship between knee kinematics and specific areas of tissue changes.

This study included a validation of the surface roughness measurements using digital phantom surfaces but did not include a validation using physical surfaces. μCT is a well-established and validated technique that has been shown to accurately represent the 3D structure of numerous materials and tissues, including cartilage[65], [99], [107]. As demonstrated by the excellent linear fits in the digital phantom validation data (r^2>98%), the algorithm used in this study can accurately measure roughness values greater than ~50% of a given surface's voxel size. In addition, even though the feature resolution of 16μm scans is not high enough to resolve individual cartilage fibrils, the large increase in surface roughness (124%) with high effect size (19.7) in the *in vivo* surface roughness data demonstrate that the utilized voxel size is sufficient to detect the increase in macroscale surface roughness associated with cartilage fibrillation in the MMT model. Thus, the digital phantom and *in vivo* data demonstrate that 16μm scans have sufficient accuracy and sensitivity to detect changes in cartilage surface roughness associated with fibrillations resulting from MMT surgery.

Surface roughness analysis of joints that received treatment with μ-dHACM demonstrate that surface roughness analysis does provide additional information when analyzing potential OA therapeutics. The three-week study in Willett, et al, saw no difference in attenuation or lesion volume between the acutely delivered μ-dHACM group and the unoperated control[40] but surface roughness analysis performed in this aim demonstrated that there were still substantial changes on the cartilage surface. This suggests that μ-

dHACM delivery did not prevent OA development, simply delayed it. This conclusion is supported by the six-week study (see Appendix 4) which showed that an acute delivery of μ-dHACM resulted in no difference in overall joint damage compared to saline-treated controls. The delayed delivery of μ-dHACM, however, did result in decreased surface roughness compared to saline-treated controls, implying that delayed μ-dHACM may be more effective as a delayed treatment than an acute treatment.

The scope of the data presented here is limited in that it is from one model of post-traumatic osteoarthritis in one strain of rat. As has been shown in other studies, the parameters quantified in this study will be different in different rat strains and in different models of OA[3], [107]. In addition, the sensitivity of the different analysis parameters in this study could influence the detected sequence of tissue changes. Further expansion of EPIC-μCT analyses, such as adapting voxel-based techniques from magnetic resonance imaging[109] to increase sensitivity of attenuation changes, could alter this detected sequence of changes. This study also did not include robust comparison to traditional histological measures of OA development[49], [50], and the ability of histological staining to assess microscale fibrillation, cellular health, more specific protein concentration, synovium health, calcified cartilage, and other relevant parameters in OA research are not replicated with EPIC-μCT. One of the advantages of contrast enhanced μCT analysis of OA models is that it is non-destructive and does not preclude further histological analyses. The scope of this study was not to provide a comparison to histology, which previous studies have done[3], [99]; rather, the purpose of this study was to demonstrate how the measured EPIC-μCT parameters varied as a function of disease and time and to validate that changes in surface roughness could be quantified using EPIC-μCT. Despite the limitations, this study and previous

EPIC-μCT studies demonstrate the utility and adaptability of contrast enhanced μCT imaging in OA pre-clinical research.

In conclusion, this work has established that an algorithm using EPIC-μCT images can accurately quantify increases in cartilage surface roughness resulting from MMT surgery. It has characterized early degenerative changes in joint tissues in a preclinical OA model, displaying the extent of cartilage fibrillation, proteoglycan loss, subchondral bone sclerosis, and lesion and osteophyte development quantified using nondestructive EPIC-μCT techniques. With the continued unmet need for effective OA therapeutics, this work demonstrates the utility of EPIC-μCT imaging in understanding early stage pathological development in small animal OA models and its potential to evaluate disease modifying therapeutics that specifically address these early disease manifestations.

CHAPTER 4. *IN VIVO* EVALUATION OF THE EFFECT OF PARTICLE SIZE ON AN ECM BASED OA THERAPEUTIC

4.1 Introduction

Osteoarthritis (OA), the most common form of arthritis, affects an estimated 13% of the adult population in the US (~27 million people) with an estimated 37% of the U.S. adult population over 60 years of age being affected by knee OA alone[2], [27]. OA is characterized by overall joint degeneration that includes cartilage loss, bone sclerosis, osteophyte formation, and synovial changes[110]. While researchers continue to explore many promising disease modifying therapies, including platelet rich plasma and stem cells, there is still a lack of FDA-approved treatments that prevent the progression of OA[110].

Recently, multiple researchers have tested the safety and efficacy of amniotic membrane suspensions to treat OA progression. This extracellular matrix-based therapy has been shown to possess immunomodulatory properties and multiple soluble factors that encourage tissue healing[44], [111]–[114], and amniotic membrane has been used extensively to treat ocular tears and skin ulcers[111], [115]. Due to these factors and the abundant clinical availability, amniotic membrane suspensions are an attractive potential OA therapy and various formulations have been studied for their effect on OA. Willett *et al.* showed that intra-articular injection of micronized dehydrated amnion/chorion membrane (μ-dHACM) reduced OA progression three weeks after surgery in the rat medial meniscus transection (MMT) model[40]. Raines *et al.* showed that treating MMT joints two weeks post-surgery with suspensions of combined amniotic membrane and umbilical

cord particles reduced damage progression[116]. Vines *et al.* tested the safety of suspensions consisting of combined amniotic membrane particles and amniotic fluid derived cells in human knee joints and showed no adverse reactions to the suspension injections[117]. While these results are consistently promising, many of the factors influencing the potential therapeutic efficacy of these amniotic membrane suspensions remain unexplored.

The size of the amniotic membrane particles could play a large role in the therapeutic efficacy of the suspension. Size of particles would likely affect the release of factors, clearance of particles, and degradation of particles. A recent study by Chen *et al.* explored the factor release kinetics and degradation patterns of drug-loaded poly(lactide-*co*-glycolide) (PLGA) microparticles fractionated along well defined sizes (<20, 20-50, 50-100, and >100 μm)[118]. Smaller particles resulted in more of a burst release of the drug, independent of particle degradation, while the drug release from the large particles was dependent on both short-term diffusion and long-term particle degradation. While PLGA is a different material, these results are consistent for particles in general and support the hypothesis that changing the particle size could alter the factor release from and degradation of micronized amniotic membrane particles.

This work investigated two commercially available formulations of micronized amniotic membrane that were expected to have two different distributions of particle sizes (AmnioFix® Injectable and AmnioFix® Sports Medicine, MiMedx Group, Inc., Marietta, GA). Specifically, the particle size profiles of both formulations were quantified and the influence of the different size profiles on the *in vivo* therapeutic efficacy of μ-dHACM in the MMT model was evaluated using equilibrium partitioning of an ionic contrast agent

microcomputed tomography (EPIC-μCT) and histology. In addition, the effect of the size profiles on *in vivo* particle retention within the joint and on *in vitro* protein elution was quantified. We hypothesized that varying the size profile of the μ-dHACM particles would alter the therapeutic efficacy, particle retention, and protein elution of the particles.

4.2 Materials and Methods

4.2.1 Manufacture and preparation of μ-dHACM

Particulate amniotic membrane was produced using the proprietary PURION® process (MiMedx Group, Inc.) that generates a dehydrated, devitalized amnion and chorion tissue graft which is then sterilized and micronized into particulate form. Two different formulations were used in this study: μ-dHACM (AmnioFix® Injectable, MiMedx Group Inc.) and reduced particle size μ-dHACM (RPS μ-dHACM; AmnioFix® Sports Medicine, MiMedx Group, Inc.). For each formulation, independently processed samples from five donors were pooled while in dehydrated form, and the required amount by mass was measured from the pooled material and rehydrated for each experiment in this study.

4.2.2 Size Characterization

μ-dHACM and RPS μ-dHACM particles were stained for 30 minutes in Eosin, centrifuged at 6000 RCF for 3 minutes, and washed with 0.1% Triton X-100 after injecting through a 25-gauge needle. The particles were suspended in Triton X and mixed well throughout the process to prevent clumping. Particles were suspended in 0.1% Triton X-100 at 6mg/mL, and 10uL of each particle suspension was imaged via Zeiss LSN 700 confocal microscope (Carl Zeiss, Inc Thornwood, NY). The maximum intensity images were then imported into

Volocity Quantitation (Perkin Elmer, Inc, Waltham, MA, USA) and the area of each particle was calculated. All particles from both formulations were combined and then binned according to particle area (<10μm^2, 10-<20μm^2, 20-<50μm^2, 50-<100μm^2, 50-<100μm^2, 100-<250μm^2, 250-<500μm^2, and >500 μm^2).

4.2.3 Animal Study and EPIC-μCT Imaging

The Georgia Institute of Technology IACUC approved all animal studies (Protocol # A14019). Weight matched male Lewis rats (300-350g) underwent sham or MMT in the left leg. One day after surgery, μ-dHACM and RPS μ-dHACM were resuspended in saline at a concentration of 80mg/mL, and 50μL of either saline, μ-dHACM, or RPS μ-dHACM were injected intra-articularly using a 25-gauge needle (BD, Franklin Lakes, NJ, USA) through the infrapatellar ligament. Three weeks post-surgery all animals were euthanized with CO_2 inhalation, and the left legs were harvested and prepared for equilibrium partitioning of an ionic contrast agent microcomputed tomography (EPIC-μCT) scans as described previously[65]. EPIC-μCT imaging is a contrast-enhanced μCT imaging technique that allows simultaneous 3D quantification of cartilage, subchondral bone, and osteophyte parameters. Briefly, after formalin fixation for 3-4 days, the knee joints were disarticulated and the femurs retained for later histological analysis. The soft tissue surrounding the tibias was removed and the tibias were incubated in 30% Hexabrix™ 320 (Mallinckrodt Inc., St. Louis, MO, USA) contrast agent in PBS without calcium and magnesium at 37°C for 30 minutes. The tibias were then scanned using a Scanco μCT 40 (Scanco Medical, Brüttisellen, Switzerland) at 45 kVp, 177 μA, 200 ms integration time, and a voxel size of 16 μm. After scanning, the tibias were incubated in PBS at 37°C for 30 minutes to remove contrast agent.

The 2D axial greyscale EPIC-μCT images were rotated to sagittal sections, and cartilage, subchondral bone, and lesion volume analyses were performed as described previously[3], [99], [119]. Briefly, three sets of contours were used to indicate cartilage, subchondral bone, or lesions in the medial tibial plateau. Global thresholds and Gaussian filters (sigma = 1.0, support = 1) were then applied to separate cartilage, subchondral bone, and air. Analyzed parameters included cartilage X-ray attenuation (as an indicator of proteoglycan content[63], [66]), cartilage thickness, cartilage lesion volume, subchondral bone mineral density, and subchondral bone thickness. A validated, custom-built surface roughness algorithm was also used to quantify cartilage surface roughness[119]. Cartilage and subchondral bone analyses were performed for the central and medial thirds of the medial tibial plateau while lesion volumes were quantified for any lesions found throughout the medial tibial plateau.

Osteophytes are a thickening and partial mineralization of the medial edge of the medial tibial plateau. As a measure of osteophyte growth, the 2D axial images were rotated to coronal sections and the edge of the medial tibial plateau was contoured to include any bony outgrowth and cartilage thickening. Two sets of contours were used, one for mineralized tissue outgrowth that included extraneous soft tissue on the tibial edge, and another for cartilage volume that excluded the soft tissue. After contouring, two ranges of thresholds where used: one range to include only mineralized tissue and the other to include only cartilage the thickness and volume of marginal cartilage thickening as well as the volume of mineralized tissue within the osteophyte were measured.

4.2.4 Protein Elution Comparison

Pooled μ-dHACM and RPS μ-dHACM were suspended at 20mg/mL in Krebs-Ringer bicarbonate buffer with 0.4mM added calcium and 1% bovine serum albumin (BSA). Three samples from each formulation were incubated at 37°C under constant agitation for 21 days. The samples were centrifuged and the supernatant was collected for analysis at 0.5, 1, 2, 3, 7, 14, and 21 days. Fresh buffer with calcium and BSA was added at each time point. For two other samples of each formulation, collagenase I was added at 1mg/mL to the buffer immediately after resuspension, and the samples were incubated at 37°C for 4.5 hours with frequent mixing. Afterwards, the samples were centrifuged and the supernatant was collected for analysis. 41 different cytokines and chemokines were analyzed in both the extract and digested samples using the MILLIPLEX MAP Human Cytokine/Chemokine Magnetic Bead Panel – Immunology Multiplex Assay (Millipore Corporation, Billerica MA, USA). The concentration of all 41 analytes were calculated and the extract levels between μ-dHACM and RPS μ-dHACM were compared for the analytes with sufficiently detectible levels in both the digested and extracted samples.

4.2.5 Fluorescent Tagging and Tracking of μ-dHACM

Pooled μ-dHACM and RPS μ-dHACM were each suspended at 1mg/mL in 50mM sodium bicarbonate buffer per VivoTag® manufacturer's instructions. VivoTag® 680XL (Perkin Elmer, Inc, Waltham, MA, USA) was suspended at 10mg/ml in dimethyl sulfoxide and was added to the μ-dHACM suspensions at a ratio of 1 mg dye to 20 mg μ-dHACM. The suspensions were mixed for an hour at room temperature then centrifuged and washed two times in saline to remove excess dye. The tagged particles were then suspended in saline at 80 mg/mL in preparation for the intra-articular injections.

Weight matched Lewis rats (300-350g) underwent MMT surgery in their left legs. One day after surgery animals received a 50µL intra-articular injection of fluorescently tagged particles, either µ-dHACM or RPS µ-dHACM (n=7). Fluorescent imaging was performed at the specified timepoints: immediately following the injections, every two days for the first week, and then twice a week until six-weeks post-surgery. The fluorescent signal of the tagged particles in the intra-articular space was imaged using an IVIS® Spectrum (Perkin-Elmer, Inc) at 675-720nm excitation-emission, 0.5 sec exposure, f-stop 8, and 6.5cm field of view. The fluorescent intensity was measured as total efficiency (calculated by normalizing the fluorescent signal of the sample to the transmission image measured with the same emission filter and open excitation filter) within an area of interest that included any contiguous pixels with an efficiency within 27-100% of the peak signal at the knee joint and was presented as both absolute efficiency and normalized to the day 7 efficiency.

4.2.6 Histology

After EPIC-µCT scanning of the tibias, tibias and femurs were decalcified in Cal-Ex II (Thermo Fisher Scientific, Waltham, MA), embedded in paraffin, sectioned into 5 µm sections, and stained with hematoxylin and eosin (H&E).

4.2.7 Statistics

All other statistical analyses were performed using GraphPad Prism® (GraphPad Software, Inc. 5.01, La Jolla, CA). EPIC-µCT data were analyzed using one-way ANOVA with Tukey post-hoc tests to compare means across treatment groups. Comparisons between µ-dHACM and RPS µ-dHACM in both fluorescent particle tracking and growth factor

elution were performed using repeated measure ANOVA with Bonferroni post-hoc tests when warranted. Significance in all statistical tests was set at $p<0.05$.

4.3 Results

4.3.1 Particle Size Characterization

The area of particles of µ-dHACM and RPS µ-dHACM were calculated and then binned according to particle size. A representative image of eosin stained µ-dHACM particles is shown in Figure 4.1.A. The percentage of particles from each formulation within each bin are displayed in **Error! Reference source not found.**.B.

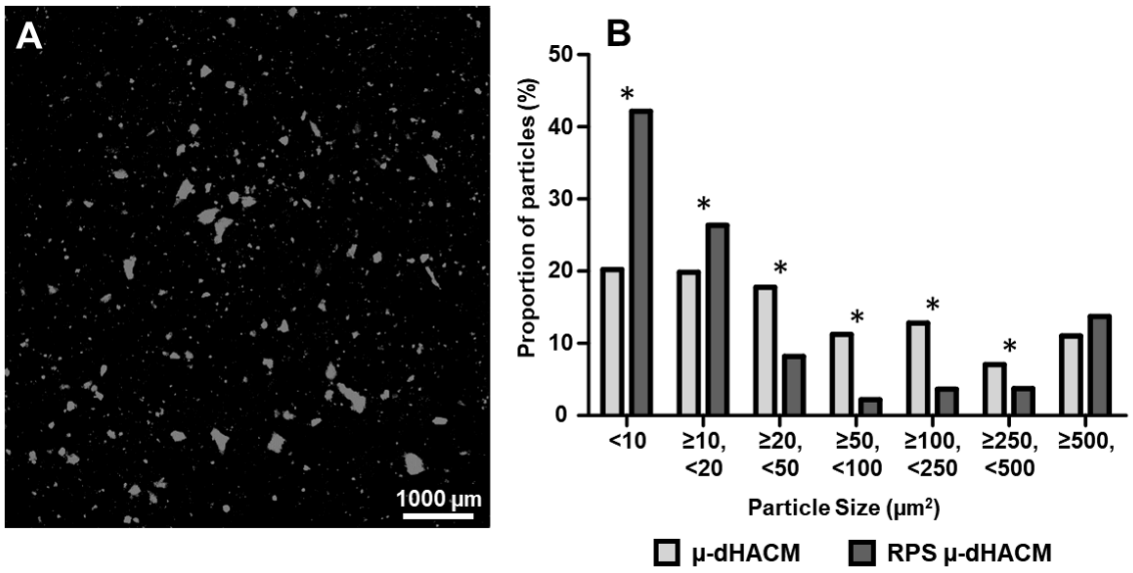

Figure 4.1: Particle size distribution of µ-dHACM and RPS µ-dHACM. A. Representative section of eosin stained µ-dHACM particles imaged under a fluorescent confocal microscope. B. Proportion of µ-dHACM (lighter bars) and RPS µ-dHACM (dark bars) samples split into bins based on particle area. Significant differences (* = $p<0.05$) between the two groups in each bin were determined using Jackknife analysis involving 1000 analyses of 500 particle samples in each bin

4.3.2 Cartilage EPIC-µCT Analysis

EPIC-µCT analysis indicated significant differences in cartilage, subchondral bone, and osteophyte parameters three weeks after surgery. Representative sagittal cuts from 3D EPIC-µCT x-ray attenuation maps qualitatively showed increased X-ray attenuation (decreased proteoglycan content[63], [66]) in MMT+saline (saline), MMT+µ-dHACM (µ-dHACM), and MMT+RPS µ-dHACM (RPS µ-dHACM) samples compared to sham samples and reduced lesion formation after µ-dHACM treatment compared to both saline and RPS µ-dHACM treatment (Figure 4.2.A-D).

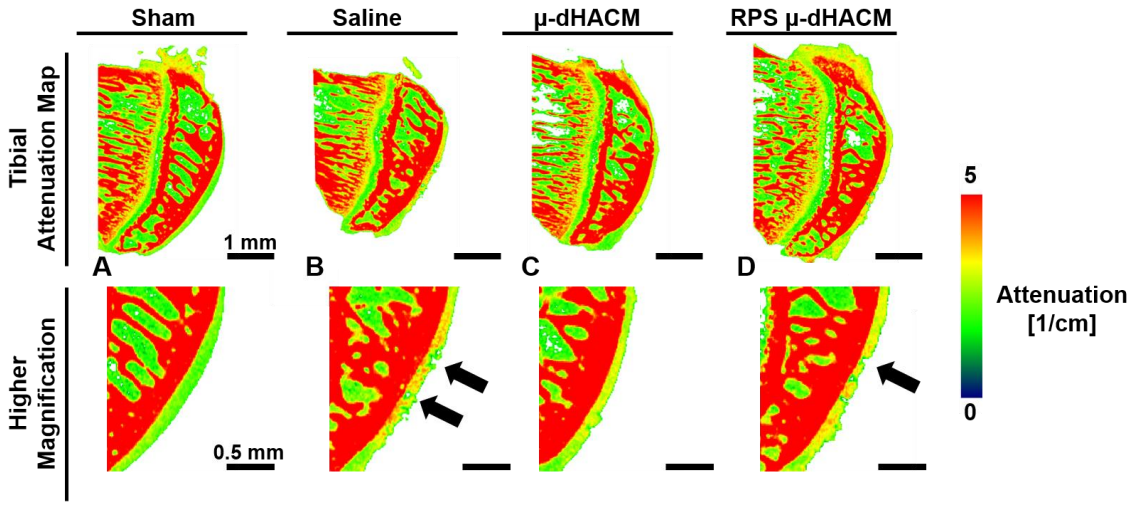

Figure 4.2: Representative EPIC-µCT imaging. A-D Representative medial tibial cartilage attenuation maps show lower attenuation in sham treatment samples. Pseudocolor attenuation bar at bottom indicates red as high attenuation and green as low attenuation. A. Sham sample displays smooth cartilage surface with green color indicating healthy sulfated glycosaminoglycan (sGAG) content. B. Saline treatment sample displays high attenuation indicating lower sGAG content and lesion formation (black arrow). C. Sample receiving micronized dehydrated human amnion/chorion membrane (µ-dHACM) displays increased attenuation but reduced lesion development D. Sample receiving reduced particle size µ-dHACM (RPS µ-dHACM) displays high attenuation and lesion formation (black arrow). Scale bars = 1mm; higher magnification scale bars = 0.5 mm

Saline treatment resulted in significantly increased cartilage X-ray attenuation (signifying proteoglycan loss) in the medial third of the medial tibial plateau as well as increased

cartilage volume, thickness, and surface roughness in the central and medial thirds compared to the sham group (Figure 4.3.A-F). Lesion volume in the entire medial tibial plateau was significantly increased in the saline group compared to sham (Figure 4.3.G).

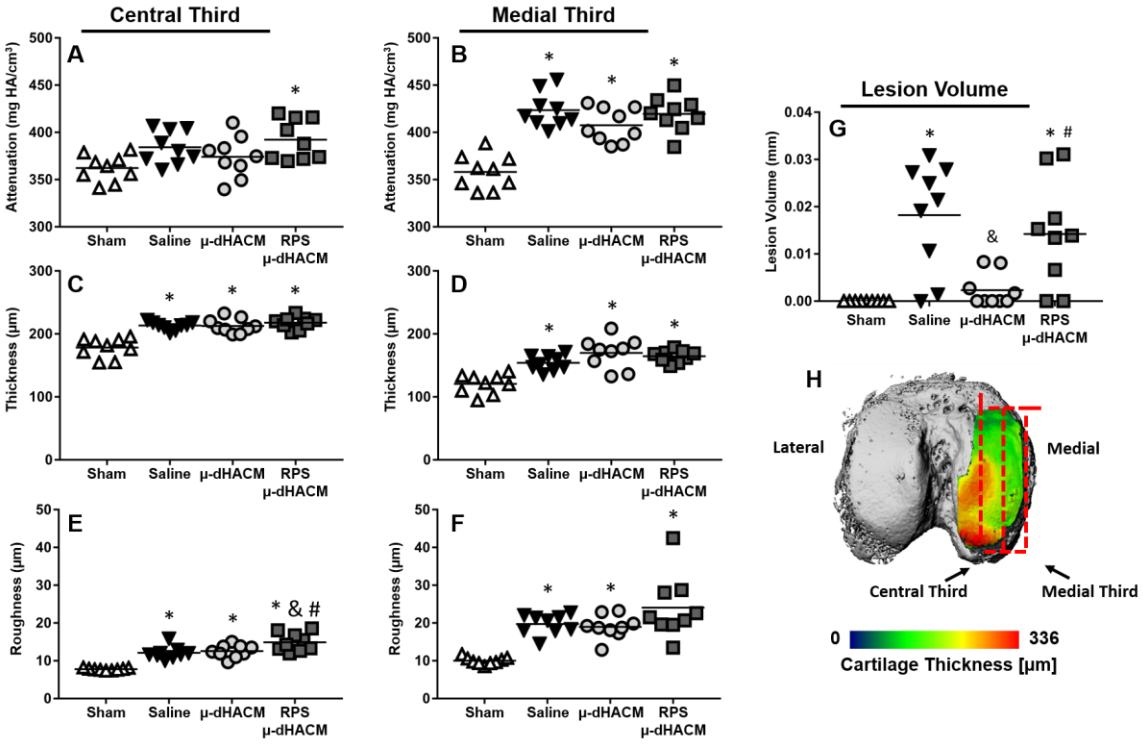

Figure 4.3: EPIC-μCT cartilage parameters – attenuation (A,B), thickness (C,D), and surface roughness (E,F) in the central (A,C,E) and medial (B,D,F) thirds of the medial tibial plateau; and lesion volume (G) in the entire medial tibial plateau. H. Evaluation areas of the central and medial thirds of medial tibial plateau indicated by red rectangles. Pseudocolor cartilage thickness bar in H indicates cartilage thickness throughout entire medial tibial plateau. Significance was determined using one-way ANOVAs with Tukey post-hoc tests. n = 9. * = p<0.05 vs Sham, & = p<0.05 vs Saline, # = p<0.05 vs μ-dHACM.

μ-dHACM treatment in MMT animals resulted in significantly increased cartilage X-ray attenuation in the medial third of the medial tibial plateau as well as significantly increased cartilage volume, thickness, and surface roughness in the central and medial thirds

compared to the sham group (Figure 4.3.A-F). μ-dHACM treatment, however, resulted in a significantly decreased lesion volume compared to the saline group (Figure 4.3.G).

RPS μ-dHACM treatment in MMT animals resulted in significantly increased cartilage X-ray attenuation (signifying proteoglycan loss), volume, thickness, and surface roughness in the central and medial thirds compared to the sham group (Figure 4.3.A-F). There was significantly increased cartilage surface roughness in the central third compared to saline and μ-dHACM treated groups (Figure 4.3.E). Lesion volume in the RPS μ-dHACM group was significantly increased compared to both sham and μ-dHACM (Figure 4.3.G).

4.3.3 Subchondral Bone μCT Analysis

There were no significant differences in the subchondral bone mineral density or thickness between any of the groups in the central third of the medial tibial plateau (Figure 4.4.A, C). Changes due to surgery or treatment were isolated to the medial third of the medial tibial plateau (Figure 4.4.B, D). Subchondral bone thickness in the medial third was significantly increased in the saline group compared to sham. There were significant increases in subchondral bone mineral density, and thickness in the medial third of the μ-dHACM group compared to sham. There were significant increases in the subchondral bone mineral density and thickness in the medial third of the RPS μ-dHACM group compared to sham.

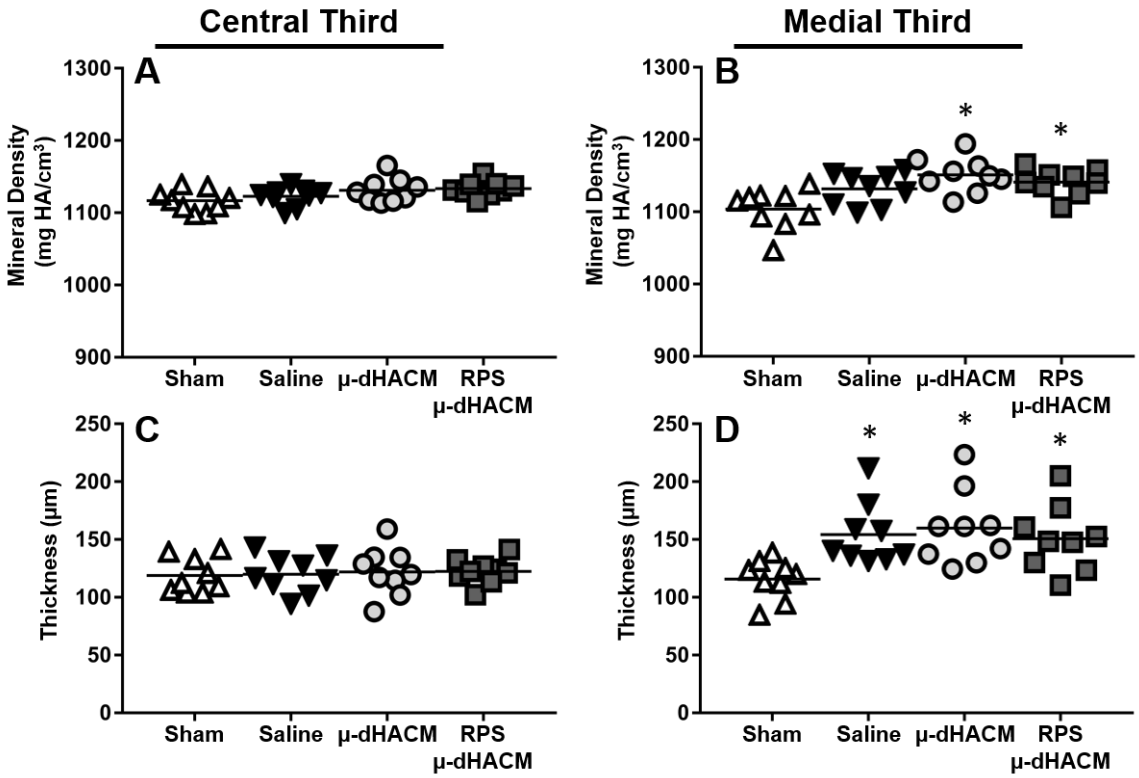

Figure 4.4: EPIC-µCT subchondral bone parameters – mineral density (A,B), thickness (C,D) in the central (A,C) and medial (B,D) thirds of the medial tibial plateau. Significance was determined using one-way ANOVAs with Tukey post-hoc tests. n = 9. * = p<0.05 vs Sham.

4.3.4 Osteophyte Volume EPIC-µCT Analysis

Osteophyte cartilage thickness, cartilage thickness, and mineralized volume in the saline injection group were significantly increased compared to sham (Figure 4.5.A-C). Osteophyte cartilage thickness, cartilage volume, and mineralized volume were all significantly increased in the µ-dHACM group compared to sham, and osteophyte cartilage volume was also increased in the µ-dHACM group compared to the saline group. Osteophyte cartilage thickness and cartilage volume in the RPS µ-dHACM group were significantly greater than both the sham and saline groups.

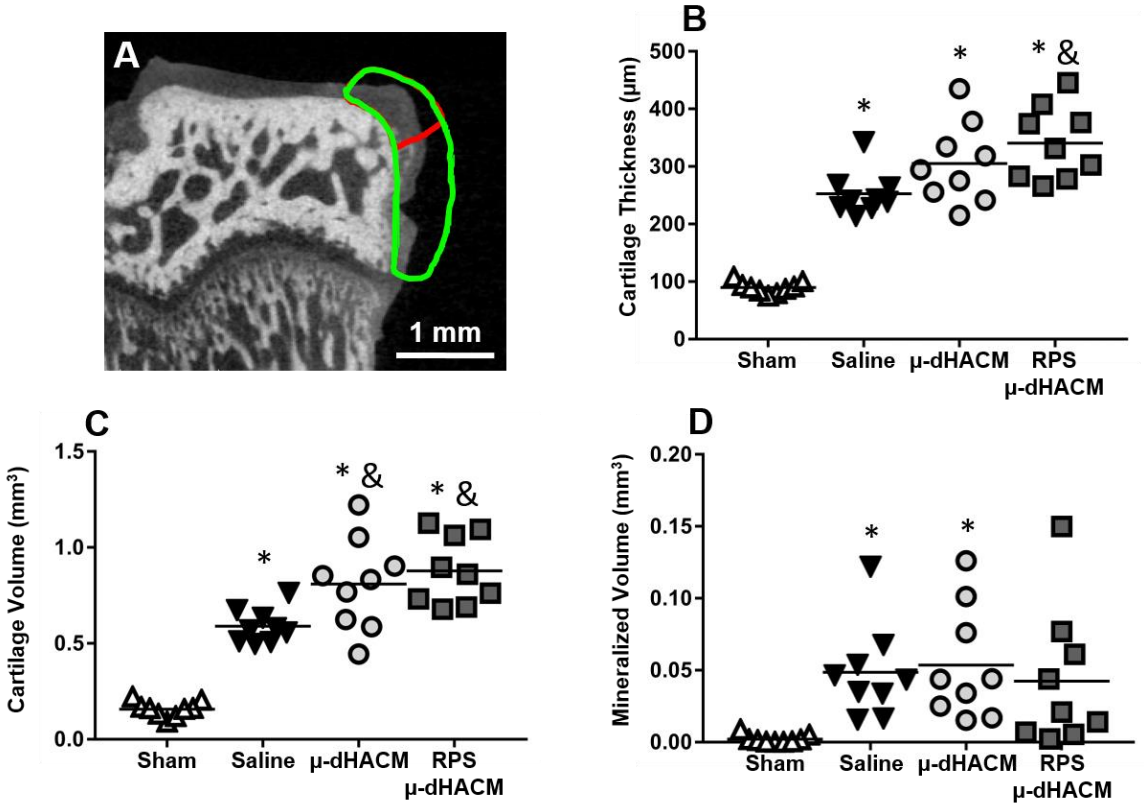

Figure 4.5: EPIC-μCT osteophyte (OP) parameters – A. Representative image of an OP observed on the tibia in the rat medial meniscal transection model with volumes of interest for cartilage (red) and mineralized tissue (green). OP cartilage thickness (B), OP cartilage volume (C), and OP mineralized volume (D) along the medial edge of the medial tibial plateau. Significance was determined using one-way ANOVAs with Tukey post-hoc tests. n = 9. * = p<0.05 vs Sham, & = p<0.05 vs Saline.

4.3.5 Protein Elution

Of 41 analytes quantified using the MILLIPLEX assay, 12 analytes had detectable levels in both the digested and extracted samples (the other analytes were below the limit of detection). Of these 12, four (epithelial growth factor (EGF), fibroblast growth factor 2 (FGF2), platelet derived growth factor BB (PDGF-BB), and chemokine (C-C motif) ligand 5 (CCL5)) had significantly different levels between the μ-dHACM and RPS μ-dHACM

samples, with all having increased factor eluted from the RPS µ-dHACM samples compared to the µ-dHACM. See Figure 4.6.

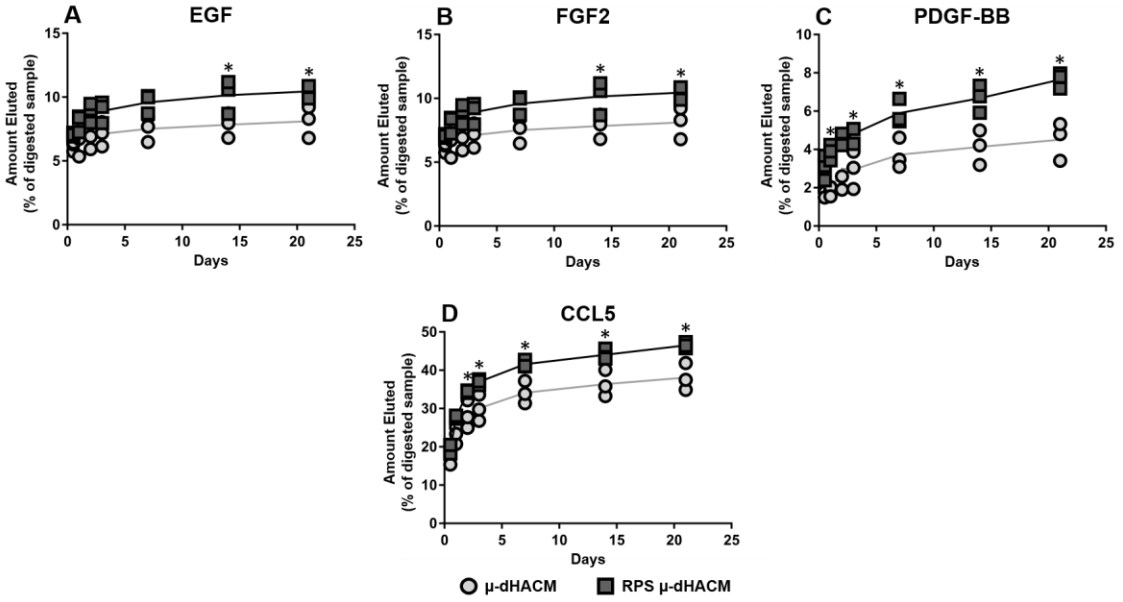

Figure 4.6: Protein elution from µ-dHACM and RPS µ-dHACM samples. The amounts of 41 factors contained in collagenase-digested samples or eluted into buffer over 21 days were quantified using a multiplex ELISA. The four factors with significant differences between µ-dHACM and RPS µ-dHACM samples are shown here. normalized to the amount of that factor in collagenase digested samples of the same µ-dHACM formulation. Epidermal growth factor (EGF; A), fibroblast growth factor 2 (FGF2; B), platelet derived growth factor-BB (PDGF-BB; C), and chemokine (C-C motif) ligand 5 (CCL5; D) all showed increased factor elution within the 3 weeks *in vitro.* Significance determined using repeated measures ANOVA with Bonferroni post-hoc tests. n=3.

4.3.6 In Vivo Particle Tracking

Error! Reference source not found..A-D show representative images of fluorescent signal seen in µ-dHACM (**Error! Reference source not found.**.A, C) and RPS µ-dHACM (**Error! Reference source not found.**.B, D) injected joints at 7-and 28-days post-surgery. There were no differences seen in fluorescent efficiency between tagged µ-dHACM and RPS µ-dHACM over four weeks in either the raw fluorescent efficiency data (**Error!**

Reference source not found..E) or normalized data (**Error! Reference source not found.**.F) indicating that there was no difference in particle clearance over the 28-day period.

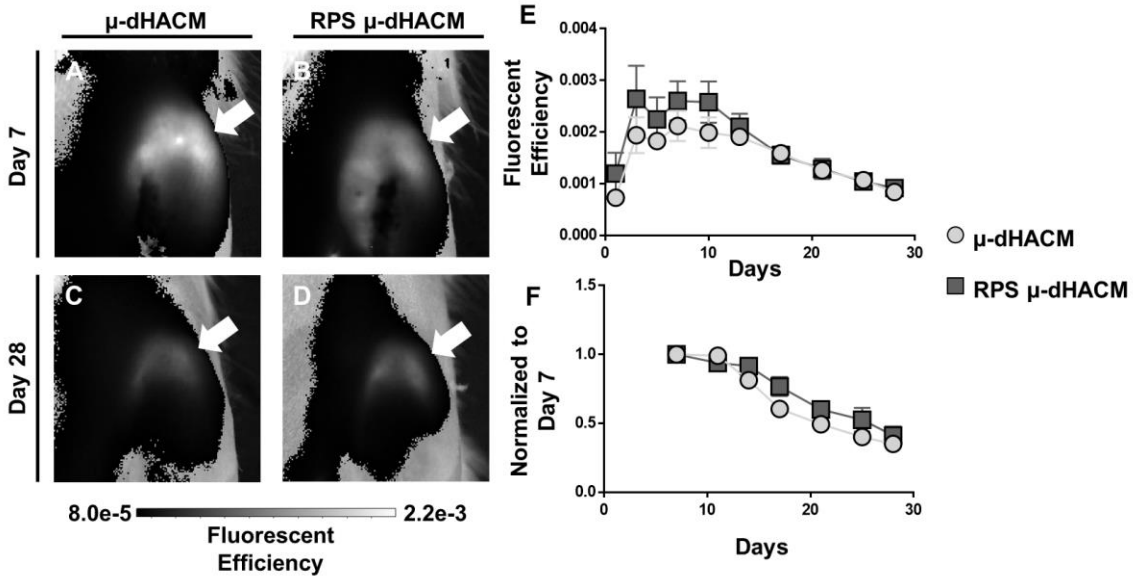

Figure 4.7: *In vivo* μ-dHACM particle tracking. A-D. Representative images of fluorescent signal in μ-dHACM (A,C) and RPS μ-dHACM (B,D) at Day 7 (A,B) and Day 28 (C,D) with arrows indicating the location of the knee. E-F. Fluorescent efficiency (E) and after normalizing to Day 7 efficiency (F) of fluorescently tagged μ-dHACM and RPS μ-dHACM particles. There was no significant difference as a result of treatment found using a repeated measures ANOVA in either dataset though there were significant effects of time in both. Fluorescent efficiency is calculated by normalizing the sample fluorescent signal to the transmission image measured with the same emission filter and open excitation filter. Data shown as mean ± standard error of the mean and n=3.

4.3.7 Histology

Figure 4.8 shows representative histological images of H&E stained medial tibial plateaus sectioned in the coronal plan. Sham samples showed no cartilage damage (Figure 4.8.A-B). Saline samples exhibited cartilage surface damage on the medial plateau indicated by fibrillations and lesions and osteophyte development indicated by cartilage thickening on

the medial edge of the plateau (Figure 4.8.C-D). µ-dHACM treatment reduced lesion development but not osteophyte development (Figure 4.8.E-F). RPS µ-dHACM treatment did not reduce lesion nor osteophyte development (Figure 4.8.G-H).

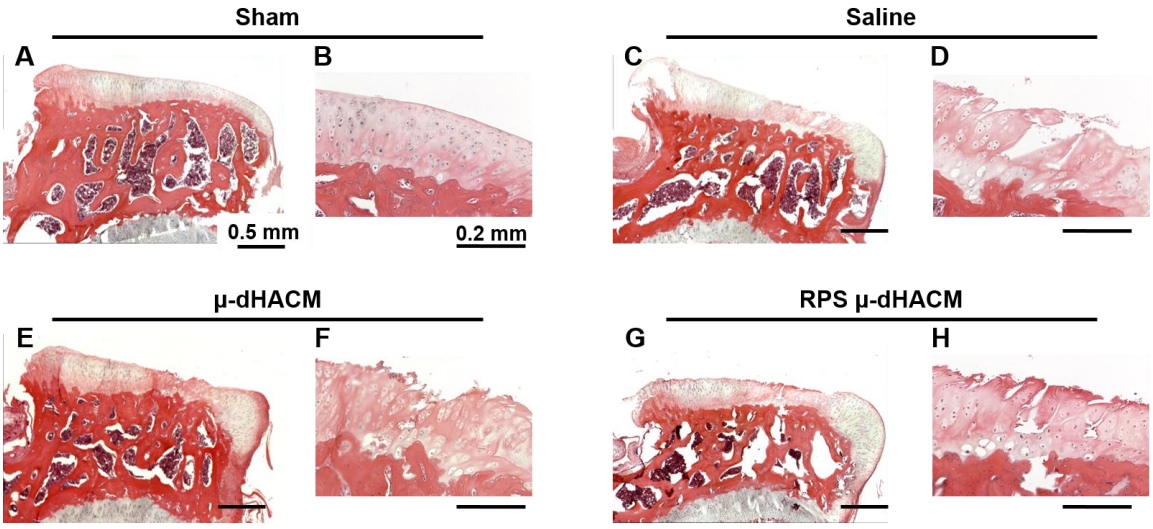

Figure 4.8: Representative H&E histology images for the tibiae. A–B. Sham sample showed no cartilage damage. C-D. Saline sample exhibited cartilage surface damage on the medial plateau indicated by fibrillations and lesions and osteophyte development indicated by cartilage thickening on the medial edge of the plateau. E-F. Micronized dehydrated human amnion/chorion membrane (µ-dHACM) treatment reduced lesion development but not osteophyte development. G-H. Reduced particle size µ-dHACM treatment did not reduce lesion nor osteophyte development. Scale bars in A, C, E, G are equal to 0.5 mm and bars in B, D, F, H are equal to 0.2 mm.

4.4 Discussion

Numerous extracellular matrix based therapeutics are being investigated for their potential efficacy in treating OA[120]. Amniotic membrane based therapeutics have shown efficacy at preventing OA development both when delivered acutely after injury (surgically induced) to the joint[40] or after OA disease has already developed[116]. However, many of the mechanisms and bioengineering factors that potentially influence the efficacy of this

treatment, including particle size, have yet to be explored. The purpose of this study was to investigate how altering the size of the amniotic membrane particles influences therapeutic efficacy, and we hypothesized that decreasing the size profile of the particles would increase factor elution and particle clearance rate from the joint.

In this study, two commercially available formulations of µ-dHACM, AmnioFix® Injectable (µ-dHACM) and AmnioFix® Sports Medicine (RPS µ-dHACM), were shown to have significantly different particle size profiles with the RPS µ-dHACM having a higher proportion of particles between 5 and 20µm^2. The study demonstrated that altering the particle size of the µ-dHACM does affect the therapeutic efficacy of the micronized amniotic membrane particles, as demonstrated by the increased lesion volume and surface roughness in the RPS µ-dHACM samples compared to the µ-dHACM samples. This study also confirmed that acute delivery of µ-dHACM, as shown previously[40], resulted in a significant decrease in lesion volume three-weeks post-surgery. While some of the protective effects of µ-dHACM treatment were observed in this study, the overall efficiency in preventing all measured parameters was not the same as previous studies. This could be due to the procedure used to pool and then weigh the µ-dHACM, slight differences between surgeons and severity of the induced OA, or slight variability in the product.

Unlike in previous studies investigating the use of amniotic membrane particles in which each experimental animal was treated with amnion from a single donor, pooled samples from five donors was used for both µ-dHACM and RPS µ-dHACM. Because of the manufacturing processes used to produce µ-dHACM and RPS µ-dHACM, it was not feasible to receive both µ-dHACM and RPS µ-dHACM from the same donors. To reduce

potential donor-to-donor variability between single samples in each formulation, pooled samples were used to achieve average sample properties for the formulations tested.

This study was the first to look at osteophyte growth in the MMT model three weeks after an acute delivery of µ-dHACM. After treatment with either formulation of µ-dHACM, we observed a significant increase in osteophyte cartilage volume and, with the RPS µ-dHACM, in osteophyte cartilage thickness. Amniotic membrane is known to contain FGF2, a known regulator of cartilage formation[121], [122], and this is corroborated by our own data (see Figure 4.6). The release of FGF2 could be stimulating cartilage growth, increasing the osteophyte volume. As there is no accompanying increase in mineralized tissue, this could indicate that that the increased cartilage volume is related to a chondrogenic pathway that could later undergo endochondral ossification.

µ-dHACM is known to contain a number of growth and immunomodulatory factors[44], [111], [123] and it has been hypothesized that this factor release could play a role in the mechanisms of µ-dHACM reducing OA progression[40]. Particle size, both in theory and in practice, affects factor elution from PLGA particles[118] and thus could play a role in the release of factors from µ-dHACM. In this study, as expected with smaller particles, the RPS-µ-dHACM was shown to secrete a greater percentage of several contained factors *in vitro*. However, *in vivo*, this 0-70% increase in factor secretion from RPS µ-dHACM did not translate into greater prevention of disease progression. This suggests that µ-dHACM acts as more than simply a factor pool and that timing of factor release may also be important. *In vivo*, the smaller particles could result in a greater burst release of factors, while the larger particles could act as a reservoir of factors that are released in a more delayed fashion. Further analyses, including flow cytometry and immunohistochemistry to

identify fibroblast- and macrophage-like synoviocytes[21], [22] as well as macrophage polarization[124], could provide greater insight into the mechanisms of µ-dHACM and if the differences in µ-dHACM particle size and release of immunomodulatory factors result in differences in cell recruitment, proliferation, or differentiation.

Previous work with µ-dHACM in the MMT model have shown that the µ-dHACM particles are sequestered into the synovium within three days of injections and are still present 21 days after injections[40]. While in this study the µ-dHACM particles were not apparent after three weeks in the synovium, fluorescent signal from tagged µ-dHACM was detectable in the joint out to four-weeks post-injection. This discrepancy could be explained by the difficulty in locating and recognizing ECM based particles using traditional 2D histological measures. Clearance of these fluorescently tagged µ-dHACM particles from the joint does not appear to be affected by the size profiles differences in these two formulations, suggesting that the majority of particles in both formulations are of a sufficient size to not be readily cleared from the joint[125].

While a significantly greater proportion of the RPS µ-dHACM particles were in the <10 to <20µm^2 range, there was also a greater proportion of RPS µ-dHACM particles in the >500µm^2 bin. While this difference did not reach significance, it could be that these larger particles, which make up a much larger proportion of the total volume of the particles are have a greater influence on the therapeutic efficacy than the smaller particles. As such, future work comparing particle size distributions with less overlap would clarify which size distribution has the greatest therapeutic effect.

This study has shown that altering µ-dHACM particle size distribution does affect therapeutic efficacy in a rat MMT model of OA. While the depth of the conclusions of this work is constrained by the large overlap in particle size between the two formulations, the results of this study further supports the potential of micronized amniotic membrane particles as a future OA therapeutic and demonstrates the possibility for engineers to customize the therapeutic action of the µ-dHACM through iterative design of the particle size.

CHAPTER 5. *IN VITRO* EVALUATION OF AN ECM BASED OA THERAPEUTIC

5.1 Introduction

Osteoarthritis, the most common form of arthritis, affects an estimated 13% of the adult population in the US (~27 million people) with an estimated 37% of the U.S. adult population over 60 years of age being affected by knee OA alone [2], [27]. It is characterized by overall joint degeneration that includes cartilage loss, bone sclerosis, osteophyte formation, and synovial changes[110]. While research is ongoing concerning many promising disease modifying therapies, including platelet rich plasma and stems cells, there is still a lack of treatments that prevent the progression of OA[110].

Amniotic membrane with its anti-inflammatory properties, multiple soluble factors that encourage tissue healing, and easy clinical availability has been used extensively in the clinic to treat ocular tears and skin ulcers. Amniotic membrane has also shown potential as a disease modifying OA therapy by preserving chondrocyte viability[45] and phenotype and repair osteochondral defects in rabbits[126]. Recently, multiple groups have tested the efficacy of micronized dehydrated amnion membrane at treat OA progression in rat models and have shown that particulates of amniotic membrane with and without umbilical cord tissue reduced OA progression in the rat medial meniscus transection model[40], [116]. Vines et al. tested the safety of suspended amnion particles in humans[117]. However, many of the factors influencing the therapeutic efficacy of these amnion suspensions are unexplored.

The intimal layer of the synovial membrane is a specialized connective tissue consisting of two main cell types: fibroblast-like synoviocytes and macrophage-like synoviocytes. These cells are responsible for maintaining the homeostasis of the joint cavity by removing debris and waste, regulating the inflammatory environment, and producing the hyaluronan and other proteoglycans necessary for the synovial fluid to perform its load-bearing and motion-enabling function[22]. Previous work in our lab exploring the therapeutic efficacy of amniotic membrane in the rat MMT model showed that the amnion membrane is sequestered into the synovial membrane of the joint[40]. This suggests that interactions between the synovium and the amnion play a crucial role in the mechanisms behind the therapeutic efficacy of amnion *in vivo*. A better understanding of the interactions between synoviocytes and amnion could elucidate the specific mechanisms of therapeutic efficacy in vivo.

In vitro cultures of synoviocytes have proven useful in providing information on the role of the synovium may play in OA development[127] and of the effects of potential OA therapies[128], [129]. PDGF-AA[130], interferon-γ[131], and hyaluronic acid[132] have all been shown to reduce inflammation or protease signaling from synoviocytes in vitro while platelet rich plasma has increased synoviocyte death and inflammatory signaling[133]. In addition to the culture of synoviocytes alone, a number of researchers have also used synovium/cartilage co-cultures to better recapitulate the actual *in vivo* environment[84], [87], [90], [134]–[138], with one study showing that culture of synoviocytes with chondrogenic stem cell pellets appears to result in increased levels of IL-8 and MMP-1[90].

Because of the previous work showing an important role of the synovium in OA development and, potentially, the therapeutic benefit of µ-dHACM, this work was designed to investigate the effect of interactions between synoviocytes and µ-dHACM in *in vitro* culture. Specifically, it will investigate what effect µ-dHACM has on the cytokine, chemokine, and MMP production of IL-1β- and TNF-α-activated synoviocytes and how the particle size of the µ-dHACM may influence thus interaction. We also explore how the co-culture of synoviocytes and µ-dHACM affects the loss of proteoglycans in cytokine-stimulated chondrocyte pellets. This outcome of this study will help explain the therapeutic efficacy of µ-dHACM treatment in OA models.

5.2 Materials and Methods

5.2.1 Preparation of µ-dHACM

µ-dHACM was prepared using the proprietary PURION® process (MiMedx Group, Inc. Marietta, GA). Specifically, AmnioFix Injectable was used for all the studies while AmnioFix Sports Medicine, which has been shown to have a larger proportion of small particles (see Chapter 4) was also used to investigate the effect of particle size. To account for donor to donor variations in the µ-dHACM, five different batches of each formulation, each from a different donor, were pooled prior to adding them to *in vitro* cultures.

To obtain the amnion particle extract used in this study, the amnion particles were extracted at 20mg/mL at 4°C for 24 hours in culture media (CM) consisting of MEM-alpha with 16% FBS, 1% PSA, and 1% L-Glutamine. After extraction, the particles were removed from the 20mg/mL extract by centrifugation and filtration.

5.2.2 Activation of Synoviocyte Cultures

Human fibroblast-like synoviocytes from three separate donors were purchased and cultured to passage 3 in proprietary Synoviocyte Growth Media (Cell Applications, Inc, San Diego, CA). For all following experiments, synoviocytes from all three donors were pooled in equal amounts. After recovery from frozen and seeding in 96-well plates in Synoviocyte Growth Media, synoviocytes were activated for 24 hours with human interleukin-1β and tumor necrosis factor α (5ng/mL each) in 0.2 mL CM. CM without cytokines was added to control wells.

5.2.3 Synoviocyte and Amnion Dosing Study

24-hours after synoviocyte activation with the cytokines, 200 µL of CM; CM with 10, 1, 0.1, or 0.01 mg/mL µ-dHACM particles separated with a 5.0µm-pore-size transwell insert (Corning®, Corning, NY, USA); or 10, 1, or 0.1 mg/mL µ-dHACM extract in CM were added to the wells. 3 days after µ-dHACM addition, the media was removed for cytokine, chemokine, and matrix metalloprotease (MMP) content quantification and MMP activity assay. (Figure 5.1)

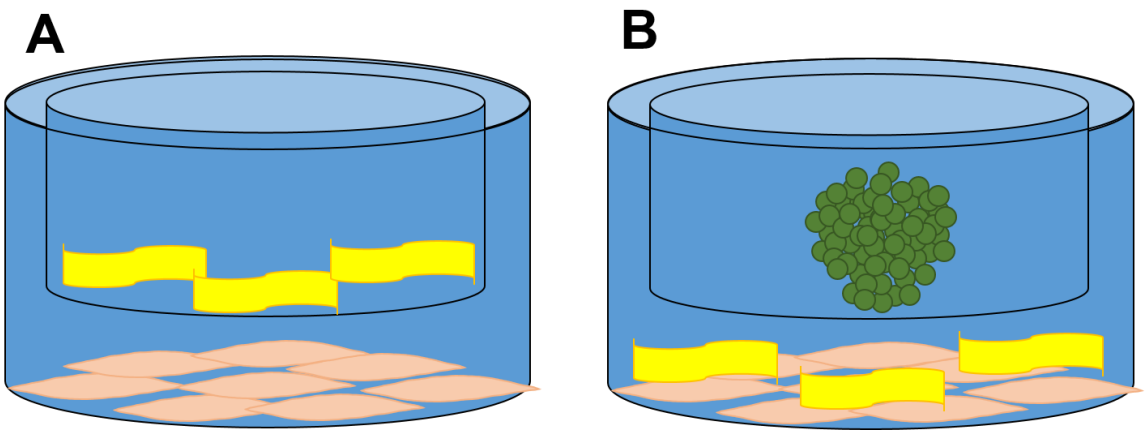

Figure 5.1: Experimental design for *in vitro* studies. A) Experimental setup for synoviocyte/µ-dHACM co-culture. B) Experiment setup for chondrocyte pellet/synoviocyte/µ-dHACM co-culture.

5.2.4 Synoviocyte and Amnion Particle Size Study

24-hours after synoviocyte activation, 300 µL of CM; CM with 10 mg/mL of either µ-dHACM or RPS µ-dHACM with in a 5.0-pore-size transwell insert; or CM with 10mg/mL µ-dHACM or RPS µ-dHACM extract was added to the synoviocytes. Acellular plates with the same treatments were also prepared. 3 days after µ-dHACM addition, the media was removed for cytokine, chemokine, and matrix metalloprotease (MMP) content quantification and MMP activity assay. Synoviocytes are washed in PBS, fixed in 4%PFA overnight, washed twice in PBS, stained with 1% DAPI in PBS, washed twice in PBS, and imaged using BioTek Cytation 3 Imaging Plate Reader (BioTek, Winooski, VT, USA). BioTek Gen 5 Software was used to count cell nuclei for synoviocyte cell count. Cytokine and chemokine content was analyzed using the MILLIPLEX MAP Human Cytokine/Chemokine Magnetic Bead Panel – Immunology Multiplex Assay (EMD Millipore). MMP content was quantified using MILLIPLEX MAP Human MMP Magnetic Bead Panel 1 – Immunology Multiplex Assay (EMD Millipore). MMP activity was

quantified using the MMP Activity Assay Kit from Abcam after a 24hour incubation with 2mM 4-Aminophenylmercuric Acetate to quantify MMP activity.

5.2.5 Direct µ-dHACM

5.2.6 Chondrocyte Pellet Co-culture

Primary bovine articular chondrocytes were purchased frozen from Astarte Biologics, thawed, and pelleted to form pellets of 200,000 cells each. They were cultured in serum-free media (DMEM with sodium pyruvate, high glucose, l-glutamine, ITS+, non-essential amino acids, ascorbic acid-2-phospate, gentamicin, and dexamethasone) with media changes 3 times a week for two weeks prior to starting co-culture with synoviocytes and µ-dHACM.

24-hours after synoviocyte activation, pellets (one per well), µ-dHACM (10ng/mL), and cytokines (5ng/mL IL-1β and 5ng/mL TNF-α) were added to the 96 well plates in 5 different culture combinations: pellets alone (P), pellets + cytokines (P+C), pellets + synoviocytes + cytokines (P+S+C), pellets + µ-dHACM + cytokines (P+A+C), and pellets + synoviocytes + µ-dHACM + cytokines (P+S+A+C). The pellets were placed in transwell inserts to keep them separate from the synoviocytes and µ-dHACM was added directly to the bottom of the 96-well plates. The wells with cytokines had cytokines added both during synoviocyte activation and during co-culture with pellets and µ-dHACM. Three days after co-culture initiation, the pellets were collected for DMMB, DNA, and histological analyses.

Five pellets from each group were digested using proteinase K for 3 hours with periodic mixing. The digest was analyzed using DMMB and Picogreen DNA assays.

5.2.7 Statistics

For the purposes of analysis, the groups in synoviocyte and amnion particle size experiment were split into two 2x2 experimental layouts: 1) with vs without cytokine activation, and with vs without amnion treatment; and 2) µ-dHACM vs RPS µ-dHACM, and transwell vs extract culture. Partial least square discriminate analyses on both sets were performed using in-house software and 2-way ANOVAs with Sidak post-hoc tests were performed using GraphPad Prism® (GraphPad Software, Inc. 7.03, La Jolla, CA). Comparisons for the direct µ-dHACM and chondrocyte pellet co-culture experiments were made using one-way ANOVAs with Tukey Post-hoc tests.

5.3 Results

5.3.1.1 Synoviocyte Culture

Throughout the experiments, synoviocytes showed a fibroblast-like morphology, indicating that the synoviocytes were of a fibroblast-like lineage and not a macrophage lineage.

5.3.1.2 Activation vs Treatment Groups

A 2-way ANOVA for cell number did result in significant interactions between the activation and treatment groups, thus all cell means were compared to each other. Both activation of synoviocytes with cytokines and treatment with µ-dHACM individually

resulted in decreased cell number compared to unactivated, untreated synoviocytes while the activated and µ-dHACM treated group had significantly lower cell number than the three other groups (See Figure 5.3.A).

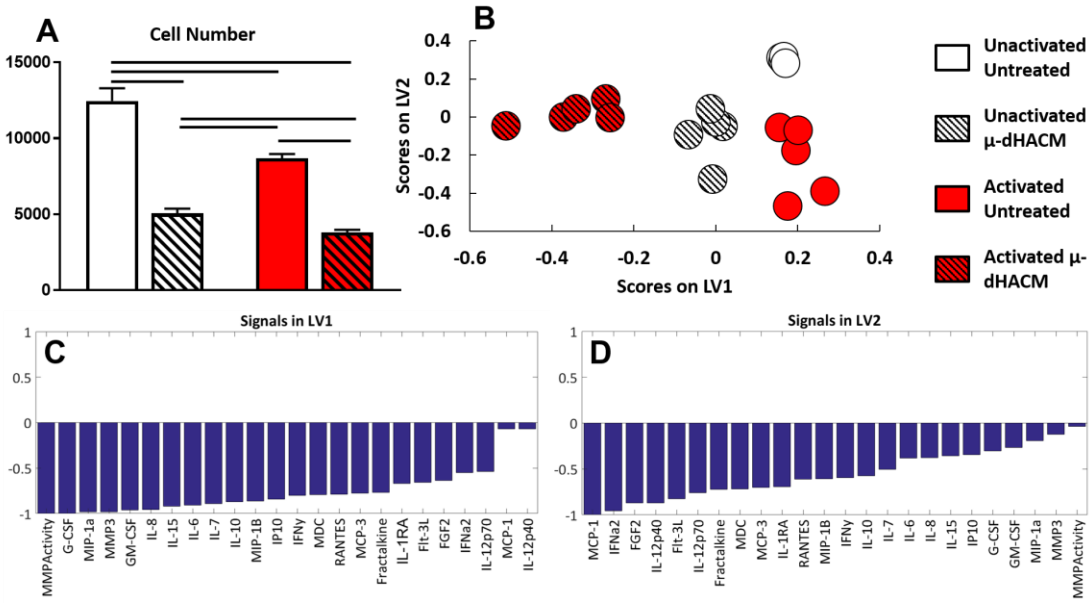

Figure 5.2: Synoviocyte Activation (Unactivted or Activated with 5ng/mL IL-1β and TNF-α) vs Treatment (Untreated or Treated with 10mg/mL µ-dHACM) Experiment. A) Synoviocyte cell number of groups showed that activation and µ-dHACM treatment, both independently and combined, reduced cell numbers compared to unactivated, untreated controls. B) Plot showing each sample's score on latent variable 1 (LV1) and latent variable 2 (LV2) from the partial least squares discrimate analysis (PLSDA) of the factor content of the samples. C and D) Weighted signals of each factor from the PLSDA.

The amount of each factor in pg per 1000 cells for each group is given Table 5.1. The partial least square discriminate analysis resulted in good separation between the groups (see Figure 5.2.B) and Figures 5.2.C,D show the weighted signals for both latent variables (LV1 and LV2) in the analysis. The clear majority of the factors heavily influenced LV1, which separated the differently treated groups while less of the factors heavily influenced LV2, which separated the unactivated, untreated group from the activated, untreated group.

Table 5.1: Factor Contents for Synoviocyte Activation (Unactivted or Activated with 5ng/mL IL-1β and TNF-α) vs Treatment (Untreated or Treated with 10mg/mL µ-dHACM) Experiment. Factor values are normalized to pg/1k cells and '*' in Int, Act, and Trt columns indicate significant effects of interactions, activation, or treatment, respectively, in the 2-way ANOVA. '#' indicate that that factor was significantly different in that group compared to the matching untreated group while '$' indicate that that factor was sigificantly different compared to matching unactivated group as indicated by Sidak's post-hoc test. N=4-5.

Factor (pg/1k cells)	Int	Act	Trt	Unactivated Untreated	Unactivated µ-dHACM Treated	Activated Untreated	Activated µ-dHACM Treated
FGF2	*	*	*	0.00	3.55±1.72 #	2.63±1.30 $	3.82±2.03
G-CSF	*	*	*	0.00	174.35±29.07 #	51.44±27.66 $	283.94±48.66 # $
Flt-3L		*	*	0.08±0.23	1.96±0.20 #	1.72±1.45 $	2.52±0.83
GM-CSF	*	*	*	0.00	1.59±0.51 #	1.64±0.84 $	7.50±1.89 # $
Fractalkine	*	*	*	0.63±0.45	24.13±5.76 #	13.85±5.63 $	27.03±2.34 #
IFNa2		*	*	0.00	3.27±2.43 #	3.35±2.65 $	4.43±1.21
IFNy	*	*	*	0.00	3.37±1.08 #	1.35±0.44 $	3.48±0.86 #
IL-10		*	*	0.00	0.57±0.15 #	0.30±0.23 $	0.77±0.37 #
MCP-3		*	*	0.34±0.31	2.15±0.44 #	2.25±0.46 $	3.56±0.42 # $
IL-12p40		*		0.00	0.35±0.98	1.21±0.96 $	0.85±1.18
MDC		*	*	0.11±0.18	1.40±0.50 #	1.14±0.68 $	2.10±0.33 # $
IL-12p70		*		0.00	0.67±0.23	0.74±1.27	1.08±0.51
IL-15			*	0.00	0.82±0.63 #	0.18±0.35	1.35±0.76 #
IL-1RA		*	*	0.00	1.48±1.53 #	1.32±0.99	2.17±1.04
IL-6		*	*	2.15±0.43	1774.32±66.28 #	558.77±195.55 $	2294.51±273.47 # $
IL-7	*	*	*	0.00	7.23±0.50 #	3.48±0.63 $	9.63±1.07 # $
IL-8	*	*	*	1.84±0.53	2350.17±353.80 #	1157.55±286.21 $	4105.75±614.18 # $
IP10		*	*	0.00	1.840±0.70	1.25±0.96	4.49±4.32 #
MCP-1	*	*	*	46.31±8.91	403.23±42.83 #	550.96±48.65 $	443.86±29.82 #
MIP-1α	*	*	*	0.00	0.32±0.31	0.09±0.25	1.39±0.64 # $
MIP-1B		*	*	0.00	1.26±0.69 #	0.77±0.90	2.11±0.65 # $
RANTES		*	*	0.00	2.61±1.98 #	3.45±1.05 $	5.23±1.36 # $
MMP3	*	*	*	0.00	7288.06±2504.72 #	4422.26±1641.46	36093.00±9603.83 # $
MMPActivity	*	*	*	151.64±581.15	2214.53±1622.81 #	1062.50±251.16 $	9576.29±947.04 # $

5.3.1.3 Size vs Exposure Groups

A 2-way ANOVA for cell number did result in significant interactions between the size and exposure groups, thus all cell means were compared to each other. There was no difference in cell number in the µ-dHACM and RPS µ-dHACM transwell groups. Both µ-dHACM and RPS µ-dHACM extract resulted in increased cell number compared to the transwell groups, and RPS µ-dHACM extract resulted in decreased cell number compared to µ-dHACM extract (See Figure 5.3.A).

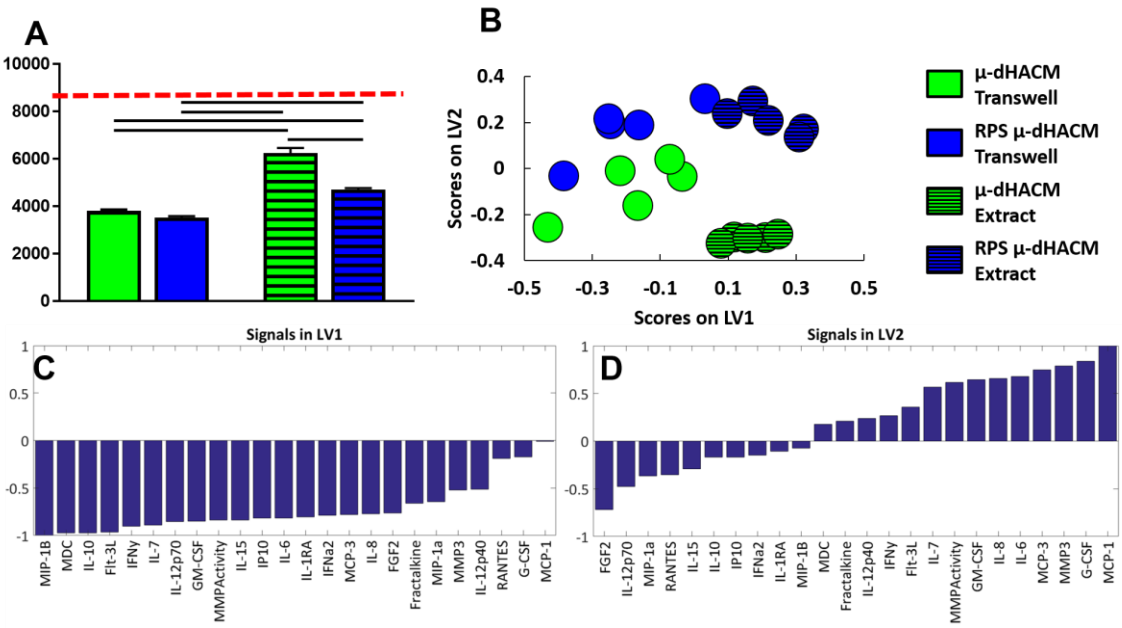

Figure 5.3: Size (μ-dHACM or Reduced Particle Size (RPS) μ-dHACM) vs Exposure (Transwell or Extract) μ-dHACM Synoviocyte Experiment. A) Synoviocyte cell number of groups show that all four groups had lower cell numbers than stimulated untreated group (red line) while both extract groups had significantly higher cell numbers than the transwell groups and RPS μ-dHACM extract group had signficantly reduced cell numbers compared to μ-dHACM. B) Plot showing each sample's score on latent variable 1 (LV1) and latent variable 2 (LV2) from the partial least squares discrimate analysis (PLSDA) of the factor content of the samples. C and D) Weighted signals of each factor from the PLSDA.

The amount of each factor in pg per 1000 cells for each group is given Table 5.1. The partial least square discriminate analysis resulted in separation between the groups (see Figure 5.3.B) and Figures 5.3.C,D show the weighted signals for both latent variables (LV1 and LV2) in the analysis. The clear majority of the factors heavily influenced LV1, which resulted in separating of the transwell and extract groups, indicating that there were many differences between the transwell and extract groups. Several factors influenced LV2, which resulted in separation of μ-dHACM and RPS μ-dHACM, indicating that there were some differences as a result of μ-dHACM particle size.

Table 5.2: Factor Contents for Size (µ-dHACM or Reduced Particle Size (RPS) µ-dHACM) vs Exposure (Transwell or Extract) µ-dHACM Synoviocyte Experiment. Factor values are normalized to pg/1k cells and '*' in Int, Act, and Trt columns indicate significant effects of interactions, activation, or treatment, respectively, in the 2-way ANOVA. N=4-5.

Factor	Int	Siz	Exp	µ-dHACM Transwell	RPS µ-dHACM Transwell	µ-dHACM Extract	RPS µ-dHACM Extract
FGF2		*		3.82±2.03	2.12±3.71	2.88±1.95	-0.21±2.05
G-CSF	*	*		283.94±48.66	285.56±54.91	186.33±31.11	351.98±44.23
Flt-3L		*	*	2.52±0.83	3.44±0.78	1.48±0.48	1.69±0.32
GM-CSF		*	*	7.50±1.89	9.93±1.73	3.80±0.88	5.95±0.96
Fractalkine			*	27.03±2.34	30.03±5.77	23.90±6.89	23.40±6.74
IFNa2			*	4.43±1.21	6.17±4.72	3.57±2.69	1.97±2.81
IFNy			*	3.48±0.86	4.86±1.55	2.28±0.63	2.29±0.87
IL-10			*	0.77±0.37	0.68±0.49	0.39±0.08	0.23±0.54
MCP-3		*	*	3.56±0.42	4.25±0.41	2.61±0.40	3.36±0.58
IL-12p40				0.85±1.18	3.11±4.61	0.66±1.20	1.15±2.39
MDC			*	2.10±0.33	2.22±0.90	1.19±0.24	1.24±0.57
IL-12p70		*	*	1.08±0.51	0.89±0.75	0.64±0.30	0.07±0.26
IL-15		*	*	1.35±0.76	0.58±1.03	0.28±0.50	-0.95±1.13
IL-1RA			*	2.17±1.04	2.86±1.28	1.52±1.82	0.17±2.00
IL-6	*	*	*	2294.51±273.47	2448.12±160.77	1157.41±120.50	1745.02±108.32
IL-7		*	*	9.63±1.07	9.98±0.52	6.06±0.91	7.54±0.16
IL-8	*	*	*	4105.75±614.18	4197.82±456.53	2184.06±268.39	3113.44±391.87
IP10			*	4.49±4.32	5.06±4.95	2.55±1.60	0.64±2.48
MCP-1	*	*		443.86±29.82	484.77±62.55	380.38±39.70	510.76±69.93
MIP-1a		*	*	1.39±0.64	0.88±0.69	0.81±0.15	0.48±0.38
MIP-1B			*	2.11±0.65	2.10±1.68	0.91±0.46	0.31±1.44
RANTES	*	*		5.23±1.36	1.02±2.80	3.00±0.89	3.58±1.35
MMP3		*	*	36093.00±9603.83	42681.19±13533.93	17139.76±4870.22	34717.93±16591.33
MMP Activity		*	*	9576.29±947.04	11088.98±1016.22	2874.25±1330.03	6057.52±2702.17

5.3.1.4 Synoviocyte and µ-dHACM Direct Study

As shown in figure 5.4, treatment of activated synoviocytes with µ-dHACM added directly on top of the synoviocytes resulted in a reduced MCP-1 content compared to activated, untreated synoviocytes while there was no change in IL-6 production.

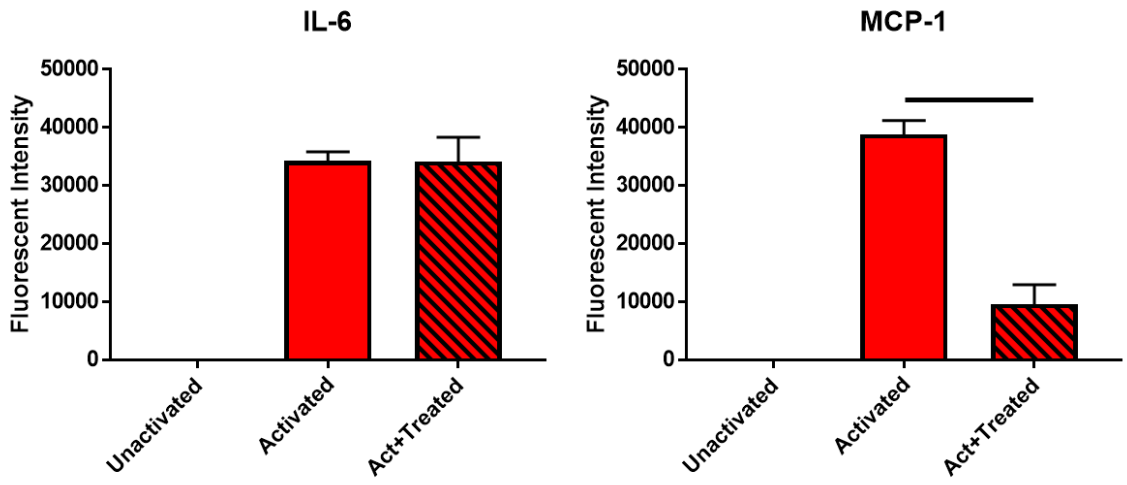

Figure 5.4: IL-6 and MCP-1 content in synoviocytes treated directly with µ-dHACM. Fluorescent intensity values for Interleukin-6 and Monocyte Chemoattractant Protein-1 from multiplex ELISA for unactivated, activated, and activated+10mg/mL direct µ-dHACM.

5.3.1.5 Synoviocyte and Pellet Co-Culture

Dimethyl-methylene blue assay showed that pellets cultured with 5ng/mL each of IL-1β and TNF-α (cytokines) or with cytokines and synoviocytes had significantly less GAG content than pellets cultured in culture media alone. Adding 10mg/mL µ-dHACM to pellets+cytokines significantly increased GAG content compared to both pellets+cytokines and pellets+cytokines+synoviocytes groups. Adding 10mg/mL µ-dHACM to the pellets+cytokines+synoviocytes group significantly increased GAG content compared to the pellets+cytokines+synoviocytes group. See 5.5.

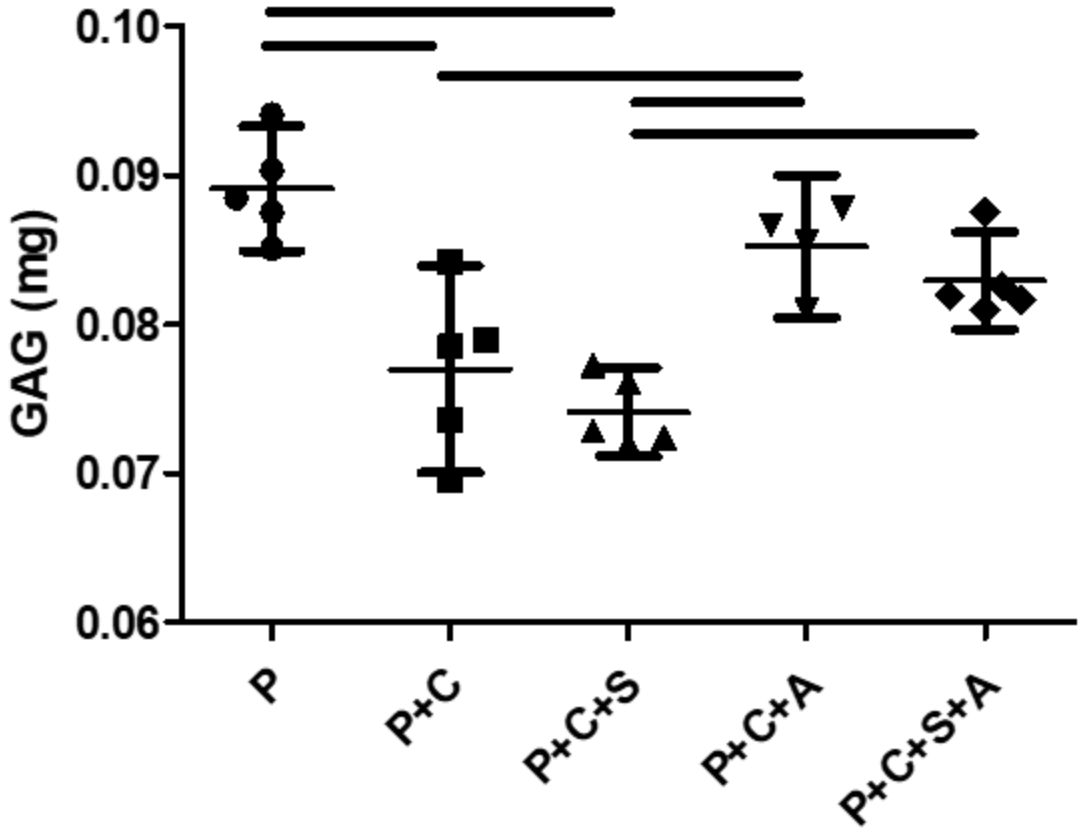

Figure 5.5: Proteoglycan (PG) content of bovine articular chondrocyte pellets. Pellets were co-cultured with interleukin 1-β and tumor necrosis factor-α (cytokines), synoviocytes, and µ-dHACM. Pellets were split into five groups: pellets alone (P), pellets with 5 ng/mL cytokines (P+C), pellets with cytokines and synoviocytes (P+C+S), pellets with cytokines and 10mg/mL µ-dHACM (P+C+A), and pellets with cytokines, synoviocytes, and µ-dHACM (P+C+S+A). Pellets cultured with cytokines had less sGAG. n=4-5 and data shown as mean±95% confidence interval of the mean. Lines indicate pairs that are significantly different ($p<0.05$) from each other.

5.4 Discussion

Numerous extracellular matrix based therapeutics are being investigated for their potential efficacy in treating OA[120]. Amniotic membrane based therapeutics have shown efficacy at preventing OA development both when delivered acutely[40] or after the disease has

developed[116]. However, many of the mechanisms and bioengineering factors that potentially influence the efficacy of these treatments, such as synoviocyte interactions, have yet to be explored. The purpose of this study was to explore how amnion particle interact with synoviocytes *in vitro*.

The current study demonstrated that amnion, both in a transwell co-culture and as extract, reduces synoviocyte proliferation. Synoviocyte hyperplasia is a known feature of osteoarthritis development[139], thus part of the therapeutic benefit of amnion *in vivo* could be due to a reduction of synoviocyte proliferation. While there have been few studies looking at the effect of reducing cellular hyperplasia, one study looking at the effects of cadmium on OA showed that cadmium both reduced synoviocyte proliferation and OA clinical scores in a rat OA model[140] thus support the theory that reducing synoviocyte proliferation can help reduce OA progression.

While no previous work has been done showing the effect of devitalized amniotic membrane on synoviocytes, one recent paper by Parolini, et al did investigate the effect of amniotic membrane cells on rheumatoid arthritis synovial membrane cells[141]. The authors of that study showed that amniotic membrane cells did reduce TNFα production and proteinase activity in the synovial membrane cells. The differences between the proteinase activity of the Parolini, et al study and the current one could be explained by the fact that devitalized ECM is added to the culture in the current study while the Parolini, et al study included only cells. More work is needed to see if ECM from any source, such as small intestinal submucosa[142] or collagen only, also induces this increase in proteinase activity.

Synoviocyte secretion of G-CSF and IL-8 (also known as neutrophil attractant protein) were both greatly increased as a result of amnion co-culture and both of these cytokines are known recruiters/stimulators of granulocytes, specifically neutrophils. In addition, synoviocyte secretion of monocyte chemoattractant protein-1 (MCP-1) was shown to be decreased in amnion co-culture, indicating that monocyte, and thus macrophage, recruitment may be decreased as a result of µ-dHACM treatment. These results suggest that amnion treatment could increase the neutrophil to macrophage ratio within the synovium, and increased neutrophil to amnion ratio has been shown to correlate with decreased osteoarthritis disease grade. Macrophages are also known to be the characteristic cell type in chronic inflammation[143] and reducing macrophage recruitment could decrease chronic inflammation. In addition, the increased levels of IL-6 and fractalkine suggest µ-dHACM treatment could result in an increase in acute inflammation proteins and cells[144]. This acute inflammation could thus assist in resolving the disease state and reducing later chronic inflammation. Altogether, the changes in cytokine production shown in this study indicate that µ-dHACM treatment could result in reduced chronic inflammation in the joint space, and show that further studies are warranted that investigate µ-dHACM treatment of chronic inflammation in joints.

This work demonstrated that experimental setup is important when evaluating tissue based therapies. While there were few differences between µ-dHACM and RPS µ-dHACM when added directly to the synoviocyte culture, this was not the case with the extracts. RPS µ-dHACM extract resulted in effects on cytokine and MMP production more similar to the direct µ-dHACM groups than µ-dHACM extract. This could be explained by greater factor

elution due to the smaller particle size[118] and demonstrates the potential importance of factor elution in the mechanism of action of µ-dHACM.

The results of this study showed that µ-dHACM protects chondrocyte pellets against cytokine-induced GAG loss and this was the first study to show that co-culture of particulate amniotic membrane can protect chondrocyte pellets in this fashion. Previous studies have shown that amniotic membrane can act as substrates for chondrocyte proliferation and GAG production[45], [46], [126] but no studies have investigated the influence of particulate amniotic membrane or the co-culture of chondrocytes with amniotic membrane without direct contact between the two. The mechanism by which µ-dHACM protects chondrocytes against proteoglycan loss still needs to be elucidated but µ-dHACM is known to contain tissue inhibitors of metalloproteinases[44] and thus could be suppressing MMP activity. However, this study quantified MMP activity for synoviocytes co-cultured with µ-dHACM and found that MMP activity from activated synoviocytes was increased with the addition of µ-dHACM. This suggest that reducing MMP activity may not be the only mechanism by which µ-dHACM may be protecting proteoglycan loss in chondrocyte pellets. Synoviocytes are known to secrete hyaluronic acid in co-culture with µ-dHACM, which is also known to help prevent GAG loss in cartilage[145]. Thus, though MMP activity is increased in synoviocytes treated with amnion, the amnion may also be stimulating protective elements such as hyaluronic acid. In addition, the protection of the GAG content in the chondrocyte pellets suggest that the MMPs may be acting more to remove the amnion instead of digesting GAG. A disintegrin and metalloproteinase with thrombospondin motifs-5 (ADAMTS5) is also known to more efficiently cleave GAGs than MMP3[146], but the content and activity of this protease was not quantified in the

current study. Future work studying the effect of amnion on ADAMTS content and activity could show if amnion reduces ADAMTS activity and protects against GAG loss in osteoarthritis.

In the activation and µ-dHACM size experiment, the µ-dHACM was kept separate from the synoviocytes using a transwell insert. This was to allow counting of the synoviocytes at the end of the experiment. However, in the chondrocyte pellet co-culture experiment, the µ-dHACM was added directly on top of the synoviocytes to not have the chondrocyte pellets in contact with the µ-dHACM. While the experimental setup was different between the two, the direct µ-dHACM study (which had the amnion added directly on the synoviocytes) showed similar effects on MCP-1 and IL-6 production as the later transwell study (see Figure 5.4) thus indicating that there are similar effects between the two experimental setups.

While the synoviocytes used in this study did show a fibroblast like morphology throughout the experiment and were cultured to passage 4 before use, future work with these cells could use reverse transcription polymerase chain reaction to verify the presence of CD44 and lack of CD14 expression, verifying that the synoviocytes were from a fibroblast-like lineage and not a macrophage-like lineage[128], [147]. In addition, as with all studies that measure factor production from cells, it is unknown how much cell metabolism of factor affected the final media content measurements as cells not only are producing these factors but are also metabolizing them and removing them from the media.

While the dosing study performed did indicate that the largest effects were seen in the 10mg/mL dose, this is a large dose that does not reflect the doses seen in vivo. This dosage

resulted in approximately 3mg µ-dHACM per 3800 synoviocytes which is much a much higher µ-dHACM:cell ratio than would be seen *in vivo* as previous work in our lab has utilized 4mg per rat joint[40]. One previous study did find that a 1mg/mL µ-dHACM dose resulted in a significant increase in hyaluronic acid production in synoviocytes from patients with rheumatoid arthritis[145]. Thus, further study into the effects of lower dosages of µ-dHACM are warranted as well as investigations into their effects on other cell types such as macrophages and stem cells.

This study was the first to look at the effects of particulate amniotic membrane on the cytokine and MMP production of synoviocytes. It has shown that particulate amniotic membrane does alter the secretome of synoviocytes and prevents the cytokine-induced loss of GAG in chondrocyte pellets. This study has demonstrated the complex nature of synoviocyte and particulate amniotic membrane interactions, while it also illustrated the chondroprotective effects of µ-dHACM. These results suggest that further research into the mechanisms behind the therapeutic effect of amniotic membrane is needed but also add to the literature that suggest µ-dHACM can serve as a disease-modifying OA treatment.

CHAPTER 6. CONCLUSIONS AND FUTURE DIRECTIONS

6.1 Contributions to the Field

This work aimed to expand current capabilities to evaluate disease modifying OA therapeutics and to then utilize these capabilities to evaluate the effect of µ-dHACM in both *in vivo* and *in vitro* models. Thus, this work represents important contributions to the fields of pre-clinical OA and ECM therapeutic testing.

6.1.1 Temporal and Spatial Characterization of Joint Degeneration

Small animal models are increasingly being used to investigate the pathophysiology of osteoarthritis and the efficacy of potential disease modifying therapeutics. In these studies, it is important to have accurate understanding of the changes within the joint tissue and there is a lot of work going into developing imaging techniques that aid in gaining this understanding[3], [99], [107]. The work in this thesis has demonstrated how EPIC-µCT can be utilized to quantify both the spatial and temporal changes within the joint tissues in small animal models. It had not previously been shown that all the following parameters could be gleaned from one µCT scan of a rat tibia: cartilage sGAG content, thickness, volume, and surface roughness; subchondral bone mineral density, volume, porosity, and thickness; lesion volume; and osteophyte mineralized and cartilage volume. In addition, EPIC-µCT was sensitive enough to quantify the changes in many of these parameters at both early time points and in specific locations of the tibial plateau. While most of these parameters had previously been quantified using µCT and EPIC-µCT, this work was the first to demonstrate how these changes relate to each other over time and space. This work

thus demonstrates that EPIC-μCT can be used to understand many different pathological developments in small animal models and how they relate to each other both spatially and temporally. These techniques were also utilized in the Chapter 4 to investigate the effect of particle size on the therapeutic effectiveness of μ-dHACM to treat the MMT rat model.

6.1.2 In Vivo Analysis of Mechanisms of μ-dHACM

Multiple studies have shown the therapeutic benefit of micronized amniotic membrane in the small animal MMT model[40], [116]. However, not much has been know about the mechanisms behind this benefit. This work has found that particle size does alter the therapeutic benefit of micronized amniotic membrane with a particle size distribution with more large particles resulting in greater prevention of lesion formation in the MMT model. This work was also the first to show that acute treatment of micronized amniotic membrane resulted in increased osteophyte cartilage volume, potentially indicating that these micronized amniotic membrane particles are increasing cartilage production in the medial tibial plateau. Reducing the particle size was also found to increase protein elution from the particles, supporting previous work showing that decreased particle size results in increased elution of small molecules[118]. This work also showed that decreasing the particle size did not significantly alter the particle clearance from the joint suggesting that even in the RPS μ-dHACM sample, most the tissue was of a sufficient size to not be readily cleared from the joint. Altogether, the work in Chapter 4 supports that the EPIC-μCT techniques described in Chapter 3 can be used to evaluate potential disease modifying OA therapeutics and adds to the growing body of evidence showing that micronized amniotic membrane prevents cartilage degradation in OA development.

6.1.3 In Vitro Analysis of Mechanisms of µ-dHACM

In addition to the further *in vivo* studies of micronized amniotic membrane carried out in Chapter 4, this work added valuable understanding into the influence of micronized amniotic membrane on *in vitro* cell cultures. While synoviocytes have been used extensively to evaluate potential OA and rheumatoid arthritis therapeutics[84], [135], [148], [149], this was the first to look at the effects of a particulate ECM therapeutic on the cytokine and MMP production of synoviocytes. It has shown that particulate amniotic membrane does alter the secretome of synoviocytes and prevents the cytokine-induced loss of GAG in chondrocyte pellets. This study has demonstrated the complex nature of synoviocyte and particulate amniotic membrane interactions, while it also illustrated the chondroprotective effects of µ-dHACM. In addition, this work explored the importance of *in vitro* experimental setup when evaluating tissue based therapies by demonstrating different effects in extract cultures vs co-cultures. These results suggest that further research into the mechanisms behind the therapeutic effect of amniotic membrane is needed but also add to the literature that suggest µ-dHACM can serve as a disease-modifying OA treatment.

6.1.4 Summary

The work in this thesis has demonstrated 1) that surface roughness from contrast enhanced, non-destructive µCT imaging can be used as an early indicator of OA progression and that these µCT images can provide temporal and spatial mapping to tissue level changes in pre-clinical models, 2) the therapeutic benefit of µ-dHACM is influenced by particle size and therefore can be tuned to improve therapeutic efficacy, and 3) µ-dHACM has both a

stimulatory and inhibitory effect on synoviocyte production of cytokines and chemokines that may increase acute inflammation while decreasing chronic inflammation, thus improving tissue healing/inflammation resolution in damaged knees.

6.2 Future Directions

6.2.1 Evaluation of small animal OA models

This work has demonstrated that contrast enhanced μCT can detect a wide range of changes in joint tissue ranging from cartilage composition to osteophyte growth to subchondral bone sclerosis and that it is sensitive enough to elicit the temporal and spatial nature of these changes. Future work could use the parameters described in this work to investigate how all the various small animal models of osteoarthritis are similar and divergent from one another. This can aid our understanding of how different small animal models of OA, such as the rat monoiodoacetate model, the rat collagen induced arthritis, the rat anterior cruciate ligament transection and meniscectomy, and the rat tibial plateau fracture model all differentially effect cartilage and bone tissues.

However, major limitations of the imaging techniques described in this work are that there remains a high amount of manual contouring that is necessary to achieve these results and that it is an ex vivo technique, eliminating the possibility of longitudinal studies. While contrast-enhanced μCT imaging is less time-intensive then histopathological studies, automated contouring and segmentation of the CT images could drastically decrease the amount of time required to produce these results. Multiple research groups have started developing automated contouring methods for the quantification of cartilage and bone changes and have shown their utility in both rat [107] and mouse [150], [151] models of

OA. These methods have only quantified a limited number of the parameters described in this current work and there is still much work to be done in this area.

In addition to the need to develop automated contouring algorithms, the further development of *in vivo* contrast enhanced μCT imaging would both dramatically reduce the number of animals needed in these studies [54] and potentially increase the statistical power to detect differences between groups and timepoints. Some work has been done in developing *in vivo* contrast enhanced μCT imaging for both pre-clinical[80], [150]–[152] and clinical[153] settings with promising results. In our own lab, preliminary pilot projects have shown that it is possible to track osteophyte growth *in vivo* using automated registration and rotation of the tibial plateaus of rats that underwent MMT surgery. The development of the automatic contouring methods mentioned in the previous paragraph would also be important for longitudinal tracking of disease changes because of the large datasets that would be produced from these studies.

In addition to the pressing needs of developing automated contouring algorithms and *in* vivo imaging techniques, there is potential future work in the development of more sensitive measures of proteoglycan changes using EPIC-μCT. Voxel-based techniques from MRI have been shown to increase sensitivity to compositional changes [109] and could perhaps be adapted to increase sensitivity of attenuation changes in EPIC-μCT imaging.

The surface shape changes described in chapter 3 may indicate local changes in cartilage thickness caused by altered joint kinematics in the MMT animals. In humans, it has been found that knee kinematics are correlated with ratios of medial to lateral cartilage thickness,

and these correlations change with age and presence of knee OA[25], [108]. Future work combining gait mechanics and EPIC-μCT imaging in the MMT model could lead to greater understanding of the relationship between knee kinematics and specific areas of tissue changes.

One of the benefits of the techniques described in chapter 3 is that a large amount of information on various parameters describing multiple tissues can be extracted from one scan. Future work could use these techniques to explore the pathological development of other rat models of OA. This could lead to a greater understanding of how different disease initiations could lead to differential development but then result in similar end results in joint degeneration.

6.2.2 In Vivo Therapeutic Mechanisms of μ-dHACM

This work has explored one possible mode of tuning particulate amniotic membrane for the treatment of OA by investigating the effect of particle size. While this work did show that particle size did effect both factor elution and *in vivo* therapeutic efficacy of the particulate amniotic membrane, there was a large amount of overlap between the size profiles. More specific conclusions could be drawn if the particle sizes were more distinct as this would allow researchers to understand exactly which sizes are the most therapeutically beneficial.

In addition, there are still numerous other tuneable aspects of particulate amniotic membrane such as using the particles as cell carriers[43], [154] or loading more proteins onto the particles. Amniotic membrane sheets are already known to facilitate chondrocyte culture *in vitro*[45], [126] and to contain large quantities of proteins[44], [145]. Enhancing

these natural traits of particulate amniotic membrane could lead to greater therapeutic effectiveness at treating OA. However, significant amounts of bioactive components can be eluted from the µ-dHACM in just 24 hours, as demonstrated by the extract studies in both Chapter 4 and Chapter 5; thus, care should be taken to not deplete beneficial protein content when adding cells or proteins to µ-dHACM.

In the data presented in chapter 4, there was a therapeutic difference between µ-dHACM and RPS µ-dHACM and a difference in protein elution over 21 days but no difference between clearance of µ-dHACM and RPS µ-dHACM from the joint. The clearance results suggest that much of the tissue in both formulations is still retained in the joint out to six weeks but the therapeutic benefit has worn off (as demonstrated in the 6-week study contained in Appendix D). This, along with the differences seen in chapter 5 between direct and extract µ-dHACM and RPS µ-dHACM, suggests that the mechanism of µ-dHACM is more of a reservoir of growth factors rather than as cellular substrate for cartilage repair. This agrees with the lack of µ-dHACM and cartilage interactions in the previous study by Willett, et al[40]. Future work could further investigate this question of factor reservoir vs cellular substrate by investigating the effect of denatured amniotic membrane where the growth factors are no longer bioactive or by injection of other ECM particles such as collage or fibronectin of a similar particle size. Previous work in our lab has also investigated the use of heparin microparticles to sequester growth factors from mesenchymal stem cells to increase bone repair. These same microparticles could be used with µ-dHACM extract to investigate the effect of µ-dHACM growth factors without the bioactive ECM.

6.2.3 In Vitro Therapeutic Mechanisms of µ-dHACM

The *in vitro* synoviocyte/µ-dHACM results described in chapter 5 demonstrate the effect of µ-dHACM on cytokine and MMP secretion from synoviocytes as well as shows the chondroprotective nature of µ-dHACM co-culture against IL-1β and TNF-α. However, there are many unanswered questions about the µ-dHACM that could be investigated with *in vitro* models.

Fibroblast-like synoviocytes were utilized in this work but are only one of two cell types commonly described in the synovium, the other being macrophage-like synoviocytes[21], [22], [155]. Previous studies have looked at the effect of macrophage culture with synoviocytes and with chondrocytes[90], [138] and similar experiments could be performed to investigate how micronized amniotic membrane would interact with the different cell types. While more complex than the model used in this work, such models could provide a more complete understanding of micronized amniotic membranes interactions with the synovium.

The increased MMP-3 content and MMP activity in the synovium/µ-dHACM cultures seem at odds with the GAG protection that the µ-dHACM provides both in the *in vivo* model in Chapter 4 and in the *in vitro* synovium/chondrocyte pellet co-cultures in Chapter 5. Further work could investigate if other MMPs (such as MMP-1) or members of the ADAMTs family have lower concentrations in the synoviocyte/µ-dHACM cocultures. MMP zymography could also be used to identify which MMPs are most active in the synovium/µ-dHACM co-culture and in the pellet/synovium/µ-dHACM co-culture.

The increase in IL-6, IL-8, fractalkine, and G-CSF seen in the synoviocyte-µdHACM co-culture suggest that µ-dHACM may increase acute inflammatory mediators *in* vivo while

increasing neutrophil numbers. In addition, the decreased MCP-1 secretion may indicate a decrease in macrophage numbers. Immunohistochemistry and flow cytometry analysis of the synovial cells surrounding the µ-dHACM *in vivo* would provide further information on if this increase in neutrophils and decrease in macrophages is occurring *in vivo*. In addition, studies are needed that investigate systemic (serum) vs local (synovial fluid) levels of cytokines and how these levels change over time (acute vs chronic) in response to µ-dHACM treatment. Finally, as there were differences in the RPS µ-dHACM vs µ-dHACM studies both *in vivo* and *in vitro*, studies that investigate the *in vivo* cytokines levels and their relationship with particle size could provide further information on how altering the particle size of the amnion influences its immunomodulatory function.

Research utilizing µ-dHACM to treat more inflammatory models of arthritis, such as the antigen-induced arthritis model [156], [157] or the collagen-induced arthritis[158], which has been used to investigate the role of MCP-1 in arthritis development, would be useful to understand the effect of µ-dHACM in different arthritis etiologies. This, in turn, could help provide information concerning the role of µ-dHACM in modulating acute vs chronic inflammatory interactions.

6.2.4 Large Animal Studies and Clinical Application

While the small animal models and *in vitro* models described in this work show promise and add to the body of literature supporting the potential of particulate amniotic membrane as a disease modifying OA therapeutic, large animal studies and clinical trials would need to be performed to validate the efficacy of µ-dHACM to reduce OA progression.

Large animal studies provide greater understanding of the clinical potential of disease modifying OA drugs than small animal models because their size and mechanical environment more closely resembles the clinical environment. While amniotic membrane is indicated for and used extensively to treat multiple pathologies in large animals[159], there are few pre-clinical studies looking at the therapeutic effect of amniotic membrane in large animal orthopaedic models. One study did show that amniotic membrane has been shown to improve outcomes in sheep full thickness osteochondral defects[160]. Currently, our lab is collaborating with the San Antonio Military Medical Center to perform sheep studies investigating the effect of µ-dHACM in the sheep meniscectomy model and it is expected that this study will provide greater illumination of the clinical potential of µ-dHACM to treat OA.

Amniotic membrane has been used in humans for decades for successfully treating burns, skin wounds, and ocular defects, and several case studies have been performed to apply amniotic membrane to tendon, ligament, and spine applications[145]. As has been shown in these clinical applications, amniotic membrane can be transplanted into humans without rejection by the immune system. While amniotic membrane has shown promise in orthopaedic applications[161], [162], including OA[117], future work is needed to study the effectiveness of amniotic membrane in prevent OA progression in a clinical setting.

APPENDIX A. CONTOURING GUIDELINES FOR EVALUATION OF THE RAT MMT MODEL USING EPIC-UCT

A.1 Introduction and General Points

These guidelines were developed for the analyses performed during the study described in Chapter 2. They are specifically for contouring medial plateaus of rat tibias at 1 and 3 weeks following MMT surgery scanned using Scanco systems and evaluated using Scanco software. While the authors tried to rely on the use of common anatomical features that have been seen during these studies, factors like anatomical variability and rotational variability could cause images to appear different from the ones represented here. Other animal models and locations could also require different contouring guidelines.

These guidelines only address contouring after the imaging has already been performed. For more details on EPIC-μCT imaging, please see references [3], [65], [66], [99].

A.2 Cartilage Attenuation, Volume, Thickness

The entire medial plateau is contoured with set points at intervals of 5 to 10 slices and these set points are then morphed to create the rest of the contours. The boundaries are set as described below and the contours are drawn to include all cartilage and extend slightly into the air and subchondral bone. If there are any subchondral pores that would be thresholded as cartilage (this can be checked by using the preview button in the 3D-Evaluation window with the proper thresholds), avoid including them within the contours, even if that requires contouring directly on the cartilage/subchondral bone interface instead of slightly into the bone. After morphing from the set points, review all contours to make sure they do not

extend too far into the subchondral bone. Residual soft tissue on the cartilage surface can be recognized by the lack of continuity with the cartilage surface (see Figure A.6.5), and the obvious soft tissue should not be included within the contours.

A.2.1. Sagittal Contouring (Figure A.6.1 and Figure A.6.2)

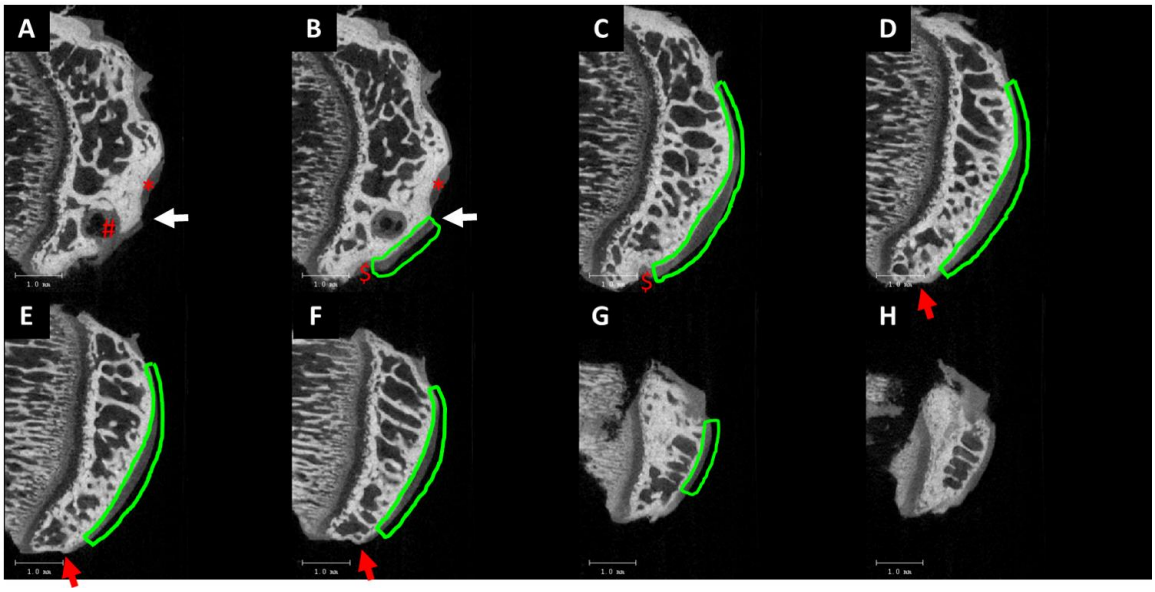

Figure A.6.1: Sham Sagittal Contours. A) 5 slices lateral to the lateral contour end, B) lateral contour end, C-F) slices between contour ends, G) medial contour end, and H) 5 slices medial to the medial end. Notice ligament insertion point (*), non-intact subchondral bone (#), subchondral bone edges (red arrows), missing soft tissue (white arrows), and proximal end divots ($) that influence the location of the anterior and posterior contour ends.

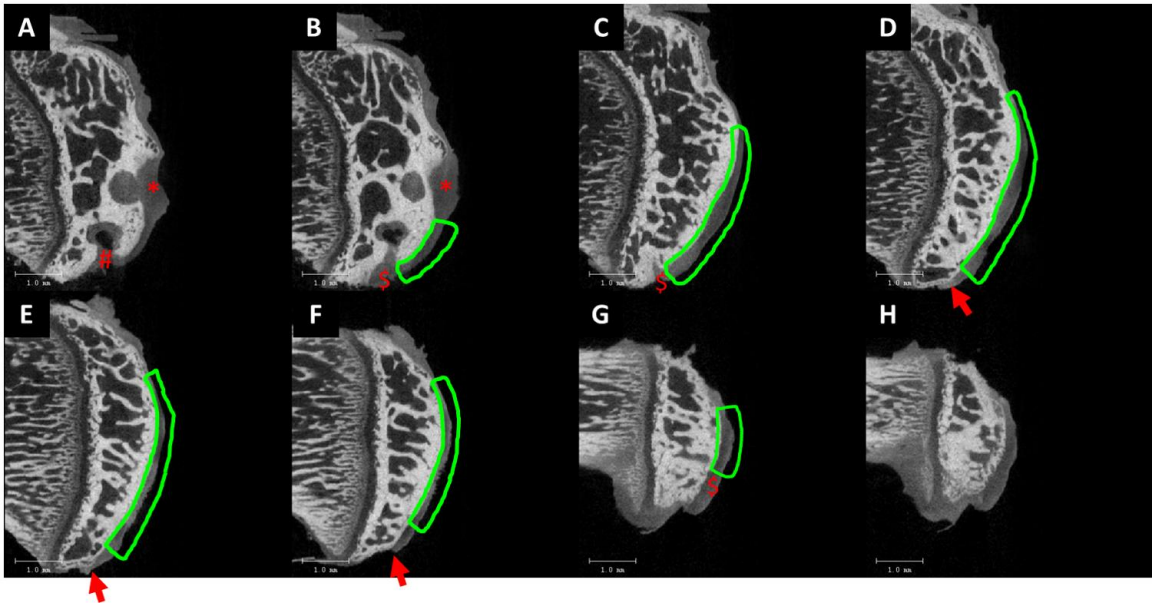

Figure A.6.2: MMT Sagittal Contours. A) 5 slices lateral to the lateral contour end, B) lateral contour end, C-F) slices between contour ends, G) medial contour end, and H) 5 slices medial to the medial end. Notice ligament insertion point (*), non-intact subchondral bone (#), proximal subchondral bone edges (red arrows), and proximal end divots ($) that influence the location of the anterior and posterior contour ends.

A.2.1.1. Anterior Boundary

The contour extends along the intact subchondral bone either to the ligament insertion point (this occurs on the very lateral side, toward the center of the full joint, between the plateaus) or to the inflection point of the subchondral bone curvature (during the middle portion of the plateau) or to where there is a sharp edge to the subchondral bone (on the medial side).

A.2.1.2. Posterior Boundary

On the posterior side, the contour extends along the intact subchondral bone and stops either at a) 0.5 mm before the posterior corner of subchondral bone, b) where a divot starts to slope into the subchondral bone (see Figure A.6.1.A-D), or c) any soft tissue covering

the cartilage that cannot be contoured around. The most anterior of these points is the one that should be used.

A.2.1.3. Lateral Boundary

The first contoured slice on the lateral side is where the subchondral bone is intact and measures greater than or equal to 1.25 mm between the anterior and posterior boundary.

A.2.1.4. Medial Boundary

The first contoured slice on the medial side is where the distance between the anterior and posterior boundary is greater than or equal to 1.25 mm or where the subchondral bone is no longer smooth or distinguishable from the cartilage over the majority of the surface, whichever occurs more laterally.

A.2.2. Coronal Contouring (Figure A.6.3 and Figure A.6.4)

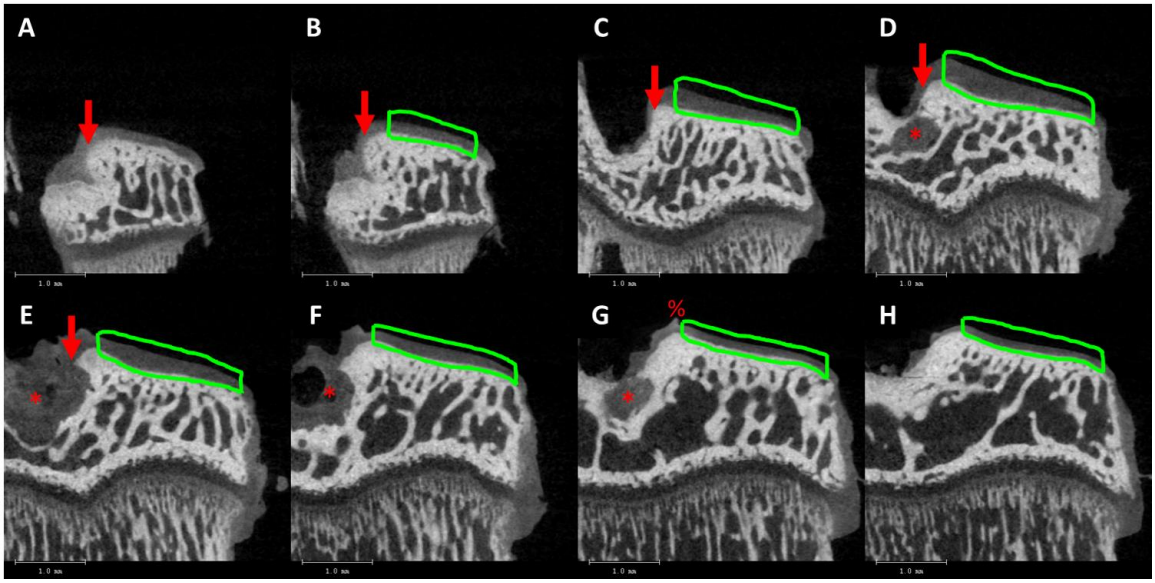

Figure A.6.3: Sham Coronal Contours. A) 5 slices posterior to the posterior contour end, B) posterior contour end, C-G) slices between contour ends, and H) anterior

contour end. Notice ligament insertion points (*), subchondral bone edge (red arrow), and soft tissue (%) that influence the location of the contours.

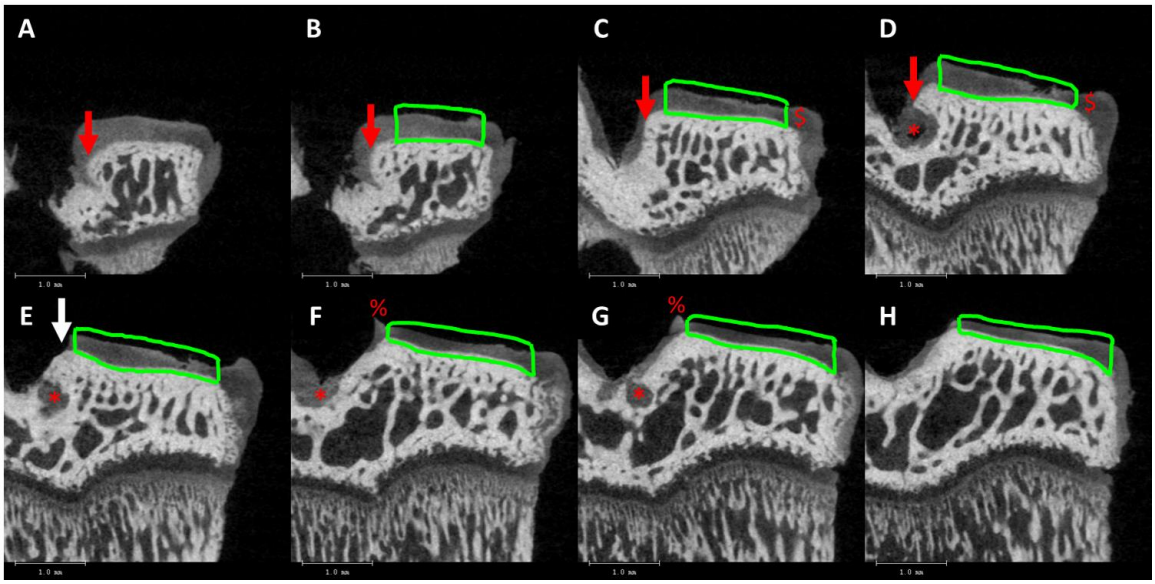

Figure A.6.4: MMT Coronal Contours. A) 5 slices posterior to the posterior contour end, B) posterior contour end, C-G) slices between contour ends, and H) anterior contour end. Notice ligament insertion points (*), subchondral bone edge (red arrows), missing tissue (white arrow), soft tissue (%), and divots ($) that influence the location of the contours.

A.2.2.1. Posterior Boundary

The first contoured slice on the medial side is where the distance between the lateral and medial edges of the contour is 1.25 mm or greater and surface of the subchondral bone is smooth and intact.

A.2.2.2. Anterior Boundary

The first contoured slice on the anterior side is just anterior to the disappearance of the most anterior ligament insertion point which appears as a big hole in the subchondral bone between the lateral and medial plateaus (see Figure A.6.3.D-F and Figure A.6.4.D-F).

A.2.2.3. Medial Boundaries

On the medial side, the contours go to the edge of the subchondral bone. For curved edges, go to where the subchondral bone is at 45 degrees relative to the subchondral bone surface under the plateau. When there is a divot at the corner of the subchondral bone, stop the contour on the lateral side of that divot. Any contours posterior to that divot should not extend more medial than that edge even if the divot hasn't developed yet; copying and pasting of previous contours can help to ensure this if necessary.

A.2.2.4. Lateral Boundaries

On the lateral side, the contours go either a) to 0.35 mm from the vertical edge of the subchondral bone, b) at the middle of the peak in the subchondral bone (if there are two, then use the more medial one), or c) to where soft tissue is present or dissection cuts in the cartilage are visible. The most medial of these points should be used.

A.2.3. Analysis Thresholds

The cartilage-air and bone-cartilage thresholds should be chosen for each new experiment and should include as much cartilage as possible while not extending into the bone or air. Be aware that diseased joints have higher average attenuation than controls so make sure to base thresholding decisions on sampling multiple slices from multiple specimens, including specimens from all experimental groups.

A.2.4. Analysis

After proper thresholds have been set, run the 3D evaluations for each sample and record the mean density / attenuation, mean thickness, and volume values. For the results shown in the main paper, the entire medial plateau was analyzed as well as the lateral, central, and medial thirds of the plateau.

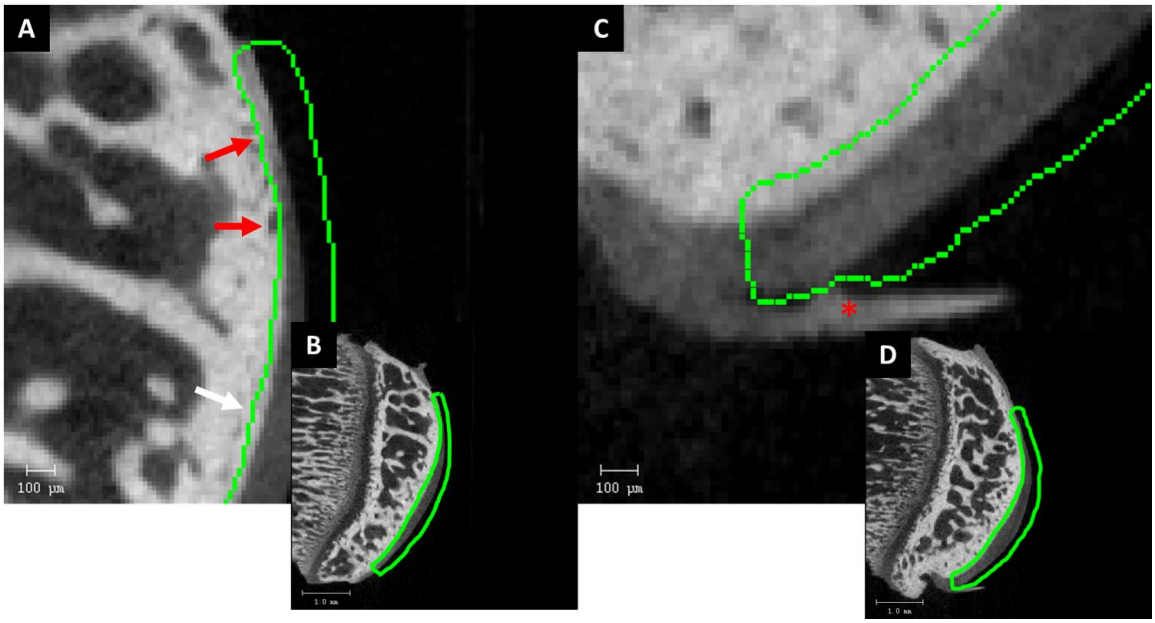

Figure A.6.5: Cartilage contour examples of subchondral bone pores and soft tissue. A) Example of contour extending into subchondral bone. Subchondral pores (red arrows) are avoided but normally the contours extend a few pixels into subchondral bone (white arrow). B) Entire medial tibial plateau with contour example from A. C) Example of contour avoiding obvious soft tissue (*). Notice that the contour stops where the soft tissue in no longer distinguishable from the cartilage surface. D) Entire medial tibial plateau with contour example from C.

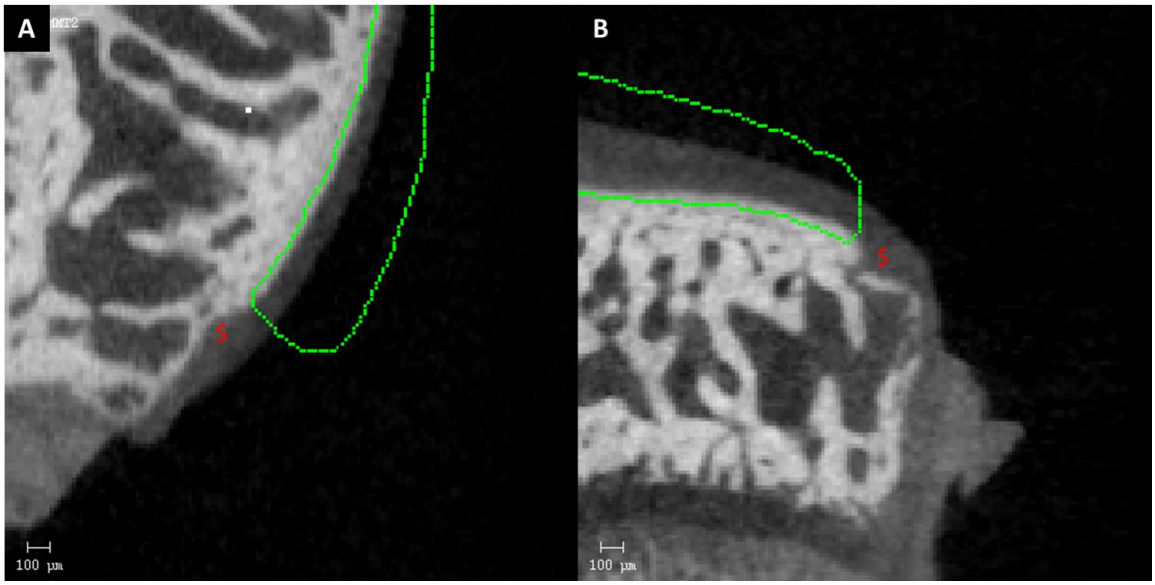

Figure A.6.6: Cartilage contouring examples of subchondral bone divots ($) in a) sagittal and b) coronal slices. These divots are the posterior and medial ending points of the sagittal and coronal contours, respectively.

A.3 Subchondral Bone Mineral Density, Volume, Thickness, Porosity (Figure A.6.7)

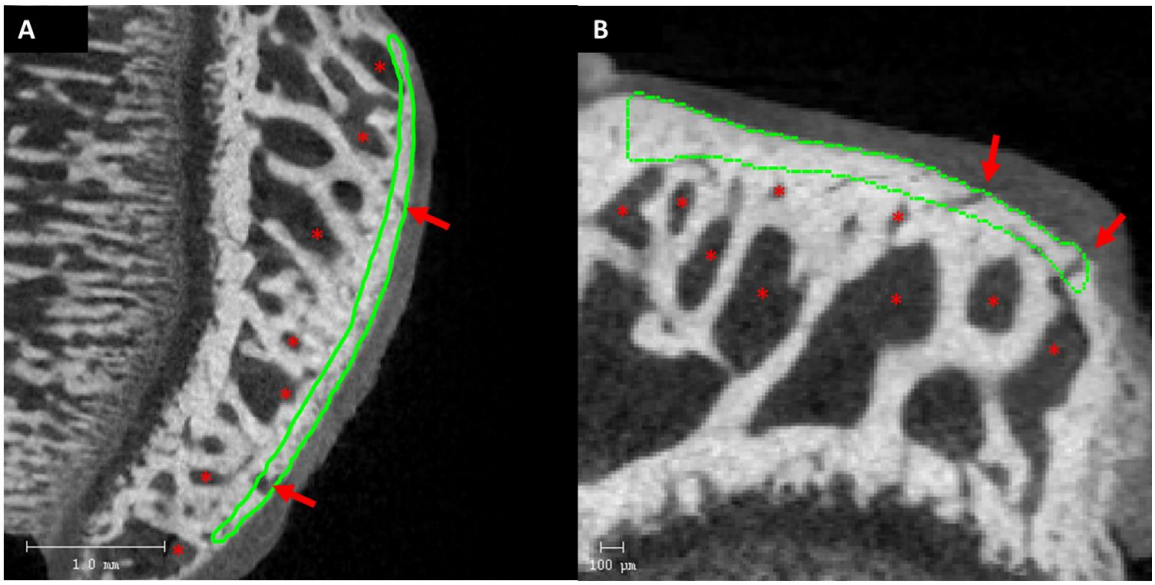

Figure A.6.7: Subchondral Bone Contours. A) Example of subchondral bone contour in sagittal plane, B) example of subchondral bone contour in coronal plane. Notice that subchondral pores (red arrows) are included in the contours but trabecular spaces (*) are not included.

A.3.1. Contouring for either the Sagittal or Coronal Plane

The anterior, posterior, medial, and lateral boundaries are all the same as the cartilage analyses. The contours should include all the subchondral bone between the cartilage-bone interface and the endocortical boundary. Because subchondral bone porosity is one of the parameters measured and is calculated from the total and bone volumes, the contours should tightly follow the cartilage-bone interface and endocortical boundary. As such, it is recommended to have set points at intervals of a maximum of five slices. Using the preview button in the 3D-Evaluation window can also be helpful to check for areas of lower attenuation than the lower threshold.

A.3.2. Analysis Thresholds

The lower threshold for the subchondral bone analysis is the upper threshold used in the cartilage analysis. The upper threshold for the subchondral bone analysis is then set as the maximum value possible (1000 in the Scanco μCT40).

A.3.3. Analysis

After proper thresholds have been set, run the 3D evaluations for each sample and record the mean density, mean thickness, volume, and volume fraction (Bone Volume/Total Volume) values. Porosity can be calculated as $1 - \frac{Bone\ Volume}{Total\ Volume}$. For the results shown in the main paper, the entire medial plateau was analyzed as well as the lateral, central, and medial thirds of the plateau.

A.4 Cartilage Lesion Volume (Figure A.6.8)

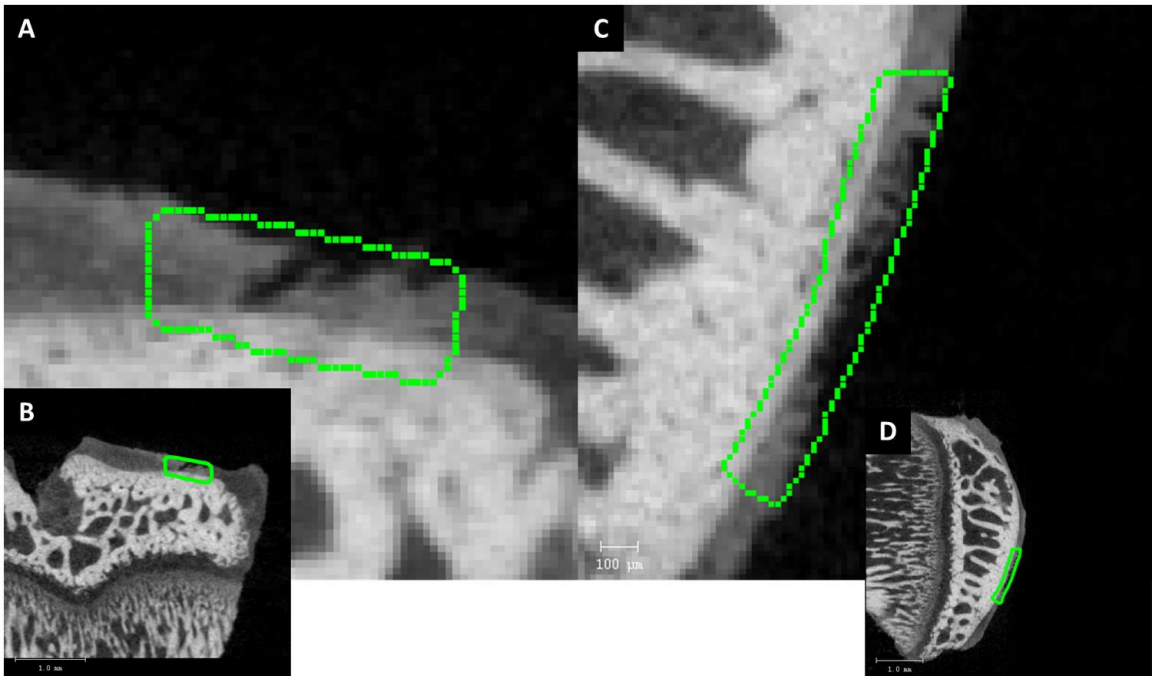

Figure A.6.8: Lesion Contours. A) Example of lesion contour in coronal plane, B) entire medial tibial plateau with lesion contour from A, C) example of lesion contour in sagittal plane, D) entire medial tibial plateau with lesion contour from C. Notice that the contour can extend into the subchondral bone but not into the air.

A.4.1. Contouring

The lesion volume analysis can be performed using either the sagittal or coronal plane sections. A lesion is defined as a loss of cartilage that extends through 50% or greater of the cartilage thickness. The contours are drawn to encompass the entire width of the lesion. The top of the contour should trace a visual continuation of the smooth surrounding cartilage, as if there was no lesion present, and extend into the subchondral bone but avoid any subchondral pores that have attenuation lower than cartilage. Surrounding erosions in the cartilage are only included in the lesion contour if they are obviously a continuous part of the lesion.

A.4.2. Analysis

After the contours have been drawn, the 3D evaluations are run with the lower threshold set as the lower threshold from the cartilage analyses and the upper threshold set as the maximum value possible (1000 in the Scanco μCT40). The lesion volume is then calculated by subtracted the bone volume (BV) value from the total volume (TV) value.

A.5 Osteophyte Volume (Figure A.6.9)

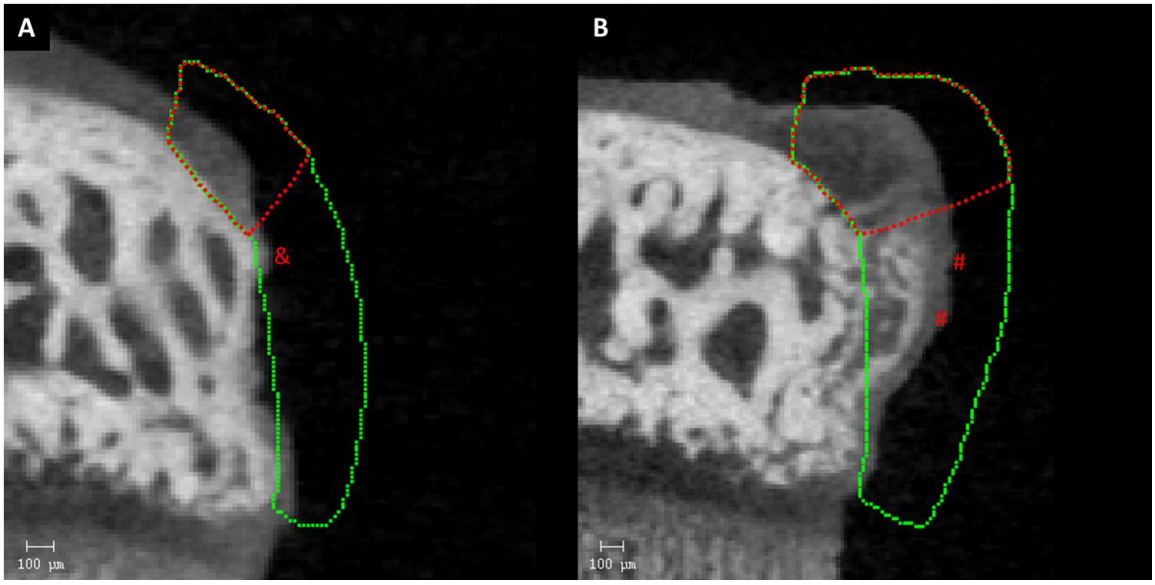

Figure A.6.9: Osteophyte Contours. A) Example of contour for mineralized tissue (green contour) and cartilage tissue (red contour) portions of the marginal tissue thickening in coronal plane in a sham sample. Notice the lack of soft tissue used to indicate the end of the cartilage contour (&). B) Example of contour for mineralized tissue (green contour) and cartilage tissue (red contour) portions of the marginal tissue thickening in coronal plane in a MMT sample. Notice the soft tissue used to indicate where to end the cartilage contour. (#)

For osteophyte analysis, two different contours are used, one for the mineralized tissue and one for the cartilaginous tissue. The mineralized tissue contours are bigger to include all the mineralized osteophyte, some of which may be adjacent to non-cartilaginous soft tissue, while the cartilaginous tissue contours are smaller to avoid inclusion of any residual soft tissue on the medial margins of the tibia. As the mineralized tissue contours are bigger, it

is suggested to start with those contours and then alter the contours for the cartilage analysis.

It can be difficult to distinguish the soft tissue/bone interface because the mineralized osteophyte tissue looks like the subchondral bone and vice versa. Refer to sham and naïve samples to recognize natural joint structure; the newly mineralized tissue in osteophytes often has a disorganized appearance compared to healthy tibial plateaus. It is also suggested that one person perform these analyses for the whole experiment to increase consistency.

A.5.1. Contouring – Mineralized Tissue

Anterior and posterior starting slices are the same as the starting slices from the cartilage analysis described in Section A.2.2 above. On the plateau, the contours start just before the subchondral bone surface curves down towards the growth plate. The contour then extends along the bone surface down to the growth plate and includes all the soft and mineralized tissue medial to that bone surface, as shown in Figure A.6.9.

A.5.2. Contouring – Cartilage

Anterior and posterior starting slices are the same as the starting slices from the cartilage analysis described in Section A.2.2 above. On the plateau, the contours start just before the subchondral bone surface curves down towards the distal end. The contour then extends along the bone surface and includes all the soft and mineralized tissue medial to that bone surface. The contour stops where the residual soft tissue starts (indicated by fragments hanging from the surface and an increase in attenuation) or where the cartilage is no longer present. In practice, creating the cartilage contours can be as simple as taking the

mineralized tissue contours and transecting it with the contour correction tool, just above the soft tissue. Above the soft tissue, the contours should be the same.

A.5.3. Analysis

Run the 3D evaluations for all samples using the same thresholds as the cartilage and subchondral bone analyses and record the volume values.

APPENDIX B. MATLAB PROGRAM FOR EVALUATING SURFACE ROUGHNESS

B.1 Program Description

The parameters that can be extracted from this surface roughness program include cartilage surface roughness and exposed bone. There is the possibility of developing other lesion volume measurements from this program as well.

Cartilage surface roughness is calculated by 1) creating a 3D surface of the cartilage from the CT images, 2) fitting a user defined curve to that surface to account for the curvature of the surface, and 3) calculating the root mean square value of the pixel by pixel differences between the actual 3D surface and the fitted surface.

Exposed bone is calculated by 1) creating 3D surfaces of both the cartilage and the subchondral bone from the CT images, and summing all the pixels where the two surfaces come within a defined distance of one another. Because of attenuation averaging that occurs when analog surfaces are discretized into pixels, the two surfaces are seldom defined by the same pixels, thus the defined distance (called the minimum thickness) is needed.

All files listed here are available online at http://guldberglab.gatech.edu/downloads along with two sets of sample files (one damaged tibia and one control tibia) and their datasheet (SampleDatasheet.xlsx) as examples of the required format.

B.2 Program Instructions

1. The files for analysis must be labeled in numerical, sequential order.
2. The following M and FIG files should be in the one directory folder and that directory folder should be set as the ‘Current Folder’ when MATLAB is running:
    a. angleGUI.fig
    b. angleGUI.m
    c. calculateSurfaceRoughness.m
    d. create2DProf.m
    e. create3DSurf.m
    f. dctFitting.m
    g. getInputsGUI.fig
    h. getInputsGUI.m
    i. plotGUI.fig
    j. plotGUI.m
    k. Surface_Roughness.fig
    l. Surface_Roughness.m
3. The images for analysis should be placed in the same folder as the M and FIG files. Example: In Figure 3.1, the folder ‘Sample Files’ is in ‘Current Folder’ along with the necessary .m and .fig files. The folder Sample Files contains a folder for each set of sample files (‘Control’ and ‘Damaged’).

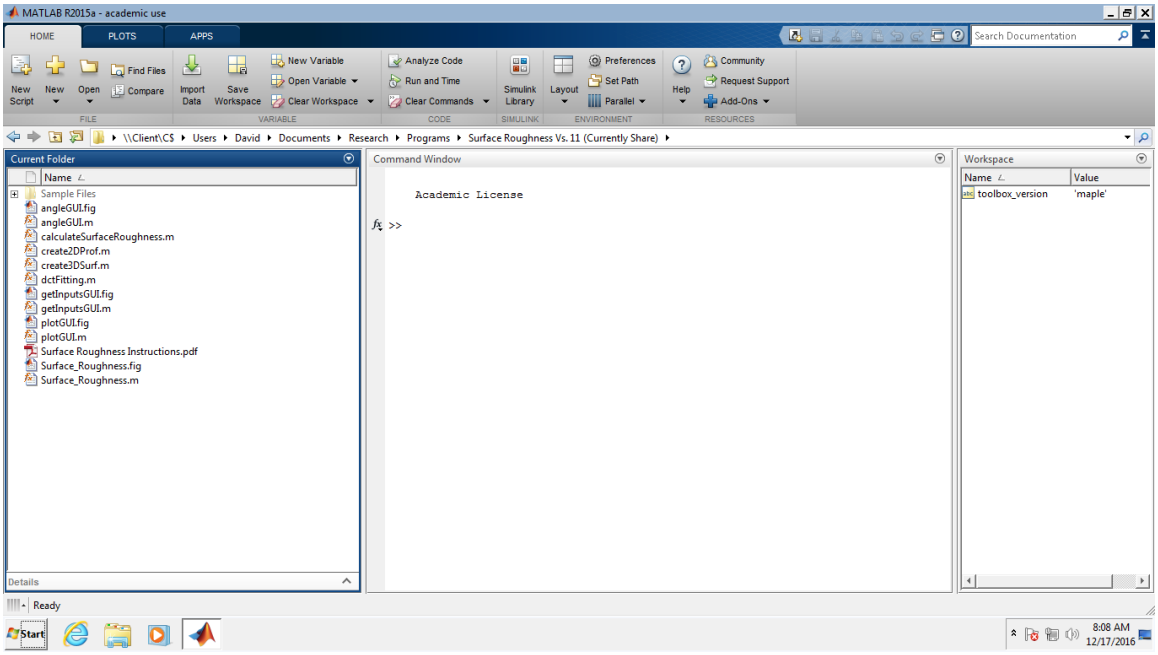

Figure B.7.1: Example of file locations for running surface roughness algorithm. Notice that 'Sample Files' is in ‘Current Folder’ along with the necessary .m and .fig files.

4. A datasheet must also be included in either Current Folder or in the folder containing the samples (Example: The sample datasheet, 'SampleDatasheet.xlsx', is contained in the 'Sample Files' folder) and must contain the following information:
    a. Sample Name
        i. The name of the folder containing the image files: eg. 'Sample Files/Damaged'
    b. File Heading
        i. The part of image files' names that does not change from image to image in one file. For the Scanco generated images in the sample folder this is the letters and numbers up to the first 0 following the underscore: eg. 'R0014638_0'.
    c. File Ending
        i. The file type of the images: eg. '.TIF'.
    d. First File #
        i. The number for the first image slice of the analysis. This number makes up the part of the image files' names that does change from image to image: eg. '407'.
    e. Last File #
        i. The number for the last image slice of the analysis. By changing the first and last file numbers, different areas of the cartilage can be analyzed (e.g. medial or lateral; anterior or posterior)
5. Run the surface roughness program by typing "Surface_Roughness" in the command window. This brings up the Surface Roughness Program opening screen.
6. Provide each requested value (See Figure B.7.2 for the proper inputs for the samples provided)
    a. Datasheet Name
        i. This is the name of the datasheet and needs to include the path (if there is one) to the datasheet from the 'Current Folder'
    b. Pixel size
        i. The size of the pixels in the analysis images as set by the scanner settings
    c. Fits
        i. The desired fit for the analysis used to account for the natural curvature of the surface. As explained Chapter 3, the surface roughness of the analyzed surface is calculated by taking the root mean square value of the difference between the actual cartilage surface and the fitted surface. Polynomial surfaces, discrete cosine transform functions, or LOWESS spline surfaces can all be used.
            1. Polynomial surfaces are written as 'Poly24' where the first digit ('2') is the polynomial order along the different

images files and the second digit (‘4’) is the polynomial order within one images file

2. Discrete cosine transform functions are written as ‘dct80’ where the number following dct (‘80’) is the cutoff, in um, where cosine wavelengths below it are removed from the fitting surface and wavelengths above it are retained in the fitting surface.
3. LOWESS spline surfaces are written simply as ‘lowess’.

d. Input
    i. Choose what amount of inputs are desired for the analysis
        1. Rotation and Boundaries
            a. When the ‘Run’ button is pressed, the program will ask the user to provide the rotation angle and top, bottom, right, and left boundaries for the analysis (See Steps 8 and 9)
        2. Boundaries only
            a. When the ‘Run’ button is pressed, the program will ask the user to provide only the top, bottom, right, and left boundaries for the analysis (see step 9)
        3. No Input
            a. When the ‘Run’ button is pressed, the program will not request any additional input
e. Cartilage Threshold
    i. Enter the threshold used for cartilage analysis. It may be necessary to try out a number of different values to find the appropriate threshold for the cartilage surface
f. Bone and Lesion Measurements
    i. When checked, the program will not only calculate the cartilage surface roughness, but also map out the bone surface and calculate how much of the bone surface is exposed because of cartilage erosion.
g. Bone Threshold (visible when Bone and Lesion Measurements is checked)
    i. Enter the threshold used for bone analysis. It may be necessary to try out a number of different values to find the appropriate threshold for the cartilage surface
h. Min Thickness (visible when Bone and Lesion Measurements is checked)
    i. The minimum thickness that will be defined as cartilage and not exposed bone. This is the defined distance between the cartilage and bone surfaces described in the description of the exposed bone parameter at the beginning of these instructions.

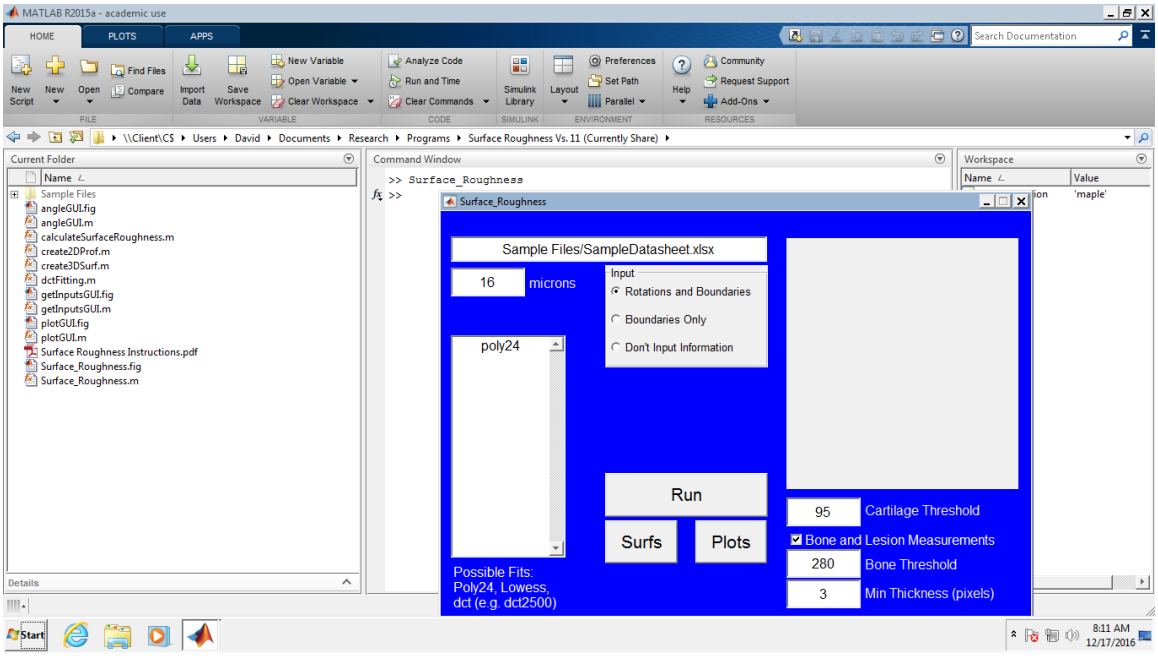

Figure B.7.2: Surface_Roughness GUI with example settings

7. When all values have been defined in the opening screen, press the run button to run the surface roughness program. If any requested values have not been added properly, an error will show up on the GUI.
8. If rotation and boundary inputs were chosen on the opening screen, the rotational input window (shown in Figure B.7.3) will appear displaying a CT image slice from the first sample on the datasheet. The image shown is the middle image slice between the first and last file # given in the datasheet.
    a. For the program to work properly, it is necessary to have the area of interest of the tibial plateau be vertical and the proximal end of the plateau be facing the right side of the screen. The white vertical lines in the window are to assist in ensuring it is vertical. Rotate the CT image using the ‘up’ or ‘down’ buttons in the rotational input window or by inputting an angle of rotation into the window. When the CT image is in the proper position, click the next button.

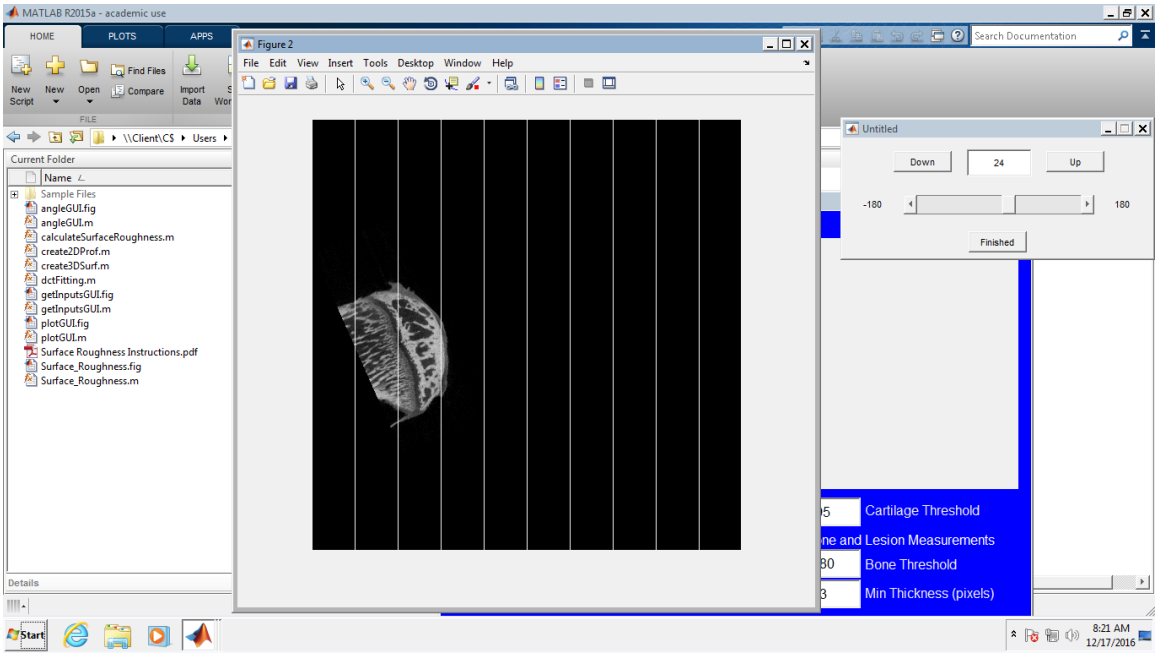

Figure B.7.3: angleGUI.m with example 2D image

9. After the rotation has been set, or if only boundary inputs were chosen on the opening screen, the boundary input window (shown in Figure B.7.4) will appear displaying two CT image slices from the first sample on the datasheet. The left and right images are the first and last image slices, respectively, as defined by the first and last file # given in the datasheet.
    a. In this window, the user will define the area of interest that will be analyzed in the program. The user will choose, in this order, the top and bottom boundaries, followed by the right most boundary, followed by the left most boundary.
    b. The fitting function in MATLAB requires a rectangular surface, thus the same top and bottom boundaries are required for all CT image slices in a given sample. The boundaries are chosen to match, as closely as possible, the boundaries described in the contouring guidelines found in Chapter 3 and they must pass through the cartilage surface on both images.
    c. The left and right most boundaries do not directly affect the cartilage surface roughness or subchondral bone analysis but rather are provided to reduce the amount of pixels scanned. Only the pixels between the four boundaries are scanned in the program thus the left and right boundaries can be used to remove any artifacts from the scanning procedure, such as the holding tube, that could be thresholded as cartilage or bone by the program.
    d. If any of the boundaries or the rotation need to be corrected after they have been set, the buttons at the bottom of the boundary input window can be

used to remove the boundaries so new ones can be chosen or to return to the rotation input window.

e. After the rotation and boundaries are correct, press the next button to move to the next sample in the datasheet. This will continue until all the samples in the datasheet have been set.

f. After the rotation and boundaries for all samples have been set, clicking the next button in the boundary input window will start the analysis.

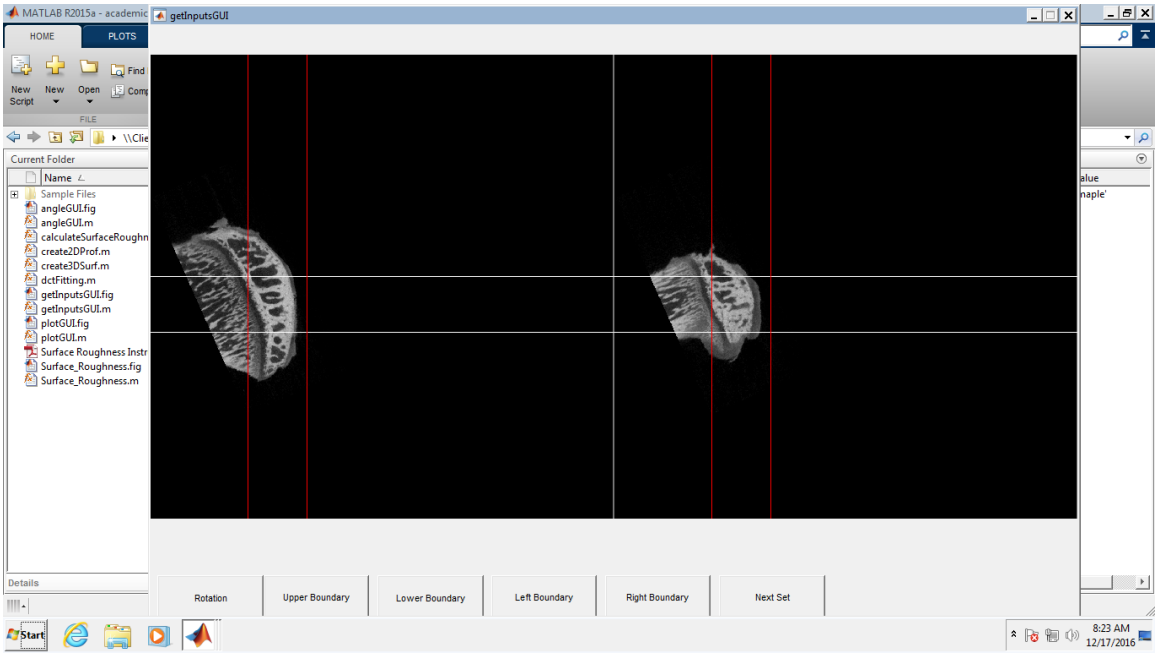

Figure B.7.4: getInputsGUI.m with example 2D images for boundary input

10. If no rotational or boundary inputs are chosen on the opening screen, or when the last sample's rotation and boundaries are defined, the program will save all the rotation and boundaries inputs in an excel spreadsheet labeled the same as the datasheet but with 'wParameters' added to the end. These rotation and boundaries can be copied to the original datasheet and can be used for future analyses without needing to redo the rotation and boundary inputs.
11. The program will then run though all the samples contained in the datasheet and calculate the requested parameters. These parameters will then be saved in the same spreadsheet where the inputs were saved ("Datasheet Name" wParameters).

B.3 angleGUI.m

B.3.1. File Description

angleGUI.m is a MATLAB® file that is called when the user needs to choose an angle for rotating the 2D images uploaded from the μCT machine in preparation for performing the surface roughness algorithm. This file is a GUI file and requires the MATLAB® figure angleGUI.fig to properly execute. See Figure B.7.5.

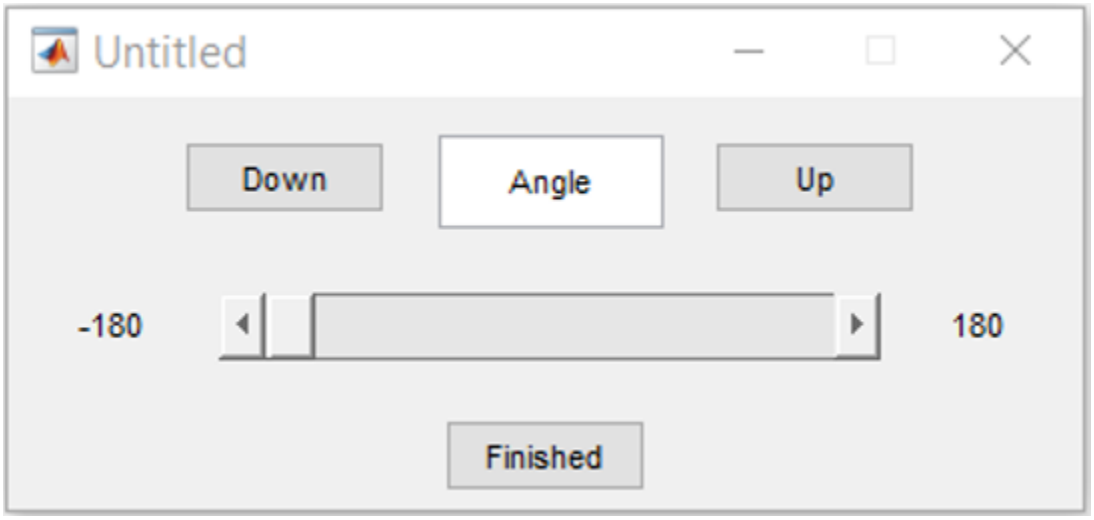

Figure B.7.5: Image of angleGUI.m

B.3.2. File Text

```
function varargout = angleGUI(varargin)
% ANGLEGUI MATLAB code for angleGUI.fig
%      ANGLEGUI, by itself, creates a new ANGLEGUI or raises the existing
%      singleton*.
%
%      H = ANGLEGUI returns the handle to a new ANGLEGUI or the handle to
%      the existing singleton*.
%
%      ANGLEGUI('CALLBACK',hObject,eventData,handles,...) calls the local
%      function named CALLBACK in ANGLEGUI.M with the given input arguments.
%
```

```
%      ANGLEGUI('Property','Value',...) creates a new ANGLEGUI or raises the
%      existing singleton*.  Starting from the left, property value pairs are
%      applied to the GUI before angleGUI_OpeningFcn gets called.  An
%      unrecognized property name or invalid value makes property application
%      stop.  All inputs are passed to angleGUI_OpeningFcn via varargin.
%
%      *See GUI Options on GUIDE's Tools menu.  Choose "GUI allows only one
%      instance to run (singleton)".
%
% See also: GUIDE, GUIDATA, GUIHANDLES

% Edit the above text to modify the response to help angleGUI

% Last Modified by GUIDE v2.5 02-Sep-2015 08:07:12

% Begin initialization code - DO NOT EDIT
gui_Singleton = 1;
gui_State = struct('gui_Name',       mfilename, ...
                   'gui_Singleton',  gui_Singleton, ...
                   'gui_OpeningFcn', @angleGUI_OpeningFcn, ...
                   'gui_OutputFcn',  @angleGUI_OutputFcn, ...
                   'gui_LayoutFcn',  [] , ...
                   'gui_Callback',   []);
if nargin && ischar(varargin{1})
   gui_State.gui_Callback = str2func(varargin{1});
end

if nargout
   [varargout{1:nargout}] = gui_mainfcn(gui_State, varargin{:});
else
   gui_mainfcn(gui_State, varargin{:});
end
% End initialization code - DO NOT EDIT


% --- Executes just before angleGUI is made visible.
function angleGUI_OpeningFcn(hObject, eventdata, handles, varargin)
% This function has no output args, see OutputFcn.
% hObject    handle to figure
% eventdata  reserved - to be defined in a future version of MATLAB
% handles    structure with handles and user data (see GUIDATA)
% varargin   command line arguments to angleGUI (see VARARGIN)
handles.fileName = varargin{2};

% Choose default command line output for angleGUI
handles.output = hObject;
```

```
% Update handles structure
guidata(hObject, handles);
set(handles.rotAngle,'String','29');
set(handles.slider1,'Value',29);
set(handles.slider1,'Min',-180);
set(handles.slider1,'Max',180);
displayImage(handles);

% UIWAIT makes angleGUI wait for user response (see UIRESUME)
uiwait(handles.figure1);


% --- Outputs from this function are returned to the command line.
function varargout = angleGUI_OutputFcn(hObject, eventdata, handles)
% varargout  cell array for returning output args (see VARARGOUT);
% hObject    handle to figure
% eventdata  reserved - to be defined in a future version of MATLAB
% handles    structure with handles and user data (see GUIDATA)

% Get default command line output from handles structure
% close(handles.figure2)
varargout{1} = str2double(get(handles.rotAngle,'String'));
close(handles.figure1)



function rotAngle_Callback(hObject, eventdata, handles)
% hObject    handle to rotAngle (see GCBO)
% eventdata  reserved - to be defined in a future version of MATLAB
% handles    structure with handles and user data (see GUIDATA)

% Hints: get(hObject,'String') returns contents of rotAngle as text
%        str2double(get(hObject,'String')) returns contents of rotAngle as a double
if str2double(get(handles.imageNumber,'String')) < handles.Num(1)
   set(handles.rotAngle,'String',num2str(handles.Num(1)));
elseif str2double(get(handles.imageNumber,'String')) > handles.Num(2)
   set(handles.rotAngle,'String',num2str(handles.Num(2)));
end
set(handles.slider1,'Value',str2double(get(handles.rotAngle,'String')));
displayImage(handles);

% --- Executes during object creation, after setting all properties.
function rotAngle_CreateFcn(hObject, eventdata, handles)
% hObject    handle to rotAngle (see GCBO)
% eventdata  reserved - to be defined in a future version of MATLAB
```

```
% handles    empty - handles not created until after all CreateFcns called

% Hint: edit controls usually have a white background on Windows.
%       See ISPC and COMPUTER.
if ispc && isequal(get(hObject,'BackgroundColor'),
get(0,'defaultUicontrolBackgroundColor'))
   set(hObject,'BackgroundColor','white');
end


% --- Executes on button press in downButton.
function downButton_Callback(hObject, eventdata, handles)
% hObject    handle to downButton (see GCBO)
% eventdata  reserved - to be defined in a future version of MATLAB
% handles    structure with handles and user data (see GUIDATA)
currentRotAngle = str2double(get(handles.rotAngle,'String'));
if currentRotAngle <= -180
   set(handles.rotAngle,'String',num2str(currentRotAngle));
else
   set(handles.rotAngle,'String',num2str(currentRotAngle - 1));
end
set(handles.slider1,'Value',str2double(get(handles.rotAngle,'String')));
displayImage(handles);

% --- Executes on button press in upButton.
function upButton_Callback(hObject, eventdata, handles)
% hObject    handle to upButton (see GCBO)
% eventdata  reserved - to be defined in a future version of MATLAB
% handles    structure with handles and user data (see GUIDATA)
currentRotAngle = str2double(get(handles.rotAngle,'String'));
if currentRotAngle >= 180
   set(handles.rotAngle,'String',num2str(currentRotAngle));
else
   set(handles.rotAngle,'String',num2str(currentRotAngle + 1));
end
set(handles.slider1,'Value',str2double(get(handles.rotAngle,'String')));
displayImage(handles);

% --- Executes on slider movement.
function slider1_Callback(hObject, eventdata, handles)
% hObject    handle to slider1 (see GCBO)
% eventdata  reserved - to be defined in a future version of MATLAB
% handles    structure with handles and user data (see GUIDATA)

% Hints: get(hObject,'Value') returns position of slider
%        get(hObject,'Min') and get(hObject,'Max') to determine range of slider
```

```
set(handles.rotAngle,'String',int2str(round(get(hObject,'Value'))));
displayImage(handles)

% --- Executes during object creation, after setting all properties.
function slider1_CreateFcn(hObject, eventdata, handles)
% hObject    handle to slider1 (see GCBO)
% eventdata  reserved - to be defined in a future version of MATLAB
% handles    empty - handles not created until after all CreateFcns called

% Hint: slider controls usually have a light gray background.
if isequal(get(hObject,'BackgroundColor'), get(0,'defaultUicontrolBackgroundColor'))
   set(hObject,'BackgroundColor',[.9 .9 .9]);
end


% --- Executes on button press in finishedButton.
function finishedButton_Callback(hObject, eventdata, handles)
% hObject    handle to finishedButton (see GCBO)
% eventdata  reserved - to be defined in a future version of MATLAB
% handles    structure with handles and user data (see GUIDATA)
close(figure(2))
uiresume(handles.figure1);

function displayImage(handles)
imageRaw = imread(handles.fileName);
myImage = imrotate(imageRaw,str2double(get(handles.rotAngle,'String')));

myImageSize = size(myImage);
gridIndex = 1;
while gridIndex < myImageSize
   myImage(:,gridIndex) = 250;
   gridIndex = gridIndex + round(myImageSize/10);
end

figure(2);
warning('off','images:initSize:adjustingMag')
imshow(myImage);
warning('on','images:initSize:adjustingMag')
```

B.4 calculateSurfaceRoughness.m

B.4.1. File Description

calculateSurfaceRoughness is the main file behind the surface roughness calculations. It receives all the inputs from the other functions, creates the 3D surfaces from the 2D images, calculates the desired parameters, and then writes the output Excel spreadsheet. All parameter calculations are in this file.

B.4.2. File Text

```
function [] =
calculateSurfaceRoughness(dataSheetName,Num,Txt,Headers,Fits,pixelSize,cartThreshS
canco,boneThreshScanco,minThick,includeBone)
% This function is called by Surface_Roughness.m after the input parameters
% have been set. It calculates the surfaces for the roughness and lesion
% volume calculations, runs the calculations and saves them as in the
% output file

%% Inputs from parent function
% dataSheetName - the name of the input excel datasheet
% Num - Double array of the starting and ending file numbers, rotation
%       angles, and boundaries
% Txt - Cell array with the file names from the input datasheet
% Headers - Cell array with the header row from the input data sheet
% Fits - Cell array with the list of fits that will be used in the analysis
% pixelSize - Double with the size of the pixels in the original CT files
% cartThreshScanco - Cartilage threshold that was submitted in the starting
%                    screen. Should be the same value as the threshold used
%                    in the Scanco analyses
% boneThreshScanco - Bone threshold that was submitted in the starting
%                    screen. Should be the same value as the threshold used
%                    in the Scanco analyses
% minThick - The minimum thickness in pixels that will be counted as
%            cartilage and not exposed bone. Submitted in the starting
%            screen
% includeBone - Binary to indicate whether all the parameters that use the
%               bone surface should be used to in this analysis. These
%               parameters include exposed bone and lesion volume

%% Set up and Input Save
% This portion sets up the necessary variables. It also saves the rotation
% angles and boundaries in the output excel file.
[N,~] = size(Num); % Number of files that are being analyzed
[NofFits,~] = size(Fits); % Number of fits that are to be utilized
```

```
cartThreshMatLab = cartThreshScanco/1000*32767/20000*256; %Converts the input
Scanco threshold to greyscale threshold for use in matlab
boneThreshMatLab = boneThreshScanco/1000*32767/20000*256; %Converts the input
Scanco threshold to greyscale threshold for use in matlab

% Create and save new datasheet with the input parameters
newDataSheetName = strcat(dataSheetName,'wParameters.xlsx'); %Name of output
excel file
newDataSheet = cell(N + 1,10); %Creates cell array for later use in output excel file
Txt = Txt(:,1:3); % Cut out extra cells in Txt array
newDataSheet(1,:) = Headers; % Place Header into output cell array
newDataSheet(2:(N + 1),1:3) = Txt; % Place Txt into output cell array
newDataSheet(2:(N + 1),4:10) = num2cell(Num); % Convert Num to cell array and place
into output cell array
xlswrite(newDataSheetName,newDataSheet,1) % Save output cell to output excel file

display('Setup Complete and Saved'); % Signals to user that this section of the function is
completed

%% Creates the surfaces and calculates the parameters for each the files
for i = 1:N
   %% This section creates the cartilage and bone surfaces for one file
   nameStart = strcat(Txt{i,1}, '/', Txt{i,2}); % Create naming variable used when calling
create3Dsurf
   [fitCartSurf,plotCartSurf] = create3DSurf(nameStart, Txt{i,3}, Num(i,1), Num(i,2),
Num(i,3), Num(i,4), Num(i,5), Num(i,6), Num(i,7), cartThreshMatLab);
   % The previous function creates cartilage surface matrices from images:
   % fitCartSurf - A 3 column matrix with the x,y,z values of the
   %           cartilage surface for use in fitting the surface using
   %           the 'fit' function. The x values are the tif image
   %           number and the y values are the row numbers within the
   %           tif images
   % plotCartSurf - A mxn matrix the size of the analysis surface with the
   %           z value for each point on that suface. m is the number
   %           of tif images analyzed and n is the number of rows
   %           analyzed in each tif. This matrix is used for plotting
   %           the surfaces using the 'surf' function and for
   %           calculating the lesion areas and volumes.

   if includeBone
      [fitBoneSurf,plotBoneSurf] = create3DSurf(nameStart, Txt{i,3}, Num(i,1),
Num(i,2), Num(i,3), Num(i,4), Num(i,5), Num(i,6), Num(i,7), boneThreshMatLab);
      % The previous function created bone surface matrices from the
      % images: fitBoneSurf and plotBoneSurf are the same as for the
      % cartilage surfaces, but with the bone threshold
      display([Txt{i,1}, ' surfaces created']);
```

```
    else
        display([Txt{i,1}, ' surface created']);
    end
    surfSize = size(plotCartSurf);

    %% This section fits the surfaces with the requested fits and calculates the requested
parameters using each requested fit.
    for j = 1:NofFits
        %% This section checks if the requested fit is dct and, if true,
        % then fits the dct surface to the cartilage surface and creates
        % the Z surface, which is the difference between the actual
        % cartilage surface (plotCartSurf) and the fitted cartilage surface
        % (fittedCartSurf)
        tempStr = Fits{j}; % This string is necessary for checking if the requested fit is a
discrete cosine transformation (dct)
        if strcmp(tempStr(1:3),'dct') % Check if the requested fit is a dct
            cutoff = str2double(tempStr(4:length(tempStr))); % Set the cutoff for the dct from
the requested fit
            fittedCartSurf = dctFitting(plotCartSurf,pixelSize,cutoff); % Fit the cartilage
surface with the requested dct fit with the proper cutoff

            if includeBone % Check if the bone surface and the resulting parameters are to be
included in this analysis
                fittedBoneSurf = dctFitting(plotBoneSurf,pixelSize,cutoff); % Fit the bone
surface with the requested dct fit with the proper cutoff
            end

        else
            %% If the requested fit is not dct, this section fits the
            % cartilage and bone surface with the requested fit (poly or
            % lowess) and saves the fit to cartSurfFit and boneSurfFit,
            % respectively. It then creates matrices of the fitted surfaces
            % called fittedCartSurf and fittedBoneSurf that are the same
            % sizes as their respective plotting surfaces.
            cartSurfFit = fit([fitCartSurf(:,1),fitCartSurf(:,2)],fitCartSurf(:,3),Fits{j});
            fittedCartSurf = zeros(surfSize(1),surfSize(2));
            for k = 1:surfSize(1)
                for l = 1:surfSize(2)
                    fittedCartSurf(k,l) = cartSurfFit(k,l);
                end
            end

            if includeBone
                boneSurfFit = fit([fitBoneSurf(:,1),fitBoneSurf(:,2)],fitBoneSurf(:,3),Fits{j});
                fittedBoneSurf = zeros(surfSize(1),surfSize(2));
                for k = 1:surfSize(1)
```

```
            for l = 1:surfSize(2)
               fittedBoneSurf(k,l) = boneSurfFit(k,l);
            end
         end
      end
   end

%
plotGUI(Num(i,:),Txt(i,:),0,cartThreshScanco,boneThreshScanco,3,1,1,fittedCartSurf,fitt
edBoneSurf);
%       pause

   %% This section creates zSurf, the surface that is used to
   % calculate the surface roughness value
   zSurf = plotCartSurf - fittedCartSurf;

   %% If lesion parameters are requested by the user, this section
   % creates the surfaces used to calculate those parameters.
   % Because the sham samples have thin cartilage at the edges,
   % 5% of length or width along the respective edges is not
   % included in the anlaysis. If 100% of the surface is desired,
   % replace the 'for k' and 'for l' arguments with the comments
   % at the end of their lines.
   if includeBone
      z50LesionSurf = zeros(surfSize(1),surfSize(2));
      zExBoneSurf = zeros(surfSize(1),surfSize(2));
      for k = round(surfSize(1)/20):(surfSize(1) - round(surfSize(1)/20)) % for k =
1:surfSize(1)
         for l = round(surfSize(2)/20):(surfSize(2) - round(surfSize(2)/20)) % for l =
1:surfSize(2)
            if (plotCartSurf(k,l) - plotBoneSurf(k,l)) < minThick
               zExBoneSurf(k,l) = plotCartSurf(k,l) - fittedCartSurf(k,l);
            end
            if (plotCartSurf(k,l) - fittedCartSurf(k,l)) < 0.5*(fittedBoneSurf(k,l) -
fittedCartSurf(k,l))
               z50LesionSurf(k,l) = plotCartSurf(k,l) - fittedCartSurf(k,l);
            end
         end
      end
   end

   %% This section calculates the requested parameters and adds the
   % names and values to the Header and Num arrays.
   if ~includeBone
      NofParameters = 1;
   else
```

```
            NofParameters = 4;
        end

        Headers(11 + (j - 1)*NofParameters) = strcat(Fits(j),' Sq (um)'); % Add parameter
name to the Header array
        Num(i,8 + (j - 1)*NofParameters) = sqrt(mean2((abs(zSurf)).^2))*pixelSize; % Add
parameter to the Num array

        if includeBone
            Headers(12 + (j - 1)*NofParameters) = strcat(Fits(j),' Lesion Area (50%
Thickness) (um^2)'); % Add parameter name to the Header array
            Num(i,9 + (j - 1)*NofParameters) = sum(sum(abs(z50LesionSurf <
0)))*pixelSize^2/10^6; % Add parameter to the Num array

            Headers(13 + (j - 1)*NofParameters) = strcat(Fits(j),' Lesion Volume (50%
Thickness) (um^3)'); % Add parameter name to the Header array
            Num(i,10 + (j - 1)*NofParameters) = sum(sum(abs(z50LesionSurf(z50LesionSurf
< 0))))*pixelSize^3/10^9; % Add parameter to the Num array

            Headers(14 + (j - 1)*NofParameters) = strcat(Fits(j),' Exposed Bone Area
(um^2)'); % Add parameter name to the Header array
            Num(i,11 + (j - 1)*NofParameters) = sum(sum(abs(zExBoneSurf <
0)))*pixelSize^2/10^6; % Add parameter to the Num array
        end

        save([dataSheetName,'ErrorsFile.mat']); %This creates an error mat file with all of
the variables used up to this point that can be loaded to recover lost data in the case of
fatal program errors
        display([Txt{i,1}, ' ', Fits{j}, ' completed']);
    end
end

display('Calculations complete. Saving data...');

Num(N+2,1) = cartThreshScanco;
Txt{N+2,1} = 'Scanco Cartilage Threshold:';
Num(N+3,1) = cartThreshMatLab;
Txt{N+3,1} = 'MatLab Cartilage Threshold:';

if ~includeBone
    newDataSheet = cell(N + 4,10 + NofFits*NofParameters);
    TxtSize = size(Txt);
    Txt(:,4:TxtSize(2)) = [];
    newDataSheet(1,:) = Headers;
    newDataSheet(2:(N + 4),1:3) = Txt;
```

```
   newDataSheet(2:(N + 4),4:(10 + NofFits*NofParameters)) = num2cell(Num(:,1:(7 +
NofFits*NofParameters)));
else
   Num(N+4,1) = boneThreshScanco;
   Txt{N+4,1} = 'Scanco Bone Threshold:';
   Num(N+5,1) = boneThreshMatLab;
   Txt{N+5,1} = 'MatLab Bone Threshold:';
   newDataSheet = cell(N + 6,10 + NofFits*NofParameters);
   TxtSize = size(Txt);
   Txt(:,4:TxtSize(2)) = [];
   newDataSheet(1,:) = Headers;
   newDataSheet(2:(N + 6),1:3) = Txt;
   newDataSheet(2:(N + 6),4:(10 + NofFits*NofParameters)) = num2cell(Num(:,1:(7 +
NofFits*NofParameters)));
end

xlswrite(newDataSheetName,newDataSheet,1)

display(['Data saved to ', newDataSheetName]);
display('Program finished');

end
```

B.5 create2DProf.m

B.5.1. File Description

create2DProf.m receives a filename for a specific image as well as a rotation angle, analysis boundaries, and threshold. It rotates the image per the rotation angle and scans the image between the provided top, bottom, left, and right boundaries to find the right most pixel of each row that has a grayscale value above the threshold. It then returns the row and column number of these pixels to the calling function.

B.5.2. File Text

```
% create2DProf.m
% Author: David Reece
% Created: 3/23/13
% Last Modified: 07/29/16
```

```
% This file has inputs of the name of a specific tiff and the rotation angle and boundaries
of the analysis. It uses these inputs to upload the tiff and create an array with the
coordinates of the right most points of the tiff between the boundaries that have values
above the given threshold.
% Inputs:       nameStart(string) - a string consisting of the first two columns for a
particular row of the datasheet
%                       nameEnd(string) - a string consisting of the third column for a
particular row of the datasheet
%                       fileNumber(double) - a double consisting of the fileNumber of the
particular tiff within a set of tiffs defined by datasheet
%                       rotAngle(double) - a double with the angle (in degrees) to rotate
the tiffs
%                       topRow(double) - a double with the row number for the top of the
analysis
%                       bottomRow(double) - a double with the row number for the bottom
of the analysis
%                       rightCol(double) - a double with the column number for the right
of the analysis
%                       leftCol(double) - a double with the column number for the left of
the analysis
%                       threshold(double) - a double of the greyscale threshold used to
create the surfaces

function [twoDProf] = create2DProf(nameStart, nameEnd, fileNumber, rotAngle,
topRow, bottomRow, rightCol, leftCol, threshold)
NofRows = bottomRow - topRow + 1;

if fileNumber == 0
   fileNumberStr = '000';
elseif fileNumber < 10
   fileNumberStr = strcat('00',num2str(fileNumber));
elseif fileNumber < 100
   fileNumberStr = strcat('0',num2str(fileNumber));
else
   fileNumberStr = num2str(fileNumber);
end

twoDProf = zeros(NofRows,2);
% Create file name and import and rotate images
fileName = strcat(nameStart,fileNumberStr,nameEnd);
% display('UploadingImage');
try
   currentImageRaw = imread(fileName);
catch imreadError
   try currentImageRaw = imread(fileName);
   catch imreadError
```

```
      display('Please enter: currentImageRaw = imread(fileName)');
      beep
      keyboard
   end
end
% display('Creating Prof');

currentImage = imrotate(currentImageRaw,rotAngle);

% imageSize = size(currentImage);
% currentImage(:,rightCol:imageSize(2)) = [];

% Go through each row and find the last pixel to the right that has a value
% greater or equal to threshold
thresholdError = 0;
for i = 1:NofRows
   twoDProf(i,1) = i;
   tempProf = leftCol - 1 + find(currentImage((i + topRow - 1),leftCol:rightCol) >=
threshold,1,'last');
   try
      twoDProf(i,2) = tempProf(1);
   catch
      if i <= 2 || i > (NofRows-2)
         thresholdError = 1;
      end
      twoDProf(i,2) = leftCol;
   end
end
if thresholdError
   display(['File # ',fileNumberStr,' did not hit required threshold. Please reposition
boundaries or change thresholds.']);
end
```

B.6 create3DSurf.m

B.6.1. File Description

create3DSurf receives the file names for the 2D images being used in the analysis along with analysis boundaries and threshold. It calls create2DProf.m to create the 2D surface profiles for each of the 2D images and compiles those profiles into a 3D surface which is then returned to the calling function.

B.6.2. File Text

```
% create3DSurf.m
% Author: David Reece
% Created: 3/23/13
% Last Modified: 11/13/13

function [fittingSurf,plottingSurf] = create3DSurf(nameStart, nameEnd, firstFile, lastFile,
rotAngle, topRow, bottomRow, rightCol, leftCol, threshold)

NofFiles = lastFile - firstFile + 1;
NofRows = bottomRow - topRow + 1;

fittingSurf = zeros(NofFiles*NofRows,3);
plottingSurf = zeros(NofFiles,NofRows,1);

for i = 1:NofFiles
   fileNumber = firstFile + i - 1;

%     Map the cartilage surface and add to the end of fittingSurf
   fittingSurf((i - 1)*NofRows + 1:i*NofRows, 1) = i;
   fittingSurf((i - 1)*NofRows + 1:i*NofRows, 2:3) = create2DProf(nameStart, nameEnd,
fileNumber, rotAngle, topRow, bottomRow, rightCol, leftCol, threshold);

%     Take the most recent values from create2DProf and put into plottingSurf
   plottingSurf(i,:) = fittingSurf((i - 1)*NofRows + 1:i*NofRows, 3)';
end

end
```

B.7 dctFitting.m

B.7.1. File Description

dctFitting.m receives a 3D surface along with a cutoff period. It then uses a discrete cosine transform to convert the surface to cosine functions, removes all functions with periods longer than the cutoff period, converts the remain cosine functions back to a 3D surface, and returns the new surface to the calling function.

B.7.2. File Text

```
% dctFitting.m
% Author: David Reece
% Created: 5/7/13
% Last Modified: 5/7/13

function fittedSurf = dctFitting(originalSurf,T,Tc)

surfSize = size(originalSurf);
L1 = surfSize(1);
L2 = surfSize(2);
Fs = 1/T;
Fc = 1/Tc;

f1 = Fs/2*linspace(0,1,L1);
f2 = Fs/2*linspace(0,1,L2);

index1 = find(f1 > Fc,1,'first');
index2 = find(f2 > Fc,1,'first');

filter = zeros(L1,L2);
filter(1:index1 - 1,1:index2 - 1) = ones(index1 - 1,index2 - 1);

dctSurf = dct2(originalSurf).*filter;

fittedSurf = idct2(dctSurf);
```

B.8 getInputsGUI.m

B.8.1. File Description

getInputsGUI.m is a GUI that is called when the user needs to input the analysis boundaries. It displays both the first and last files from the range given in the data sheet and allows the user to choose top, bottom, left, and right boundaries. See Figure B.7.6

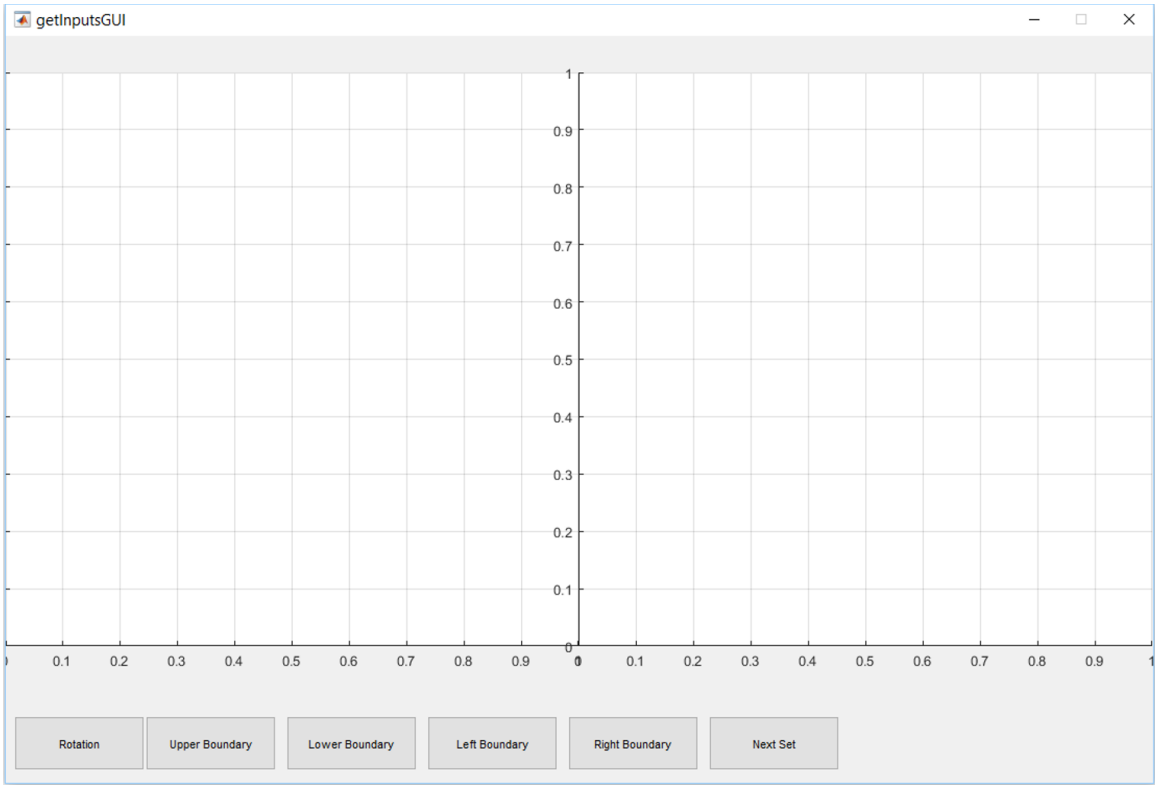

Figure B.7.6 Image of getInputsGUI.m

B.8.2. File Text

```
function varargout = getInputsGUI(varargin)
% GETINPUTSGUI MATLAB code for getInputsGUI.fig
%      GETINPUTSGUI, by itself, creates a new GETINPUTSGUI or raises the existing
%      singleton*.
%
%      H = GETINPUTSGUI returns the handle to a new GETINPUTSGUI or the handle
to
%      the existing singleton*.
%
%      GETINPUTSGUI('CALLBACK',hObject,eventData,handles,...) calls the local
%      function named CALLBACK in GETINPUTSGUI.M with the given input
arguments.
%
%      GETINPUTSGUI('Property','Value',...) creates a new GETINPUTSGUI or raises
the
%      existing singleton*.  Starting from the left, property value pairs are
%      applied to the GUI before getInputsGUI_OpeningFcn gets called.  An
%      unrecognized property name or invalid value makes property application
```

```
%      stop.  All inputs are passed to getInputsGUI_OpeningFcn via varargin.
%
%      *See GUI Options on GUIDE's Tools menu.  Choose "GUI allows only one
%      instance to run (singleton)".
%
% See also: GUIDE, GUIDATA, GUIHANDLES

% Edit the above text to modify the response to help getInputsGUI

% Last Modified by GUIDE v2.5 24-Sep-2015 14:47:42

% Begin initialization code - DO NOT EDIT
gui_Singleton = 1;
gui_State = struct('gui_Name',       mfilename, ...
                   'gui_Singleton',  gui_Singleton, ...
                   'gui_OpeningFcn', @getInputsGUI_OpeningFcn, ...
                   'gui_OutputFcn',  @getInputsGUI_OutputFcn, ...
                   'gui_LayoutFcn',  [] , ...
                   'gui_Callback',   []);
if nargin && ischar(varargin{1})
   gui_State.gui_Callback = str2func(varargin{1});
end

if nargout
   [varargout{1:nargout}] = gui_mainfcn(gui_State, varargin{:});
else
   gui_mainfcn(gui_State, varargin{:});
end
% End initialization code - DO NOT EDIT
% --- Executes just before getInputsGUI is made visible.
function getInputsGUI_OpeningFcn(hObject, eventdata, handles, varargin)
% This function has no output args, see OutputFcn.
% hObject    handle to figure
% eventdata  reserved - to be defined in a future version of MATLAB
% handles    structure with handles and user data (see GUIDATA)
% varargin   command line arguments to getInputsGUI (see VARARGIN)
handles.Num = varargin{1,1};
handles.Txt = varargin{1,2};
handles.askforRotAngles = varargin{1,3};
handles.askforRotAnglesActual = varargin{1,3};
handles.dataSheetName = varargin{1,4};
handles.cartThresh = varargin{1,5}/1000*32767/20000*256; %This converts the input
threshold from CT attenuation values to the equivalent TIF greyscale value.
handles.boneThresh = varargin{1,6}/1000*32767/20000*256;
handles.figNum = 1;
```

```
% Choose default command line output for getInputsGUI
handles.output = hObject;

% Update handles structure
guidata(hObject, handles);
setBoundaries(handles);

% UIWAIT makes getInputsGUI wait for user response (see UIRESUME)
uiwait(handles.figure1);

% --- Outputs from this function are returned to the command line.
function varargout = getInputsGUI_OutputFcn(hObject, eventdata, handles)
% varargout  cell array for returning output args (see VARARGOUT);
% hObject    handle to figure
% eventdata  reserved - to be defined in a future version of MATLAB
% handles    structure with handles and user data (see GUIDATA)

% Get default command line output from handles structure
close(handles.figure1)
varargout{1} = handles.Num;

% --- Executes on button press in nextButton.
function nextButton_Callback(hObject, eventdata, handles)
% hObject    handle to nextButton (see GCBO)
% eventdata  reserved - to be defined in a future version of MATLAB
% handles    structure with handles and user data (see GUIDATA)
cla
handles.figNum = handles.figNum + 1;

NumSize = size(handles.Num);
if handles.figNum > NumSize(1)
   uiresume(handles.figure1);
else
   axes(handles.axes1);
   hold off;
   axes(handles.axes2);
   hold off;
   guidata(handles.figure1, handles);
   setBoundaries(handles);
end

% --- Executes on button press in upperBoundButton.
function upperBoundButton_Callback(hObject, eventdata, handles)
% hObject    handle to upperBoundButton (see GCBO)
% eventdata  reserved - to be defined in a future version of MATLAB
% handles    structure with handles and user data (see GUIDATA)
```

```
delete(handles.yBoundPlot(1,:));
askforBoundary = true;
while askforBoundary
   [~, yBoundaries] = ginput(1);
   yBoundaries = int16(yBoundaries);
   askforBoundary = checkBoundaries(handles, yBoundaries);
end

if int16(yBoundaries) > handles.Num(handles.figNum,5)
   delete(handles.yBoundPlot(2,:));
   axes(handles.axes1);
   handles.yBoundPlot(1,1) = plot([0
2000],[handles.Num(handles.figNum,5),handles.Num(handles.figNum,5)],'w-');
   handles.yBoundPlot(2,1) = plot([0 2000],[yBoundaries,yBoundaries],'w-');
   axes(handles.axes2);
   handles.yBoundPlot(1,2) = plot([0
2000],[handles.Num(handles.figNum,5),handles.Num(handles.figNum,5)],'w-');
   handles.yBoundPlot(2,2) = plot([0 2000],[yBoundaries,yBoundaries],'w-');
   handles.Num(handles.figNum,4) = handles.Num(handles.figNum,5);
   handles.Num(handles.figNum,5) = int16(yBoundaries);
else
   axes(handles.axes1);
   handles.yBoundPlot(1,1) = plot([0 2000],[yBoundaries,yBoundaries],'w-');
   axes(handles.axes2);
   handles.yBoundPlot(1,2) = plot([0 2000],[yBoundaries,yBoundaries],'w-');
   handles.Num(handles.figNum,4) = int16(yBoundaries);
end

guidata(handles.figure1, handles);
% --- Executes on button press in lowerBoundButton.
function lowerBoundButton_Callback(hObject, eventdata, handles)
% hObject    handle to lowerBoundButton (see GCBO)
% eventdata  reserved - to be defined in a future version of MATLAB
% handles    structure with handles and user data (see GUIDATA)
delete(handles.yBoundPlot(2,:));
askforBoundary = true;
while askforBoundary
   [~, yBoundaries] = ginput(1);
   yBoundaries = int16(yBoundaries);
   askforBoundary = checkBoundaries(handles, yBoundaries);
end

if int16(yBoundaries) < handles.Num(handles.figNum,4)
   delete(handles.yBoundPlot(1,:));
   axes(handles.axes1);
```

```
   handles.yBoundPlot(2,1) = plot([0
2000],[handles.Num(handles.figNum,4),handles.Num(handles.figNum,4)],'w-');
   handles.yBoundPlot(1,1) = plot([0 2000],[yBoundaries,yBoundaries],'w-');
   axes(handles.axes2);
   handles.yBoundPlot(2,2) = plot([0
2000],[handles.Num(handles.figNum,4),handles.Num(handles.figNum,4)],'w-');
   handles.yBoundPlot(1,2) = plot([0 2000],[yBoundaries,yBoundaries],'w-');
   handles.Num(handles.figNum,5) = handles.Num(handles.figNum,4);
   handles.Num(handles.figNum,4) = int16(yBoundaries);
else
   axes(handles.axes1);
   handles.yBoundPlot(2,1) = plot([0 2000],[yBoundaries,yBoundaries],'w-');
   axes(handles.axes2);
   handles.yBoundPlot(2,2) = plot([0 2000],[yBoundaries,yBoundaries],'w-');
   handles.Num(handles.figNum,5) = int16(yBoundaries);
end

guidata(handles.figure1, handles);
% --- Executes on button press in rotButton.
function rotButton_Callback(hObject, eventdata, handles)
% hObject    handle to rotButton (see GCBO)
% eventdata  reserved - to be defined in a future version of MATLAB
% handles    structure with handles and user data (see GUIDATA)
handles.askforRotAnglesActual = handles.askforRotAngles;
handles.askforRotAngles = true;
guidata(handles.figure1, handles);
setBoundaries(handles)


% --- Executes to set boundaries for each new set of images
function setBoundaries(handles)
cla
i = handles.figNum;
firstFile = handles.Num(i,1);
lastFile = handles.Num(i,2);
middleFile = ceil((firstFile + lastFile)/2);

%% Changes the file numbers to strings
if firstFile == 0
   firstFileStr = '000';
elseif firstFile < 10
   firstFileStr = strcat('00',num2str(firstFile));
elseif firstFile < 100
   firstFileStr = strcat('0',num2str(firstFile));
else
   firstFileStr = num2str(firstFile);
```

```
end
firstFileName =
strcat(char(handles.Txt(i,1)),'/',char(handles.Txt(i,2)),firstFileStr,char(handles.Txt(i,3)));
if middleFile == 0
   middleFileStr = '000';
elseif middleFile < 10
   middleFileStr = strcat('00',num2str(middleFile));
elseif middleFile < 100
   middleFileStr = strcat('0',num2str(middleFile));
else
   middleFileStr = num2str(middleFile);
end
middleFileName =
strcat(char(handles.Txt(i,1)),'/',char(handles.Txt(i,2)),middleFileStr,char(handles.Txt(i,3))
);
if lastFile == 0
   lastFileStr = '000';
elseif lastFile < 10
   lastFileStr = strcat('00',num2str(lastFile));
elseif lastFile < 100
   lastFileStr = strcat('0',num2str(lastFile));
else
   lastFileStr = num2str(lastFile);
end
lastFileName =
strcat(char(handles.Txt(i,1)),'/',char(handles.Txt(i,2)),lastFileStr,char(handles.Txt(i,3)));

%% Import middle image and prompt user for rotation angle
if handles.askforRotAngles
   try
      imread(middleFileName,1);
   catch readError
      display(readError.message);
      newDataSheetName = strcat(handles.dataSheetName,'wFileError.xlsx');
      xlswrite(newDataSheetName,handles.Txt,1,'A2');
      xlswrite(newDataSheetName,handles.Num,1,'D2');
   end
   handles.Num(i,3) = angleGUI('JaneReeceisCute',middleFileName);
end

%% Checks the files to make sure they exist and if not, program spits out spreadsheet
with parameters up to this file
try
   imread(firstFileName,1);
catch readError
   display(readError.message);
```

```
    newDataSheetName = strcat(handles.dataSheetName,'wFileError.xlsx');
    xlswrite(newDataSheetName,handles.Txt,1,'A2');
    xlswrite(newDataSheetName,handles.Num,1,'D2');
end

try
    imread(lastFileName,1);
catch readError
    display(readError.message);
    newDataSheetName = strcat(handles.dataSheetName,'wFileError.xlsx');
    xlswrite(newDataSheetName,handles.Txt,1,'A2');
    xlswrite(newDataSheetName,handles.Num,1,'D2');
end


%% Rotate and display images in GUI
firstImageRaw = imread(firstFileName,1);
firstImage = imrotate(firstImageRaw,handles.Num(i,3));
axes(handles.axes1);
imshow(firstImage);
lastImageRaw = imread(lastFileName,1);
lastImage = imrotate(lastImageRaw,handles.Num(i,3));
axes(handles.axes2);
set(handles.axes2,'Visible','on');
imshow(lastImage);

handles.firstImage = firstImage;
handles.lastImage = lastImage;

guidata(handles.figure1, handles);

%% Ask for Boundaries, check that they cross cartilage and bone, and display
askforFirstBoundary = true;
while askforFirstBoundary
    [~, yBoundaries(1)] = ginput(1);
    askforFirstBoundary = checkBoundaries(handles, int16(yBoundaries(1)));
end
axes(handles.axes1);
hold on;
handles.yBoundPlot(1,1) = plot([0 2000],[yBoundaries(1),yBoundaries(1)],'w-');
axes(handles.axes2);
hold on;
handles.yBoundPlot(1,2) = plot([0 2000],[yBoundaries(1),yBoundaries(1)],'w-');

askforSecondBoundary = true;
while askforSecondBoundary
```

```
    [~, yBoundaries(2)] = ginput(1);
    askforSecondBoundary = checkBoundaries(handles, int16(yBoundaries(2)));
end
axes(handles.axes1);
handles.yBoundPlot(2,1) = plot([0 2000],[yBoundaries(2),yBoundaries(2)],'w-');
axes(handles.axes2);
handles.yBoundPlot(2,2) = plot([0 2000],[yBoundaries(2),yBoundaries(2)],'w-');

[rightXBoundary, ~] = ginput(1);
axes(handles.axes1);
handles.xBoundPlot(1,1) = plot([rightXBoundary,rightXBoundary],[0 2000],'r-');
axes(handles.axes2);
handles.xBoundPlot(1,2) = plot([rightXBoundary,rightXBoundary],[0 2000],'r-');

[leftXBoundary, ~] = ginput(1);
axes(handles.axes1);
handles.xBoundPlot(2,1) = plot([leftXBoundary,leftXBoundary],[0 2000],'r-');
axes(handles.axes2);
handles.xBoundPlot(2,2) = plot([leftXBoundary,leftXBoundary],[0 2000],'r-');

handles.Num(i,4) = int16(min(yBoundaries));
handles.Num(i,5) = int16(max(yBoundaries));
handles.Num(i,6) = int16(rightXBoundary);
handles.Num(i,7) = int16(leftXBoundary);

if ~handles.askforRotAnglesActual
    handles.askforRotAngles = false;
end

guidata(handles.figure1, handles);

% --- Executes to check if boundaries cross bone and cartilage
function boundaryIsBad = checkBoundaries(handles, boundary)
set(handles.errorPanel,'Visible','off');
boundaryIsBad = false;
if isempty(find(handles.firstImage(boundary,:) >= handles.cartThresh,1));
    boundaryIsBad = true;
    set(handles.errorPanel,'String','Boundary doesn''t cross cartilage surface of first image.
Please select different boundary.');
    set(handles.errorPanel,'Visible','on');
elseif isempty(find(handles.firstImage(boundary,:) >= handles.boneThresh,1));
    boundaryIsBad = true;
    set(handles.errorPanel,'String','Boundary doesn''t cross bone surface on first image.
Please select different boundary.');
    set(handles.errorPanel,'Visible','on');
elseif isempty(find(handles.lastImage(boundary,:) >= handles.cartThresh,1));
```

```
    boundaryIsBad = true;
    set(handles.errorPanel,'String','Boundary doesn''t cross cartilage surface on last image.
Please select different boundary.');
    set(handles.errorPanel,'Visible','on');
elseif isempty(find(handles.lastImage(boundary,:) >= handles.boneThresh,1));
    boundaryIsBad = true;
    set(handles.errorPanel,'String','Boundary doesn''t cross bone surface on last image.
Please select different boundary.');
    set(handles.errorPanel,'Visible','on');
end

guidata(handles.figure1, handles);
% --- Executes on button press in rightXBoundButton. Added 2/20/14
function rightXBoundButton_Callback(hObject, eventdata, handles)
% hObject    handle to rightXBoundButton (see GCBO)
% eventdata  reserved - to be defined in a future version of MATLAB
% handles    structure with handles and user data (see GUIDATA)
delete(handles.xBoundPlot(1,:));
[rightXBoundary, ~] = ginput(1);
axes(handles.axes1);
handles.xBoundPlot(1,1) = plot([rightXBoundary,rightXBoundary],[0 2000],'r-');
axes(handles.axes2);
handles.xBoundPlot(1,2) = plot([rightXBoundary,rightXBoundary],[0 2000],'r-');
handles.Num(handles.figNum,6) = int16(rightXBoundary);
guidata(handles.figure1, handles);


% --- Executes on button press in leftXBoundButton.
function leftXBoundButton_Callback(hObject, eventdata, handles)
% hObject    handle to leftXBoundButton (see GCBO)
% eventdata  reserved - to be defined in a future version of MATLAB
% handles    structure with handles and user data (see GUIDATA)
delete(handles.xBoundPlot(2,:));
[leftXBoundary, ~] = ginput(1);
axes(handles.axes1);
handles.xBoundPlot(2,1) = plot([leftXBoundary,leftXBoundary],[0 2000],'r-');
axes(handles.axes2);
handles.xBoundPlot(2,2) = plot([leftXBoundary,leftXBoundary],[0 2000],'r-');
handles.Num(handles.figNum,7) = int16(leftXBoundary);
guidata(handles.figure1, handles);
```

B.9 plotGUI.m

B.9.1. File Description

plotGUI.m is a GUI that is opened when the user chooses to ‘Run Plots’ on the main Surface_Roughness GUI. It allows the user to choose a 2D image with the file chosen on the Surface_Roughness GUI and then displays that image along with the cartilage and/or bone surfaces created in create3DSurf.m for the chosen image. It is a resource to help the user understand the algorithm and to troubleshoot any issues. It can also be used to create images of the 2D images with their cartilage and/or bone surfaces. See Figure B.7.7

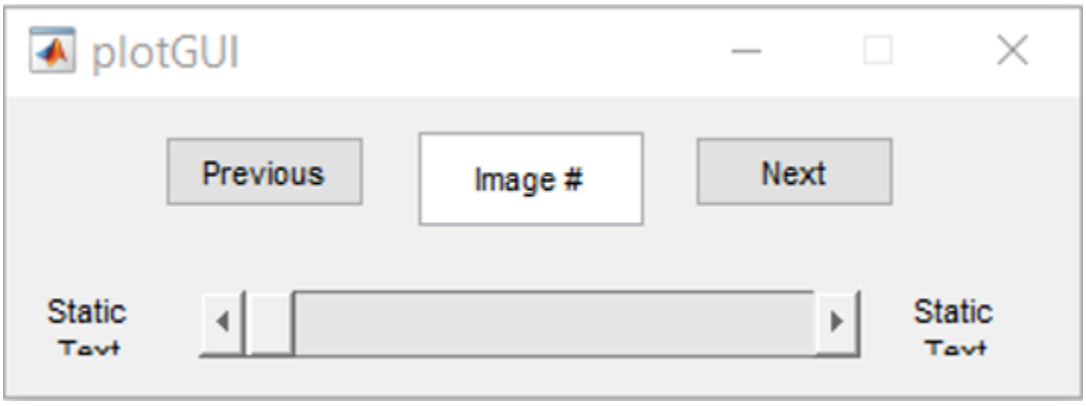

Figure B.7.7: Image of plotGUI.m

B.9.2. File Text

```
function varargout = plotGUI(varargin)
% PLOTGUI MATLAB code for plotGUI.fig
%      PLOTGUI, by itself, creates a new PLOTGUI or raises the existing
%      singleton*.
%
%      H = PLOTGUI returns the handle to a new PLOTGUI or the handle to
%      the existing singleton*.
%
%      PLOTGUI('CALLBACK',hObject,eventData,handles,...) calls the local
%      function named CALLBACK in PLOTGUI.M with the given input arguments.
%
%      PLOTGUI('Property','Value',...) creates a new PLOTGUI or raises the
%      existing singleton*.  Starting from the left, property value pairs are
%      applied to the GUI before plotGUI_OpeningFcn gets called.  An
%      unrecognized property name or invalid value makes property application
%      stop.  All inputs are passed to plotGUI_OpeningFcn via varargin.
```

```
%
%     *See GUI Options on GUIDE's Tools menu.  Choose "GUI allows only one
%     instance to run (singleton)".
%
% See also: GUIDE, GUIDATA, GUIHANDLES

% Edit the above text to modify the response to help plotGUI

% Last Modified by GUIDE v2.5 14-Apr-2014 13:18:55

% Begin initialization code - DO NOT EDIT
gui_Singleton = 1;
gui_State = struct('gui_Name',       mfilename, ...
                   'gui_Singleton',  gui_Singleton, ...
                   'gui_OpeningFcn', @plotGUI_OpeningFcn, ...
                   'gui_OutputFcn',  @plotGUI_OutputFcn, ...
                   'gui_LayoutFcn',  [] , ...
                   'gui_Callback',   []);
if nargin && ischar(varargin{1})
   gui_State.gui_Callback = str2func(varargin{1});
end

if nargout
   [varargout{1:nargout}] = gui_mainfcn(gui_State, varargin{:});
else
   gui_mainfcn(gui_State, varargin{:});
end
% End initialization code - DO NOT EDIT

% --- Executes just before plotGUI is made visible.
function plotGUI_OpeningFcn(hObject, eventdata, handles, varargin)
% This function has no output args, see OutputFcn.
% hObject    handle to figure
% eventdata  reserved - to be defined in a future version of MATLAB
% handles    structure with handles and user data (see GUIDATA)
% varargin   command line arguments to plotGUI (see VARARGIN)
handles.Num = varargin{1,1};
handles.Txt = varargin{1,2};
handles.askforRotAngles = varargin{1,3};
handles.cartThresh = varargin{1,4}/1000*32767/20000*256;
handles.boneThresh = varargin{1,5}/1000*32767/20000*256;
handles.minThick = varargin{1,6};
handles.calExBone = varargin{1,7};
handles.plotLesion = varargin{1,8};
if handles.plotLesion
   handles.cartFitSurf = varargin{1,9};
```

```
   handles.boneFitSurf = varargin{1,10};
end
set(handles.startText,'String',num2str(handles.Num(1)));
set(handles.endText,'String',num2str(handles.Num(2)));

% Choose default command line output for plotGUI
handles.output = hObject;

% Update handles structure
guidata(hObject, handles);
set(handles.imageNumber,'String',num2str(handles.Num(1)));
set(handles.slider,'Value',handles.Num(1));
set(handles.slider,'Min',handles.Num(1));
set(handles.slider,'Max',handles.Num(2));
displayPlots(handles);

% UIWAIT makes plotGUI wait for user response (see UIRESUME)
% uiwait(handles.figure1);

% --- Outputs from this function are returned to the command line.
function varargout = plotGUI_OutputFcn(hObject, eventdata, handles)
% varargout  cell array for returning output args (see VARARGOUT);
% hObject    handle to figure
% eventdata  reserved - to be defined in a future version of MATLAB
% handles    structure with handles and user data (see GUIDATA)

% Get default command line output from handles structure
varargout{1} = handles.output;

function imageNumber_Callback(hObject, eventdata, handles)
% hObject    handle to imageNumber (see GCBO)
% eventdata  reserved - to be defined in a future version of MATLAB
% handles    structure with handles and user data (see GUIDATA)
% Hints: get(hObject,'String') returns contents of imageNumber as text
%        str2double(get(hObject,'String')) returns contents of imageNumber as a double
if str2double(get(handles.imageNumber,'String')) < handles.Num(1)
   set(handles.imageNumber,'String',num2str(handles.Num(1)));
elseif str2double(get(handles.imageNumber,'String')) > handles.Num(2)
   set(handles.imageNumber,'String',num2str(handles.Num(2)));
end
set(handles.slider,'Value',str2double(get(handles.imageNumber,'String')));
displayPlots(handles);

% --- Executes during object creation, after setting all properties.
function imageNumber_CreateFcn(hObject, eventdata, handles)
% hObject    handle to imageNumber (see GCBO)
```

```
% eventdata  reserved - to be defined in a future version of MATLAB
% handles    empty - handles not created until after all CreateFcns called

% Hint: edit controls usually have a white background on Windows.
%       See ISPC and COMPUTER.
if ispc && isequal(get(hObject,'BackgroundColor'),
get(0,'defaultUicontrolBackgroundColor'))
   set(hObject,'BackgroundColor','white');
end

% --- Executes on button press in preButton.
function preButton_Callback(hObject, eventdata, handles)
% hObject    handle to preButton (see GCBO)
% eventdata  reserved - to be defined in a future version of MATLAB
% handles    structure with handles and user data (see GUIDATA)
currentImageNumber = str2double(get(handles.imageNumber,'String'));
if currentImageNumber <= handles.Num(1)
   set(handles.imageNumber,'String',num2str(currentImageNumber));
else
   set(handles.imageNumber,'String',num2str(currentImageNumber - 1));
end
set(handles.slider,'Value',str2double(get(handles.imageNumber,'String')));
displayPlots(handles);

% --- Executes on button press in nextButton.
function nextButton_Callback(hObject, eventdata, handles)
% hObject    handle to nextButton (see GCBO)
% eventdata  reserved - to be defined in a future version of MATLAB
% handles    structure with handles and user data (see GUIDATA)
currentImageNumber = str2double(get(handles.imageNumber,'String'));
if currentImageNumber >= handles.Num(2)
   set(handles.imageNumber,'String',num2str(currentImageNumber));
else
   set(handles.imageNumber,'String',num2str(currentImageNumber + 1));
end
set(handles.slider,'Value',str2double(get(handles.imageNumber,'String')));
displayPlots(handles);

function displayPlots(handles)
nameStart = strcat(char(handles.Txt(1)),'/',char(handles.Txt(2)));
nameEnd = handles.Txt{3};

imageNumber = str2double(get(handles.imageNumber,'String'));

%Map the cartilage and bone surfaces and give back the coordinates
```

```
[cartProf] = create2DProf(nameStart, nameEnd, imageNumber, handles.Num(3),
handles.Num(4), handles.Num(5), handles.Num(6), handles.Num(7),
handles.cartThresh);

if handles.calExBone
   [boneProf] = create2DProf(nameStart, nameEnd, imageNumber, handles.Num(3),
handles.Num(4), handles.Num(5), handles.Num(6), handles.Num(7),
handles.boneThresh);
end

if imageNumber == 0
   imageNumberStr = '000';
elseif imageNumber < 10
   imageNumberStr = strcat('0',num2str(imageNumber));
% elseif imageNumber < 100
%     imageNumberStr = strcat('0',num2str(imageNumber));
else
   imageNumberStr = num2str(imageNumber);
end

fileName = strcat(nameStart,imageNumberStr,nameEnd);
imageRaw = imread(fileName);
myImage = imrotate(imageRaw,handles.Num(3));
offsetVal = 25;

imageSize = size(myImage);
if imageSize(2) - handles.Num(6) < offsetVal
   offsetVal = imageSize(2) - handles.Num(6);
end
if handles.Num(7) < offsetVal
   offsetVal = handles.Num(7);
end

myImage(handles.Num(5)+offsetVal:end,:) = [];
myImage(1:handles.Num(4)-offsetVal,:) = [];
myImage(:,handles.Num(6)+offsetVal:end) = [];
myImage(:,1:handles.Num(7)-offsetVal) = [];

figure(2);
imshow(myImage);
hold on;

plot(cartProf(:,2) - handles.Num(7) + offsetVal,cartProf(:,1) + offsetVal - 1,'wo');

if handles.calExBone && handles.plotLesion
   indexValue = imageNumber - handles.Num(1) + 1;
```

```
   plot(boneProf(:,2) - handles.Num(7) + offsetVal,boneProf(:,1) + offsetVal,'ro');
   for i = 1:length(cartProf)
      if (cartProf(i,2) - handles.cartFitSurf(indexValue,i)) <
0.25*(handles.boneFitSurf(indexValue,i) - handles.cartFitSurf(indexValue,i))
         plot([cartProf(i,2) - handles.Num(7) + offsetVal,boneProf(i,2) - handles.Num(7) +
offsetVal],[cartProf(i,1) + offsetVal,boneProf(i,1) + offsetVal],'g-','LineWidth',6);
      end
   end
   plot(handles.cartFitSurf(indexValue,:) - handles.Num(7) + offsetVal,cartProf(:,1) +
offsetVal,'w-');
   plot(handles.boneFitSurf(indexValue,:) - handles.Num(7) + offsetVal,boneProf(:,1) +
offsetVal,'r-');
end

if handles.calExBone && ~handles.plotLesion
   plot(boneProf(:,2) - handles.Num(7) + offsetVal,boneProf(:,1) + offsetVal,'ro');

%    (6/10/16 DSR) I changed how the exposed bone was calculated in
%    calculateSurfaceRoughness.m by having it calculate exposed bone from
%    the fitted bone surface instead of the actual bone point. This should
%    help reduce the errors that would be caused by high attenuation
%    cartilage. However, that means in order for the plots from plotGUI to
%    match the actual values, we need to get fitted surfaces into here.
%    Once Kaley does that, I will add this feature of plotting the exposed
%    bone back.

%    for i = 1:length(cartProf)
%       if cartProf(i,2) - boneProf(i,2) < handles.minThick
%          plot([cartProf(i,2) - handles.Num(7) + offsetVal,boneProf(i,2) -
handles.Num(7) + offsetVal],[cartProf(i,1) + offsetVal,boneProf(i,1) + offsetVal],'g-
','LineWidth',6);
%       end
%    end
end
hold off;

% --- Executes on slider movement.
function slider_Callback(hObject, eventdata, handles)
% hObject    handle to slider (see GCBO)
% eventdata  reserved - to be defined in a future version of MATLAB
% handles    structure with handles and user data (see GUIDATA)

% Hints: get(hObject,'Value') returns position of slider
%       get(hObject,'Min') and get(hObject,'Max') to determine range of slider
set(handles.imageNumber,'String',int2str(round(get(hObject,'Value'))));
displayPlots(handles)
```

```
% --- Executes during object creation, after setting all properties.
function slider_CreateFcn(hObject, eventdata, handles)
% hObject    handle to slider (see GCBO)
% eventdata  reserved - to be defined in a future version of MATLAB
% handles    empty - handles not created until after all CreateFcns called

% Hint: slider controls usually have a light gray background.
if isequal(get(hObject,'BackgroundColor'), get(0,'defaultUicontrolBackgroundColor'))
   set(hObject,'BackgroundColor',[.9 .9 .9]);
end
```

B.10 Surface_Roughness.m

B.10.1. File Description

Surface_Roughness.m is the parent program for all the files listed here. This program is the run the user should run to start the analysis. When this program is run, it will open a GUI that allows the user to input the datasheet name, pixel size, and desired fits and what inputs should be requested and if the bone analyses should be performed. It also has options to allow the user to display the 2D profiles and 3D surfaces that the program uses in the surface roughness calculations. See Figure B.7.8.

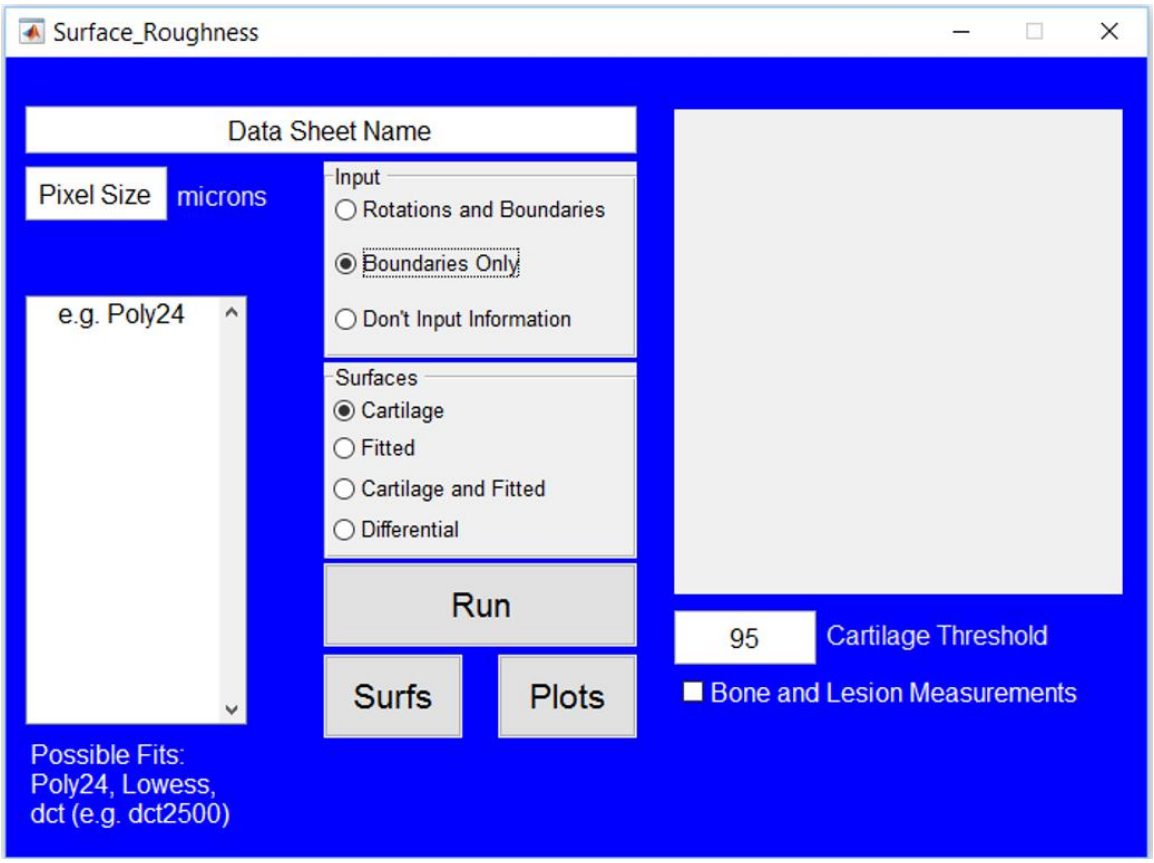

Figure B.7.8: Image of Surface_Roughness GUI

B.10.2. File Text

```
function varargout = Surface_Roughness(varargin)
% SURFACE_ROUGHNESS MATLAB code for Surface_Roughness.fig
%      SURFACE_ROUGHNESS, by itself, creates a new SURFACE_ROUGHNESS or
raises the existing
%      singleton*.
%
%      H = SURFACE_ROUGHNESS returns the handle to a new
SURFACE_ROUGHNESS or the handle to
%      the existing singleton*.
%
%      SURFACE_ROUGHNESS('CALLBACK',hObject,eventData,handles,...) calls the
local
%      function named CALLBACK in SURFACE_ROUGHNESS.M with the given input
arguments.
%
```

```
%      SURFACE_ROUGHNESS('Property','Value',...) creates a new
SURFACE_ROUGHNESS or raises the
%      existing singleton*.  Starting from the left, property value pairs are
%      applied to the GUI before Surface_Roughness_OpeningFcn gets called.  An
%      unrecognized property name or invalid value makes property application
%      stop.  All inputs are passed to Surface_Roughness_OpeningFcn via varargin.
%
%      *See GUI Options on GUIDE's Tools menu.  Choose "GUI allows only one
%      instance to run (singleton)".
%
% See also: GUIDE, GUIDATA, GUIHANDLES

% Edit the above text to modify the response to help Surface_Roughness

% Last Modified by GUIDE v2.5 02-Feb-2016 11:39:25

% Begin initialization code - DO NOT EDIT
gui_Singleton = 1;
gui_State = struct('gui_Name',       mfilename, ...
                   'gui_Singleton',  gui_Singleton, ...
                   'gui_OpeningFcn', @Surface_Roughness_OpeningFcn, ...
                   'gui_OutputFcn',  @Surface_Roughness_OutputFcn, ...
                   'gui_LayoutFcn',  [] , ...
                   'gui_Callback',   []);
if nargin && ischar(varargin{1})
   gui_State.gui_Callback = str2func(varargin{1});
end

if nargout
   [varargout{1:nargout}] = gui_mainfcn(gui_State, varargin{:});
else
   gui_mainfcn(gui_State, varargin{:});
end
% End initialization code - DO NOT EDIT

% --- Executes just before Surface_Roughness is made visible.
function Surface_Roughness_OpeningFcn(hObject, eventdata, handles, varargin)
% This function has no output args, see OutputFcn.
% hObject    handle to figure
% eventdata  reserved - to be defined in a future version of MATLAB
% handles    structure with handles and user data (see GUIDATA)
% varargin   command line arguments to Surface_Roughness (see VARARGIN)

% Set inital error, figure, and input handles to match GUI starting values
handles.noNameError = false;
handles.noFitsError = false;
```

```
handles.noPixelError = false;
handles.noFileNumError = false;
handles.noMinThickError = true;
handles.noCartThreshError = true;
handles.noBoneThreshError = true;
handles.askforRotAngles = true;
set(handles.surfFiguresPanel,'Visible','off');

% Choose default command line output for Surface_Roughness
handles.output = hObject;

% Update handles structure
guidata(hObject, handles);

% UIWAIT makes Surface_Roughness wait for user response (see UIRESUME)
% uiwait(handles.figure1);

% --- Outputs from this function are returned to the command line.
function varargout = Surface_Roughness_OutputFcn(hObject, eventdata, handles)
% varargout  cell array for returning output args (see VARARGOUT);
% hObject    handle to figure
% eventdata  reserved - to be defined in a future version of MATLAB
% handles    structure with handles and user data (see GUIDATA)
% There are no outputs for this GUI

% --- Executes when bone threshold has been altered and makes sure it is a number.
function boneThresh_Callback(hObject, eventdata, handles)
% hObject    handle to boneThresh (see GCBO)
% eventdata  reserved - to be defined in a future version of MATLAB
% handles    structure with handles and user data (see GUIDATA)

% Hints: get(hObject,'String') returns contents of boneThresh as text
%        str2double(get(hObject,'String')) returns contents of boneThresh as a double

if isnan(str2double(get(hObject,'String'))) % Check if bone threshold is not a number
   set(handles.errorPanel,'String','Please enter only a numerical value for the bone
threshold.'); % Display error on error panel
   handles.noBoneThreshError = false;
else
   set(handles.errorPanel,'String',''); % Clear error panel
   handles.noBoneThreshError = true;
end
guidata(handles.figure1, handles); % Update handles structure;

% --- Executes on button press in calBone and updates GUI accordingly.
function calBone_Callback(hObject, eventdata, handles)
```

```
% hObject    handle to calBone (see GCBO)
% eventdata  reserved - to be defined in a future version of MATLAB
% handles    structure with handles and user data (see GUIDATA)

% Hint: get(hObject,'Value') returns toggle state of calBone

if get(hObject,'Value') % If calBone is checked, show bone threshold and minimum
thickness items in GUI
   set(handles.boneThresh,'Visible','on');
   set(handles.boneThresh,'String','280');
   set(handles.boneThreshText,'Visible','on');
   set(handles.minThick,'Visible','on');
   set(handles.minThickText,'Visible','on');
else % If calBone is not checked, hide bone threshold and minimum thickness items in
GUI
   set(handles.boneThresh,'Visible','off');
   set(handles.boneThresh,'String','0');
   set(handles.boneThreshText,'Visible','off');
   set(handles.minThick,'Visible','off');
   set(handles.minThickText,'Visible','off');
end

% --- Executes when cartilage threshold has been altered and makes sure it is a number.
function cartThresh_Callback(hObject, eventdata, handles)
% hObject    handle to cartThresh (see GCBO)
% eventdata  reserved - to be defined in a future version of MATLAB
% handles    structure with handles and user data (see GUIDATA)

% Hints: get(hObject,'String') returns contents of cartThresh as text
%        str2double(get(hObject,'String')) returns contents of cartThresh as a double
if isnan(str2double(get(hObject,'String'))) % Check if cartilage threshold is not a number
   set(handles.errorPanel,'String','Please enter only a numerical value for the cartilage
threshold.'); % Display error on error panel
   handles.noCartThreshError = false;
else
   set(handles.errorPanel,'String',''); %Clear error panel
   handles.noCartThreshError = true;
end
guidata(handles.figure1, handles); % Update handles structure;

% --- Executes when datasheet name has been altered and makes sure it can be read into
matlab.
function dataSheetName_Callback(hObject, eventdata, handles)
% hObject    handle to dataSheetName (see GCBO)
% eventdata  reserved - to be defined in a future version of MATLAB
% handles    structure with handles and user data (see GUIDATA)
```

```
% Hints: get(hObject,'String') returns contents of dataSheetName as text
%        str2double(get(hObject,'String')) returns contents of dataSheetName as a double
try % See if datasheet can be read into matlab
   [~,~] = xlsread(get(hObject,'String'));
   handles.noNameError = true;
   set(handles.errorPanel,'String',''); %Clear error panel
catch fileError % If datasheet cannot be read, save error message as fileError
   set(handles.errorPanel,'String',fileError.message); % Display fileError on error panel
   handles.noNameError = false;
end
guidata(handles.figure1, handles); % Update handles structure

% --- Executes when file number has been altered and verifies it is in the datasheet.
function fileNum_Callback(hObject, eventdata, handles)
% hObject    handle to fileNum (see GCBO)
% eventdata  reserved - to be defined in a future version of MATLAB
% handles    structure with handles and user data (see GUIDATA)

% Hints: get(hObject,'String') returns contents of fileNum as text
%        str2double(get(hObject,'String')) returns contents of fileNum as a double
if handles.noNameError % Only executes if the datasheet name has already been
validated.
   [~,Txt] = xlsread(get(handles.dataSheetName,'String')); % Reads datasheet and saves
the text from the datasheet as a matrix of strings called Txt
   Txt(1,:) = []; % Trims off the column headings from Txt
   txtSize = size(Txt);
   i = str2double(get(handles.fileNum,'String')) - 1;
%     [i,~] = find(strcmp(get(handles.fileNum,'String'),Txt) == true); % Searches Txt for
the file number matching the file number drawn fileNum
   if i > 0 && i <= txtSize(1) %isempty(i)
      handles.noFileNumError = true;
      set(handles.errorPanel,'String',''); %Clear error panel
   else
      set(handles.errorPanel,'String','Row Number not found in datasheet. Please try
again.');
      handles.noFileNumError = false;
   end
end

guidata(handles.figure1, handles); % Update handles structure

% --- Executes when the table is edited.
function fitsTable_Callback(hObject, eventdata, handles)
% hObject    handle to fitsTable (see GCBO)
% eventdata  reserved - to be defined in a future version of MATLAB
```

```
% handles    structure with handles and user data (see GUIDATA)

% Hints: get(hObject,'String') returns contents of fitsTable as text
%        str2double(get(hObject,'String')) returns contents of fitsTable as a double
handles.Fits = cellstr(get(hObject,'String'));
handles.Fits = handles.Fits(~cellfun('isempty',handles.Fits));
handles.Fits = strtrim(handles.Fits);
set(hObject,'String',handles.Fits);
handles.noFitsError = true;
NofFits = length(handles.Fits);
errorStr = strcat('Please correct the following fit entries:',{' '});
for i = 1:NofFits
   tempStr = handles.Fits{i};
   if length(tempStr) < 4
      errorStr = strcat(errorStr,tempStr,{' '});
      set(handles.errorPanel,'String',errorStr);
      handles.noFitsError = false;
   elseif strcmp(tempStr(1:4),'lowe')
      if ~strcmp(tempStr(1:length(tempStr)),'lowess')
         errorStr = strcat(errorStr,tempStr,{' '});
         set(handles.errorPanel,'String',errorStr);
         handles.noFitsError = false;
      end
   elseif strcmp(tempStr(1:3),'dct') || strcmp(tempStr(1:3),'DCT') ||
strcmp(tempStr(1:3),'Dct')
      if isnan(str2double(tempStr(4:length(tempStr))))
         errorStr = strcat(errorStr,tempStr,{' '});
         set(handles.errorPanel,'String',errorStr);
         handles.noFitsError = false;
      end
   else
      try
         fitoptions(handles.Fits{i});
      catch dummyVariable
         errorStr = strcat(errorStr,tempStr,{' '});
         set(handles.errorPanel,'String',errorStr);
         handles.noFitsError = false;
      end
   end
end
if handles.noFitsError
   set(handles.errorPanel,'String','');
end
guidata(handles.figure1, handles); % Update handles structure

% --- Executes on button press in goBackButton.
```

```
function goBackButton_Callback(hObject, eventdata, handles)
% hObject    handle to goBackButton (see GCBO)
% eventdata  reserved - to be defined in a future version of MATLAB
% handles    structure with handles and user data (see GUIDATA)
set(handles.pixelSize,'Visible','on');
set(handles.text3,'Visible','on');
set(handles.fitsTable,'Visible','on');
set(handles.possibleFits,'Visible','on');
set(handles.runButton,'Visible','on');
set(handles.surfRunButton,'Visible','off');
set(handles.plotRunButton,'Visible','off');
set(handles.goBackButton,'Visible','off');
set(handles.fileNum,'Visible','off');
set(handles.surfFiguresPanel,'Visible','off');

% --- Executes when selected object is changed in inputPanel.
function inputPanel_SelectionChangeFcn(hObject, eventdata, handles)
% hObject    handle to the selected object in inputPanel
% eventdata  structure with the following fields (see UIBUTTONGROUP)
%        EventName: string 'SelectionChanged' (read only)
%        OldValue: handle of the previously selected object or empty if none was selected
%        NewValue: handle of the currently selected object
% handles    structure with handles and user data (see GUIDATA)
if get(handles.rotateButton,'Value')
   handles.askforRotAngles = true;
elseif get(handles.boundariesButton,'Value')
   handles.askforRotAngles = false;
   handles.askforBoundaries = true;
elseif get(handles.noInputButton,'Value')
   handles.askforRotAngles = false;
   handles.askforBoundaries = false;
end
guidata(handles.figure1, handles); % Update handles structure

% --- Executes when object has been altered.
function minThick_Callback(hObject, eventdata, handles)
% hObject    handle to minThick (see GCBO)
% eventdata  reserved - to be defined in a future version of MATLAB
% handles    structure with handles and user data (see GUIDATA)

% Hints: get(hObject,'String') returns contents of minThick as text
%        str2double(get(hObject,'String')) returns contents of minThick as a double
if isnan(str2double(get(hObject,'String')))
   set(handles.errorPanel,'String','Please enter only a numerical value for the minimum
thickness');
   handles.noMinThickError = false;
```

```
else
   set(handles.errorPanel,'String',''); %Clear error panel
   handles.noMinThickError = true;
end
guidata(handles.figure1, handles); % Update handles structure

% --- Executes when object has been altered.
function pixelSize_Callback(hObject, eventdata, handles)
% hObject    handle to pixelSize (see GCBO)
% eventdata  reserved - to be defined in a future version of MATLAB
% handles    structure with handles and user data (see GUIDATA)

% Hints: get(hObject,'String') returns contents of pixelSize as text
%        str2double(get(hObject,'String')) returns contents of pixelSize as a double
if isnan(str2double(get(hObject,'String')))
   set(handles.errorPanel,'String','Please enter only a numerical value for the pixel size');
   handles.noPixelError = false;
else
   set(handles.errorPanel,'String',''); %Clear error panel
   handles.noPixelError = true;
end
guidata(handles.figure1, handles); % Update handles structure

% --- Executes on button press in plotRunButton.
function plotRunButton_Callback(hObject, eventdata, handles)
% hObject    handle to plotRunButton (see GCBO)
% eventdata  reserved - to be defined in a future version of MATLAB
% handles    structure with handles and user data (see GUIDATA)
clc %Clear command window
set(handles.errorPanel,'String',''); %Clear error panel
if ~handles.noNameError
   set(handles.errorPanel,'String','Please correct datasheet name.');
elseif ~handles.noFileNumError
   fileNum_Callback([],[],handles);
elseif ~handles.noBoneThreshError
   set(handles.errorPanel,'String','Please enter only a numerical value for the bone
threshold.');
elseif ~handles.noCartThreshError
   set(handles.errorPanel,'String','Please enter only a numerical value for the cartilage
threshold.');
elseif ~handles.noMinThickError
   set(handles.errorPanel,'String','Please enter only a numerical value for the minimum
thickness.');
else
   [Num,Txt] = xlsread(get(handles.dataSheetName,'String'));
   Txt(1,:) = [];
```

```
    Txt(:,4:5) = [];
    i = str2double(get(handles.fileNum,'String')) - 1;
%     [i,~] = find(strcmp(get(handles.fileNum,'String'),Txt) == true);
    if handles.askforRotAngles || handles.askforBoundaries
        updatedNum =
getInputsGUI(Num(i,:),Txt(i,:),handles.askforRotAngles,get(handles.dataSheetName,'Str
ing'),str2double(get(handles.cartThresh,'String')),str2double(get(handles.boneThresh,'Stri
ng')));
    else
        updatedNum = Num(i,:);
    end

plotGUI(updatedNum,Txt(i,:),handles.askforRotAngles,str2double(get(handles.cartThres
h,'String')),str2double(get(handles.boneThresh,'String')),str2double(get(handles.minThick
,'String')),get(handles.calBone,'Value'),0);
end

% --- Executes on button press in plotsButton.
function plotsButton_Callback(hObject, eventdata, handles)
% hObject    handle to plotsButton (see GCBO)
% eventdata  reserved - to be defined in a future version of MATLAB
% handles    structure with handles and user data (see GUIDATA)
set(handles.pixelSize,'Visible','off');
set(handles.text3,'Visible','off');
set(handles.fitsTable,'Visible','off');
set(handles.possibleFits,'Visible','off');
set(handles.runButton,'Visible','off');
set(handles.surfRunButton,'Visible','off');
set(handles.surfFiguresPanel,'Visible','off');
set(handles.plotRunButton,'Visible','on');
set(handles.goBackButton,'Visible','on');
set(handles.fileNum,'Visible','on');

% --- Executes on button press in runButton.
function runButton_Callback(hObject, eventdata, handles)
% hObject    handle to runButton (see GCBO)
% eventdata  reserved - to be defined in a future version of MATLAB
% handles    structure with handles and user data (see GUIDATA)
clc; %Clear command window
set(handles.errorPanel,'String',''); %Clear error panel
if ~handles.noNameError
    set(handles.errorPanel,'String','Please correct datasheet name.');
elseif ~handles.noPixelError
    set(handles.errorPanel,'String','Please enter a numerical value for the pixel size.');
elseif ~handles.noFitsError
    set(handles.errorPanel,'String','Please enter desired fit.');
```

```
elseif ~handles.noBoneThreshError
   set(handles.errorPanel,'String','Please enter only a numerical value for the bone
threshold.');
elseif ~handles.noCartThreshError
   set(handles.errorPanel,'String','Please enter only a numerical value for the cartilage
threshold.');
elseif ~handles.noMinThickError
   set(handles.errorPanel,'String','Please enter only a numerical value for the minimum
thickness.');
else
   [Num,Txt] = xlsread(get(handles.dataSheetName,'String'));
   Headers = [Txt(1,1) Txt(1,2) Txt(1,3) Txt(1,4) Txt(1,5) 'Rot Angle' 'Top Row' 'Bottom
Row' 'Right Column' 'Left Column'];
   Txt(1,:) = [];
   Txt(:,4:5) = [];
   if handles.askforRotAngles || handles.askforBoundaries
      updatedNum =
getInputsGUI(Num,Txt,handles.askforRotAngles,get(handles.dataSheetName,'String'),str
2double(get(handles.cartThresh,'String')),str2double(get(handles.boneThresh,'String')));
   else
      updatedNum = Num;
   end

calculateSurfaceRoughness(get(handles.dataSheetName,'String'),updatedNum,Txt,Heade
rs,handles.Fits,str2double(get(handles.pixelSize,'String')),str2double(get(handles.cartThre
sh,'String')),str2double(get(handles.boneThresh,'String')),str2double(get(handles.minThic
k,'String')),get(handles.calBone,'Value'));
end

% --- Executes on button press in surfRunButton.
function surfRunButton_Callback(hObject, eventdata, handles)
% hObject    handle to surfRunButton (see GCBO)
% eventdata  reserved - to be defined in a future version of MATLAB
% handles    structure with handles and user data (see GUIDATA)
clc;
set(handles.errorPanel,'String','');
if ~handles.noNameError
   set(handles.errorPanel,'String','Please correct datasheet name.');
elseif ~handles.noFileNumError
   fileNum_Callback([],[],handles);
elseif ~handles.noBoneThreshError
   set(handles.errorPanel,'String','Please enter only a numerical value for the bone
threshold.');
elseif ~handles.noCartThreshError
   set(handles.errorPanel,'String','Please enter only a numerical value for the cartilage
threshold.');
```

```
elseif ~handles.noMinThickError
   set(handles.errorPanel,'String','Please enter only a numerical value for the minimum
thickness.');
else
   [Num,Txt] = xlsread(get(handles.dataSheetName,'String'));
   Txt(1,:) = [];
   Txt(:,4:5) = [];
   i = str2double(get(handles.fileNum,'String')) - 1;
%     [i,~] = find(strcmp(get(handles.fileNum,'String'),Txt) == true);
   nameStart = strcat(Txt{i,1}, '/', Txt{i,2});
   if handles.askforRotAngles || handles.askforBoundaries
      updatedNum =
getInputsGUI(Num(i,:),Txt(i,:),handles.askforRotAngles,get(handles.dataSheetName,'Str
ing'),str2double(get(handles.cartThresh,'String')),str2double(get(handles.boneThresh,'Stri
ng')));
   else
      updatedNum = Num(i,:);
   end
   [fitCartSurf,plotCartSurf] =
create3DSurf(nameStart,Txt{i,3},updatedNum(1),updatedNum(2),updatedNum(3),updat
edNum(4),updatedNum(5),updatedNum(6),updatedNum(7),str2double(get(handles.cartT
hresh,'String'))/1000*32767/20000*256);

   if get(handles.cartSurfButton,'Value')
      figure
      h = surf(plotCartSurf);
      axis equal;
      axis off
      colormap 'Jet'
%       set(h,'edgecolor','none')
      if get(handles.calBone,'Value')
         [~,plotBoneSurf] =
create3DSurf(nameStart,Txt{i,3},updatedNum(1),updatedNum(2),updatedNum(3),updat
edNum(4),updatedNum(5),updatedNum(6),updatedNum(7),str2double(get(handles.bone
Thresh,'String'))/1000*32767/20000*256);
         hold on;
         surf(plotBoneSurf);
         surfSize = size(plotCartSurf);
         for j = 1:surfSize(1)
            for k = 1:surfSize(2);
               if plotCartSurf(j,k) - plotBoneSurf(j,k) <
str2double(get(handles.minThick,'String'))
                  plot3(k,j,plotCartSurf(j,k),'wo');
               end
            end
         end
```

```
            hold off;
        end
    elseif ~handles.noFitsError
        set(handles.errorPanel,'String','Please enter desired fit.');
    elseif any(strncmp('dct',handles.Fits,3)) && ~handles.noPixelError
        set(handles.errorPanel,'String','Please enter a numerical value for the pixel size.');
    else
        for j = 1:size(handles.Fits)
            tempStr = handles.Fits{j};
            if strcmp(tempStr(1:3),'dct')
                cutoff = str2double(tempStr(4:length(tempStr)));
                fittedCartSurf =
dctFitting(plotCartSurf,str2double(get(handles.pixelSize,'String')),cutoff);
            else
                cartSurfFit =
fit([fitCartSurf(:,1),fitCartSurf(:,2)],fitCartSurf(:,3),handles.Fits{j});
                surfSize = size(plotCartSurf);
                fittedCartSurf = zeros(surfSize(1),surfSize(2));
                for k = 1:surfSize(1)
                    for l = 1:surfSize(2)
                        fittedCartSurf(k,l) = cartSurfFit(k,l);
                    end
                end
            end

            if get(handles.fittedSurfButton,'Value')
                figure
                h = surf(fittedCartSurf)
                axis equal
                axis off
                colormap 'Jet'
                set(h,'edgecolor','none')

            elseif get(handles.bothSurfButton,'Value')
                figure
                hold on
                surf(plotCartSurf)
                surf(fittedCartSurf)
                view(-38,30)
                axis equal
                hold off

            elseif get(handles.diffSurfButton,'Value')
                zSurf = plotCartSurf - fittedCartSurf;
                figure
                h = surf(zSurf);
```

```
            axis equal % Makes the aspect ratio such that the axis appear equally spaced
%               axis([1 229 1 47 -7.5098 5.9275]) % Can be used to set the axis for all
figures to the same values so they appear as the same size
            axis off % Turns off axis
            colormap 'Jet'
            set(h,'edgecolor','none') % Turns off edge of surface
            caxis([-7,5.5]) % Sets the colormap to between two set values
%               saveas(h,[get(handles.fileNum,'String'),'MedialFigure.tif'])
         end
      end
   end
end

% --- Executes on button press in surfsButton.
function surfsButton_Callback(hObject, eventdata, handles)
% hObject    handle to surfsButton (see GCBO)
% eventdata  reserved - to be defined in a future version of MATLAB
% handles    structure with handles and user data (see GUIDATA)
set(handles.runButton,'Visible','off');
set(handles.plotRunButton,'Visible','off');

set(handles.text3,'Visible','on');
set(handles.pixelSize,'Visible','on');
set(handles.surfRunButton,'Visible','on');
set(handles.goBackButton,'Visible','on');
set(handles.fileNum,'Visible','on');
set(handles.surfFiguresPanel,'Visible','on');
set(handles.fitsTable,'Visible','on');

% --- Executes when selected object is changed in surfFiguresPanel.
function surfFiguresPanel_SelectionChangedFcn(hObject, eventdata, handles)
% hObject    handle to the selected object in surfFiguresPanel
% eventdata  reserved - to be defined in a future version of MATLAB
% handles    structure with handles and user data (see GUIDATA)

%%
% These functions below all execute during object creation, after setting all
% properties. They are required for the GUI to function and are created
% automatically. No alterations have been made to them. DSR 11.3.14
function dataSheetName_CreateFcn(hObject, eventdata, handles)
% hObject    handle to dataSheetName (see GCBO)
% eventdata  reserved - to be defined in a future version of MATLAB
% handles    empty - handles not created until after all CreateFcns called

% Hint: edit controls usually have a white background on Windows.
%       See ISPC and COMPUTER.
```

```
if ispc && isequal(get(hObject,'BackgroundColor'),
get(0,'defaultUicontrolBackgroundColor'))
   set(hObject,'BackgroundColor','white');
end

function pixelSize_CreateFcn(hObject, eventdata, handles)
% hObject    handle to pixelSize (see GCBO)
% eventdata  reserved - to be defined in a future version of MATLAB
% handles    empty - handles not created until after all CreateFcns called

% Hint: edit controls usually have a white background on Windows.
%       See ISPC and COMPUTER.
if ispc && isequal(get(hObject,'BackgroundColor'),
get(0,'defaultUicontrolBackgroundColor'))
   set(hObject,'BackgroundColor','white');
end

function cartThresh_CreateFcn(hObject, eventdata, handles)
% hObject    handle to cartThresh (see GCBO)
% eventdata  reserved - to be defined in a future version of MATLAB
% handles    empty - handles not created until after all CreateFcns called

% Hint: edit controls usually have a white background on Windows.
%       See ISPC and COMPUTER.
if ispc && isequal(get(hObject,'BackgroundColor'),
get(0,'defaultUicontrolBackgroundColor'))
   set(hObject,'BackgroundColor','white');
end

function boneThresh_CreateFcn(hObject, eventdata, handles)
% hObject    handle to boneThresh (see GCBO)
% eventdata  reserved - to be defined in a future version of MATLAB
% handles    empty - handles not created until after all CreateFcns called

% Hint: edit controls usually have a white background on Windows.
%       See ISPC and COMPUTER.
if ispc && isequal(get(hObject,'BackgroundColor'),
get(0,'defaultUicontrolBackgroundColor'))
   set(hObject,'BackgroundColor','white');
end

function minThick_CreateFcn(hObject, eventdata, handles)
% hObject    handle to minThick (see GCBO)
% eventdata  reserved - to be defined in a future version of MATLAB
% handles    empty - handles not created until after all CreateFcns called
```

```
% Hint: edit controls usually have a white background on Windows.
%       See ISPC and COMPUTER.
if ispc && isequal(get(hObject,'BackgroundColor'),
get(0,'defaultUicontrolBackgroundColor'))
   set(hObject,'BackgroundColor','white');
end

function fileNum_CreateFcn(hObject, eventdata, handles)
% hObject    handle to fileNum (see GCBO)
% eventdata  reserved - to be defined in a future version of MATLAB
% handles    empty - handles not created until after all CreateFcns called

% Hint: edit controls usually have a white background on Windows.
%       See ISPC and COMPUTER.
if ispc && isequal(get(hObject,'BackgroundColor'),
get(0,'defaultUicontrolBackgroundColor'))
   set(hObject,'BackgroundColor','white');
end

function fitsTable_CreateFcn(hObject, eventdata, handles)
% hObject    handle to fitsTable (see GCBO)
% eventdata  reserved - to be defined in a future version of MATLAB
% handles    empty - handles not created until after all CreateFcns called

% Hint: edit controls usually have a white background on Windows.
%       See ISPC and COMPUTER.
if ispc && isequal(get(hObject,'BackgroundColor'),
get(0,'defaultUicontrolBackgroundColor'))
   set(hObject,'BackgroundColor','white');
end
```

APPENDIX C. CORONAL EPIC-UCT CARTILAGE, SUBCHONDRAL BONE, AND LESION VOLUME DATA FROM CHAPTER 3

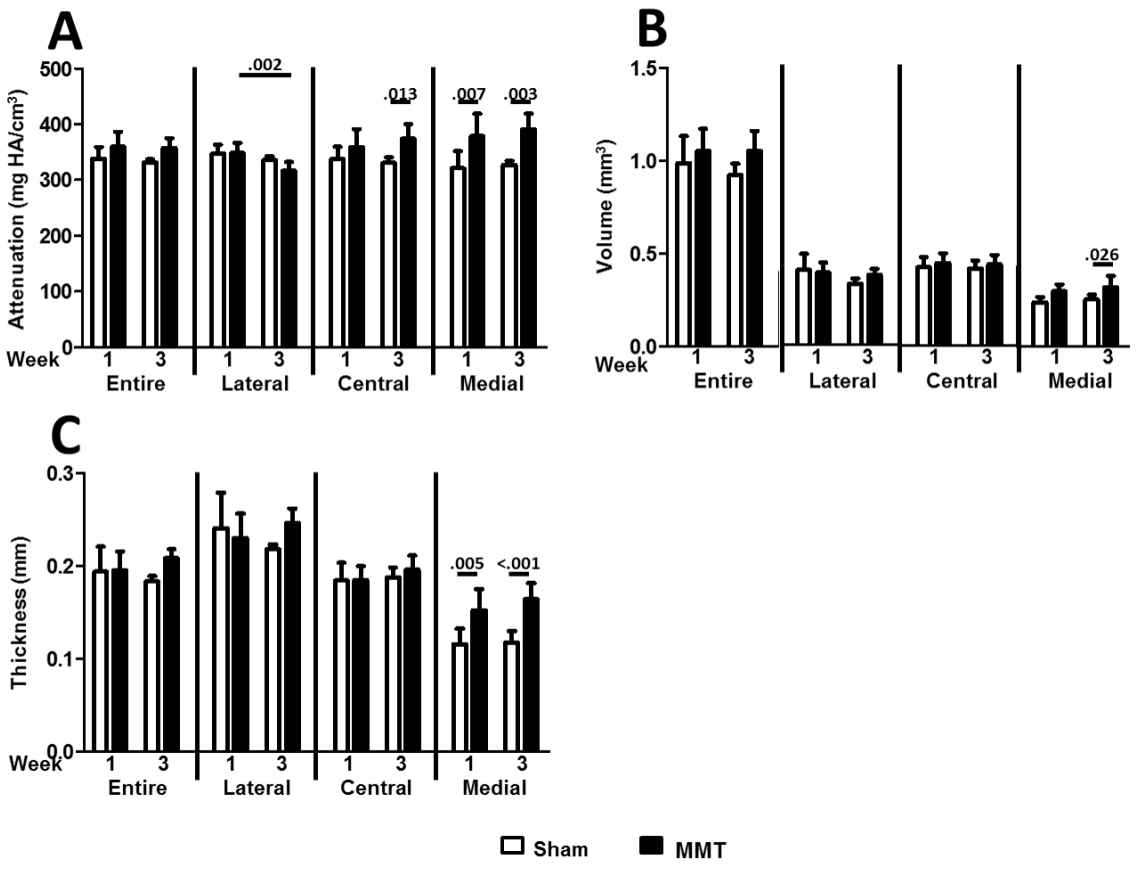

Figure C.8.1: EPIC-µCT cartilage parameters in the coronal slice method of analysis – attenuation (A), volume (B), and thickness (C) in the coronal slice method of analysis. Data are grouped by location (entire medial tibial plateau and lateral, central, and medial thirds thereof), time point (one- or three-weeks post-surgery), and surgery group (sham or medial meniscus transection {MMT}). Data shown as mean ± 95% confidence interval and significance was determined using two-way ANOVAs with Bonferroni post-hoc tests. n = 7-8.

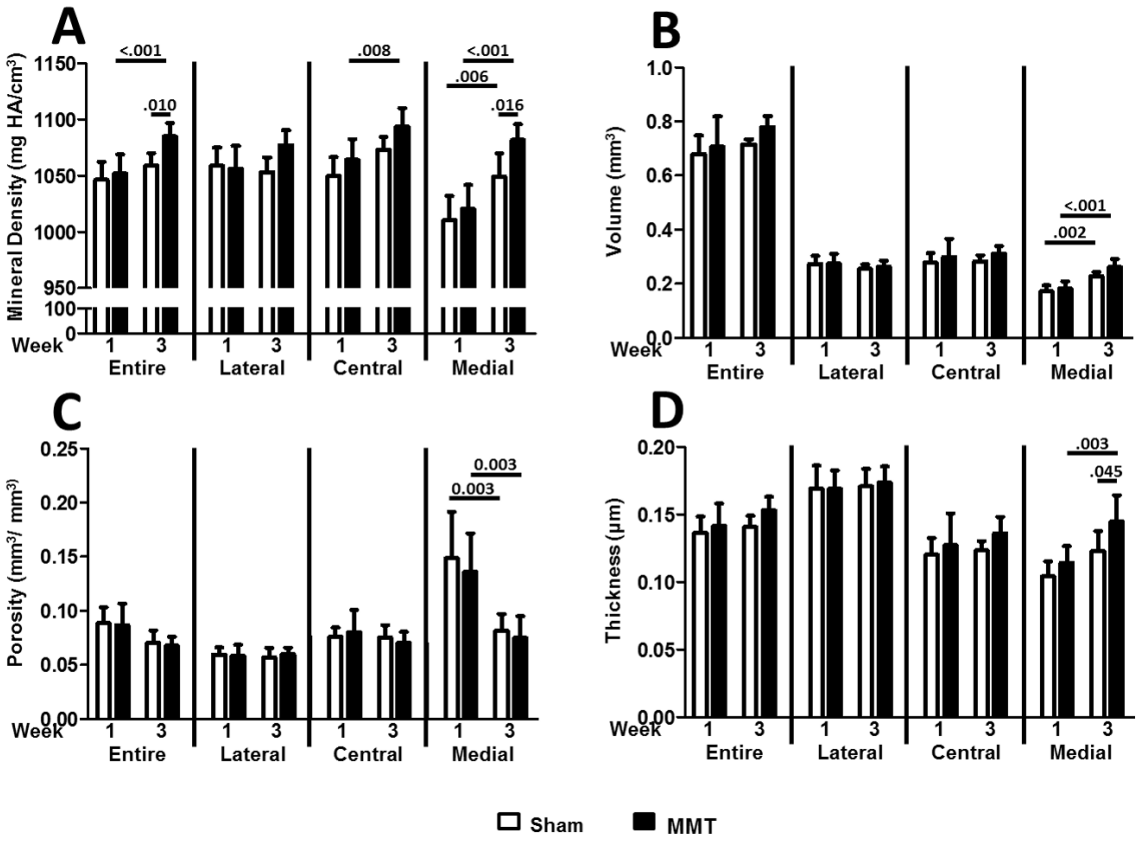

Figure C.8.2: EPIC-µCT subchondral plate parameters in the coronal slice method of analysis – mineral density (A), volume (B), porosity (C), and thickness (D) in the coronal slice method of analysis. Data are grouped by location (entire medial tibial plateau and lateral, central, and medial thirds thereof), time point (one- or three-weeks post-surgery), and surgery group (sham or medial meniscus transection {MMT}). Data shown as mean ± 95% confidence interval and significance was determined using two-way ANOVAs with Bonferroni post-hoc tests. n = 7-8.

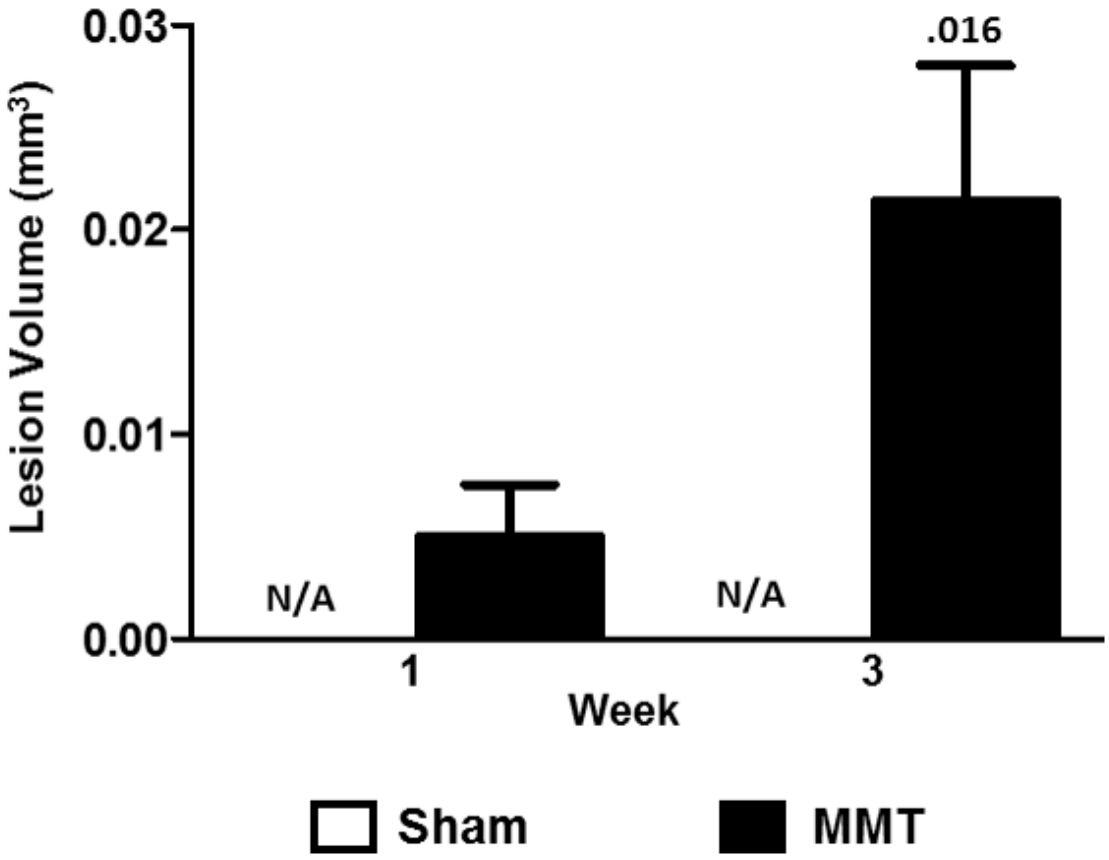

Figure C.8.3: EPIC-µCT lesion volume in the coronal slice method of analysis. Data shown as mean ± 95% confidence interval. n = 7-8. Significance was determined using from Wilcoxon signed rank test comparing if lesion volumes are significantly different from 0.000mm^3.

APPENDIX D. INTRA-ARTICULAR DELIVERY OF MICRONIZED DEHYDRATED HUMAN AMNION/CHORION MEMBRANE REDUCES DEGENERATIVE CHANGES IN OSTEOARTHRITIC JOINTS

The following paper contains data from a study that was designed and started by Tanu Thote, PhD. Her graduation necessitated that I complete the study and manuscript. The preliminary data was already included in her dissertation so it is contained here in the appendices rather than in the main body of my dissertation.

9.1 Introduction

Osteoarthritis (OA) is a leading cause of chronic disability in the US[163] and is estimated to affect over 13% of adults in the US[164]. OA is a complex disease characterized by various morphological and compositional changes in the joint including cartilage surface erosion, loss of proteoglycans, lesion and osteophyte formation, and synovial inflammation[165]. The current standard of therapy is targeted towards symptomatic relief in the form of non-steroidal anti-inflammatory drugs, steroid injections, viscosupplementation, and eventual total knee replacement[166]. A variety of disease modifying OA drugs (DMOADs) have been tested in clinical trials though none have shown a clear therapeutic benefit to date[167]–[169]. Despite this extensive research on potential DMOADs, OA remains a disease without approved and efficacious treatment options.

Extracellular matrix (ECM) therapies are under development for various regenerative medicine applications including wound healing, muscle loss, and periodontal applications[170]–[172]. One such therapy is amnion membrane derived from donated placentae. Amnion has been shown to possess anti-inflammatory properties, display low immunogenicity, and promote wound healing while inhibiting scar formation[112]–[114]. This tissue has been previously used in the clinic for applications such as repairing tendons and corneal defects[173]–[178].

A dehydrated preparation of human amnion/chorion membrane (dHACM) has been developed using the PURION® process, which maintains bioactive components following devitalization and dehydration of the tissue (US Patent 8,357,403-Placenta Tissue Grafts. US Patent 8,372,437-Placenta Tissue Grafts. US Patent 8,409,626-Placenta Tissue Grafts). dHACM has been previously shown to retain numerous growth factors such as basal fibroblast growth factor (bFGF), transforming growth factor β(TGFβ) and platelet derived growth factor (PDGF), as well as cytokines and tissue inhibitors of metalloproteinases (TIMPs)[44], [111], [123].

In a previous study, we demonstrated the therapeutic potential of a micronized, injectable version of dHACM (μ-dHACM; EpiFix® Injectable, MiMedx Group, Inc. Marietta, GA) to slow post-traumatic joint degeneration, by testing its efficacy in a pre-clinical rat OA model. Articular cartilage changes were analyzed via equilibrium partitioning of an ionic contrast agent micro-computed tomography (EPIC-μCT). A single intra-articular injection of μ-dHACM administered 24 hours after surgical injury inhibited lesion formation and reduced cartilage proteoglycan loss in the widely used rat medial meniscal transection (MMT) model[40]. While this previous study demonstrated ameliorated OA development

at three weeks following surgery with acute delivery of a micronized amnion ECM treatment, critical issues such as the duration of therapeutic effect and the potential to treat joints with established OA have yet to be evaluated.

In the present study, we examined both the longer-term effects (six-weeks post-surgery) of immediate delivery of µ-dHACM in the MMT model and the effects of a delayed injection, where µ-dHACM was injected three-weeks post-MMT surgery. As has been shown in previous work[3], [40], [99], features consistent with OA progression are consistently developed by three-weeks post-surgery in the MMT model, hence treating at this time point rather than acutely is more relevant to clinical OA, i.e. a patient typically presents with symptoms and is treated after joint damage and disease progression have begun.

The objective of the present study was to characterize the longer-term effects of immediate delivery (24-hours post-surgery) of a micronized amnion ECM treatment and to determine whether this treatment could reduce the progression of established OA as evaluated by EPIC-µCT and histology. It was hypothesized that the duration of therapeutic effect of acute µ-dHACM treatment would extend to the six-week endpoint and that delayed injection, administered three weeks after induction of OA, would attenuate further joint degeneration in the rat MMT model.

9.2 Materials and Methods

9.2.1 Preparation of µ-dHACM

µ-dHACM was manufactured using the proprietary PURION® process and is compliant with the American Association of Tissue Banks' regulations for donor tissues (MiMedx

Group, Inc. Marietta, GA). This process produces a dehydrated, devitalized amnion and chorion tissue graft which is then sterilized and micronized.

9.2.2 Surgical Methods

The Georgia Institute of Technology IACUC approved experimental procedures for these *in vivo* studies. Weight matched adult male Lewis rats (Charles River, Wilmington, MA) weighing 300-325g were acclimated for 1 week after receipt. The animals were anesthetized with isoflurane and given sustained-released buprenorphine injections. The skin over the medial aspect of the left femoro-tibial joint was shaved and aseptically prepared. For the MMT surgery, the medial collateral ligament was exposed by blunt dissection and transected to reflect the meniscus toward the femur. The joint space was visualized, and a full thickness cut was made through the meniscus at its narrowest point[48]. For sham surgeries (n=7), the medial collateral ligament was exposed and transected but the meniscus was not transected. The muscle was closed with 4.0 Vicryl sutures and the skin stapled using wound clips.

The MMT animals received an intra-articular injection at 24-hours (acute treatment; n=7) or three-weeks (delayed treatment; n=5) post-surgery of 50 µL of µ-dHACM (EpiFix® Injectable, MiMedx Group Inc. Marietta GA). µ-dHACM was resuspended in saline at 80mg/mL and injected into the articular joint space using a 25-gauge needle (BD, Franklin Lakes, NJ). As a control, separate MMT animals received an intra-articular injection of 50 µL saline at three-weeks post-surgery (n=6). All animals were euthanized at six-weeks post-surgery via CO_2 inhalation.

9.2.3 EPIC-µCT Analysis of Articular Cartilage and Subchondral Bone

EPIC-μCT was used to quantitatively evaluate articular cartilage structure, composition and subchondral bone as described previously[3], [69]. Dissected tibiae were immersion fixed in 10% neutral buffered formalin for 48 hours then stored in 70% ethanol (v/v) until ready for scanning. Immediately prior to scanning, tibiae were patted dry and then immersed in 2 ml of 30% Hexabrix™ 320 contrast agent (Covidien, Hazelwood, MO) and 70% PBS at 37°C for 30 minutes[63], [65]. Samples were placed in covered sample chambers and scanned in air using a μCT 40 (Scanco Medical, Brüttisellen, Switzerland) at 45 kVp, 177 μA, 200 ms integration time, a voxel size of 16 μm, and with a scan time of ~26 min[65]. Raw data were automatically reconstructed to 2D grayscale tomograms. These were orthogonally transposed to yield sagittal sections for cartilage and subchondral bone analysis and coronal sections for osteophyte analysis. Segmentation for all EPIC-μCT analyses was performed using a semi-automatic contouring method that uses global thresholds (based on visual inspection and attenuation histograms) and Gaussian filtering (sigma = 1.00, support = 1). Direct distance transformation algorithms were used to quantify 3D thickness[65], [179], [180].

For cartilage analysis, sagittal sections were evaluated in the medial third of the medial tibial plateau (Figure D.9.1.A) and the air-cartilage and cartilage-bone thresholds for the analysis were 179 and 740 mg hydroxyapatite per cubic centimeter (mg HA/cm^3), respectively. Outcome measures included average articular cartilage attenuation and thickness. Cartilage attenuation is a quantitative parameter that has been demonstrated to be inversely proportional to sulfated glycosaminoglycan (sGAG) content[63], [66]. Degraded cartilage has a lower sGAG content and therefore, after incubation in Hexabrix, a higher contrast agent content and higher attenuation values[65]. Subchondral bone was

also analyzed in the medial third region of the medial tibial plateau with thresholds of 740-3047 mg HA/cm^3 and mineral density and thickness were calculated.

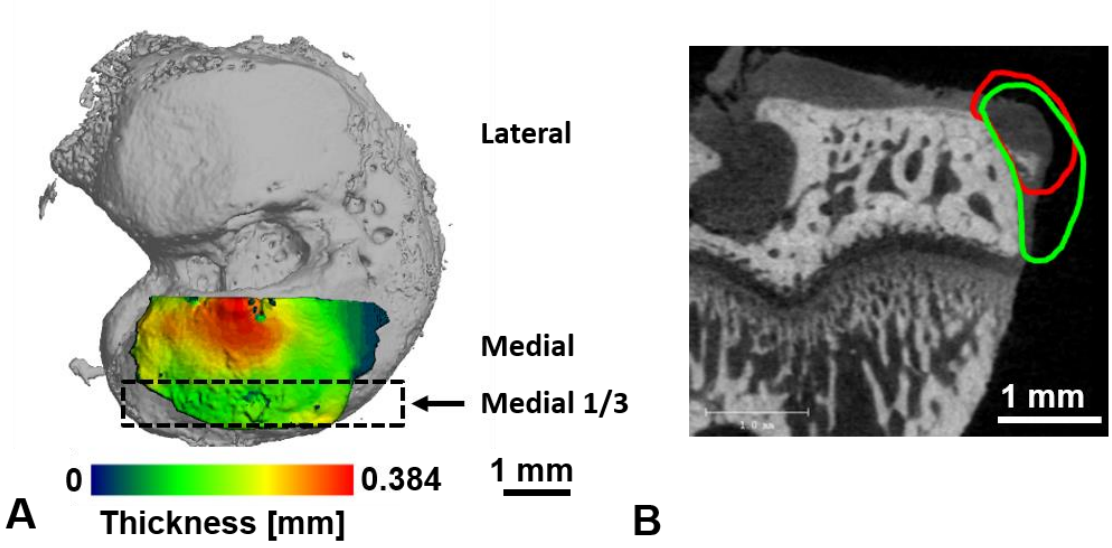

Figure D.9.1: Representative figures illustrating evaluation areas. A. Medial third of medial tibial plateau indicated by black rectangle. B. Representative image of an osteophyte observed on the tibia in the rat medial meniscal tear model with volumes of interest for cartilage volume (red) and mineralized volume (green)

Coronal sections were used to analyze osteophytes, defined as a thickening on the medial tibial margin[99] (Figure D.9.1.B). The osteophyte cartilage volume was measured in volumes of interest that excluded peripheral soft tissue because the soft tissue has similar x-ray attenuation as cartilage. Threshold values of 179-670 mg HA/cm^3 were used to segment the cartilage from air and bone. The osteophyte mineralized volume measurements were made in volumes of interest that did include the peripheral soft tissue, and the mineralized tissue was segmented from air, cartilage, and the soft tissue using threshold values of 670-3047 mg HA/cm^3. A lower cartilage-bone threshold was used in the osteophyte analysis compared to the previous cartilage and subchondral bone analyses

because the newly mineralized tissue in the osteophytes has lower mineral density than subchondral cortical bone.

9.2.4 Articular Cartilage Surface Roughness and Lesion Area

For surface roughness measurements, sequential 2D grayscale images of sagittal slices of the medial third of the tibial plateau were imported into MATLAB® (MathWorks, Natick, MA). A custom built algorithm, using the same global thresholds as the previous cartilage analysis to separate the bone and cartilage surfaces from each other and the surrounding air, scanned each image sequentially to create a 3D digital representation of the cartilage and bone surfaces[181]. The cartilage surface was fit with a 3D polynomial surface that was fourth order along the ventral/dorsal axis and second order along the medial/lateral axis. The surface roughness was then calculated as the root mean square of the differences between the cartilage and polynomial surfaces. Exposed subchondral bone was calculated as a measure of cartilage lesion area by summing the total area where the bone and cartilage surfaces were separated by less than 2 pixels (32 μm). This 2-pixel cutoff was chosen based off the 2D images of the lesions and accounts for the partial volume effects that occur at the interface of high and low density materials in μCT imaging.

9.2.5 Histology

Following EPIC-μCT scanning of the tibiae, tibiae and femora were decalcified in Cal-Ex II (Thermo Fisher Scientific, Waltham, MA) on a shaker plate for 7-8 days. Dehydrated samples were routinely processed into paraffin embedded blocks. Sections were cut at 5μm thickness and sections were stained with hematoxylin and eosin (H&E).

9.2.6 *Statistical analysis*

All quantitative data were expressed as mean ± 95% confidence interval of the mean. All joint parameters between groups were evaluated using one factor (treatment) ANOVA with Tukey's test for post-hoc analysis except for the exposed bone parameter. Exposed bone was analyzed using the nonparametric Kruskal-Wallace one-way analysis of variance with Dunn's post-hoc analysis because this parameter was not normally distributed for all groups. Statistical significance was set at $p < 0.05$. All data were analyzed using GraphPad Prism software version 7.0 (GraphPad Software, Inc., La Jolla, CA).

9.3 Results

EPIC-μCT analyses at six-weeks post-surgery revealed significant differences in articular cartilage and subchondral bone structure and composition among the experimental groups. Representative sagittal cuts from 3D contrast-enhanced cartilage x-ray attenuation maps show higher attenuation (i.e. lower sGAG content) of cartilage for the MMT + saline treatment (saline) and MMT + 24-hour μ-dHACM treatment (acute treatment) groups compared to sham and MMT + 3-week μ-dHACM treatment (delayed treatment) groups (Figure D.9.2, red = high attenuation/low sGAG content, green = low attenuation/high sGAG content). Quantitative analysis of 3D EPIC-μCT images within the medial third of the medial tibial plateau revealed significantly lower cartilage attenuation in sham and delayed treatment groups compared to saline and acute treatment groups, indicating higher sGAG content in sham and delayed treatment groups (Figure D.9.3.A). Cartilage thickness was significantly lower in sham and delayed treatment groups compared to saline and acute

treatment groups (Figure D.9.3.B). In contrast, no significant difference in cartilage attenuation or thickness was observed between the sham and delayed treatment groups. Subchondral bone mineral density was significantly higher in saline, acute treatment, and delayed treatment groups compared to sham while the delayed treatment group had significantly lower mineral density compared to the acute treatment group (Figure D.9.3.C). Only the acute treatment group had significantly thicker subchondral bone than sham group (Figure D.9.3.D).

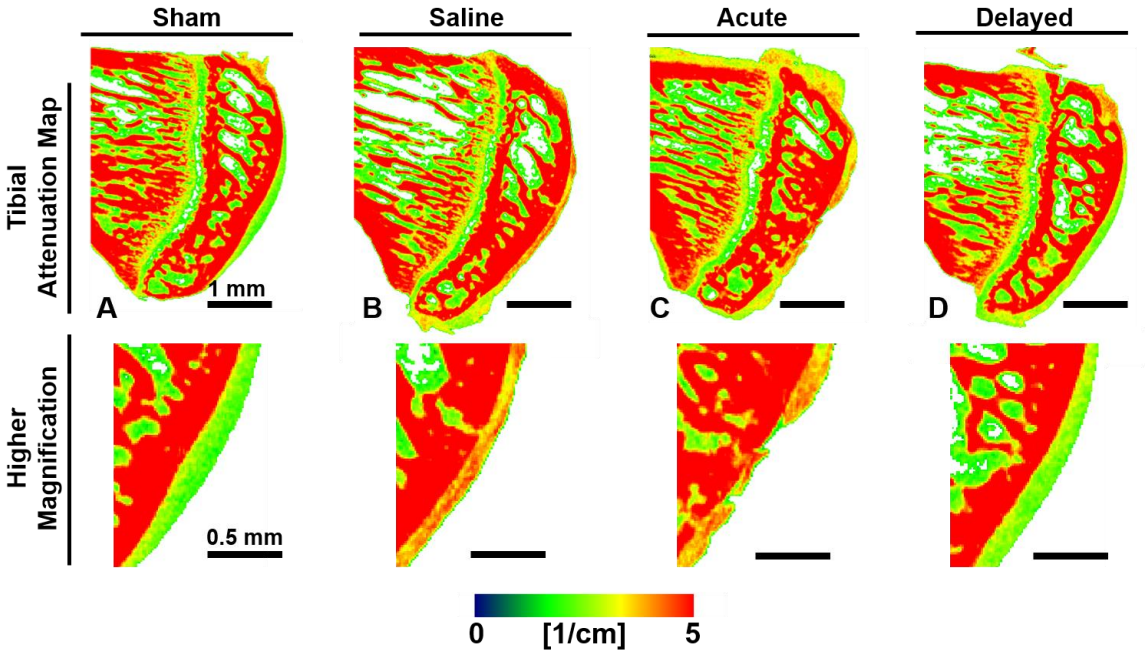

Figure D.9.2: Representative medial tibial cartilage attenuation maps. The maps show lower attenuation in sham and delayed treatment samples. Pseudocolor attenuation bar at bottom indicates red as high attenuation and green as low attenuation. A. Sham sample displays smooth cartilage surface with green color indicating healthy sulfated glycosaminoglycan (sGAG) content. B. Saline treatment sample displays high attenuation indicating lower sGAG content. C. Sample receiving acute treatment (24-hours post-surgery) with micronized dehydrated human amnion/chorion membrane (μ-dHACM) displays high attenuation and the beginning of lesion development D. Sample with delayed treatment (three-weeks post-surgery) with μ-dHACM displays green central portion indicating healthy sGAG content. Scale bars = 1mm; higher magnification scale bars = 0.5 mm

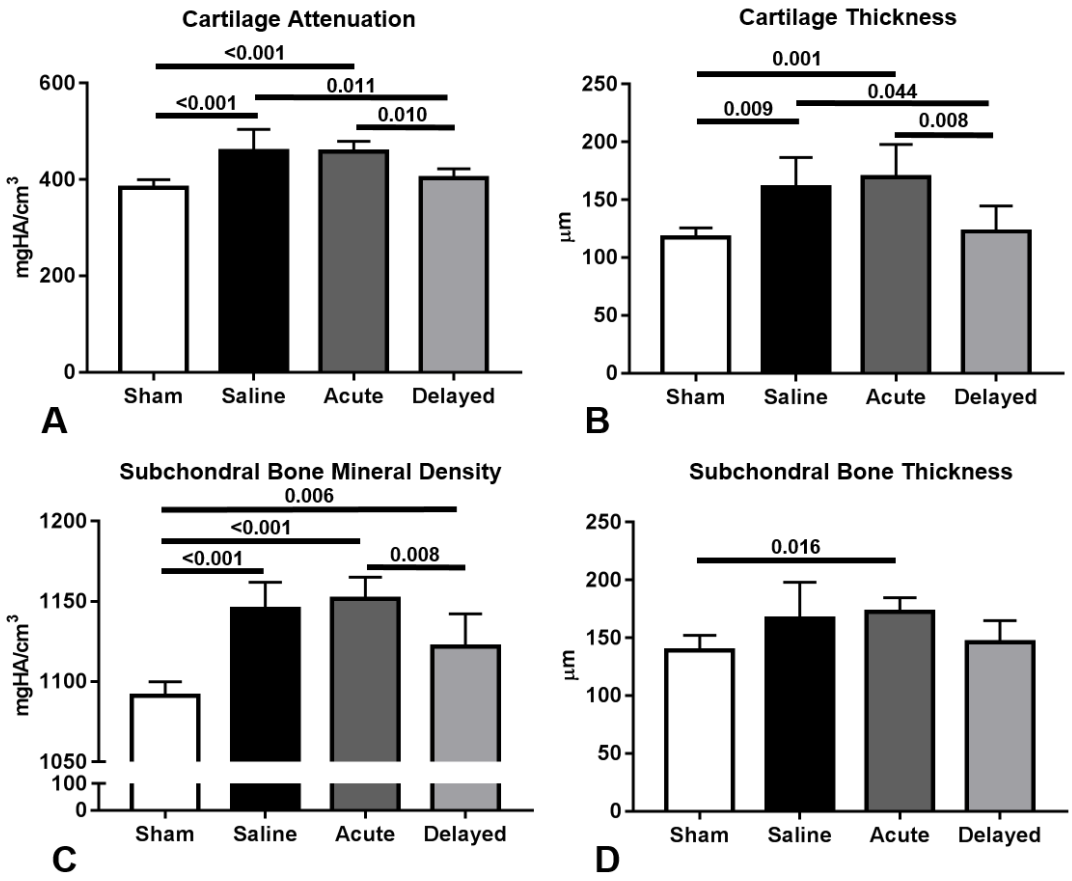

Figure D.9.3: EPIC-µCT cartilage and subchondral bone parameters. Delayed treatment (three-weeks post-surgery) of micronized dehydrated human amnion/chorion membrane (µ-dHACM) results in lower cartilage attenuation and thickness and subchondral bone mineral density in the medial third of the medial tibial plateau compared to saline and acute µ-dHACM treatment (24-hours post-surgery) groups. A,B. Cartilage attenuation and thickness were significantly higher than sham in the saline and acute µ-dHACM treatment groups, while both parameters in the delayed treatment group were significantly lower than saline and acute treatment groups. C. Subchondral bone mineral density was significantly higher than sham in all other groups while mineral density in the delayed treatment group was significantly lower than acute treatment groups. Data shown as mean ± 95% confidence interval. n = 5-7.

Surface roughness and exposed bone area were calculated using a custom program. Analysis of the medial third of the medial tibial plateau showed an increase in surface roughness in saline and acute treatment groups compared to sham and delayed treatment (Figure D.9.4.A). Exposed bone area was calculated as a measure of cartilage lesion size

and was significantly higher in the saline and acute treatment groups compared to sham while the delayed treatment group had significantly lower exposed bone area compared to the acute delivery group (Figure D.9.4.B).

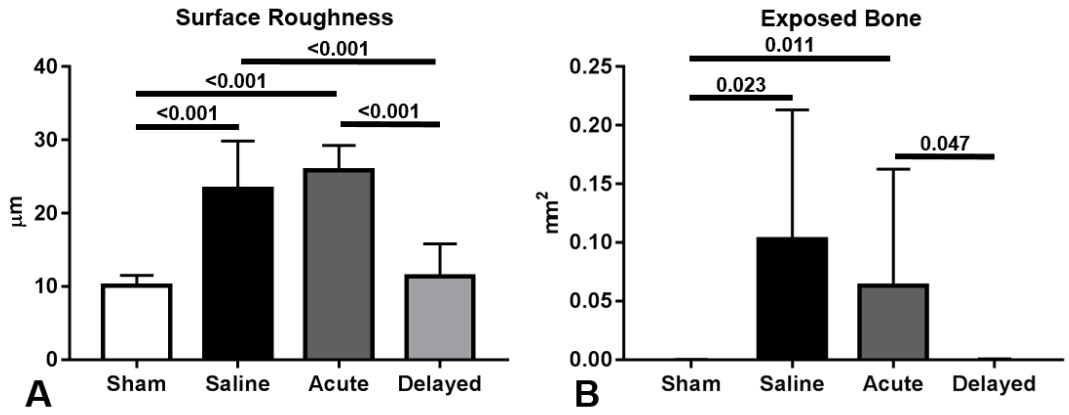

Figure D.9.4: Evaluation of surface roughness and exposed bone using custom program. A. Cartilage surface roughness was significantly higher than sham in the saline and acute (24-hours post-surgery) micronized dehydrated human amnion/chorion membrane (µ-dHACM) treatment groups, while surface roughness in the delayed µ-dHACM treatment (three-weeks post-surgery) group was significantly lower than saline and acute treatment groups. B. Exposed bone was significantly greater in saline and acute treatment groups compared to the sham, and significantly less in delayed treatment compared to acute treatment. Data shown as mean ± 95% confidence interval. n = 5-7.

Osteophytes are a thickening and partial mineralization of cartilage tissue at the marginal edge of the medial tibial plateau. The cartilage and mineralized tissue volume along the medial edge of the tibial plateau were quantified in 3D using coronal EPIC-µCT images to quantify thickening from osteophyte formation. Osteophyte cartilage volume was significantly higher in the saline and acute treatment groups compared to sham (Figure D.9.5.A). Osteophyte cartilage volume was not significantly increased in the delayed treatment group relative to sham controls. Similar results were observed for osteophyte mineralized volume with a significant increase in the saline and acute treatment groups

compared to sham (Figure D.9.5.B). Osteophyte cartilage and mineralized volumes were not significantly increased in the delayed treatment group compared to the sham controls and osteophyte cartilage volume was significantly less in the delayed treatment group compared to the acute treatment group.

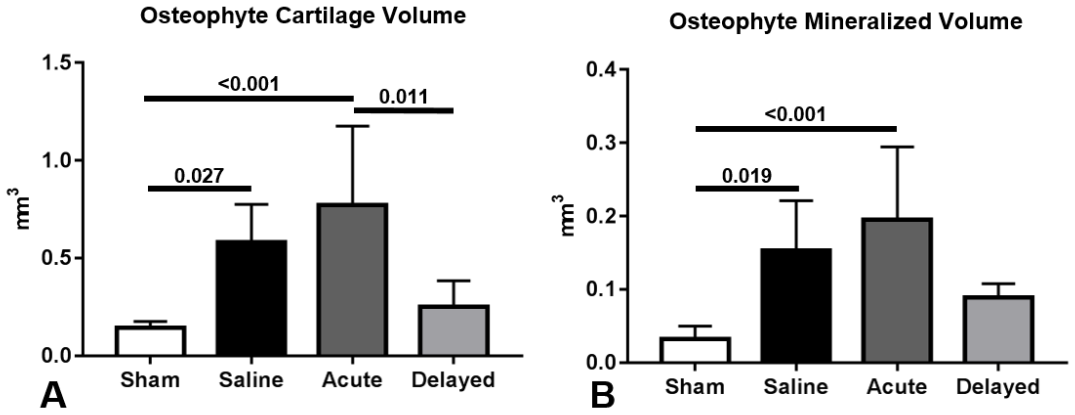

Figure D.9.5: EPIC-µCT osteophyte parameters. Saline and acute (24-hour post-surgery) micronized dehydrated human amnion/chorion membrane (µ-dHACM) treatment groups display osteophyte progression compared to sham. A. Osteophyte cartilage volume was significantly greater in saline and acute treatment groups compared to the sham group and significantly less in the delayed µ-dHACM treatment (three-weeks post-surgery) group compared to the acute treatment group. B. Marginal mineralized volume was significantly greater in saline and acute treatment groups compared to the sham group. Data shown as mean ± 95% confidence interval. n = 5-7.

Histology was performed on tibiae and femora at the six-week time point. µ-dHACM was not visible in the synovium surrounding the femur (data not shown). Representative images of coronal tibial sections showed degradation of cartilage surface and development of osteophytes in the saline (Figure D.9.6.C&D) and acute treatment groups (Figure D.9.6.E&F). The sham group demonstrated smooth cartilage surfaces with no osteophyte development (Figure D.9.6.A&B). The delayed treatment group demonstrated smooth cartilage surfaces and reduced osteophyte development (Figure D.9.6.G&H).

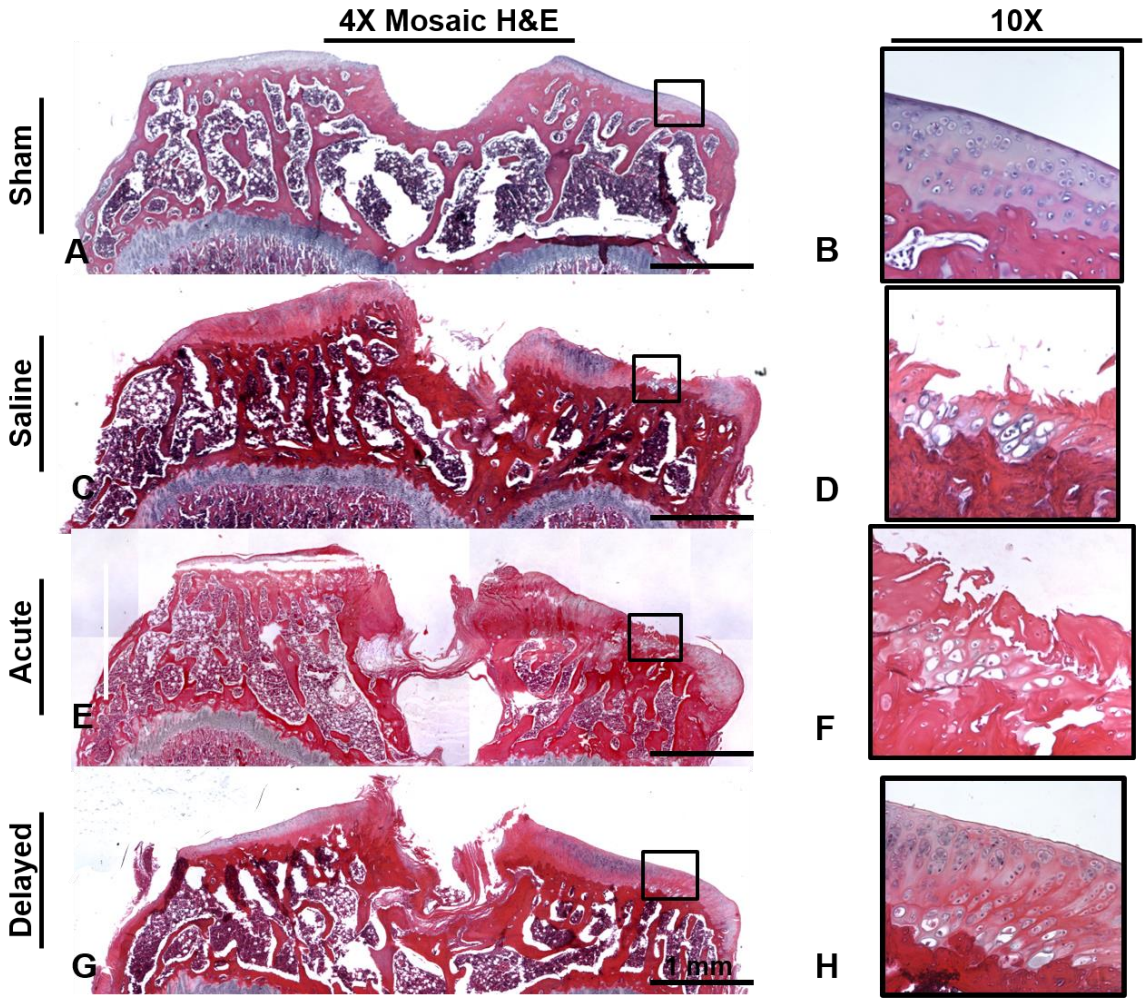

Figure D.9.6: Representative H&E histology images for the tibiae. A–B. Sham sample showed no cartilage damage. C-D. Saline sample exhibited cartilage surface damage on the medial plateau indicated by fibrillations and lesions and osteophyte development indicated by cartilage thickening on the medial edge of the plateau. E-F. Acute micronized dehydrated human amnion/chorion membrane (μ-dHACM) treatment (24-hour post-surgery) did not protect against cartilage damage or osteophyte development as surface fibrillations and cartilage thickening are still observed. G-H. Delayed μ-dHACM treatment protected cartilage against damage as cartilage lesions are not observed. Delayed treatment also reduced osteophyte development as indicated by the reduced cartilage thickening. Scale bar in 4x mosaics are equal to 1 mm.

9.4 Discussion

ECM based therapeutics have shown promise for multiple therapeutic applications and are currently being investigated as clinical treatment options for OA[142]. In a previous study, we demonstrated the therapeutic benefit of a single intra-articular injection of µ-dHACM (24 hours post-surgery) in the rat MMT model after three weeks[40]. The purpose of the present study was to evaluate whether the same single acute treatment with µ-dHACM would provide a protective effect at six-weeks post-surgery and whether the delivery of a single treatment would have a beneficial effect once disease had been established.

It was hypothesized that an acute treatment of µ-dHACM at 24-hours post-surgery would show sustained therapeutic benefit at six-weeks post-surgery but this was not the case as illustrated by the EPIC-µCT results. The lack of a chondro-protective effect of the single 24 hour µ-dHACM injection could be attributed to the unrepaired destabilization of the joint that resulted in continued disease development throughout the six-week study period. The standard end point for therapeutic evaluation in the MMT model is three-weeks post-surgery and few studies of potential therapeutics have been extended to six weeks[182]–[184].

In previous MMT studies, OA-like symptoms such as lower proteoglycan content and lesion formation were already present in the medial tibial plateau at three weeks[3], [40], [48]; therefore, the delayed treatment at three weeks was intended to be more representative of the clinical scenario, where the patient is seeking treatment after disease symptoms have already developed. The delayed intra-articular injection of µ-dHACM delivered at three-weeks post-MMT surgery, when the rat tibial plateau has already demonstrated significant disease progression[3], [48], resulted in reduced disease progression in the MMT model at the six week time point. Lower cartilage attenuation and surface roughness were observed

in the delayed treatment group compared to saline controls. Delayed treatment also reduced subchondral bone sclerosis and osteophyte formation compared to the acute treatment. A recent study by Raines et al., where MMT animals were treated two weeks after surgery with a particulate amniotic membrane and umbilical cord matrix, also showed reduced disease progression at six weeks post-surgery compared to controls[116]. Taken together, the Raines study and this present study suggest that amniotic membrane based treatments could provide a therapeutic benefit even when injected into joints with established osteoarthritis-like pathology.

In the previous study with a three week end point, articular surface fibrillation, lesion number and lesion volume were used as indicators of reduced cartilage damage in animals receiving an intra-articular injection at 24 hours post-surgery compared to the saline control group[40]. In this six-week study, more widespread cartilage lesions necessitated the use of exposed bone area as an alternative indicator of lesion size as this metric is less prone to user bias for samples with larger lesions compared with calculating lesion volume.

We were not able to identify µ-dHACM in the synovium at six weeks by histology. In a previous study, µ-dHACM particles were still present in the synovium three weeks after injection but appeared reduced in size[40]. Taken together, this study and our previous work indicate that the µ-dHACM particles are rapidly sequestered within a few days into the synovial membrane where they appear to be fully remodeled between 3 and 6 weeks.

While the mechanism by which micronized amnion ECM produces a therapeutic effect are not clearly understood, the growth factor composition of µ-dHACM, including bFGF, TGF-beta, and TIMPs, could be a contributory factor[44], [123]. Osteophyte formation

results from endochondral ossification brought about by alterations in bone turnover[185], [186] and can be attenuated by bFGF[187]. In addition, FGF protein signaling, among others, determines the rate of chondrocyte proliferation[121]. TGF-beta has previously been implicated in proliferation of perichondrium derived chondro-progenitor cells[188]. Moreover, matrix metalloproteinase inhibitors such as TIMPs have been implicated in reducing subchondral bone sclerosis and cartilage damage in osteoarthritis models[189].

Other potential mechanisms of micronized amnion ECM action could involve its potential as a cell recruiter and substrate. Amnion ECM has been shown to induce migration of mesenchymal stem cells and recruit mesenchymal progenitor cells to implantation sites[44]. Amniotic membrane has been shown to be a suitable substrate to culture cells and also to amplify chondrocytes *in vitro*[126]. These properties, in addition to the micronized particle dimensions which may help prevent rapid clearance from the joint, could be contributing towards the observed therapeutic effect. Further research is needed to understand how amnion ECM influences the joint, including the development of suitable *in vivo* and *in vitro* evaluation methods to examine cellular and genetic responses.

Micronized amnion ECM has previously been demonstrated to slow the development of post-traumatic OA following meniscal injury in the rat MMT model. This study extended the previous work to determine that the duration of acute treatment benefit is transitory in the face of continued joint instability. However, contrast-enhanced μCT analysis further revealed that a single intra-articular injection of micronized amnion ECM at three-weeks post MMT surgery, after OA features have developed, significantly slowed and partially reversed OA progression. This study therefore supports continued investigation of

micronized amnion as a promising potential future clinical intervention for OA disease modification.

REFERENCES

[1] National Institute for Health and Care Excellence, "Osteoarthritis: Care and management in adults," 2014. [Online]. Available: http://www.nice.org.uk/guidance/cg177/resources/guidance-osteoarthritis-pdf.

[2] R. C. Lawrence, D. T. Felson, C. G. Helmick, L. M. Arnold, H. Choi, R. a Deyo, S. Gabriel, R. Hirsch, M. C. Hochberg, G. G. Hunder, J. M. Jordan, J. N. Katz, H. M. Kremers, and F. Wolfe, "Estimates of the prevalence of arthritis and other rheumatic conditions in the United States. Part II.," *Arthritis Rheum.*, vol. 58, no. 1, pp. 26–35, Jan. 2008.

[3] T. Thote, A. S. P. Lin, Y. Raji, S. Moran, H. Y. Stevens, M. Hart, R. Kamath, R. E. Guldberg, and N. J. Willett, "Localized 3D analysis of cartilage composition and morphology in small animal models of joint degeneration.," *Osteoarthr. Cartil.*, vol. 21, no. 8, pp. 1132–41, Jun. 2013.

[4] S. Thysen, F. P. Luyten, and R. J. U. Lories, "Targets, models and challenges in osteoarthritis research," *Dis. Model. Mech.*, vol. 8, no. 1, pp. 17–30, 2015.

[5] K. A. Athanasiou, E. M. Darling, and J. C. Hu, *Articular Cartilage Tissue Engineering*. Morgan & Claypool, 2010.

[6] H. J. Mankin and L. Lippiello, "The Turnover of Adult Rabbit Articular Cartilage," *J. Bone Joint Surg. Am.*, vol. 51, no. 8, pp. 1591–600, 1969.

[7] C. W. Archer, J. McDowell, M. T. Bayliss, M. D. Stephens, and G. Bentley,

"Phenotypic modulation in sub-populations of human articular chondrocytes in vitro," *J. Cell Sci.*, vol. 97 (Pt 2), pp. 361–371, 1990.

[8] B. P. O'Hara, J. P. G. Urban, and A. Maroudas, "Influence of cyclic loading on the nutrition of articular cartilage," *Ann. Rheum. Dis.*, vol. 49, pp. 536–539, 1990.

[9] F. C. Linn and L. Sokoloff, "Movement and Composition of Interstitial Fluid of Cartilage," *Arthritis Rheum.*, vol. 8, no. 4, pp. 481–494, 1965.

[10] F. Guilak, L. A. Setton, and V. B. Kraus, "Structure and Function of Cartilage," in *Principles And Practice Of Orthopaedic Sports Medicine*, W. E. J. Garrett, K. P. Speer, and D. T. Kirkendall, Eds. Philadelphia, PA: Lippincott Williams & Wilkins, 2000.

[11] B. K. Deshmukh and M. E. Nimni, "Isolation and Characterization of Cyanogen Bromide Peptides from the Collagen of Bovine Articular Cartilage," *Biochem. J.*, vol. 133, pp. 615–622, 1973.

[12] D. R. Eyre and J. J. Wu, "Collagen structure and cartilage matrix integrity," *J. Rheumatol.*, vol. 43, pp. 82–85, 1995.

[13] J. M. Clark, "The organisation of collagen fibrils in the superficial zones of articular cartilage," *J. Anat.*, vol. 171, pp. 117–130, 1990.

[14] P. J. Roughley and E. R. Lee, "Cartilage Proteoglycans : Structure and Potential Functions," *Microsc. Res. Tech.*, vol. 28, pp. 385–397, 1994.

[15] E. B. Hunziker, M. Michel, D. Studer, and M. E. Mu, "Ultrastructure of Adult

Human Articular Cartilage Matrix After Cryotechnical Processing," *Microsc. Res. Tech.*, vol. 37, pp. 271–284, 1997.

[16] M. A. MacConaill, "The movements of bones and joints; the mechanical structure of articulating cartilage," *J. Bone Joint Surg. Br.*, vol. 33 B, no. 2, pp. 251–7, 1951.

[17] I. Redler, V. C. Mow, M. L. Zimny, and J. Mansell, "The Ultrastructure and Biomechanical Significance of the Tidemark of Articular Cartilage," *Clin. Orthop. Relat. Res.*, no. 112, pp. 357–62, 1975.

[18] B. K. Jones, C. T. Hung, and G. A. Ateshian, "Biphasic Analysis of Cartilage Stresses in the Patellofemoral Joint," *J. Knee Surg.*, vol. 29, no. 2, pp. 92–98, 2016.

[19] L. A. Setton, W. Zhu, and V. C. Mow, "The Biphasic Poroviscoelastic Behavior of Articular Cartilage: Role of the Surface Zone in Governing the Compressive Behavior," *J. Biomech.*, vol. 26, no. 4/5, pp. 581–592, 1993.

[20] A. Poole, G. Rizkalla, M. Ionescu, A. Reiner, E. Brooks, C. Rorabeck, R. Bourne, and E. Bogoch, "Osteoarthritis in the human knee: a dynamic process of cartilage matrix degradation, synthesis and reorganization," *Agents Actions*, vol. 39, pp. 3–13, 1993.

[21] M. D. Smith and M. D. Wechalekar, "The Synovium," in *Rheumatology*, Sixth., 2014, pp. 27–32.

[22] A. L. Mescher, Ed., "Joints," in *Junqueira's Basic Histology*, 14e ed., New York, NY: McGraw-Hill, 2017.

[23] R. F. Loeser, S. R. Goldring, C. R. Scanzello, and M. B. Goldring, “Osteoarthritis: a disease of the joint as an organ.,” *Arthritis Rheum.*, vol. 64, no. 6, pp. 1697–707, Jun. 2012.

[24] M. Blagojevic, C. Jinks, A. Jeffery, and K. P. Jordan, “Risk factors for onset of osteoarthritis of the knee in older adults: a systematic review and meta-analysis.,” *Osteoarthr. Cartil.*, vol. 18, no. 1, pp. 24–33, Jan. 2010.

[25] T. P. Andriacchi, J. Favre, J. C. Erhart-Hledik, and C. R. Chu, “A Systems View of Risk Factors for Knee Osteoarthritis Reveals Insights into the Pathogenesis of the Disease.,” *Ann. Biomed. Eng.*, vol. 43, no. 2, pp. 376–387, Sep. 2015.

[26] V. B. Kraus, F. J. Blanco, M. Englund, M. a. Karsdal, and L. S. Lohmander, “Call for standardized definitions of osteoarthritis and risk stratification for clinical trials and clinical use,” *Osteoarthr. Cartil.*, pp. 1–9, 2015.

[27] D. J. Hunter, D. Schofield, and E. Callander, “The individual and socioeconomic impact of osteoarthritis.,” *Nat. Rev. Rheumatol.*, pp. 1–5, Mar. 2014.

[28] H. Kotlarz, C. L. Gunnarsson, H. Fang, and J. a. Rizzo, “Insurer and out-of-pocket costs of osteoarthritis in the US: Evidence from national survey data,” *Arthritis Rheum.*, vol. 60, no. 12, pp. 3546–3553, 2009.

[29] J. M. Hootman and C. G. Helmick, “Projections of US prevalence of arthritis and associated activity limitations,” *Arthritis Rheum.*, vol. 54, no. 1, pp. 226–229, 2006.

[30] L. Murphy, T. A. Schwartz, C. G. Helmick, J. B. Renner, G. Tudor, G. Koch, A.

Dragomir, W. D. Kalsbeek, G. Luta, and J. M. Jordan, “Lifetime risk of symptomatic knee osteoarthritis,” *Arthritis Care Res. (Hoboken).*, vol. 59, no. 9, pp. 1207–1213, 2008.

[31] L. Fernandes, K. B. Hagen, J. W. J. Bijlsma, O. Andreassen, P. Christensen, P. G. Conaghan, M. Doherty, R. Geenen, A. Hammond, I. Kjeken, L. S. Lohmander, H. Lund, C. D. Mallen, T. Nava, S. Oliver, K. Pavelka, I. Pitsillidou, J. A. da Silva, J. de la Torre, G. Zanoli, and T. P. M. Vliet Vlieland, “EULAR recommendations for the non-pharmacological core management of hip and knee osteoarthritis.,” *Ann. Rheum. Dis.*, vol. 72, no. 7, pp. 1125–35, 2013.

[32] T. E. McAlindon, R. R. Bannuru, M. C. Sullivan, N. K. Arden, F. Berenbaum, S. M. Bierma-Zeinstra, G. a. Hawker, Y. Henrotin, D. J. Hunter, H. Kawaguchi, K. Kwoh, S. Lohmander, F. Rannou, E. M. Roos, and M. Underwood, “OARSI guidelines for the non-surgical management of knee osteoarthritis,” *Osteoarthr. Cartil.*, vol. 22, no. 3, pp. 363–388, 2014.

[33] J. J. Edwards, M. Khanna, K. P. Jordan, J. L. Jordan, J. Bedson, and K. S. Dziedzic, “Quality indicators for the primary care of osteoarthritis: a systematic review.,” *Ann. Rheum. Dis.*, pp. 1–9, 2013.

[34] N. Taylor, “Nonsurgical Management of Osteoarthritis Knee Pain in the Older Adult,” *Clin. Geriatr. Med.*, vol. 33, no. 1, pp. 41–51, 2017.

[35] C. J. M. Bachmeier, L. M. March, M. J. Cross, H. M. Lapsley, K. L. Tribe, B. G. Courtenay, and P. M. Brooks, “A comparison of outcomes in osteoarthritis patients

undergoing total hip and knee replacement surgery," *Osteoarthr. Cartil.*, vol. 9, no. 2, pp. 137–146, 2001.

[36] L. Shan, B. Shan, D. Graham, and a. Saxena, "Total hip replacement: A systematic review and meta-analysis on mid-term quality of life," *Osteoarthr. Cartil.*, vol. 22, no. 3, pp. 389–406, 2014.

[37] L. Shan, B. Shan, A. Suzuki, F. Nouh, and A. Saxena, "Intermediate and Long-Term Quality of Life After Total Knee Replacement," *J. Bone Joint Surg. Am.*, vol. 97–A, no. 2, pp. 156–168, 2015.

[38] V. K. Aggarwal, N. Goyal, G. Deirmengian, A. Rangavajulla, J. Parvizi, and M. S. Austin, "Revision total knee arthroplasty in the young patient: is there trouble on the horizon?," *J. Bone Joint Surg. Am.*, vol. 96, no. 7, pp. 536–542, 2014.

[39] W. J. Long, C. D. Bryce, C. S. Hollenbeak, R. W. Benner, and W. N. Scott, "Total Knee Replacement in Young, Active Patients: Long-Term Follow-up and Functional Outcome A Concise Follow-up of a Previous Report*," *J. Bone Joint Surg. Am.*, vol. 96, no. 18, p. e159, 2014.

[40] N. J. Willett, T. Thote, A. S. Lin, S. Moran, Y. Raji, S. Sridaran, H. Y. Stevens, and R. E. Guldberg, "Intra-articular injection of micronized dehydrated human amnion/chorion membrane attenuates osteoarthritis development.," *Arthritis Res. Ther.*, vol. 16, no. 1, p. R47, Feb. 2014.

[41] Y. Garfias, V. Zaga-Clavellina, F. Vadillo-Ortega, M. Osorio, and M. C. Jimenez-Martinez, "Amniotic membrane is an immunosuppressor of peripheral blood

mononuclear cells.," *Immunol. Invest.*, vol. 40, no. 2, pp. 183–196, 2011.

[42] a. C. Mamede, M. J. Carvalho, a. M. Abrantes, M. Laranjo, C. J. Maia, and M. F. Botelho, "Amniotic membrane: from structure and functions to clinical applications," *Cell Tissue Res.*, vol. 349, no. 2, pp. 447–458, 2012.

[43] S. Ji, S. Xiao, P. Luo, G. Huang, G. Wang, S. Zhu, M. Wu, and Z. Xia, "An epidermal stem cells niche microenvironment created by engineered human amniotic membrane.," *Biomaterials*, vol. 32, no. 31, pp. 7801–11, Nov. 2011.

[44] T. J. Koob, R. Rennert, N. Zabek, M. Massee, J. J. Lim, J. S. Temenoff, W. W. Li, and G. Gurtner, "Biological properties of dehydrated human amnion/chorion composite graft: Implications for chronic wound healing," *Int. Wound J.*, vol. 10, no. 5, pp. 493–500, 2013.

[45] S. Díaz-Prado, M. E. Rendal-Vázquez, E. Muiños-López, T. Hermida-Gómez, M. Rodríguez-Cabarcos, I. Fuentes-Boquete, F. J. de Toro, and F. J. Blanco, "Potential use of the human amniotic membrane as a scaffold in human articular cartilage repair.," *Cell Tissue Bank.*, vol. 11, no. 2, pp. 183–95, May 2010.

[46] G. Krishnamurithy, P. N. Shilpa, R. E. Ahmad, S. Sulaiman, C. L. L. Ng, and T. Kamarul, "Human amniotic membrane as a chondrocyte carrier vehicle/substrate: in vitro study.," *J. Biomed. Mater. Res. A*, vol. 99, no. 3, pp. 500–6, Dec. 2011.

[47] A. M. Bendele, "Animal models of osteoarthritis," *J. Musculoskelet. Neuronal Interact.*, vol. 1, no. 4, pp. 363–376, 2001.

[48] M. J. Janusz, A. M. Bendele, K. K. Brown, Y. O. Taiwo, L. Hsieh, and S. A. Heitmeyer, “Induction of osteoarthritis in the rat by surgical tear of the meniscus: Inhibition of joint damage by a matrix metalloproteinase inhibitor,” *Osteoarthr. Cartil.*, vol. 10, no. 10, pp. 785–791, 2002.

[49] N. Gerwin, A. M. Bendele, S. Glasson, and C. S. Carlson, “The OARSI histopathology initiative - recommendations for histological assessments of osteoarthritis in the rat.,” *Osteoarthr. Cartil.*, vol. 18 Suppl 3, pp. S24-34, Oct. 2010.

[50] P. C. Pastoureau, E. B. Hunziker, and J.-P. Pelletier, “Cartilage, bone and synovial histomorphometry in animal models of osteoarthritis.,” *Osteoarthr. Cartil.*, vol. 18 Suppl 3, pp. S106-12, Oct. 2010.

[51] P. G. Conaghan, D. J. Hunter, J. F. Maillefert, W. M. Reichmann, and E. Losina, “Summary and recommendations of the OARSI FDA osteoarthritis Assessment of Structural Change Working Group,” *Osteoarthr. Cartil.*, vol. 19, no. 5, pp. 606–610, 2011.

[52] D. J. Hunter, R. D. Altman, F. Cicuttini, M. D. Crema, J. Duryea, F. Eckstein, A. Guermazi, R. Kijowski, T. M. Link, J. Martel-Pelletier, C. G. Miller, T. J. Mosher, R. E. Ochoa-Albíztegui, J. P. Pelletier, C. Peterfy, J. P. Raynauld, F. W. Roemer, S. M. Totterman, and G. E. Gold, “OARSI Clinical Trials Recommendations: Knee imaging in clinical trials in osteoarthritis,” *Osteoarthr. Cartil.*, vol. 23, no. 8, pp. 698–715, 2015.

[53] Y.-X. Wang, “In vivo magnetic resonance imaging of animal models of knee

osteoarthritis," *Lab. Anim.*, vol. 42, no. 3, pp. 246–264, 2008.

[54] M. Marenzana and G. Vande Velde, "Refine, reduce, replace: Imaging of fibrosis and arthritis in animal models," *Best Pract. Res. Clin. Rheumatol.*, vol. 29, pp. 715–740, 2015.

[55] S. Saarakkala, J. Töyräs, J. Hirvonen, M. S. Laasanen, R. Lappalainen, and J. S. Jurvelin, "Ultrasonic quantitation of superficial degradation of articular cartilage.," *Ultrasound Med. Biol.*, vol. 30, no. 6, pp. 783–92, Jun. 2004.

[56] T. Virén, S. Saarakkala, E. Kaleva, H. J. Nieminen, J. S. Jurvelin, and J. Töyräs, "Minimally invasive ultrasound method for intra-articular diagnostics of cartilage degeneration.," *Ultrasound Med. Biol.*, vol. 35, no. 9, pp. 1546–54, Sep. 2009.

[57] H. Niu, Q. Wang, Y. Wang, D. Li, Y. Fan, and W. Chen, "Ultrasonic reflection coefficient and surface roughness index of OA articular cartilage : relation to pathological assessment," *BMC Musculoskelet. Disord.*, vol. 13, no. 34, 2012.

[58] M. Schöne, N. Männicke, M. Gottwald, F. Göbel, and K. Raum, "3-D High-Frequency Ultrasound Improves the Estimation of Surface Properties in Degenerated Cartilage.," *Ultrasound Med. Biol.*, vol. 39, no. 5, pp. 834–44, May 2013.

[59] T. Virén, S. Saarakkala, J. S. Jurvelin, H. J. Pulkkinen, V. Tiitu, P. Valonen, I. Kiviranta, M. J. Lammi, and J. Töyräs, "Quantitative evaluation of spontaneously and surgically repaired rabbit articular cartilage using intra-articular ultrasound method in situ.," *Ultrasound Med. Biol.*, vol. 36, no. 5, pp. 833–9, May 2010.

[60] N. Männicke, M. Schöne, M. Oelze, and K. Raum, “Articular cartilage degeneration classification by means of high-frequency ultrasound.,” *Osteoarthr. Cartil.*, vol. 22, no. 10, pp. 1577–82, Oct. 2014.

[61] T. Virén, S. Saarakkala, V. Tiitu, J. Puhakka, I. Kiviranta, J. S. Jurvelin, and J. Toyras, “Ultrasound Evaluation of Mechanical Injury of Bovine Knee Articular Cartilage Under Arthroscopic Control,” *IEEE Trans. Ultrason. Ferroelectr. Freq. Control*, vol. 58, no. 1, pp. 148–155, 2011.

[62] K. Nishitani, M. Kobayashi, H. Kuroki, K. Mori, T. Shirai, T. Satake, S. Nakamura, R. Arai, Y. Nakagawa, T. Nakamura, and S. Matsuda, “Ultrasound can detect macroscopically undetectable changes in osteoarthritis reflecting the superficial histological and biochemical degeneration: ex vivo study of rabbit and human cartilage.,” *PLoS One*, vol. 9, no. 2, p. e89484, Jan. 2014.

[63] A. W. Palmer, R. E. Guldberg, and M. E. Levenston, “Analysis of cartilage matrix fixed charge density and three-dimensional morphology via contrast-enhanced microcomputed tomography.,” *Proc. Natl. Acad. Sci. U. S. A.*, vol. 103, no. 51, pp. 19255–60, Dec. 2006.

[64] J. D. Sandy and C. Verscharen, “Analysis of aggrecan in human knee cartilage and synovial fluid indicates that aggrecanase (ADAMTS) activity is responsible for the catabolic turnover and loss of whole aggrecan whereas other protease activity is required for C-terminal processing in vivo,” *Biochem. J.*, vol. 358, no. Pt 3, pp. 615–626, 2001.

[65] L. Xie, A. S. P. Lin, M. E. Levenston, and R. E. Guldberg, “Quantitative assessment of articular cartilage morphology via EPIC-microCT.,” *Osteoarthr. Cartil.*, vol. 17, no. 3, pp. 313–20, Mar. 2009.

[66] L. Xie, A. S. P. Lin, R. E. Guldberg, and M. E. Levenston, “Nondestructive assessment of sGAG content and distribution in normal and degraded rat articular cartilage via EPIC-microCT.,” *Osteoarthr. Cartil.*, vol. 18, no. 1, pp. 65–72, Jan. 2010.

[67] H. R. Moyer, Y. Wang, T. Farooque, T. Wick, K. A. Singh, L. Xie, R. E. Guldberg, J. K. Williams, B. D. Boyan, and Z. Schwartz, “A New Animal Model for Assessing Cartilage Repair and Regeneration at a Nonarticular Site,” *Tissue Eng. Part A*, vol. 16, no. 7, pp. 2321–30, 2010.

[68] C. S. Lee, O. A. Burnsed, V. Raghuram, J. Kalisvaart, B. D. Boyan, and Z. Schwartz, “Adipose stem cells can secrete angiogenic factors that inhibit hyaline cartilage regeneration,” *Stem Cell Res. Ther.*, vol. 3, no. 4, p. 35, Aug. 2012.

[69] L. Xie, A. S. P. Lin, K. Kundu, M. E. Levenston, N. Murthy, and R. E. Guldberg, “Quantitative imaging of cartilage and bone morphology, reactive oxygen species, and vascularization in a rodent model of osteoarthritis.,” *Arthritis Rheum.*, vol. 64, no. 6, pp. 1899–908, Jun. 2012.

[70] N. Kotwal, J. Li, J. Sandy, A. Plaas, and D. R. Sumner, “Initial application of EPIC-μCT to assess mouse articular cartilage morphology and composition: effects of aging and treadmill running.,” *Osteoarthr. Cartil.*, vol. 20, no. 8, pp. 887–95, Aug.

2012.

[71] N. S. Joshi, P. N. Bansal, R. C. Stewart, B. D. Snyder, and M. W. Grinstaff, “Effect of contrast agent charge on visualization of articular cartilage using computed tomography: exploiting electrostatic interactions for improved sensitivity.,” *J. Am. Chem. Soc.*, vol. 131, no. 37, pp. 13234–5, Sep. 2009.

[72] P. N. Bansal, N. S. Joshi, V. Entezari, B. C. Malone, R. C. Stewart, B. D. Snyder, and M. W. Grinstaff, “Cationic Contrast Agents Improve Quantification of Glycosaminoglycan (GAG) Content by Contrast Enhanced CT Imaging of Cartilage,” *J. Orthop. Res.*, vol. 29, no. 5, pp. 704–9, 2011.

[73] P. N. Bansal, R. C. Stewart, V. Entezari, B. D. Snyder, and M. W. Grinstaff, “Contrast agent electrostatic attraction rather than repulsion to glycosaminoglycans affords a greater contrast uptake ratio and improved quantitative CT imaging in cartilage.,” *Osteoarthr. Cartil.*, vol. 19, no. 8, pp. 970–6, Aug. 2011.

[74] R. C. Stewart, P. N. Bansal, V. Entezari, H. Lusic, R. M. Nazarian, B. D. Snyder, and M. W. Grinstaff, “Contrast-enhanced CT with a High-Affinity Cationic Contrast Agent for Imaging ex Vivo Bovine, Intact ex Vivo Rabbit, and in Vivo Rabbit Cartilage,” *Radiology*, vol. 266, no. 1, pp. 141–150, 2013.

[75] P. N. Bansal, N. S. Joshi, V. Entezari, M. W. Grinstaff, and B. D. Snyder, “Contrast enhanced computed tomography can predict the glycosaminoglycan content and biomechanical properties of articular cartilage.,” *Osteoarthr. Cartil.*, vol. 18, no. 2, pp. 184–91, Feb. 2010.

[76] L. N. M. Hayward, C. M. J. de Bakker, L. C. Gerstenfeld, M. W. Grinstaff, and E. F. Morgan, “Assessment of contrast-enhanced computed tomography for imaging of cartilage during fracture healing,” *J. Orthop. Res.*, vol. 31, no. 4, pp. 567–73, Apr. 2013.

[77] H. T. Kokkonen, J. Mäkelä, K. A. M. Kulmala, L. Rieppo, J. S. Jurvelin, V. Tiitu, H. M. Karjalainen, R. K. Korhonen, V. Kovanen, and J. Töyräs, “Computed tomography detects changes in contrast agent diffusion after collagen cross-linking typical to natural aging of articular cartilage.,” *Osteoarthr. Cartil.*, vol. 19, no. 10, pp. 1190–8, Oct. 2011.

[78] K. A. M. Kulmala, H. J. Pulkkinen, L. Rieppo, V. Tiitu, I. Kiviranta, A. Brunott, H. Brommer, R. van Weeren, P. A. J. Brama, M. T. Mikkola, R. K. Korhonen, J. S. Jurvelin, and J. Toyras, “Contrast-Enhanced Micro-Computed Tomography in Evaluation of Spontaneous Repair of Equine Cartilage,” *Cartilage*, vol. 3, no. 3, pp. 235–244, Apr. 2012.

[79] H. T. Kokkonen, J. S. Jurvelin, V. Tiitu, and J. Töyräs, “Detection of mechanical injury of articular cartilage using contrast enhanced computed tomography.,” *Osteoarthr. Cartil.*, vol. 19, no. 3, pp. 295–301, Mar. 2011.

[80] M. Siebelt, J. H. Waarsing, N. Kops, T. M. Piscaer, J. a N. Verhaar, E. H. G. Oei, and H. Weinans, “Quantifying osteoarthritic cartilage changes accurately using in vivo microCT arthrography in three etiologically distinct rat models.,” *J. Orthop. Res.*, vol. 29, no. 11, pp. 1788–94, Nov. 2011.

[81] K. P. H. Pritzker, S. Gay, S. A. Jimenez, K. Ostergaard, J.-P. Pelletier, P. A. Revell, D. Salter, and W. B. van den Berg, "Osteoarthritis cartilage histopathology: grading and staging.," *Osteoarthr. Cartil.*, vol. 14, no. 1, pp. 13–29, Jan. 2006.

[82] P. Cernohorsky, A. C. Kok, D. M. De Bruin, M. J. Brandt, D. J. Faber, G. J. Tuijthof, G. M. Kerkhoffs, S. D. Strackee, and T. G. van Leeuwen, "Comparison of optical coherence tomography and histopathology in quantitative assessment of goat talus articular cartilage.," *Acta Orthop.*, vol. 85, no. 6, pp. 1–7, Oct. 2014.

[83] S. Ghosh, J. Bowen, K. Jiang, D. M. Espino, and D. E. T. Shepherd, "Investigation of techniques for the measurement of articular cartilage surface roughness," *Micron*, vol. 44, pp. 179–184, 2013.

[84] J. L. Cook, K. Kuroki, A. Stoker, H. Streppa, and D. B. Fox, "Review of In Vitro Models and Development and Initial Validation of a Novel Co-Culture Model for the Study of Osteoarthritis," *Curr. Rheumatol. Rev.*, vol. 3, no. 3, pp. 172–182, 2007.

[85] M. Rutgers, D. B. F. Saris, W. J. a Dhert, and L. B. Creemers, "Cytokine profile of autologous conditioned serum for treatment of osteoarthritis, in vitro effects on cartilage metabolism and intra-articular levels after injection.," *Arthritis Res. Ther.*, vol. 12, no. 3, p. R114, Jan. 2010.

[86] G. M. van Buul, E. Villafuertes, P. K. Bos, J. H. Waarsing, N. Kops, R. Narcisi, H. Weinans, J. a N. Verhaar, M. R. Bernsen, and G. J. V. M. van Osch, "Mesenchymal stem cells secrete factors that inhibit inflammatory processes in short-term osteoarthritic synovium and cartilage explant culture.," *Osteoarthr. Cartil.*, vol. 20,

no. 10, pp. 1186–96, Oct. 2012.

[87] P. Patwari, S. N. Lin, B. Kurz, a a Cole, S. Kumar, and a J. Grodzinsky, “Potent inhibition of cartilage biosynthesis by coincubation with joint capsule through an IL-1-independent pathway.,” *Scand. J. Med. Sci. Sports*, vol. 19, no. 4, pp. 528–35, Aug. 2009.

[88] G. M. van Buul, W. L. M. Koevoet, N. Kops, P. K. Bos, J. a N. Verhaar, H. Weinans, M. R. Bernsen, and G. J. V. M. van Osch, “Platelet-rich plasma releasate inhibits inflammatory processes in osteoarthritic chondrocytes.,” *Am. J. Sports Med.*, vol. 39, no. 11, pp. 2362–70, Nov. 2011.

[89] C. Lübke, J. Ringe, V. Krenn, G. Fernahl, S. Pelz, R. Kreusch-Brinker, M. Sittinger, and M. Paulitschke, “Growth characterization of neo porcine cartilage pellets and their use in an interactive culture model.,” *Osteoarthr. Cartil.*, vol. 13, no. 6, pp. 478–87, Jun. 2005.

[90] D. J. Blasioli, G. L. Matthews, and D. L. Kaplan, “The degradation of chondrogenic pellets using cocultures of synovial fibroblasts and U937 cells.,” *Biomaterials*, vol. 35, no. 4, pp. 1185–91, Jan. 2014.

[91] V. P. Willard, B. O. Diekman, J. Sanchez-Adams, N. Christoforou, K. W. Leong, and F. Guilak, “Use of Cartilage Derived From Murine Induced Pluripotent Stem Cells for Osteoarthritis Drug Screening,” *Arthritis Rheumatol.*, vol. 66, no. 11, pp. 3062–3072, 2014.

[92] H. Iijima, T. Aoyama, A. Ito, J. Tajino, M. Nagai, X. Zhang, S. Yamaguchi, H.

Akiyama, and H. Kuroki, “Destabilization of the medial meniscus leads to subchondral bone defects and site-specific cartilage degeneration in an experimental rat model.,” *Osteoarthr. Cartil.*, vol. 22, no. 7, pp. 1036–43, Jul. 2014.

[93] G. Mohan, E. Perilli, I. H. Parkinson, J. M. Humphries, N. L. Fazzalari, and J. S. Kuliwaba, “Pre-emptive, early, and delayed alendronate treatment in a rat model of knee osteoarthritis: effect on subchondral trabecular bone microarchitecture and cartilage degradation of the tibia, bone/cartilage turnover, and joint discomfort,” *Osteoarthr. Cartil.*, vol. 21, no. 10, pp. 1595–1604, Oct. 2013.

[94] A. Panahifar, J. L. Jaremko, A. G. Tessier, R. G. Lambert, W. P. Maksymowych, B. G. Fallone, and M. R. Doschak, “Development and reliability of a multi-modality scoring system for evaluation of disease progression in pre-clinical models of osteoarthritis: celecoxib may possess disease-modifying properties.,” *Osteoarthr. Cartil.*, vol. 22, no. 10, pp. 1639–50, Oct. 2014.

[95] D. Reece, A. Lin, and R. Guldberg, “Contrast-Enhanced MicroCT Imaging,” in *Handbook of Imaging in Biological Mechanics*, C. P. Neu and G. M. Genin, Eds. CRC Press, 2014, pp. 127–42.

[96] M. Siebelt, H. C. Groen, S. J. Koelewijn, E. de Blois, M. Sandker, J. H. Waarsing, C. Müller, G. J. van Osch, M. de Jong, and H. Weinans, “Increased physical activity severely induces osteoarthritic changes in knee joints with papain induced sulphate-glycosaminoglycan depleted cartilage.,” *Arthritis Res. Ther.*, vol. 16, no. 1, p. R32, Jan. 2014.

[97] M. Siebelt, J. H. Waarsing, H. C. Groen, C. Müller, S. J. Koelewijn, E. de Blois, J. a N. Verhaar, M. de Jong, and H. Weinans, "Inhibited osteoclastic bone resorption through alendronate treatment in rats reduces severe osteoarthritis progression.," *Bone*, vol. 66, pp. 163–70, Sep. 2014.

[98] M. Siebelt, A. E. van der Windt, H. C. Groen, M. Sandker, J. H. Waarsing, C. Müller, M. de Jong, H. Jahr, and H. Weinans, "FK506 protects against articular cartilage collagenous extra-cellular matrix degradation.," *Osteoarthr. Cartil.*, vol. 22, no. 4, pp. 591–600, Apr. 2014.

[99] N. J. Willett, T. Thote, M. Hart, S. Moran, R. E. Guldberg, and R. V. Kamath, "Quantitative pre-clinical screening of therapeutics for joint diseases using contrast enhanced micro-computed tomography," *Osteoarthr. Cartil.*, vol. 24, pp. 1604–12, 2016.

[100] Q. Wang, Z. Liu, Y. Wang, Q. Pan, Q. Feng, Q. Huang, and W. Chen, "Quantitative Ultrasound Assessment of Cartilage Degeneration in Ovariectomized Rats with Low Estrogen Levels," *Ultrasound Med. Biol.*, vol. 42, no. 1, pp. 290–298, 2016.

[101] A. Laib, O. Barou, L. Vico, M.-H. Lafage-Proust, C. Alexandre, and P. Rugsegger, "3D micro-computed tomography of trabecular and cortical bone architecture with application to a rat model of immobilisation osteoporosis," *Med. Biol. Eng. Comput.*, vol. 38, no. 3, pp. 326–332, 2000.

[102] "ASTM Standard F2791, 2009 (2015), 'Standard Guide for Assessment of Surface Texture of Non-Porous Biomaterials in Two Dimensions.'" ASTM International,

West Conshohocken, PA, 2015.

[103] Z. Xie, S. Liachenko, P.-C. Chiao, S. Carvajal-Gonzalez, S. Bove, and T. Bocan, "In vivo MRI assessment of knee cartilage in the medial meniscal tear model of osteoarthritis in rats," *Lect. Notes Comput. Sci. (including Subser. Lect. Notes Artif. Intell. Lect. Notes Bioinformatics)*, vol. 6363, no. PART 3, pp. 375–382, 2010.

[104] C. Buckland-Wright, "Subchondral bone changes in hand and knee osteoarthritis detected by radiography," *Osteoarthr. Cartil.*, vol. 12, no. SUPLL., pp. 10–19, 2004.

[105] D. B. Burr, "Anatomy and physiology of the mineralized tissues: Role in the pathogenesis of osteoarthrosis," *Osteoarthr. Cartil.*, vol. 12, no. SUPLL., pp. 20–30, 2004.

[106] D. G. Yu, S. B. Nie, F. X. Liu, C. L. Wu, B. Tian, W. G. Wang, X. Q. Wang, Z. A. Zhu, and Y. Q. Mao, "Dynamic alterations in microarchitecture, mineralization and mechanical property of subchondral bone in rat medial meniscal tear model of osteoarthritis," *Chin. Med. J. (Engl).*, vol. 128, no. 21, pp. 2879–2886, 2015.

[107] T. Maerz, M. D. Newton, H. W. T. Matthew, and K. C. Baker, "Surface roughness and thickness analysis of contrast-enhanced articular cartilage using mesh parameterization," *Osteoarthr. Cartil.*, vol. 24, no. 2, pp. 290–298, 2016.

[108] T. P. Andriacchi, S. Koo, and S. F. Scanlan, "Gait mechanics influence healthy cartilage morphology and osteoarthritis of the knee.," *J. Bone Joint Surg. Am.*, vol. 91 Suppl 1, pp. 95–101, Feb. 2009.

[109] V. Pedoia, X. Li, F. Su, N. Calixto, and S. Majumdar, “Fully Automatic Analysis of the Knee Articular Cartilage T1ρ relaxation time using Voxel Based Relaxometry,” *J. Magn. Reson. imaging*, vol. 43, no. 4, pp. 970–980, 2016.

[110] N. Gerwin, C. Hops, and A. Lucke, “Intraarticular drug delivery in osteoarthritis.,” *Adv. Drug Deliv. Rev.*, vol. 58, no. 2, pp. 226–42, May 2006.

[111] T. J. Koob, J. J. Lim, M. Massee, N. Zabek, and G. Denozière, “Properties of dehydrated human amnion/chorion composite grafts: Implications for wound repair and soft tissue regeneration,” *J. Biomed. Mater. Res. - Part B Appl. Biomater.*, vol. 102, no. 6, pp. 1353–1362, 2014.

[112] W. P. Faulk, R. Matthews, P. J. Stevens, J. P. Bennett, H. Burgos, and B. L. Hsi, “Human amnion as an adjunct in wound healing,” *Lancet*, vol. 1, no. 8179, pp. 1156–1158, 1980.

[113] C. a. Akle, M. Adinolfi, K. I. Welsh, S. Leibowitz, and I. McColl, “Immunogenicity of human amniotic epithelial cells after transplantation into volunteers,” *Lancet*, vol. 2, no. 8254, pp. 1003–1005, 1981.

[114] Y. Hao, D. H. Ma, D. G. Hwang, W. Kim, D. Ph, F. Zhang, and D. Ph, “Identification of Antiangiogenic and Antiinflammatory Proteins in Human Amniotic Membrane,” *Cornea*, vol. 19, no. 3, pp. 348–352, 2000.

[115] D. Ilic, L. Vicovac, M. Nikolic, and E. Lazic Ilic, “Human amniotic membrane grafts in therapy of chronic non-healing wounds,” *Br. Med. Bull.*, vol. 117, no. 1, pp. 59–67, 2016.

[116] A. L. Raines, M.-S. Shih, L. Chua, C.-W. Su, S. C. G. Tseng, and J. O'Connell, "Efficacy of Particulate Amniotic Membrane and Umbilical Cord Tissues in Attenuating Cartilage Destruction in an Osteoarthritis Model," *Tissue Eng. Part A*, vol. 23, no. 1 and 2, pp. 12–19, 2017.

[117] J. Vines, A. Aliprantis, A. Gomoll, and J. Farr, "Cryopreserved Amniotic Suspension for the Treatment of Knee Osteoarthritis," *J. Knee Surg.*, vol. 1, no. 212, 2015.

[118] W. Chen, A. Palazzo, W. E. Hennink, and R. J. Kok, "The effect of particle size on drug loading and release kinetics of gefitinib-loaded PLGA microspheres," *Mol. Pharm.*, p. acs.molpharmaceut.6b00896, 2016.

[119] D. S. Reece, T. Thote, A. S. P. Lin, N. J. Willett, and R. E. Guldberg, "Contrast Enhanced μCT Imaging of Early Articular Changes in a Pre-Clinical Model of Osteoarthritis," *Osteoarthr. Cartil.*, no. In Revision, 2017.

[120] R. Dua, K. Comella, R. Butler, G. Castellanos, B. Brazille, A. Claude, A. Agarwal, J. Liao, and S. Ramaswamy, "Integration of stem cell to chondrocyte-derived cartilage matrix in healthy and osteoarthritic states in the presence of hydroxyapatite nanoparticles," *PLoS One*, vol. 11, no. 2, pp. 1–19, 2016.

[121] M. B. Goldring, K. Tsuchimochi, and K. Ijiri, "The control of chondrogenesis," *J. Cell. Biochem.*, vol. 97, no. 1, pp. 33–44, 2006.

[122] S. Jingushi, J. Shida, Y. Iwamoto, T. Kinoshita, Y. Hiyama, M. Tamura, and T. Izumi, "Transient Exposure of Fibroblast Growth Factor-2 Induced Proliferative but

Not Destructive Changes in Mouse Knee Joints," *Connect. Tissue Res.*, vol. 47, pp. 242–248, 2006.

[123] T. J. Koob, J. J. Lim, M. Massee, N. Zabek, R. Rennert, G. Gurtner, and W. W. Li, "Angiogenic properties of dehydrated human amnion/chorion allografts: therapeutic potential for soft tissue repair and regeneration.," *Vasc. Cell*, vol. 6, no. 1, p. 10, 2014.

[124] S. F. Badylak, J. E. Valentin, A. K. Ravindra, G. P. McCabe, and A. M. Stewart-Akers, "Macrophage phenotype as a determinant of biologic scaffold remodeling.," *Tissue Eng. Part A*, vol. 14, no. 11, pp. 1835–42, 2008.

[125] S. H. R. Edwards, "Intra-articular drug delivery: The challenge to extend drug residence time within the joint," *Vet. J.*, vol. 190, no. 1, pp. 15–21, 2011.

[126] C. Z. Jin, S. R. Park, B. H. Choi, K.-Y. Lee, C. K. Kang, and B.-H. Min, "Human amniotic membrane as a delivery matrix for articular cartilage repair.," *Tissue Eng.*, vol. 13, no. 4, pp. 693–702, Apr. 2007.

[127] A. M. Silverstein, R. M. Stefani, E. Sobczak, E. L. Tong, M. G. Attur, R. P. Shah, J. C. Bulinski, G. A. Ateshian, and C. T. Hung, "Toward understanding the role of cartilage particulates in synovial inflammation," *Osteoarthr. Cartil.*, pp. 1–9, 2016.

[128] M. De Mattei, K. Varani, F. F. Masieri, A. Pellati, A. Ongaro, M. Fini, R. Cadossi, F. Vincenzi, P. a Borea, and A. Caruso, "Adenosine analogs and electromagnetic fields inhibit prostaglandin E2 release in bovine synovial fibroblasts.," *Osteoarthr. Cartil.*, vol. 17, no. 2, pp. 252–62, Feb. 2009.

[129] L. a. Fortier, T. Motta, R. a. Greenwald, T. J. Divers, and K. G. Mayr, “Synoviocytes are more sensitive than cartilage to the effects of minocycline and doxycycline on IL-1a and MMP-13-induced catabolic gene responses,” *J. Orthop. Res.*, vol. 28, no. 4, pp. 522–528, 2010.

[130] H. Cheon, Y. K. Sun, S. J. Yu, Y. H. Lee, J. D. Ji, G. G. Song, J. H. Lee, M. K. Kim, and J. Sohn, “Platelet-derived growth factor-AA increases IL-1beta and IL-8 expression and activates NF-kappaB in rheumatoid fibroblast-like synoviocytes.,” *Scand. J. Immunol.*, vol. 60, no. 5, pp. 455–62, 2004.

[131] C. E. Page, S. Smale, S. M. Carty, N. Amos, S. N. Lauder, R. M. Goodfellow, P. J. Richards, S. A. Jones, N. Topley, and A. S. Williams, “Interferon-γ inhibits interleukin-1β-induced matrix metalloproteinase production by synovial fibroblasts and protects articular cartilage in early arthritis,” *Arthritis Res. Ther.*, vol. 12, 2010.

[132] Y. Kataoka, W. Ariyoshi, T. Okinaga, T. Kaneuji, S. Mitsugi, T. Takahashi, and T. Nishihara, “Mechanisms involved in suppression of ADAMTS4 expression in synoviocytes by high molecular weight hyaluronic acid,” *Biochem. Biophys. Res. Commun.*, vol. 432, no. 4, pp. 580–585, 2013.

[133] H. J. Braun, H. J. Kim, C. R. Chu, and J. L. Dragoo, “The effect of platelet-rich plasma formulations and blood products on human synoviocytes: implications for intra-articular injury and therapy.,” *Am. J. Sports Med.*, vol. 42, no. 5, pp. 1204–10, May 2014.

[134] P. Patwari, J. Fay, M. N. Cook, a M. Badger, a J. Kerin, M. W. Lark, and a J.

Grodzinsky, “In vitro models for investigation of the effects of acute mechanical injury on cartilage.,” *Clin. Orthop. Relat. Res.*, vol. 391, no. Suppl, pp. S61-71, Oct. 2001.

[135] A. J. Nixon, J. L. Haupt, D. D. Frisbie, S. S. Morisset, C. W. McIlwraith, P. D. Robbins, C. H. Evans, and S. Ghivizzani, “Gene-mediated restoration of cartilage matrix by combination insulin-like growth factor-I/interleukin-1 receptor antagonist therapy.,” *Gene Ther.*, vol. 12, no. 2, pp. 177–86, Jan. 2005.

[136] D. D. Greenberg, A. Stoker, S. Kane, M. Cockrell, and J. L. Cook, “Biochemical effects of two different hyaluronic acid products in a co-culture model of osteoarthritis.,” *Osteoarthr. Cartil.*, vol. 14, no. 8, pp. 814–22, Aug. 2006.

[137] A. Anz, M. J. Smith, A. Stoker, C. Linville, H. Markway, K. Branson, and J. L. Cook, “The effect of bupivacaine and morphine in a coculture model of diarthrodial joints.,” *Arthroscopy*, vol. 25, no. 3, pp. 225–31, Mar. 2009.

[138] L. Sun, X. Wang, and D. L. Kaplan, “A 3D cartilage - Inflammatory cell culture system for the modeling of human osteoarthritis.,” *Biomaterials*, vol. 32, no. 24, pp. 5581–9, Aug. 2011.

[139] E. Kalaitzoglou, T. M. Griffin, M. B. Humphrey, and M. B. Humphrey, “Innate Immune Responses and Osteoarthritis,” *Curr. Rheumatol. Rep.*, vol. 19, no. 45, pp. 17–22, 2017.

[140] P. Bonaventura, G. Courbon, A. Lamboux, F. Lavocat, H. Marotte, F. Albarède, and P. Miossec, “Protective effect of low dose intra-articular cadmium on inflammation

and joint destruction in arthritis," *Sci. Rep.*, vol. 7, p. 2415, 2017.

[141] O. Parolini, L. Souza-Moreira, F. O 'valle, M. Magatti, P. Hernandez-Cortes, E. Gonzalez-Rey, and M. Delgado, "Therapeutic Effect of Human Amniotic Membrane–Derived Cells on Experimental Arthritis and Other Inflammatory Disorders," *Arthritis Rheumatol.*, vol. 66, no. 2, pp. 327–339, 2014.

[142] S. F. Badylak, "Regenerative medicine and developmental biology: The role of the extracellular matrix," *Anat. Rec. - Part B New Anat.*, vol. 287, no. 1, pp. 36–41, 2005.

[143] A. C. Allison, J. Ferluga, H. Prydz, and H. U. Schorlemmer, "The Role of Macrophage Activation in Chronic Inflammation," *Agents Actions*, vol. 8, no. 1–2, pp. 27–35, 1978.

[144] P. C. Heinrich, J. V Castell, and T. Andus, "Interleukin-6 and the acute phase response," *Biochem. J.*, vol. 265, no. 3, pp. 621–636, 1990.

[145] J. Lei, L. B. Priddy, J. J. Lim, and T. J. Koob, "Dehydrated Human Amnion/Chorion Membrane (dHACM) Allografts as a Therapy for Orthopedic Tissue Repair," *Tech. Orthop.*, vol. 0, no. 0, pp. 1–9, 2017.

[146] M. Durigova, H. Nagase, J. S. Mort, and P. J. Roughley, "MMPs are less efficient thatn ADAMTS5 in cleaving aggrecan core protein," *Matrix Biol.*, vol. 30, no. 2, pp. 145–153, 2011.

[147] P. R. Wardwell, M. B. Forstner, and R. A. Bader, "Investigation of the cytokine

response to NF- κ B decoy oligonucleotide coated polysaccharide based nanoparticles in rheumatoid arthritis in vitro models Investigation of the cytokine response to NF- κ B decoy oligonucleotide coated polysaccharide based nanoparticles in rheumatoid arthritis in vitro models," *Arthritis Res. Ther.*, 2015.

[148] O. Schultz, G. Keyszer, J. Zacher, M. Sittinger, and G. R. Burmester, "Development of in vitro model systems for destructive joint diseases: novel strategies for establishing inflammatory pannus.," *Arthritis Rheum.*, vol. 40, no. 8, pp. 1420–8, Aug. 1997.

[149] M. Neidhart, R. E. Gay, and S. Gay, "Anti-interleukin-1 and anti-CD44 interventions producing significant inhibition of cartilage destruction in an in vitro model of cartilage invasion by rheumatoid arthritis synovial fibroblasts.," *Arthritis Rheum.*, vol. 43, no. 8, pp. 1719–28, Aug. 2000.

[150] P. Das Neves Borges, a E. Forte, T. L. Vincent, D. Dini, and M. Marenzana, "Rapid, automated imaging of mouse articular cartilage by microCT for early detection of osteoarthritis and finite element modelling of joint mechanics.," *Osteoarthr. Cartil.*, vol. 22, no. 10, pp. 1419–28, Oct. 2014.

[151] P. N. Borges, T. L. Vincent, and M. Marenzana, "Fast-throughput assessment of osteophyte growth in murine osteoarthritis for cross-sectional or longitudinal microct studies," *Osteoarthr. Cartil.*, vol. 22, no. 2014, pp. S260–S261, 2014.

[152] T. M. Piscaer, J. H. Waarsing, N. Kops, P. Pavljasevic, J. a N. Verhaar, G. J. V. M. van Osch, and H. Weinans, "In vivo imaging of cartilage degeneration using

microCT-arthrography.," *Osteoarthr. Cartil.*, vol. 16, no. 9, pp. 1011–7, Sep. 2008.

[153] J. van Tiel, M. Siebelt, J. H. Waarsing, T. M. Piscaer, M. van Straten, R. Booij, M. L. Dijkshoorn, G. J. Kleinrensink, J. a N. Verhaar, G. P. Krestin, H. Weinans, and E. H. G. Oei, "CT arthrography of the human knee to measure cartilage quality with low radiation dose.," *Osteoarthr. Cartil.*, vol. 20, no. 7, pp. 678–85, Jul. 2012.

[154] Y. Zhang, S. Ji, H. Fang, Y. Zheng, P. Luo, H. Wu, M. Wu, Z. Wang, S. Xiao, and Z. Xia, "Use of Amniotic Microparticles Coated With Fibroblasts Overexpressing SDF-1 a to Create an Environment Conducive to Neovascularization for Repair of Full-Thickness Skin Defects," *Cell Transplant.*, vol. 25, pp. 365–376, 2016.

[155] M. D. Smith, "The normal synovium," *Open Rheumatol. J.*, vol. 5, no. Suppl 1:M2, pp. 100–6, 2011.

[156] M. D. Silva, A. Savinainen, R. Kapadia, J. Ruan, E. Siebert, N. Avitahl, R. Mosher, K. Anderson, B. Jaffee, L. Schopf, and S. Chandra, "Quantitative Analysis of Micro-CT Imaging and Histopathological Signatures of Experimental Arthritis in Rats," *Mol. Imaging*, vol. 3, no. 4, pp. 312–318, 2004.

[157] C. S. Bonnet, A. S. Williams, S. J. Gilbert, A. K. Harvey, B. a Evans, and D. J. Mason, "AMPA/kainate glutamate receptors contribute to inflammation, degeneration and pain related behaviour in inflammatory stages of arthritis.," *Ann. Rheum. Dis.*, Oct. 2013.

[158] H. Ogata, M. Takeya, T. Yoshimura, K. Takagi, and K. Takahashi, "The Role of Monocyte Chemoattractant Protein-1 (MCP-1) in the Pathogenesis of Collagen-

Induced Arthritis in Rats," *J. Pathol.*, vol. 182, pp. 106–114, 1997.

[159] C. Plummer, "The use of amniotic membrane transplantation for ocular surface reconstruction : a review and series of 58 equine ...," *Vet. Ophthalmol.*, vol. 12, no. Supplement 1, pp. 17–24, 2009.

[160] D. Garcia, U. L. Longo, J. Vaquero, F. Forriol, M. Loppini, W. Khan, and V. Denaro, "Amniotic Membrane Transplant For Articular Cartilage Repair : An Experimental Study In Sheep," *Curr. Stem Cell Res. Ther.*, vol. 9, 2014.

[161] C. M. Zelen, A. Poka, and J. Andrews, "Prospective , Randomized , Blinded , Comparative Study of Injectable Micronized Dehydrated Amniotic / Chorionic Membrane Allograft for Plantar Fasciitis — A Feasibility Study," *Foot Ankle Int.*, vol. 34, no. 10, pp. 1332–1339, 2013.

[162] J. A. Mcintyre, I. A. Jones, A. Danilkovich, and C. T. J. Vangsness, "The Placenta - Applications in Orthopaedic Sports Medicine," *Am. J. Sports Med.*, pp. 1–14, 2017.

[163] A. A. Guccione, D. T. Felson, J. J. Anderson, J. M. Anthony, Y. Zhang, P. W. F. Wilson, M. Kelly-Hayes, P. a. Wolf, B. E. Kreger, and W. B. Kannel, "The effects of specific medical conditions on the functional limitations of elders in the Framingham study," *Am. J. Public Health*, vol. 84, no. 3, pp. 351–358, 1994.

[164] M. G. Cisternas, L. Murphy, J. J. Sacks, D. H. Solomon, D. J. Pasta, and C. G. Helmick, "Alternative Methods for Defining Osteoarthritis and the Impact on Estimating Prevalence in a US Population-Based Survey," *Arthritis Care Res. (Hoboken).*, vol. Accepted A, 2015.

[165] D. J. Hunter, “Osteoarthritis,” *Best Pract. Res. Clin. Rheumatol.*, vol. 25, no. 6, pp. 801–814, 2011.

[166] J. Clouet, C. Vinatier, C. Merceron, M. Pot-vaucel, Y. Maugars, P. Weiss, G. Grimandi, and J. Guicheux, “From osteoarthritis treatments to future regenerative therapies for cartilage,” *Drug Discov. Today*, vol. 14, no. 19–20, pp. 913–925, 2009.

[167] H. a Wieland, M. Michaelis, B. J. Kirschbaum, and K. a Rudolphi, “Osteoarthritis - an untreatable disease?,” *Nat. Rev. Drug Discov.*, vol. 4, no. 4, pp. 331–344, 2005.

[168] J. Martel-Pelletier, L. M. Wildi, and J.-P. Pelletier, “Future therapeutics for osteoarthritis.,” *Bone*, vol. 51, no. 2, pp. 297–311, Aug. 2012.

[169] M. A. Karsdal, M. Michaelis, C. Ladel, A. S. Siebuhr, A. R. Bihlet, J. R. Andersen, H. Guehring, C. Christiansen, A. C. Bay-Jensen, and V. B. Kraus, “Disease-modifying treatments for osteoarthritis (DMOADs) of the knee and hip: lessons learned from failures and opportunities for the future,” *Osteoarthr. Cartil.*, vol. 24, no. 12, pp. 2013–2021, 2016.

[170] S. F. Badylak, “The extracellular matrix as a biologic scaffold material,” *Biomaterials*, vol. 28, no. 25, pp. 3587–3593, 2007.

[171] V. J. Mase, J. R. Hsu, S. E. Wolf, J. C. Wenke, D. G. Baer, J. Owens, S. F. Badylak, and T. J. Walters, “Clinical application of an acellular biologic scaffold for surgical repair of a large, traumatic quadriceps femoris muscle defect.,” *Orthopedics*, vol. 33, no. 7, p. 511, 2010.

[172] I. Velez, W. B. Parker, M. A. Siegel, and M. Hernandez, “Cryopreserved Amniotic Membrane for Modulation of Periodontal Soft Tissue Healing: A Pilot Study,” *J. Periodontol.*, vol. 81, no. 12, pp. 1797–1804, 2010.

[173] J. S. Gruss and D. W. Jirsch, “Human amniotic membrane: a versatile wound dressing,” *Can. Med. Assoc. J.*, vol. 118, no. 10, pp. 1237–46, 1978.

[174] Q. He, Q. Li, B. Chen, and Z. Wang, “Repair of flexor tendon defects of rabbit with tissue engineering method,” *Chinese J. Traumatol.*, vol. 5, no. 4, pp. 200–8, 2002.

[175] N. Mligiliche, K. Endo, K. Okamoto, E. Fujimoto, and C. Ide, “Extracellular matrix of human amnion manufactured into tubes as conduits for peripheral nerve regeneration,” *J. Biomed. Mater. Res.*, vol. 63, no. 5, pp. 591–600, 2002.

[176] K. Gajiwala and A. L. Gajiwala, “Evaluation of lyophilised, gamma-irradiated amnion as a biological dressing,” *Cell Tissue Bank.*, vol. 5, no. 2, pp. 73–80, 2004.

[177] A. Chandra, O. P. Maurya, B. Reddy, G. Kumar, K. Pandey, and G. Bhaduri, “Amniotic membrane transplantation in ocular surface disorders,” *J. Indian Med. Assoc.*, vol. 103, no. 7, p. 364–366,368, 2005.

[178] S. Thatte, “Amniotic membrane transplantation: An option for ocular surface disorders.,” *Oman J. Ophthalmol.*, vol. 4, no. 2, pp. 67–72, 2011.

[179] T. Hildebrand and P. Rüegsegger, “A new method for the model-independent assessment of thickness in three-dimensional images,” *J. Microsc.*, vol. 185, no. November 1995, pp. 67–75, 1997.

[180] a Laib, O. Barou, L. Vico, M. H. Lafage-Proust, C. Alexandre, and P. Rügsegger, "3D micro-computed tomography of trabecular and cortical bone architecture with application to a rat model of immobilisation osteoporosis.," *Med. Biol. Eng. Comput.*, vol. 38, no. 3, pp. 326–332, 2000.

[181] D. S. Reece, T. Thote, G. E. Salazar-Noratto, L. Krishnan, A. S. P. Lin, N. J. Willett, and R. E. Guldberg, "Novel Method of Evaluating Cartilage Surface Roughness in a Rat OA Model using Contrast Based MicroCT Imaging," in *Annual Meeting of the Orthopedic Research Society*, 2014.

[182] a. M. Bendele, "Animal models of osteoarthritis in an era of molecular biology," *J. Musculoskelet. Neuronal Interact.*, vol. 2, no. 6, pp. 501–503, 2002.

[183] E. E. Moore, a. M. Bendele, D. L. Thompson, a. Littau, K. S. Waggie, B. Reardon, and J. L. Ellsworth, "Fibroblast growth factor-18 stimulates chondrogenesis and cartilage repair in a rat model of injury-induced osteoarthritis," *Osteoarthr. Cartil.*, vol. 13, no. 7, pp. 623–631, 2005.

[184] V. B. Kraus, J. L. Huebner, J. DeGroot, and a. Bendele, "The OARSI histopathology initiative - recommendations for histological assessments of osteoarthritis in the guinea pig," *Osteoarthr. Cartil.*, vol. 18, no. SUPPL. 3, pp. S35–S52, 2010.

[185] K. Gelse, S. Söder, W. Eger, T. Diemtar, and T. Aigner, "Osteophyte development - Molecular characterization of differentiation stages," *Osteoarthr. Cartil.*, vol. 11, no. 2, pp. 141–148, 2003.

[186] M. a Karsdal, a C. Bay-Jensen, R. J. Lories, S. Abramson, T. Spector, P. Pastoureau, C. Christiansen, M. Attur, K. Henriksen, S. R. Goldring, and V. Kraus, "The coupling of bone and cartilage turnover in osteoarthritis: opportunities for bone antiresorptives and anabolics as potential treatments?," *Ann. Rheum. Dis.*, vol. 73, no. 2, pp. 336–48, Feb. 2014.

[187] S. Sakano, Y. Hasegawa, Y. Murata, T. Ito, E. Genda, H. Iwata, N. Ishiguro, and H. Seo, "Inhibitory effect of bFgF on endochondral heterotopic ossification," *Biochem. Biophys. Res. Commun.*, vol. 293, no. 2, pp. 680–685, 2002.

[188] J. S. Dounchis, R. S. Goomer, F. L. Harwood, M. Khatod, R. D. Coutts, and D. Amiel, "Chondrogenic phenotype of perichondrium-derived chondroprogenitor cells in influence by transforming Growth Factor-Beta 1," *J. Orthop. Res.*, vol. 15, no. 6, pp. 803–7, 1997.

[189] E. de Bri, W. Lei, O. Svensson, M. Chowdhury, S. a Moak, and R. a Greenwald, "Effect of an inhibitor of matrix metalloproteinases on spontaneous osteoarthritis in guinea pigs.," *Adv. Dent. Res.*, vol. 12, no. 2, pp. 82–85, 1998.